Modelling of Elevated Mesoscale Convective Systems

Bethan Alice White

Submitted in accordance with the requirements for the degree of
Doctor of Philosophy

The University of Leeds
School of Earth and Environment
June 2012

Declaration of Authorship

The candidate confirms that the work submitted is her own, except where work which has formed part of jointly-authored publications has been included. The contribution of the candidate and the other authors to this work has been explicitly indicated below. The candidate confirms that appropriate credit has been given within the thesis where reference has been made to the work of others.

The candidate contributed work to the article outlined below, which has been accepted for publication in the Quarterly Journal of the Royal Meteorological Society. The candidate is a co-author of the article. The article was first published online on 1 March 2012, ahead of the publication of the journal issue, and at the time of submitting the thesis for examination, the journal issue is still awaiting publication.

Some, but not all, of the results from the modelling study presented in Chapter 5 were used in Section 4.2 of Browning, Marsham, White and Nicol (2012) to support their observational analysis. The author of this thesis performed the analysis in Chapter 5 in its entirety. The observational analysis presented in Browning, Marsham, White and Nicol (2012) is not the work of the author of this thesis and was performed by Keith Browning, John Marsham and John Nicol. As such, where the observations from Browning, Marsham, White and Nicol (2012) have been discussed in this thesis, they have been referenced accordingly.

Publication details:

Browning, K. A., Marsham, J. H., White, B. A. and Nicol, J.C. 2012. A case study of a large patch of billows surmounted by elevated convection. *Quarterly Journal of the Royal Meteorological Society*

Acknowledgements

Many people have provided help and support throughout the duration of this study. This work could not have been completed without their input.

First and foremost I would like to extend my thanks to my supervisors **Alan Blyth** and **John Marsham** for all of their help, support and guidance over the last few years. **Doug Parker** and **Keith Browning** have also been incredibly helpful and have provided many interesting and enlightening discussions.

I would also like to thank **Steven Pickering** and **Ralph Burton** for their knowledge and tireless effort in providing modelling support for WRF.

Advice for modifying the WRF microphysics scheme was very kindly given by **Chris Dearden**.

This work was funded by the National Environment Research Council (NERC). Additional financial support was provided by the UK Met Office through a CASE award.

It has been a pleasure to be a part of the friendly and supportive working environment at the Institute for Climate and Atmospheric Science, and more generally the School of Earth and Environment, at the University of Leeds.

Finally, but by no means least, I would like to thank my family and all of my friends for their support over the years.

Abstract

Elevated convection occurs when convection originates from above the boundary layer. The interaction of an elevated storm with the stable layer beneath it often generates features such as waves and bores that maintain the convection.

The Convective Storm Initiation Project (CSIP) took place in the UK in 2005. Only one case of elevated convection was observed during CSIP, in which several mesoscale convective systems (MCSs) formed. One MCS remained elevated and wave-lifted throughout the observation period. Another elevated MCS observed during IOP 3 was associated with Kelvin-Helmholtz billows. The billows and the elevated convection appeared to interact.

The aim of this thesis is to use high-resolution numerical models to investigate the processes occurring in the elevated MCSs observed during CSIP. The thesis is presented in two parts. In the first part a simulation is performed using the Weather Research and Forecasting (WRF) model. The model reproduces the wave-lifted elevated convection in the early stages of the simulation but, unlike the observations, the simulated convection becomes surface-based and gravity current-lifted. The sensitivity of the simulated MCS to surface heat fluxes and diabatic cooling processes is explored. Surface heating and advection are shown to increase the buoyancy of the boundary layer air and enhance the transition to surface-based convection. Diabatic cooling processes are shown to maintain the simulated MCS in two ways: they strengthen the descent of the rear-inflow jet, generating a wave, and they also strengthen the undercurrent via cold outflow from the north of the storm. In the second part of this thesis the Met Office Large Eddy Model is used to investigate the interaction between Kelvin-Helmholtz billows and elevated convection. It is shown that there is a strong coupling between the updraughts and downdraughts in the billows and convective clouds.

Contents

List of Figures

List of Tables

Chapter 1

Motivation and Background

1.1 Introduction

Atmospheric convection is the vertical transport of heat associated with positive buoyancy. The release of latent heat by condensation results in moist convection, where the buoyancy is provided by the latent heat release. Severe (moist) convection in the atmosphere is responsible for various hazardous weather phenomena such as large hail, damaging winds, tornadoes and heavy rain. The hazards associated with severe convection can mostly be attributed to the energy released by phase changes of water. Assuming an average condensed water content of 1 g m^{-3}, a convective cloud of radius 5 km and depth 10 km will contain about 8 x 10^8 kg of condensed water (Doswell, 2001). The latent heat energy released during the condensation of that water is about 10^{14} J, comparable to a quarter of the energy released in a 1-megaton bomb (Doswell, 2001), although the timescale of the energy release is about 25 minutes in the cloud and a fraction of a second in the bomb. Most of the energy released by the cloud is used in doing work against gravity, but some of it may also create severe weather. A significant recent example of the severe weather impact of convection in the UK was the Boscastle flash flood in Cornwall on 16 August 2004 (Burt, 2005; Golding *et al.*, 2005). A series of intense convective storms developed along the north coast of Cornwall. More than 200 mm of rain was recorded at the head of the river catchment above Boscastle, and peak rain rates may have reached 400 mm hr^{-1}. The heavy rainfall caused flash floods that destroyed buildings, vehicles and bridges.

Most of the difficulties in forecasting severe convection lie in predicting the timing and location of the initiation of new convective cells. Convective initiation can be either primary - the development of convection in a region that was not previously convective - or secondary - the initiation of convective cells by processes associated with previous convection. Current observational data is often insufficient for accurate forecasting of convection. Mesoscale features in the pre-convective environment, such as convergence lines, can influence the initiation of convection. Accurate forecasts of convection depend on the observation of such features. Small-scale differences in temperature and moisture can also be important to the location of convective initiation, and current surface and sounding observations do not have a high enough spatial or temporal resolution to resolve these variations.

Convection is often initiated within the boundary layer, and Bennett *et al.* (2006) showed that there are many local processes in the boundary layer that can contribute to convective initiation. However, convection can also be initiated and occur above the boundary layer, a phenomenon known as "elevated convection". This is discussed later in Section 1.6. Elevated convection is more difficult to forecast than convection that is based in the boundary layer, partly because the processes responsible for its initiation are not well understood, partly because initiation can occur in regions far away from areas of strong surface-based instability (such as surface heating and convergence lines), and partly because, compared to surface data, there is a lack of observational data made above the ground.

The difficulties in predicting the exact timing and location of severe convective storms mean that the severe weather with which they are associated can sometimes occur with little or no prior warning. Numerical weather prediction (NWP) models perform best at forecasting convective events when the gridscales are small enough that the model can resolve convection explicitly rather than requiring a parameterisation. Even when convection can be explicitly resolved, smaller gridlengths have been shown to represent convective processes more effectively than longer gridlengths (Lean *et al.*, 2008).

Three complementary field campaigns have recently contributed to the understanding of the processes that initiate convective storms. The International H_2O Project in 2002 (IHOP, Weckwerth *et al.*, 2004) investigated the initiation of convection over the flat, continental region of the southern great plains of the United States. The Convective Storm

Initiation Project (CSIP, Browning *et al.*, 2007), took place in 2005 and investigated the initiation of convection in the midlatitude maritime climate of the UK, an environment that is also representative of other parts of Northern Europe and North America. The Convective and Orographically Induced Precipitation Study in 2007 (COPS, Wulfmeyer *et al.*, 2008) investigated convective initiation in mountainous continental regions.

The term "mesoscale convective system" (MCS) was defined by Zipser (1982) as a weather feature that exhibits moist convective overturning contiguous with or embedded within a mesoscale circulation that is at least partially driven by the convective processes. Houze (2004) gave a descriptive definition of an MCS as "a cumulonimbus cloud system that produces a contiguous precipitation area of about 100 km or more in at least one direction". These broad definitions cover a range of scales of phenomena, from groups of individual thunderstorms with short lifetimes to long-lived tropical storms and hurricanes. Nearly all MCSs consist of deep convective components and an associated region of stratiform cloud and precipitation (Fritsch and Forbes, 2001). According to Yuter and Houze (1995), "convective conditions" are where the mean vertical air velocity is much greater than the mean terminal fall speed of precipitation-sized ice and snow particles (about 1–3 m s^{-1}), and "stratiform conditions" are where the mean vertical air velocity is much smaller than the mean terminal fall speed of precipitation particles. The convective components of an MCS tend to be organised into lines, although this is not always the case (Fritsch and Forbes, 2001). The convective part of an MCS produces the bulk of the severe weather, while the stratiform region is associated with lighter rainfall. The stratiform region is produced partly by the dissipation of older convective cells and partly by broader mesoscale ascent (Houze, 2004). MCSs advance by a combination of advection and propagation. The advective component of the movement is strongly correlated with the mean flow in the cloud layer (Fritsch and Forbes, 2001).

MCSs are often classified according to scale. (Maddox, 1980) defined meso-α scale systems to have length scales from 250 to 2500 km and time scales of more than 6 hours and meso-β scale systems to have length scales of 25 to 250 km and time scales of less than 6 hours. Meso-α systems include tropical squalls, midlatitude squall lines, tropical storms and cyclones, and midlatitude systems with large circular cloud clusters (Maddox, 1980).

Most observational case studies of MCSs presented in the literature have been in the United States, but MCSs can occur in any part of the world that is prone to deep convection (Laing and Fritsch, 1997; Smull, 1995). MCSs are an important climatological feature of the United States. According to Fritsch *et al.* (1986), MCSs account for approximately 30% to 70% of the warm-season (April to September) precipitation over the region between the Rocky Mountains and the Mississippi River. Similarly, Schumacher and Johnson (2006) found that 74% of all warm-season extreme rain events in the eastern US from 1999-2003 were associated with an MCS. Fritsch *et al.* (1986) also found that MCSs were likely to be the most prolific producers of precipitation in the Unites States, even more so than hurricanes.

MCSs have been observed significantly less frequently in the UK than in the US, but two recent cases have been analysed by Browning *et al.* (2010) and Clark *et al.* (2012b). It is more difficult to successfully predict the initiation and evolution of an MCS compared to isolated convective systems (Weckwerth *et al.*, 1996). This requires a model to resolve processes across a range of scales from large-scale uplift and baroclinic processes to small-scale convective processes and even subgrid-scale turbulence. The interactions of these processes are not well understood, and a large amount of computational power is required to resolve the full range of processes.

1.2 The thermodynamics of convective initiation

An air parcel is stable with respect to its environment if, after it has been displaced vertically, its density with respect to its new surroundings is such that it will rise or sink back towards its original level. A parcel is unstable if, after its vertical displacement, its new density is such that it will tend to move away from its original level. Conditional instability (CI) occurs if a displaced parcel is unstable if it is saturated, but stable otherwise. To reach the point of instability the parcel must undergo forced lifting through the region of stability. The level of free convection (LFC) is the level at which an air parcel lifted adiabatically in a conditionally unstable atmosphere first becomes less dense than its surroundings. Once a parcel reaches its LFC it becomes positively buoyant and hence unstable.

An effect known as "hydrometeor loading" reduces the buoyancy of a parcel. When hydrometeors fall they accelerate due to gravity. The air around them provides resistance - inducing a drag effect - and becomes more dense and therefore less buoyant.

If an air parcel is lifted adiabatically, it will eventually reach a level where it is saturated. This is known as the lifting condensation level (LCL), and is the point where condensation occurs and cloud forms.

In a conditionally unstable atmosphere energy must usually be supplied in order to lift the parcel through the LCL to its LFC. The amount of energy required to do this work is called the convective inhibition (CIN). A buoyant parcel will ascend until it reaches its level of neutral buoyancy (LNB), the height at which the lifted parcel has the same density as its surroundings. The amount of energy that is released during this ascent is known as the convective available potential energy (CAPE). Values of CAPE are used to indicate atmospheric instability; any value greater than 0 J kg^{-1} indicates instability, and values greater than 2500 J kg^{-1} tend to indicate strong instability.

1.3 The organisation and structure of linear MCSs

A group of thunderstorms that has a linear organisation is often referred to as a squall line. A rigorous definition of a squall line does not exist, although Doswell (2001) suggests that a minimal definition could be a system that consists of as few as two isolated convective cells that are close enough together that the perturbation flows from the cells can interact. An outflow boundary, with gust front winds at its leading edge, should be sufficient for a linear organisation of convective cells to be classified as a squall line. From an analysis of radar reflectivity data, Parker and Johnson (2000) proposed a classification system of linear mesoscale convective systems based upon the distribution of the stratiform precipitation associated with the MCSs. A "linear MCS" was defined to be an MCS which contained a convective line, a contiguous or nearly contiguous chain of convective echoes sharing a leading edge and moving approximately together. The arrangement of the echoes in a linear MCS could be a straight line or a gently curved arc. Three types of organisation were identified: "trailing stratiform" (TS), where most of the stratiform

precipitation occurred behind the convective line, "leading stratiform" (LS), where stratiform precipitation occurred ahead of the convective line, and "parallel stratiform" (PS), where stratiform precipitation occurred parallel to the convective line. A schematic diagram showing these three types is shown in Figure 1.1. The vertical structure of a trailing stratiform MCS is discussed later in Section 1.4

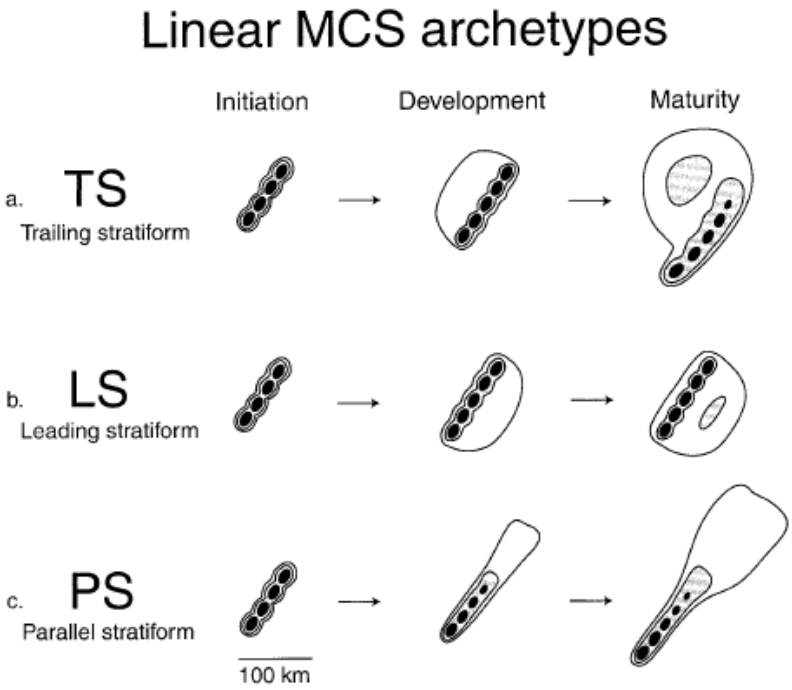

FIGURE 1.1: Schematic reflectivity drawing of idealised life cycles for three linear MCS archetypes: (a) TS, (b) LS and (c) PS. Approximate time intervals between phases for TS 3–4 h; for LS 2–3 h; for PS 2–3 h. Levels of shading roughly correspond to 20, 40 and 50 dBZ. From Parker and Johnson (2000).

Idealised simulations of the TS and LS modes of linear convection were performed by Parker and Johnson (2004), who found that the magnitude of the shear vector and its orientation with respect to a cold pool or baroclinic boundary was the most important factor in deciding which of the organisational modes would develop. Although the deep-layer shear was shown to be important, the shear in the lower troposphere had the greatest effect.

1.4 Rear-inflow jets

During the mature stage of convective systems that develop a large trailing region of stratiform precipitation, a system-relative flow of air into the stratiform precipitation region from mid-levels at the rear of the system is often observed. These "rear-inflow jets" (RIJs) provide a supply of dry, potentially cold air from the mid-levels to the convective-scale and system-scale downdraughts. RIJs have been observed in both mid-latitude squall lines (e.g. Houze *et al.*, 1989) and tropical squall lines (e.g. Chong *et al.*, 1987).

1.4.1 The structure of rear-inflow jets

A conceptual model of the broad mesoscale airflow in a mature squall line with a trailing stratiform region was constructed by Houze *et al.* (1989) using Doppler radar data obtained during the PRE-STORM [1] project (Figure 1.2). General vertical motion begins in the boundary layer near the gust front, extends up through the convective region, and slopes more gently when it enters the trailing stratiform region at mid- and upper-levels. Superimposed on this general ascent are intense, localised updraughts and downdraughts in the convective region. These updraughts and downdraughts are associated with cells within the squall line. New cells of convection have a tendency to form on or just in front of the leading edge of the region of heavy convective showers, and may be lifted by the gust front.

The trailing stratiform region is characterised by a region of high radar reflectivity, but not as high as in the convective region, which occurs immediately below the melting level (Figure 1.2). A sloping layer of descending air with a storm-relative RTF flow enters the stratiform precipitation region just below the trailing stratiform cloud (Houze *et al.*, 1989). This is the RIJ. As it descends, the RIJ passes through the melting level and reaches the back of the convective line at low levels. Ahead of the convective line is gust front outflow from the convective region. The amount of the RIJ that enters the convective region and strengthens the convergence at the gust front compared to the amount that is blocked by the convection and turns parallel to the squall line is not well known (Houze *et al.*, 1989).

[1] Preliminary Regional Experiment for Stormscale Operational and Research Meteorology - Central Phase, conducted in Oklahoma and Kansas during May and June 1985 (Cunning, 1986).

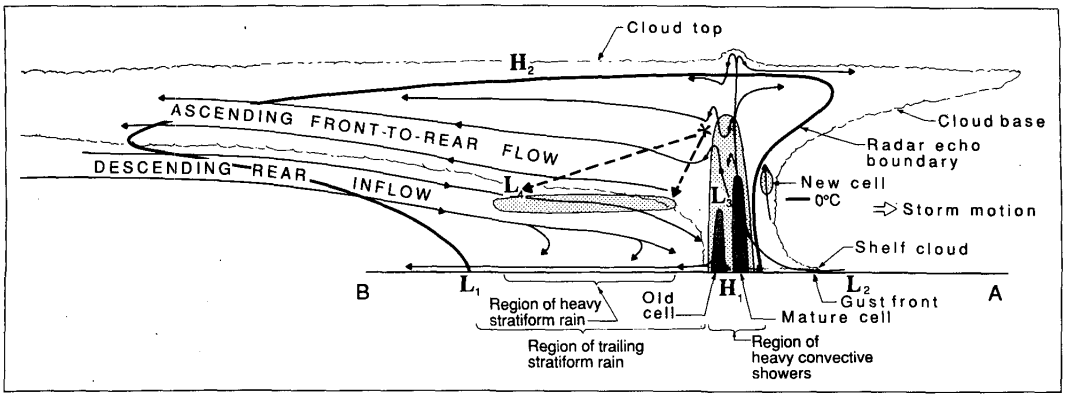

FIGURE 1.2: Conceptual model of the kinematic, microphysical, and radar echo structure of a convective line with trailing-stratiform precipitation viewed in a vertical cross section oriented perpendicular to the convective line (and generally parallel to its motion). Intermediate and strong radar reflectivity is indicated by medium and dark shading, respectively. 'H' and 'L' indicate centres of positive and negative pressure perturbations, respectively. Dashed-line arrows indicate fallout trajectories of ice particles passing through the melting layer. From Houze *et al.* (1989).

The RIJ is one of a pair of slantwise circulations that occur in the stratiform region. Above the RIJ, in the trailing stratiform region, is a sloping layer of ascending air with a storm-relative front-to-rear (FTR) flow that originates from the upper part of the convective region (Figure 1.2). This flow transports ice particles that it has detrained from the convective region to the rear of the storm (Rutledge *et al.*, 1988), seeding the stratiform region with ice particles. The layer between the ascending FTR flow and the descending RIJ is characterised by strong shear, convergence and horizontal and vertical vorticity (Houze *et al.*, 1989). The shear in this layer can be strong enough for Kelvin-Helmholtz instability to occur (Houze *et al.*, 1989). The Kelvin-Helmholtz instability is discussed later in Section 1.9.

A trailing region of stratiform precipitation is a necessary condition for a RIJ to develop, and may also allow the development of structures similar to RIJs in other types of storm. In their idealised simulations of a tropical cyclone, Franklin *et al.* (2006) found that after a rainband in the cyclone developed a stratiform region, a mid-level jet similar to a RIJ formed.

1.4.2 Mesohighs and mesolows

Two surface pressure features commonly accompany squall lines: the mesohigh and the mesolow (Haertel and Johnson, 2000). The mesohigh is centred just below the convective line and a mesolow is centred on the strong reflectivity gradient at the trailing edge of the stratiform region. The surface mesolow at the rear of the storm is known as a "wake low" The mesohighs and mesolows of the pressure field of a typical trailing stratiform mesoscale convective system are shown in Figure 1.2, indicated by 'H' and 'L'. At the back edge of the stratiform precipitation region a wake low (L_1) occurs in association with warming due to unsaturated descent. Below the convective region is a mesohigh (H_1), associated with the convective downdraughts. Ahead of the convective line, at the surface, warming by compensating downward motion causes a weak mesolow (L_2). A small hydrostatic mesolow (L_3) occurs at mid-levels underneath the main sloping convective updraught (LeMone, 1983). At the rear of the system, in or just above the melting layer, is another, larger, mesolow (L_4), which probably develops due to continued subsidence after rainfall, and its evaporation, have diminished (Brown, 1979). At upper levels, at the top of the cloud system, is a mesohigh (H_2). The upper-level mesohigh is thought to be due to a region of cold air that develops at the top of the convective system due to a combination of evaporation and convectively-forced lifting and adiabatic cooling (Maddox *et al.*, 1981).

Mesohighs are primarily hydrostatic in nature. The air above the mesohigh in the convective region is cool and dense. The hydrostatic pressure increase associated with the cool, dense air accounts for most of the increased pressure in the mesohigh (Haertel and Johnson, 2000). The coolness has been attributed to the evaporation, melting and sublimation of hydrometeors (Zhang and Gao, 1989). The local cooling of air by phase changes of water causes air parcels to become negatively buoyant, descend, and transport the coolness downward. However, additional contributions to the mesohigh can be attributed to hydrometeor loading and to the non-hydrostatic effects of the downdraught impinging on the surface (Johnson, 2001)

Mesolows are also primarily hydrostatic. The decreased pressure in the wake low approximately equals the hydrostatic pressure decrease associated with a warmer, less dense lower troposphere (Haertel and Johnson, 2000). The warming is attributed to subsidence, but

several processes have been suggested as the cause of the subsidence: that it forms dynamically by the spread of cold air near the surface, that it is a surface manifestation of a RIJ, that it is associated with latent cooling, or that it may be due to gravity wave activity (Haertel and Johnson, 2000). Idealised simulations performed by Haertel and Johnson (2000) showed that the mesohigh-wake low couplet can be thought of as a quasi-steady-state linear response to the low-level cooling associated with stratiform precipitation.

1.4.3 The formation of rear-inflow jets

The factors causing the initial development of a RIJ are dynamical rather than microphysical. In addition, the processes that generate RIJs are internal to the convective system; ambient flow into the storm is not required. In one of the cases studied by Smull and Houze (1987), a RIJ developed within the stratiform precipitation region even though there was no ambient rear-inflow. Some of the "stagnation zone" cases (defined in Section 1.4.5) described by Smull and Houze (1987) had weak rear-inflow at the back edge of the system, with strong RTF flow at mid-levels in the stratiform region close to the leading convective line. The strength of a RIJ is defined in terms of its system-relative horizontal wind speed. Chong *et al.* (1987) observed a tropical squall line in which the strength of the RIJ intensified near the main convective region. This led Smull and Houze (1987) to suggest the RIJ was generated by processes internal to the convective system without the need for ambient flow into the back edge of the stratiform region. Based on the results of LeMone (1983) and LeMone and Zipser (1984), Smull and Houze (1987) suggested that the flow is accelerated by a mesolow that develops under the warm convective updraught that slopes over the cold surface outflow. Additional evidence that RIJs are formed by processes internal to the convective system and that ambient flow into the rear of the storm is not a necessary requirement for their development is that RIJs form in idealised simulations of MCSs that use horizontally homogeneous initial conditions (e.g. Weisman, 1992).

Once a RIJ has developed, it can, however, be strengthened by ambient flow. Braun and Houze (1997) used mesoscale modelling and surface analysis to study a case where a squall line formed perpendicular to strong upper-level flow that extended below the height of the anvil. The direction of the ambient flow was towards the convective system. The upper-level flow caused ambient flow into the rear of the squall line. The RIJ was very

strong, which suggested that it had been strengthened by the upper-level ambient flow. The three "strong rear-inflow" cases analysed by Smull and Houze (1987) all had strong environmental flow across the back edge of the squall line. The numerical simulations of Zhang and Gao (1989) also showed that the RIJ could be significantly strengthened if helped by the large-scale environmental flow.

Once formed, RIJs can also be strengthened by microphysical processes. Yang and Houze (1995) studied the component of the RIJ that was generated by the convective system and found that evaporation, melting and sublimation in the stratiform region affected the strength of the RIJ. Chen and Cotton (1988) found that removing melting from their model weakened the strength of the RIJ. The sensitivity of RIJs to microphysical processes is discussed later in Section 1.4.8.

Some authors distinguish different regions of flow within the RIJ. "Rear-inflow" was used by Smull and Houze (1987) and Braun and Houze (1997) to describe the component of the RIJ that flows into the rear of the storm near the back edge of the region of trailing stratiform precipitation. "Rear-to-front" (RTF) flow was used to describe the component of the RIJ that descends from the stratiform precipitation region into the convective region.

1.4.4 The rôle of mesolows in the formation of rear-inflow jets

Smull and Houze (1987) described the presence of two velocity maxima within the RIJ of the 10-11 June 1985 PRE-STORM squall. One velocity maximum occurred near the back edge of the trailing stratiform region, and the other occurred within and behind the leading convective region. They suggested that the presence of two maxima meant that two separate mechanisms for the generation of RIJs might exist within convective systems. The two mechanisms could work together to produce a stronger RIJ. They suggested that the mid-level mesolow in the stratiform region (L_4 in Figure 1.2) acts in conjunction with the mesolow in the convective region (L_3 in Figure 1.2) to establish a broad current of RTF flow across the whole convective system. Klimowski (1994) also observed two velocity maxima within the RIJ in an MCS on 28-29 June 1989. Like the 10-11 June 1985 PRE-STORM case, one maximum was observed near the convective core, while the other was under the trailing stratiform region. Klimowski (1994) reported that the maximum in the

rear-inflow near the convective core developed first, leading to the suggestion that two independent processes produced the maxima.

Zhang and Gao (1989) used a mesoscale model to investigate the mesolow RIJ hypothesis of Smull and Houze (1987). They found that despite a strong mid-level mesolow, the RTF flow was weak and did not descend to the surface. Yang and Houze (1995) used a cloud model with explicitly-resolved convection and an initially horizontally homogeneous environment; no large-scale effects were included. They found that two separate mid-level mesolows were involved in the development of RTF flow. These two mesolows acted constructively to generate a significant RIJ across the system. It therefore appears that the RIJ is generated by the two mesolows acting in conjunction, and that the mesolows are convectively-generated. It follows that in order for a realistic RIJ to develop in a model, the model must be able to resolve convection explicitly. The simulation of Zhang and Gao (1989) probably failed to develop a strong RIJ because their mesoscale model was unable to resolve the processes that formed one of the mesolows.

1.4.5 Classification of rear-inflow jets.

In an attempt to characterise the properties of RIJs, Smull and Houze (1987) studied eighteen observed cases of RIJs in squall lines with trailing stratiform precipitation. The strength of the RIJ varied significantly from case to case. They classified their cases into three types: "strong rear-inflow", where the maximum strength of the RIJ was greater than 10 m s^{-1}, "weak rear-inflow", where the maximum strength of the RIJ was between 5 and 10 m s^{-1}, and "stagnation zone cases", where the RIJ was either nonexistent or very weak, with a storm-relative velocity of less than 5 m s^{-1}. Three of their eighteen cases were classified as strong rear-inflow. In the strong rear-inflow cases the velocity maximum in the RIJ occurred near 550 hPa. Five of their cases were classified as weak rear-inflow cases. The remaining ten cases were classified as stagnation zone cases.

The existence of the stagnation zone cases described by Smull and Houze (1987) suggested two distinct modes of airflow in squall lines with trailing stratiform precipitation. The stagnation zone cases had a 200-300 hPa-deep (about 2-3 km) layer of air that moved at about the same speed as the system. The stagnation zone cases had no significant

rear-inflow at the back edge of the system, but did have RTF flow. The RTF flow in the stagnation zone cases was weaker than the RTF flow observed in the strong rear inflow cases. This suggested that the RTF flow was generated by processes internal to the convective system, without the need for ambient flow into the rear of the storm.

1.4.6 Descending versus elevated rear-inflow jets.

RIJs tend to either remain elevated and horizontal or descend to the surface and spread out behind the leading edge of the gust front, strengthening the gust front winds. A third possibility exists, where the RIJ descends but does not reach the surface. This appears to be a rare form of RIJ behaviour that is of great dynamical significance to the storm, and is discussed in detail later. Weisman (1992) showed that whether an elevated or descending jet is produced depends on the relative strength of the horizontal buoyancy gradients at the back edge of the system. If the horizontal buoyancy gradients associated with the warm convective plume are equal to or greater than the gradients associated with the surface cold pool, then the jet tends to remain elevated. If the horizontal buoyancy gradients associated with the cold pool are greater than those in the plume, the jet descends to the surface and spreads out. This is discussed in more detail in Section 1.5.1.

Most observed cases of RIJs are of the type which descend to the surface and spread out behind the leading edge of the convective system. Ogura and Liou (1980) and Smull and Houze (1987) both described such a case on 22 May 1976, which was later simulated by Fovell and Ogura (1988). The observations revealed a RIJ with a system-relative strength of 10 m s^{-1} that descended to the surface 100 km behind the leading edge of the storm. Another case, occurring on 10-11 June 1985, was described by Smull and Houze (1987) and Rutledge *et al.* (1988). The RIJ remained elevated during the early stage of the evolution of the system, and then descended and reached the surface about 30 km behind the leading edge. The system-relative strength of the RIJ ranged from about 10 m s^{-1} at 50 km behind the leading edge to over 15 m s^{-1} at 150 km. Braun and Houze (1997) documented a squall line on 10-11 June 1985 during PRE-STORM that developed a particularly strong RIJ which descended to the surface. The RIJ in the 28-29 June 1989 case presented by Klimowski (1994) was elevated during the initial stages of its development, before descending to the surface over time.

In numerical simulations, both Fovell and Ogura (1989) and Weisman (1992) found a tendency for the RIJ to be elevated when there was strong background shear. This behaviour was explained by Weisman (1992) and is discussed later in Section 1.5.1. Smull and Houze (1987) described a case on 28 May 1985 where the observed RIJ remained elevated. The RIJ had a strength of 10-15 m s^{-1} within 20 km of the leading edge. Chong *et al.* (1987) also described a case of an elevated RIJ observed on 22 June 1981, in which the vertical wind shear was 15-20 m s^{-1} over the lowest few kilometres. Another documented case of a RIJ that remained elevated was given by Jorgensen *et al.* (2004) in a study of the evolution of a bow-echo observed during BAMEX [1] on 10 June 2003. Strong mid-level rear-inflow with a ground-relative speed of more than 40 m s^{-1} was observed along with more than 20 m s^{-1} of shear over the lowest 1.5 km. Doppler radar data showed a RIJ which began to descend during the first few hours of observation, but subsequently the descent weakened and the RIJ remained aloft.

A RIJ that did not penetrate to the surface was produced in the 2D simulations of an extratropical MCS by Chen and Cotton (1988), who found that turning off longwave radiation caused the RIJ to be weaker than that in a control run, and that the RIJ no longer penetrated to the surface. Doppler radar observations were made by Jorgensen *et al.* (2004) during BAMEX of a RIJ that failed to reach the surface. Although a strong descending RIJ was observed, no strong surface winds or gusts were associated with the passage of the bow echo, indicating that the RIJ did not penetrate to the surface. Doppler radar data showed that the RIJ weakened over time and became quasi-horizontal. Soundings taken ahead of the storm revealed that the weakening of the RIJ coincided with the stabilisation of the lower levels, from the surface to about 700 hPa. Jorgensen *et al.* (2004) suggested that the stabilisation of the low-level layer helped to prevent the RIJ from penetrating to the surface and prevented the formation of strong surface winds. Detailed observations of an MCS during CSIP on 24 June 2005 that developed a RIJ which descended but did not reach the surface were made by Browning *et al.* (2010). The interaction of the descending RIJ with a low-level stable layer had significant implications for the maintenance of the convection. This case study is described in detail later and forms the basis of the modelling studies in Chapters 3 and 4.

[1] The Bow-Echo and Mesoscale Convective Vortex Experiment

In the case of descending RIJs, it is usual for the jet to penetrate to the surface. However, under certain circumstances this may not happen, as in the RIJ observed by Browning *et al.* (2010). A clear distinction must be made between an elevated RIJ, which represents one of the regimes of RIJ dynamics, and a descending jet which does not penetrate to the surface.

1.4.7 The rôle of rear-inflow jets on the structure and evolution of an MCS

RIJs can alter the structure and evolution of a convective system and represent a way in which MCSs interact with their large-scale environment. In some cases an intense RIJ has been linked to the weakening of convection and a dissipation of the system (e.g. Ogura and Liou, 1980; Rutledge *et al.*, 1988; Smull and Houze, 1987). However, in other cases, strong convection and a strong overall system circulation remained for a long time after the development of a RIJ (e.g. Chong *et al.*, 1987; Houze *et al.*, 1989; Smull and Houze, 1987).

Lafore and Moncrieff (1989) suggested that if a RIJ descends to the surface it can increase the surface convergence along the gust front, thus strengthening the gust front from the convective outflow and enhancing the convective system by triggering new cells. The descent of the RIJ to the surface in the case described by Braun and Houze (1997) was associated with a surge in outflow from the squall line. Two of the cases studied in detail by Smull and Houze (1987) showed a RIJ descending to the leading convective line. The air in the RIJ merged with the outflow from the convective downdraughts and the resulting mixed air moved forward to the leading gust front, indicating that the RIJ was able to influence the intensity and propagation of deep convection at the leading edge of the squall line. Chong *et al.* (1987) observed a RIJ that descended to the convective line. They determined that convective and mesoscale downdraughts were responsible for 40 and 60% of the outflow, respectively, illustrating the importance of the mesoscale flow to the total outflow.

If the descent of the RIJ to the surface and its subsequent mixing with the outflow from the convective downdraughts causes the depth of the evaporatively-cooled air behind the

gust front to increase, this can cause the propagation speed of the convective system to increase (Charba, 1974). Observational evidence for this was shown by Smull and Houze (1987), who found that deeper outflow corresponded to a faster squall line..

As well as having the potential to strengthen the convective system, it has also been shown that the penetration of the RIJ to the surface through the main region of convective updraughts can contribute to the dissipation of the convective system. The RIJ modelled by Braun and Houze (1997) descended to the surface at a point where the pre-storm environment was less favourable for convection. The descending RIJ blocked the inflow to the convection, contributing to the dissipation of the storm. Lafore and Moncrieff (1989) also suggested that a RIJ could weaken a convective system if the subsidence behind the system is too strong, which could lower the overall amount of RTF circulation and make it less efficient in releasing convective instability.

1.4.8 The sensitivity of rear-inflow jets to microphysical processes

1.4.8.1 Hydrometeor types

Yang and Houze (1995) found that RIJ dynamics were sensitive to hydrometeor types. In their numerical simulations of the 10-11 June 1985 PRE-STORM squall line, they found that allowing heavy hailstones to occur during the mature and decaying stages of the squall line prevented the velocity maximum at the rear of the RIJ from developing. Their control run did not include heavy hail. In the control run, hydrometeors were transported further back into the stratiform region. Diabatic heating and cooling thus occurred over a larger region, leading to the hydrostatic generation of a mid-level mesolow in the stratiform region that favoured the development of a RIJ. With heavy hail, a weaker buoyancy gradient at the rear of the system meant that the horizontal pressure gradient associated with the mid-level mesolow was too weak to generate a wind maximum in the RIJ.

1.4.8.2 Ice phase microphysics

Ice phase microphysics have been shown to be essential to the development of realistically-structured RIJs in cloud models. Using the 10-11 June 1995 PRE-STORM case study,

Yang and Houze (1995) performed a simulation in which the ice phase microphysics were removed and found that, compared to their control run, the system propagated more slowly and did not develop a stratiform precipitation region. The stratiform region of precipitation is produced by the rearward transport and subsequent melting of snow particles. The velocity maximum at the rear of the system did not develop in the Yang and Houze (1995) experiment without ice phase microphysics. Removing the ice phase microphysics also caused the mesoscale updraughts and downdraughts to be narrower, the leading-edge convective updraught to be weaker and the potential temperature perturbation of the warm plume to be weaker.

1.4.8.3 Latent cooling by evaporation

Sensitivity tests to latent cooling by evaporation have shown that the descent of the RIJ is strengthened by dynamical and microphysical feedback processes in the trailing stratiform precipitation region. In cloud model simulations, Yang and Houze (1995) found that removing latent cooling by evaporation caused an unrealistic storm to develop. Without evaporative cooling, no cold pool developed and the system did not tilt upshear. According to RKW theory (discussed later in Section 1.5.1), in order for the system to tilt upshear the vorticity generated by the cold pool is required to overcome the vorticity associated with the environmental shear. Because the system failed to tilt upshear, a trailing stratiform precipitation region did not develop (Yang and Houze, 1995) and there was no mesoscale ascent or descent. Because the convective region did not tilt upshear, no mid-level mesolow developed, and therefore neither did the FTR flow, which would transport hydrometeors to the rear. The RTF flow in the no evaporative cooling experiment of Yang and Houze (1995) was elevated and was attributable entirely to strong mid-level winds in the large-scale environment. Franklin *et al.* (2006) performed a sensitivity study to evaporative processes in an idealised model. Using their unmodified case study which developed a RIJ, they turned off rain evaporation and the melting of graupel and snow. A mid-level jet failed to develop after these processes were switched off.

1.4.8.4 Latent cooling by melting

Leary and Houze (1979) suggested that cooling by melting may be responsible for initiating the mesoscale updraughts and downdraughts, but Yang and Houze (1995) showed that this is not the case in cloud models. However, Yang and Houze (1995) found that cooling by melting did significantly enhance the mesoscale downdraughts. In their cloud model simulations of the 10-11 June 1985 PRE-STORM case study, Yang and Houze (1995) found that the velocity maximum in the RIJ that occurred near the back edge of the stratiform precipitation region was weaker when latent cooling by melting was removed. This led to the conclusion that latent cooling by melting is responsible for at least 25% of the local velocity maximum in the RIJ at the rear of the storm. Removing melting from a 2D mesoscale model, Chen and Cotton (1988) found that the RIJ was only weakened slightly, not enough for melting to be driving the flow.

1.4.8.5 Latent cooling by sublimation

In cloud model simulations, Yang and Houze (1995) found that setting latent cooling by sublimation to zero, but still allowing warming due to deposition, caused very little change to the structure and evolution of the simulated storm. They concluded that cooling by evaporation and melting are the most important processes that determine the structure and strength of a RIJ in cloud-model simulations. However, a component of the observed RIJ in the 10-11 June 1985 PRE-STORM case, on which the simulations of Yang and Houze (1995) were based, was due to ambient flow above the melting level. Zhang and Gao (1989) showed that the ambient RTF flow was caused by a shortwave trough at upper levels. The ambient component of the RIJ that occurred above the melting level could not develop in the cloud model used by Yang and Houze (1995). Braun (1995) showed that the structure and strength of the RIJ is more sensitive to latent cooling by sublimation above the melting level. The RIJ studied in a mesoscale model by Braun and Houze (1997) showed greater sensitivity to sublimation than to evaporation. The RIJ developed a core of maximum velocity after the onset of strong sublimational cooling at the back edge of the storm. In a sensitivity test where sublimational cooling was turned off, no velocity maximum in the RIJ developed. In contrast, when evaporative cooling was turned off, only minor changes to the RIJ were seen.

1.4.8.6 The effects of moisture at mid-levels

The strength of the RIJ is affected by moisture at mid-levels. Yang and Houze (1995) showed that when the environmental moisture at mid-levels was reduced by about half the amount of its initial value, the resulting RIJ was significantly weaker. This was due to the effect that moisture has on the orientation of the convective system: Drier environmental air entrained into the convective region leads to greater evaporative cooling at mid-levels, which acts against the vorticity tendency produced by the cold pool (Rotunno *et al.*, 1988; Weisman, 1992, discussed in Section 1.5.1) and leads to the convective system becoming more upright. This reduces the FTR flow, meaning that hydrometeors are not transported as far to the rear of the storm, and therefore the stratiform region becomes weaker and narrower. As the stratiform region weakens and narrows, sublimation, melting and evaporation are all reduced. As a result, the horizontal buoyancy gradients in the stratiform region are weaker, and the RTF flow is weaker (Yang and Houze, 1995).

1.4.9 The choice of model used to study rear-inflow jets

The choice of model used to study RIJs has an effect on the features that are resolvable, and must be considered when drawing conclusions from model results. Braun and Houze (1997) compared their mesoscale modelling studies of the sensitivity of the RIJ to ice processes with the mesoscale studies of Zhang and Gao (1989) and the high-resolution studies of Yang and Houze (1995). All three studies showed that ice-phase processes were fundamental, however different processes were resolvable by the different models. Mesoscale models (Braun and Houze, 1997; Zhang and Gao, 1989) were able to capture the large-scale ambient flow as well as describing the broad features of the storm. However, small-scale microphysical processes were not resolvable, and this may be the reason that Braun and Houze (1997) found that cooling due to sublimation appeared to be much more important than the evaporation of rain to the development of the velocity maximum in the RIJ. The high-resolution cloud-scale model used by Yang and Houze (1995) was able to capture the small-scale microphysical processes, but did not include any of the interaction of the storm with the large-scale ambient flow.

The fact that sublimation was seen to be important in the mesoscale model results of Braun and Houze (1997) and Zhang and Gao (1989), while evaporation was important in the cloud-scale results of Yang and Houze (1995), suggests that ice processes are important on different scales. Braun and Houze (1997) suggested that as ice falls, it sublimates in the post-stratiform precipitation region and melts and evaporates in the convective and stratiform precipitation regions. The small-scale convective region, where melting and evaporation occurs, cannot be resolved by mesoscale models. The larger-scale stratiform region, where sublimation occurs, can be captured by mesoscale models.

1.5 The maintenance of deep convection via the cold-pool–shear interaction

A theory for the mechanics of long-lived squall lines in a shear environment was developed by Rotunno, Klemp and Weisman (1988). This mechanism is often called "RKW theory" after the names of the three authors. RKW theory states that when a storm generates a cold pool that flows into a shear environment, the optimal state for convection exists when the vorticity of the low-level shear balances the vorticity of the cold pool, causing the deepest possible lifting at the leading edge of the cold pool.

Figure 1.3 is a schematic diagram that shows how the interaction of wind shear and a cold pool can affect a buoyant updraught due to the vorticity associated with the shear and cold pool. With no shear and no cold pool (Figure 1.3a) the buoyancy distribution creates positive vorticity on one side of the updraught and negative vorticity on the other, in equal amounts, and so the updraught is vertical. With no shear and a cold pool (Figure 1.3b), the buoyancy distribution that defines the cold pool generates additional negative vorticity at the nose of the cold pool. The influence of the negative vorticity at the edge of the cold pool causes the updraught to tilt to the rear. The cold pool is thus detrimental to the updraught. In a shear environment with no cold pool (Figure 1.3c) an air parcel entering the updraught begins with positive vorticity generated by the environmental shear and the axis of the updraught tilts downshear. A shear environment is thus detrimental to convection, as the energy of the updraughts is drained by the shear, and precipitation may fall into its inflow. If both shear and a cold pool are present (Figure 1.3d), the action of

the cold pool can oppose that of the shear and a vertical updraught can develop "if the circulation associated with the cold pool's negative vorticity approximately balances the circulation associated with the positive vorticity of the low-level shear" (Rotunno *et al.*, 1988). Cold pools are located at low-levels and shear can therefore only enhance convection if it is restricted to low levels. A full vorticity budget analysis of the squall line, cold pool and shear is given in Rotunno *et al.* (1988).

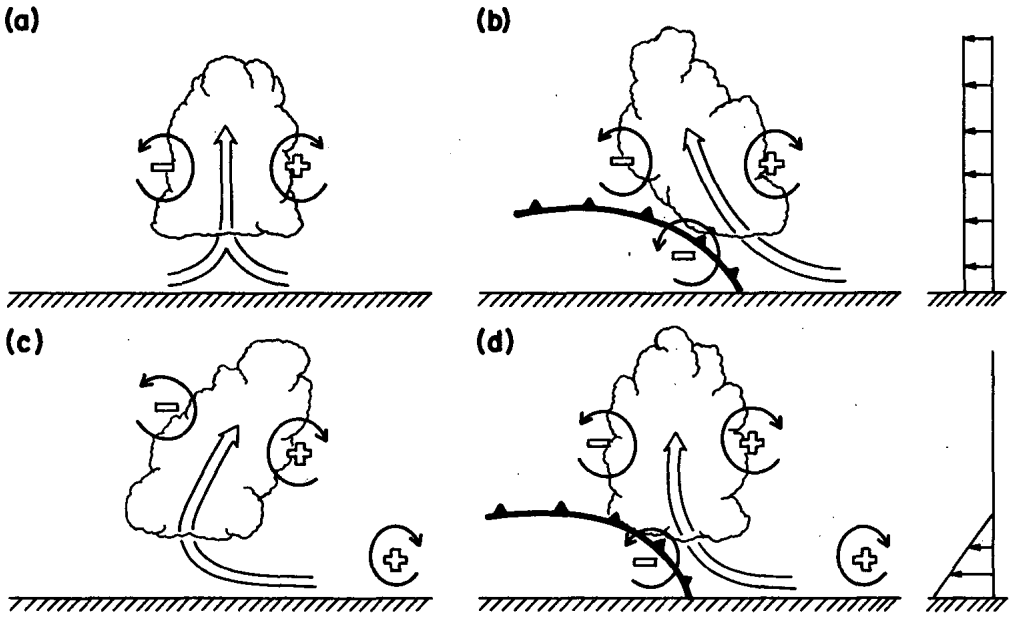

FIGURE 1.3: Schematic diagram showing how a buoyant updraught may be influenced by wind shear and/or a cold pool. (a) With no shear and no cold pool, the axis of the updraught produced by the thermally created, symmetric vorticity distribution is vertical. (b) With a cold pool, the distribution is biased by the negative vorticity of the underlying cold pool and causes the updraught to lean upshear. (c) With shear, the distribution is biased towards positive vorticity and this causes the updraught to lean back over the inflow. (d) With both a cold pool and shear, the two effects may negate each other and allow an erect updraught. From Rotunno *et al.* (1988).

Rotunno *et al.* (1988) defined the optimal state as the state in which a convective updraught can realise its full CAPE without inhibition by either the cold pool or shear. Although a cold pool in any environment may trigger new cells, the circulation of the cold pool is detrimental to the cell. The cell can only realise its full potential when sufficient shear exists to counter the circulation of the cold pool. In practice, the cold pool strength, its speed c (m s^{-1}), can be estimated from a thermodynamic sounding and the low-level shear, Δu (m s^{-1}), can be estimated from a wind profile [1]. If these two quantities are

[1]Weisman *et al.* (1988) suggested the use of the shear in the lowest 2.5 km; this was later extended by Weisman and Rotunno (2004) to 5 km

comparable (i.e. the value of the ratio $c/\Delta u$ is close to 1) then, according to Rotunno *et al.* (1988), the system is in the optimal state where the effects of the cold pool are balanced by the shear. The conditions in the optimal state promote deep lifting that generates new, strong cells along the outflow boundary. The optimal state, where the deepest possible lifting occurs, is one point in a continuum of possible states, with cold-pool-dominated systems at one end and shear-dominated systems on the other end.

Weisman *et al.* (1988) used a single thermodynamic sounding and a range of vertical shear magnitudes, depths and directions to investigate the sensitivity of numerically simulated squall lines to vertical shear. The optimal state was reached when the perpendicular component of shear to the convective line reached magnitudes of 17.5 to 25 m s^{-1} confined to the lowest 2.5 km.

Some authors have questioned the validity of RKW theory. For example, both Lafore and Moncrieff (1989) and Garner and Thorpe (1992) argued that the focus on the interaction between the cold pool and the shear was an oversimplification as it neglected the larger-scale circulations in the squall line. Other studies (Coniglio and Stensrud, 2001; Evans and Doswell, 2001) suggested that there was not such a close relationship between the low-level shear and the behaviour of squall lines in models and observations as contended by Rotunno *et al.* (1988) and Weisman *et al.* (1988). To address these issues, Weisman and Rotunno (2004) performed an extensive set of 3D squall line simulations at a higher resolution and over a wider range of environmental shear conditions than the original simulations of Weisman *et al.* (1988). They found that due to the use of a larger model domain the squall line lifetimes were generally not as sensitive to shear as was found in Rotunno *et al.* (1988) and Weisman *et al.* (1988). However, the strength of the squall line over a 6 hour period was enhanced when moderate to strong shear was restricted to low-levels. Weisman and Rotunno (2004) also extended the depth which the shear layer could occupy from the 2.5 km suggested by Weisman *et al.* (1988) to 5 km.

Stensrud *et al.* (2005) analysed 91 severe squall lines from the observational dataset of Coniglio *et al.* (2004) and also performed idealised 2D cloud-scale simulations using one thermodynamic sounding, to which they made small perturbations. They found that although an amount of shear was beneficial to squall lines, the ratio of the cold pool strength to the shear, $c/\Delta u$, was not very useful in describing the structure of the squall

lines in their simulations. They also found that environments of most long-lived squall lines had shear over a deep layer rather than shear confined to the lowest 5 km.

Weisman and Rotunno (2005) argued that the strength of the cold pool that developed in the simulations of Stensrud *et al.* (2005) was significantly stronger than a typical cold pool, and would have required a large amount of shear to balance it. Weisman and Rotunno (2005) emphasised that RKW theory is as dependent on the strength of the cold pool as it is on the strength of the shear, and therefore that it was inappropriate of Stensrud *et al.* (2005) to use just one sounding, which developed a very strong cold pool, to compare RKW theory to observations. Weisman and Rotunno (2005) repeated the analysis of the observational dataset of Coniglio *et al.* (2004) used by Stensrud *et al.* (2005), but this time using a range of cold pool and shear strengths. They found that, in contradiction to the findings of Stensrud *et al.* (2005), the optimal state in which the cold pool circulation balanced the shear did indeed compare well with the observations. Weisman and Rotunno (2005) also reiterated that RKW theory could be used to explain the full range of convective system organisation and behaviour, from upshear- to downshear-tilted systems, and including both severe and non-severe systems. They argued that a major weakness of the criticisms that Stensrud *et al.* (2005) made of RKW theory was that they only addressed derechoes, a very specific subset of the full spectrum of squall lines, because the observational cases selected by Coniglio *et al.* (2004) were all derechoes. Weisman and Rotunno (2005) considered more types of documented squall lines from both the tropics and midlatitudes, including severe and non-severe systems, and found that the structural characteristics were consistent with the $c/\Delta u$ criteria of RKW theory.

Further support for RKW theory was provided by Bryan *et al.* (2006), who compared the output from four different numerical models to evaluate whether RKW theory could generally be used to explain the structure and intensity of simulated squall lines. All previous investigations into the applicability of RKW theory to squall line properties had been based only on the model used by Rotunno *et al.* (1988) and Weisman and Rotunno (2004). Bryan *et al.* (2006) found general support for RKW theory. In all four models, the structure of the simulated squall lines was well-described by the $c/\Delta u$ criteria. Bryan *et al.* (2006) also found that system intensity, as defined by rainfall and near-surface winds, peaked when the value of $c/\Delta u$ was near the optimal state.

RKW theory has been shown by several authors to be a generally valid description of squall line structure and behaviour for storms that develop cold pool outflow in a shear environment. The theory has been supported by observations and numerical simulations from more than one model. It is important to note that RKW theory does not state that a balance between the cold pool and environmental shear is a necessary condition for the development of a long-lived squall line. Weisman and Rotunno (2004) found that long-lived convection developed over a wider range of conditions than those defined as optimal in terms of the balance between the cold pool strength and environmental shear. However, the strength of squall lines was enhanced when moderate-to-strong shear was confined to the lowest 5 km.

1.5.1 The incorporation of rear-inflow jets into RKW theory

Fovell and Ogura (1989) and Fovell (1991) suggested that a strong RIJ could advect more dry air into the storm, which would enhance precipitation and strengthen the cold pool. Following RKW theory, if the system was initially already in the optimal state then the enhanced cold pool could create more of an imbalance with the ambient vertical wind shear, weakening the convective system. However, contrary to their suggestion, Fovell and Ogura (1989) actually found that the strongest convective systems were associated with the strongest cold pools and RIJs. This result suggested that RKW theory alone could not provide a full description of the system behaviour when a RIJ was present. Additionally, Lafore and Moncrieff (1989) hypothesised that RIJs could strengthen convection by descending to the surface and enhancing the gust front but found that the strongest convective systems were associated with RIJs that remained elevated to near the leading edge of the system.

Weisman (1992) used an idealised model to develop an extension to RKW theory that included the rôle that RIJs have in the evolution of convective systems. RKW theory assumes that the flow in the cold pool is stagnant relative to the leading edge of the cold pool. However, the formation of a RIJ may mean that this assumption is not valid. In simulations with moderate environmental shear, Weisman (1992) found that the RIJ descended to the surface and spread out. The evolution of the convective system was not significantly altered from the prediction of RKW theory: that the cold pool circulation

would overcome the ambient shear, causing the convective circulation to tilt upshear and weaken. However, in simulations with strong environmental shear, an elevated RIJ formed which did not descend. This limited the upshear-tilting process of RKW theory, and a strong updraught developed at the leading edge of the system.

Weisman (1992) took the "optimal state" condition where the strength of the cold pool is balanced by the vertical shear and considered the effects of the RIJ as an additional source of horizontal vorticity. A schematic diagram showing the results is given in Figure 1.4. Figure 1.4a shows an environment where the cold pool strength is balanced by the shear. There is no RIJ. The flow within the cold pool is assumed to be stagnant relative to the leading edge of the cold air. The only sources of horizontal vorticity are the vorticity associated with the ambient shear and the vorticity generated by the buoyancy gradients along the leading edge of the cold pool. The vorticity sources are equal in magnitude but opposite in sign, causing the low-level flow to be turned vertically upwards as it approaches the cold pool.

Figure 1.4b represents the vertical circulation associated with an elevated RIJ. The jet of air is near the top of the cold pool, at height H, and remains at that height until it reaches the leading edge of the cold pool. The jet represents an additional source of horizontal vorticity, in addition to the horizontal vorticity generated by the ambient shear and at the leading edge of the cold pool. Below the level of the velocity maximum in the RIJ, the additional vorticity is of the same sign as that due to the ambient shear. Above the level of the velocity maximum in the RIJ, the additional vorticity is of the same sign as that generated by the cold pool. As such, below the RIJ velocity maximum the RIJ counterbalances some of the horizontal vorticity generated by the cold pool. The elevated RIJ produces stronger and deeper lifting at the leading edge of the cold pool. Once the air is lifted above the RIJ velocity maximum the vorticity associated with the jet is of the same sign as that generated by the cold pool and the updraught current is directed to the rear of the system.

Figure 1.4c represents the flow configuration for a RIJ that descends to the surface well behind the leading edge of the system. Above the RIJ velocity maximum the horizontal vorticity is of the same sign as that generated by the cold pool (as discussed above). As such, the surface-based RIJ enhances the upshear-tilting process that was initially started

by the cold pool, causing the lifting at the leading edge of the system to be weaker and shallower than it would have been in the absence of the RIJ.

In considering the full RKW vorticity-balance conditions required to incorporate the RIJ effects into RKW theory, Weisman (1992) noted that in order to have a significant impact, the strength of the RIJ must be greater than 10 m s^{-1}. Smull and Houze (1987) found that only three of their eighteen cases of RIJs had strengths of this magnitude, so RKW theory without the extension to include RIJs may sufficiently describe most convective systems that have RIJs.

The effect of the interaction between the cold pool, shear and the RIJ on the evolution of the convective system is shown in Figure 1.5, which Weisman (1992) developed as an extension to Figure 1.3. Figure 1.5a shows an idealised convective system with a RIJ that descends to the surface behind the leading edge of the system. The updraught gradually ascends over a surface cold pool. Light-to-moderate rainfall in the convective and stratiform regions extends well behind the leading edge of the cold pool. This structure often leads to the decay and dissipation of the convective system, because the lifting at the gust front is not strong or deep enough to generate new convective cells. The mid-level mesolow in the convective region weakens, which in turn, leads to the weakening of the mesoscale circulation.

Figure 1.5b shows an idealised convective system with an elevated RIJ. There are strong updraughts at the leading edge of the cold pool, and the updraught rises rapidly and spreads to the rear of the system. The deeper lifting causes moderate-to-heavy convective rain at the leading edge of the system, while the lighter rain to the rear remains similar to the descending RIJ case. The elevated jet structure tends to be longer-lived than the descending jet structure, because the deep lifting at the gust front is able to generate new convective cells.

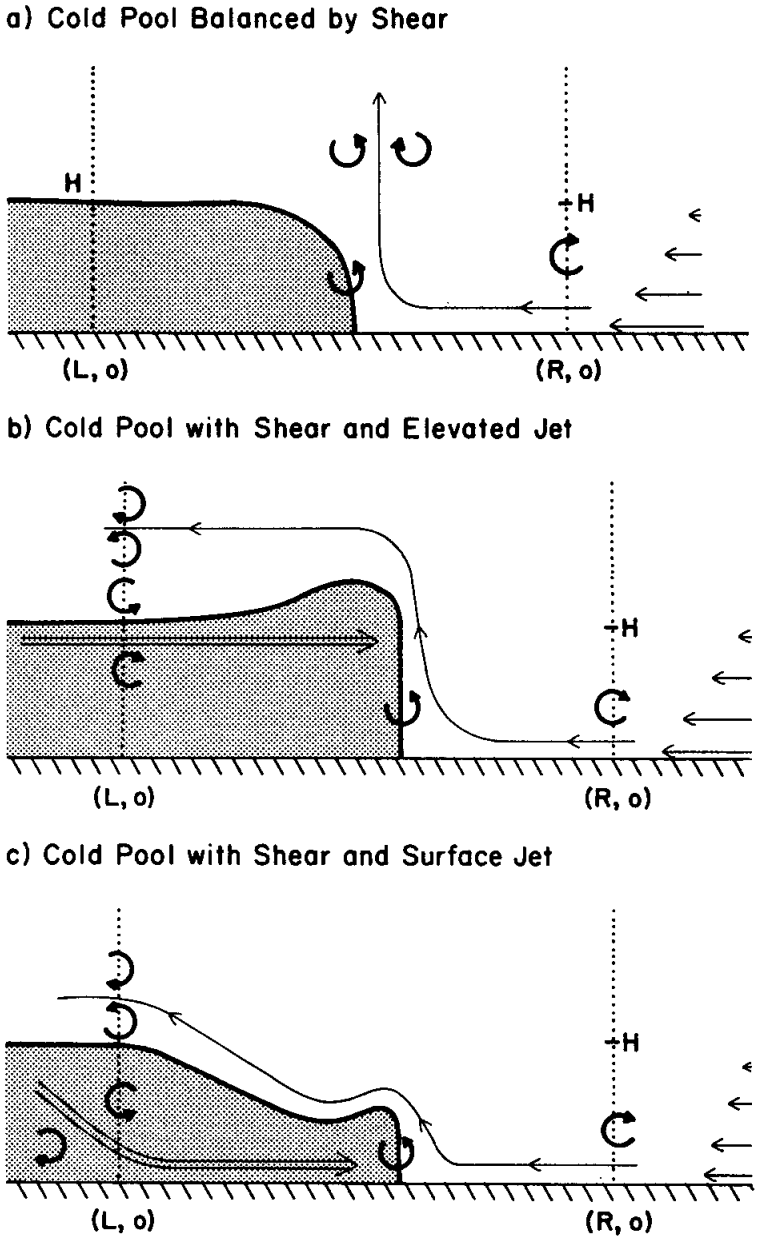

FIGURE 1.4: Schematic depiction of (a) a cold pool spreading in an environment having sufficient vertical shear to balance the cold-pool-generated circulation, (b) a cold pool balanced by the ambient vertical wind shear and an elevated rear-inflow jet, and (c) a cold pool in the presence of a surface rear-inflow jet. The thick arrows depict the sense of the vorticity that is generated at the leading edge of the cold pool or that is advected through the boundaries. From Weisman (1992).

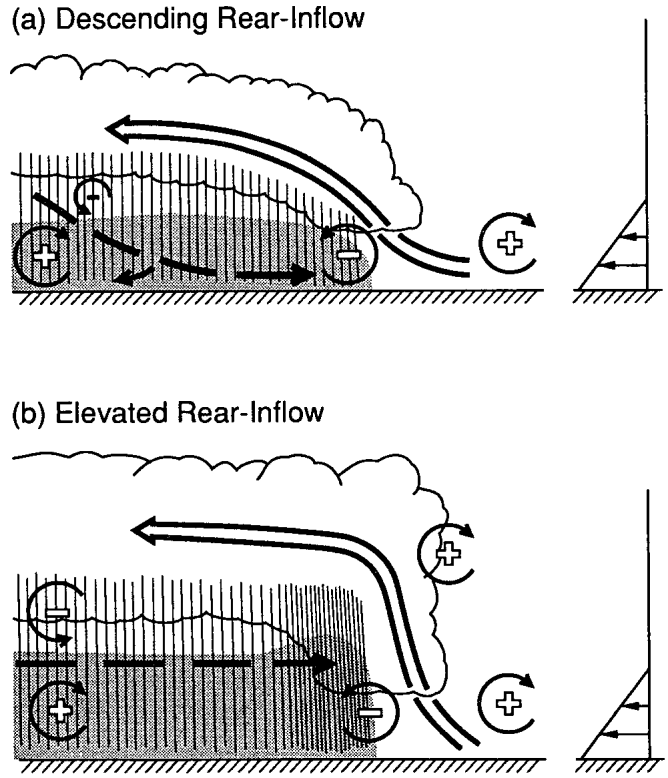

FIGURE 1.5: A conceptual model of the mature structure of a long-lived squall-line-type convective system for (a) a system with a descending rear-inflow jet and (b) a system with an elevated rear-inflow jet. The updraught current is denoted by the thick, double-lined flow vector, with the rear-inflow current denoted by the thick dashed vector. The shading denotes the surface cold pool. The thin, circular arrows depict the most significant sources of horizontal vorticity, which are either associated with the ambient shear or are generated within the convective system. Regions of lighter or heavier rainfall are indicated by the more sparsely or densely packed vertical lines, respectively. The scalloped line denotes the outline of the cloud. From Weisman (1992).

1.6 Elevated convection

Convective updraughts usually have their origins in warm boundary layer air. However, in some cases it is possible for convection to originate from air above the boundary layer. The term "elevated convection" is used to refer to convective storms (or clouds, Corfidi *et al.*, 2008) where the air parcels feeding the convection originate from above the boundary layer (Glickman, 2000). When convection originates from the boundary layer, it is referred to as "surface-based convection". Purely elevated and purely surface-based convection represent the extreme ends of a continuous spectrum of behaviour. This is discussed in Section 1.6.5.

During a workshop on the development of mesoscale observing networks, Dabberdt *et al.*

(2004) said that one of the key scientific challenges in nowcasting convective weather was "an improved understanding of the processes that initiate convection, including those forcing elevated convection".

An obvious point, although it is not discussed in the literature, is that there must be a temporal element to the definition of elevated convection. Air parcels in an elevated unstable layer may well have originated from the boundary layer some time ago. When elevated convection is discussed, however, an instantaneous comparison is made of the stability of the elevated unstable layer with that of the stable layer beneath it.

1.6.1 Environments in which elevated convection forms

Elevated convection can occur above any low-level stable layer, surface outflow, or sloping frontal surface where there is instability above the surface. The nocturnal boundary layer often provides a near-surface stable layer above which elevated convection can develop.

Observations of elevated convection show that it often occurs above low-level stable layers. Schmidt and Cotton (1989) observed a squall-line that developed from an elevated layer of high-valued θ_e air that was above a stable boundary layer. Detailed observations were made during CSIP of a series of elevated MCSs that occurred in the UK above a low-level stable layer (Browning *et al.*, 2010, 2012; Marsham *et al.*, 2010). Modelling studies have reproduced elevated convection above a low-level stable layer (e.g. Buzzi *et al.*, 1991; Parker, 2008; Schmidt and Cotton, 1990).

Elevated convection has also been observed to occur on the cold side of a front. Rochette and Moore (1996) observed an MCS that developed above a cool, stable boundary layer on the cold side of a warm front. They described the existence of "elevated convective instability", where there was nearly twice as much CAPE if the warmest, most moist parcel in the lower atmosphere was lifted compared to the lifting of a mean surface parcel. Browning and Hill (1984) observed an MCS near the British Isles that formed ahead of a cold front and above a cool, stable boundary layer.

Observations have shown that the presence of a low-level jet may also aid the development of elevated convection. In a study of twenty-one elevated thunderstorms associated with

heavy rainfall, Moore *et al.* (2003) found that in most cases a low-level jet, initially centred at 850 hPa, was important in lifting conditionally unstable air up a sloping frontal surface where the air mass behind the front was cool and statically stable. The elevated convective initiation episodes observed by Marsham *et al.* (2011) during IHOP occurred when a nocturnal low-level jet generated elevated convergence, leading to the development of an elevated squall line. Low-level jets have also been shown by modelling studies to provide a lifting mechanism for elevated conditionally unstable air. Trier *et al.* (2006) performed simulations of nocturnal convection over the central United States and found that a low-level jet provided a source of moisture and lifting. French and Parker (2010) studied the response of simulated nocturnal convective systems to the development of a low-level jet. They found that the lifting of high-valued θ_e air from above the jet was enhanced when the direction of flow in the jet was towards the squall line and reduced when the flow of the jet was away from the squall line.

In the central United States, elevated convection commonly occurs at night. This is in part due to the stabilising of the surface due to radiative cooling and also partly because conditionally unstable air can be significantly vertically displaced by the frequent interaction of nocturnal low-level jets and surface fronts (Trier *et al.*, 2006). Of the twenty-one elevated thunderstorms associated with heavy rainfall studied by Moore *et al.* (2003), nearly every case was either entirely nocturnal or had a significant nocturnal fraction of its lifetime. The cases of elevated convection observed in the southern Great Plains of the United States by Wilson and Roberts (2006) during IHOP mostly occurred at night. Three nocturnal elevated convective storms were observed by Marsham *et al.* (2011) on 13 June 2002 during IHOP. Nocturnal elevated convection has been reproduced in modelling studies. The numerical simulations of West African convective systems made by Dudhia *et al.* (1987) were initialised in a nocturnal sounding with a stable boundary layer. The resulting convective cells had bases at 600 to 700 hPa and were an example of "an elevated convective instability" (Dudhia *et al.*, 1987).

Episodes of elevated convection can occur when the passage of a previous MCS has stabilised the boundary layer. At least three of the convective initiation episodes observed by Marsham *et al.* (2011) during IHOP were elevated. These elevated initiation episodes occurred from moist layers of conditionally unstable air located above the boundary layer.

The boundary layer had been stabilised by the surface outflow of cold air from previous MCSs.

1.6.2 The impact of elevated convection

Elevated deep convection can produce the same severe weather as surface-based convection, such as heavy rainfall (Moore *et al.*, 1998, 2003; Rochette and Moore, 1996; Wilson and Roberts, 2006) that can move very slowly (Schumacher, 2009), hail (Horgan *et al.*, 2007), and occasionally very strong surface winds (Goss *et al.*, 2006; Horgan *et al.*, 2007; Schmidt and Cotton, 1989), but in regions that are a long distance away from strong surface-based instability. Flash floods have been caused by the extreme rainfall from elevated MCSs (Schumacher and Johnson, 2008).

The precipitation generated by elevated convection can be difficult to forecast accurately if large-scale processes are occurring nearby. Wilson and Roberts (2006) grouped the episodes of elevated convection that occurred during IHOP into "elevated frontal" cases which occurred on the cold side of a front, and "elevated isolated" cases which occurred several hundreds of kilometres from a front. They compared the forecast from the Rapid Update Cycle (RUC) model for each episode with the observations and found that the RUC was unable to produce accurate precipitation forecasts for the elevated frontal cases. In these cases, the nearby fronts dominated the large-scale dynamic forcing in the model and obscured the precipitation forecasts that may have resulted from elevated initiation (Wilson and Roberts, 2006).

Elevated systems do not frequently produce strong surface gusts (Corfidi *et al.*, 2008), but it is not unknown. Goss *et al.* (2006) presented an example of a supercell that remained elevated throughout the period of the observations and produced damaging surface winds. The elevated squall line observed by Schmidt and Cotton (1989) also developed severe surface winds which were attributed to the local pressure gradient associated with a mesohigh-mesolow couplet that accompanied the squall line. Horgan *et al.* (2007) found that of the cases of severe elevated convection that they studied, 37% were associated with severe winds and 4% were associated with tornadoes.

The production of strong surface winds from an elevated convective system can be dependent on the strength and depth of the stable layer beneath the convection. Strong surface winds associated with a storm are usually produced by the downdraught outflow. For a downdraught occurring above a stable layer to reach the surface, it must have enough kinetic energy to penetrate through the stable layer. Horgan *et al.* (2007) studied five cases of elevated convection that produced severe surface winds. In every case the stable layer was less than 100 hPa deep. However, elevated convective systems can also produce strong surface winds by gravity waves moving on the low-level stable layer (Bosart and Seimon, 1988; Fritsch and Forbes, 2001). Therefore the development of strong surface winds from elevated convection is not necessarily dependent only on the strength of the downdraught compared to that of the stable layer.

Predicting the location and timing of the initiation of elevated thunderstorms is difficult due to uncertainties in the understanding of the mechanisms that release elevated instability (Moore *et al.*, 2003). Marsham *et al.* (2011) noted that elevated convection is much harder than surface-based convection to forecast accurately. Orography and other surface-based forcing features such as boundary layer convergence lines are less important in the initiation of elevated convection than they are in surface-based convection. Instead, the initiation of elevated convection tends to be controlled by features that occur above the surface and boundary layer, such as low-level jets and waves (Marsham *et al.*, 2011). A lack of observational data at these levels compared to the availability of surface data contributes to the difficulty in forecasting elevated convection.

1.6.3 The climatology of elevated convective systems

Several authors have attempted to construct climatologies of elevated convection occurring in the United States. Colman (1990) studied a four-year dataset and found that the frequency of elevated convection in the United States had maxima in April and September. More recently, a five-year climatology of elevated severe convective storms east of the Rocky Mountains was constructed by Horgan *et al.* (2007) for the 1983-87 period. Potential cases of elevated convection were selected by finding reports of severe storms that occurred on the cold side of surface fronts. Cases were then determined to be elevated if they occurred at least 1° latitude on the cold side of the surface front and were associated with

a sounding that showed a low-level stable layer. During the five-year period, 91% of cases were identified as potential elevated cases, of which 8% were then classified by Horgan *et al.* (2007) to be cases of elevated severe convection. Annual variation was seen in the frequency of severe elevated convection, with a maximum occurring in May and a secondary maximum occurring in September (Horgan *et al.*, 2007). This agreed with the findings of Colman (1990). Geographical variation was also observed in the frequency of severe elevated storms, with a maximum occurring over the south-central United States in winter and a central- and eastern-U.S. maximum occurring in the spring and summer (Horgan *et al.*, 2007). Diurnal variation was also recorded, with a maximum of elevated severe storms initiating at 2100 UTC. In a summary of the elevated convection episodes that occurred during IHOP, Wilson and Roberts (2006) found that elevated convective initiation was common in the southern Great Plains of the United States, relatively common in the upper Midwest of the United States, and infrequent during the summer in Colorado and Florida.

Elevated convection may occur as frequently as surface-based convection. Of the 112 storms studied by Wilson and Roberts (2006), the initiation mechanisms were almost evenly divided between surface-based and elevated. The afternoon initiation storms were primarily surface-based, while the nocturnal initiation storms were primarily elevated (Wilson and Roberts, 2006), presumably because strong surface-based instability tended to occur during the day, while the stability of the nocturnal boundary layer was conducive to elevated convection.

Mesoscale or synoptic features have been found to be important in the development of elevated convection. The elevated convection that occurred during IHOP was frequently associated with mid-level (900 to 600 hPa) synoptic or mesoscale convergence or confluence caused by the large-scale flow, coupled with a large amount of mid-level instability (Wilson and Roberts, 2006). Mesoscale forcing features can aid the development of elevated convection but are not a necessary requirement. The idealised simulations of Parker (2008) showed that elevated convection could be sustained in the absence of a large-scale front or low-level jet.

The median lifetime of the elevated convective systems observed by Wilson and Roberts (2006) was about 4 hours, considerably less than that of the surface-based initiation

episodes. They attributed the shorter lifetime of the elevated convection to the fact that most of the elevated storms did not produce gust fronts. 31% of the elevated storms studied by Wilson and Roberts (2006) produced gust fronts. The lifetime of the elevated storms that produced gust fronts were all greater than 4 hours.

In comparison to the United States, elevated convection has been observed relatively rarely in the mid-latitude maritime climate of the United Kingdom. Browning and Hill (1984) observed an elevated MCS in the UK in 1982. During CSIP, only one out of eighteen intensive observation periods contained an episode of elevated convection (Browning *et al.*, 2007). Two of the MCSs observed during this intensive observation period were studied in detail and both were found to be elevated (Browning *et al.*, 2010, 2012; Marsham *et al.*, 2010). These are to date the only documented cases of elevated convection in the United Kingdom.

1.6.4 Lifting mechanisms in elevated convective systems

The low-level stable layer characteristic of elevated convection is not dynamically passive. In elevated convective systems that do not produce cold pool outflows the process of the downdraughts generating waves or bores in the stable layer can provide enough lifting to maintain deep convection. This is discussed in Section 1.7.

1.6.5 The continuum between elevated and surface-based convection

Elevated convection may be initiated from unstable air located above the boundary layer (e.g. Marsham *et al.*, 2011), termed "elevated initiation", or may evolve from a surface-based system (e.g. Corfidi *et al.*, 2008; Parker, 2008). Once initiated, elevated convective systems can evolve into surface-based systems (Marsham *et al.*, 2011) or may remain elevated throughout their lifetime.

Observational and modelling studies of the evolution of convective systems between surface-based and elevated types suggests that there is a continuum of convective behaviour rather than two distinct regimes. So-called "transition events" have been recorded, where an elevated storm becomes surface-based, or a surface-based storm becomes elevated. Forecasting a transition event is difficult because the processes responsible for the transition

(e.g. the strength and location of CIN, the location and depth of outflow boundaries, and any change in mesoscale forcing) are difficult to forecast (Corfidi *et al.*, 2008).

1.6.5.1 Elevated to surface-based transition

The transition from elevated to surface-based convection has been documented in both numerical simulations and observations. The simulations of Bryan *et al.* (2006) showed that elevated convection became surface-based once an elevated cold pool descended to the surface. Several observational cases of the transition from elevated to surface-based convection have been made. Corfidi *et al.* (2008) documented a case that took place in the central United States in July 2006. Elevated thunderstorms developed in the morning. The elevated storms produced outflow boundaries that encouraged the development of surface-based convection as the boundaries moved into a region of weaker convective inhibition and as diurnal heating further weakened the convective inhibition. Radar observations of an elevated thunderstorm in Oklahoma that became surface-based were made by Trapp *et al.* (2001). Detailed observations of a convective system evolving from elevated to surface-based were made by Marsham *et al.* (2011) during IHOP. Elevated convection initiated overnight in a frontal zone, the lower levels of which had been stabilised by the passage of a previous MCS. Cells of convection formed in a zone where a low-level jet generated elevated convergence. The cells organised into an MCS. One initiation episode occurred when a propagating gravity wave intersected a convergence line. The low-level jet was found to favour wave-trapping (discussed later in Section 1.7.2). While the system was elevated, waves and bores generated by the downdraughts interacting with the stable surface layer were responsible for secondary initiation in a process that Marsham *et al.* (2011) suggested was similar to that of Fovell *et al.* (2006), whereby gravity waves generated by the storm help to lift air to its level of free convection.

1.6.5.2 Surface-based to elevated transition

The transition from surface-based to elevated convection has also been shown to occur in simulations and in observational case studies. The evolution of elevated convection from surface-based systems tends to occur when the pre-convective boundary layer stabilises, either through the process of nocturnal cooling or when the storm crosses a frontal zone into

a region of more stable boundary layer air. The modelling studies of nocturnal convection performed by Trier *et al.* (2006) used a numerical model with a heterogeneous domain and explicitly-resolved deep convection. During the growth stage of the convective systems, which took place in the afternoon, convection was based in the boundary layer. During the nocturnal mature stage of the convective systems, maximum CAPE was elevated (at 1.5 km). These results are supported by the idealised modelling studies of Parker (2008), who found that a surface-based MCS evolved into an elevated MCS when it encountered a region of colder low-level air. Observations were made by Bernardet and Cotton (1998) of a surface-based convective system in Colorado on 12-13 May 1985 that formed in the afternoon and evolved into an elevated system overnight.

1.6.5.3 Differences between elevated and surface-based convective systems

There are significant differences in the behaviour of elevated and surface-based storms. Often, convection intensifies when it becomes surface-based. Corfidi *et al.* (2008) noted an increase in radar reflectivity and changes in the speed and direction of motion of the storm during the transition from being elevated to being surface-based, although they did not mention whether the system speed increased or decreased during the transition. During the elevated-to-surface-based transition observed by Rockwood and Maddox (1988), maximum intensity was seen after the elevated convection moved into a region of strong low-level instability. Another case of an elevated-to-surface-based transition presented by Janish *et al.* (1996) also showed maximum intensity after the transition to surface-based convection. When the elevated system observed during IHOP by Marsham *et al.* (2011) became surface-based, an increase in reflectivity was observed. In contrast, Coniglio *et al.* (2007) discussed an an example of an MCS that weakened as it made the transition from elevated to surface-based convection in moving from the cool side to the warm side of a cold front. The Coniglio *et al.* (2007) example was likely to have weakened as it neared the surface front because the wind profiles on the warm side were less favourable for the generation of new cells (Corfidi *et al.*, 2008). Parker (2008) presented idealised simulations of the transition from surface-based to elevated convection. The system velocity increased once the transition from surface-based to elevated convection occurred. This was due to a change in the lifting mechanism. In the surface-based stage the convection was gravity current-lifted while in the elevated stage the convection was bore-lifted.

1.6.6 Idealised modelling studies of elevated convection

Elevated convection can be difficult to study in an idealised model. Trier *et al.* (2006) stated that:

> "research cloud models that permit explicit deep convection have historically relied on idealised horizontally homogeneous initial conditions. Such models have had difficulty simulating the life cycle of elevated convection."

Idealised studies investigating the transition from surface-based to elevated convection were performed by Parker (2008), and from elevated to surface-based convection by Bryan *et al.* (2006). Bryan *et al.* (2006) initiated elevated convection with a line thermal placed in the centre of the model domain. They found that convection was difficult to initiate in a horizontally homogeneous environment with a stable surface layer. A strong positive potential temperature perturbation of 4 K was required. Parker (2008) initiated surface-based convection using an infinitely long north-south linear warm bubble with a positive potential temperature perturbation of 2 K. The transition to elevated convection was achieved by imposing cooling in the lowest 1 km of the model domain. French and Parker (2010) used the same process as Parker (2008) to initiate surface-based convection and then evolved it into elevated convection. Elevated convection was initiated in the 2D idealised simulations performed by Buzzi *et al.* (1991) using an elevated warm bubble with a positive potential perturbation of 2 K placed in the elevated unstable layer. Idealised simulations of elevated convection are not always initiated using warm-bubble potential temperature perturbations. In their investigation of the 2D dynamics of elevated nocturnal squall lines, Dudhia *et al.* (1987) found that a warm-bubble initialisation method was inappropriate for initiating convection in a nocturnal sounding with a saturated boundary layer. Instead, a region of the boundary layer was artificially cooled to represent a pre-existing gravity current propagating through a nocturnal boundary layer. The gravity current lifted the elevated unstable parcels to their levels of free convection.

1.6.7 Elevated convective systems with rear-inflow jets

Like surface-based storms, elevated storms can develop RIJs. Schmidt and Cotton (1989) observed a case of an elevated squall line that produced a RIJ that descended to the

surface and produced strong surface winds. Some of the elevated nocturnal convective systems simulated by Trier *et al.* (2006) developed a RIJ that descended to the surface and penetrated to the leading edge of convection. Other simulations of Trier *et al.* (2006) developed RIJs that remained elevated.

RIJs that develop in elevated MCSs can generate waves that interact with the convective system. An MCS that remained elevated throughout its lifetime was observed during IOP 3 of CSIP. This MCS formed above a cold near-surface stable layer and developed a RIJ that descended to the top of the stable layer but was unable to penetrate to the surface (Browning *et al.*, 2010). The impact of the RIJ on the top of the near-surface stable layer generated a wave ahead of the RIJ (Marsham *et al.*, 2010). A RIJ was also observed by Marsham *et al.* (2011) in an elevated nocturnal MCS that formed during IHOP. However, in this case the RIJ penetrated to the surface between 0700 and 1000 local time. The penetration of the RIJ to the surface was shown to coincide with the development of a surface cold-pool.

1.6.8 Elevated convective systems that develop cold pools

Elevated convective systems develop surface cold pools less frequently than surface-based storms because elevated convection occurs above stable layer and it is therefore more difficult for convective downdraughts to reach the surface and form cold pool outflow. However, as mentioned above, Marsham *et al.* (2011) observed cold pool outflow from an elevated storm. The nocturnal elevated convective system simulated by Trier *et al.* (2006) also developed a cold pool during its mature (elevated) stage.

The strengthening of the cold pool of an elevated MCS can aid the transition to surface-based convection. The elevated MCS observed by Marsham *et al.* (2011) developed a cold pool late in its lifetime. The cold pool was able to lift near-surface air to its level of free convection, contributing to the transition of the MCS from elevated to surface-based convection. The behaviour of the MCS observed by Marsham *et al.* (2011) was successfully modelled by Trier *et al.* (2011).

Cold pool formation in elevated convective systems is likely to be controlled by the strength of the downdraughts and the strength of the low-level stable layer. Horgan *et al.* (2007)

found that the formation of a cold pool by an elevated convective system was dependent on the strength and depth of the low-level stable layer through which downdraughts must penetrate. Blanchard (1990) showed that downdraught strength is controlled by diabatic cooling and therefore influenced by microphysical processes and environmental humidity,

1.6.9 Summary of elevated convection

Elevated convection, where convective updraughts are fed from air above the boundary layer, has been observed with reasonable regularity in the United States. In contrast, its occurrence appears to be more rare in the United Kingdom. Like surface-based convection, elevated convection can be associated with heavy rainfall and hail. Strong surface winds are occasionally, but not frequently, associated with elevated convection. Forecasting elevated convection is difficult due to a lack of understanding of the processes that initiate it and a lack of mid-level data compared to surface data. Elevated convection forms in environments that are characterised by a low-level stable layer surmounted by an elevated unstable layer. Elevated convection can be initiated by a low-level jet ascending a frontal surface. Lifting from gravity currents, solitary gravity waves and bores can also initiate elevated convection. Elevated convective systems have been observed to become surface-based, and surface-based convection has been observed to become elevated. As such, purely elevated and purely surface-based convection represent two extremes of a continuous spectrum of behaviour of convective systems. Elevated convection has successfully been reproduced in high-resolution numerical models with explicitly-resolved convection. Idealised simulations of elevated convection have also been made, although the initially horizontally homogeneous nature of these environments means that it can be difficult to simulate elevated convection in an idealised model. Elevated convective systems can develop RIJs and cold pool outflow. If a RIJ descends through the low-level stable layer under an elevated storm it can strengthen the cold pool outflow. The strengthening of cold pool outflow from an elevated storm can provide sufficient lifting to raise near-surface air to its level of free convection and cause or contribute to the transition from elevated to surface-based convection.

1.7 Gravity currents, bores and solitary waves

Gravity currents, bores and waves are dynamical phenomena that can be generated by, and that can initiate, deep convection. They are of particular importance to elevated convection, where the presence of a low-level stable layer provides a way in which these phenomena can interact with each other and with the convective system. The importance of gravity currents, waves and bores to elevated convection was mentioned briefly in Section 1.6, but is discussed in detail here.

1.7.1 Definitions

1.7.1.1 Gravity currents

A gravity current is a flow of dense fluid (e.g. cold air) into a region of less dense fluid (e.g. warm air). Gravity currents are primarily horizontal flows and are generated by density differences. The denser fluid weighs more than the less dense fluid, and therefore the piezometric pressure is greater inside the gravity current than in the surrounding fluid. This pressure difference drives the flow (Benjamin, 1968).

The theoretical propagation speed c of an atmospheric gravity current propagating in a fluid of infinite depth is given by

$$c^2 = -2 \int_{z=0}^{z=H} B dz, \tag{1.1}$$

where H is the depth of the gravity current and $B = g(\theta'_v/\bar{\theta_v} - q_L)$ is the total buoyancy including contributions from the virtual potential temperature perturbations, θ'_v, and the mixing ratio of all condensate, q_L (e.g. Trier *et al.*, 2006). The speed of a gravity current is often referred to as its strength.

A conceptual model of a gravity current flow is shown in Figure 1.6. The flow has five main features: the head (an elevated region of cold air near the leading edge of the flow), the nose (a region of cold air that is over-running the warm air), the wake (a region of turbulent mixing behind the head at the interface of the two fluids), the body (the flow

that is upstream of the head), and the undercurrent (a surface flow that moves away from the surface front).

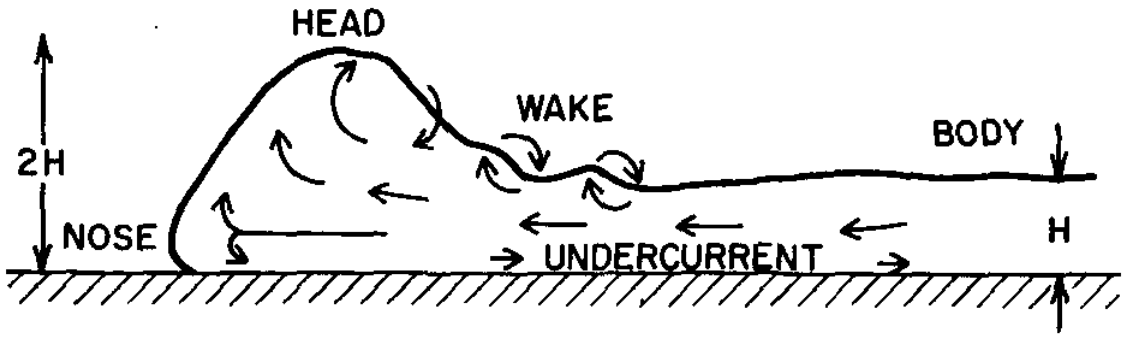

FIGURE 1.6: A conceptual model of a gravity current moving from right to left. From Mueller and Carbone (1987).

1.7.1.2 Bores

A phenomenon related to the gravity current is the bore. A gravity current is a limiting case of a bore. Similarly to gravity currents, bores are concerned with mass transport. A bore is an example of a hydraulic jump, where an increase in fluid depth is associated with a change in flow rate (Simpson, 1997). The pressure difference across a bore causes a change in momentum and energy. However, the change in energy does not balance (Simpson, 1997), and a loss of energy per unit time must occur. The way in which energy is lost is dependent on the strength of the bore and is discussed below.

The strength of a bore is defined as the ratio of the depth of the fluid downstream of the bore, h_1, to the upstream (pre-bore) fluid depth, h_0. For bores where the increase in depth at the front is small, a series of smooth waves are generated at the leading edge, each of which carries energy as it moves away from the front. These types of bores are known as "undular" and their passage is characterised by a series of wavelike undulations (Figure 1.7a). Undular bores form at strengths of about $\frac{1}{3}$ for bores at the free surface of a flow and for strengths of between 1 and 2 for internal bores (those that form at an interface between two fluid of different densities). For strengths between 2 and 4, the bore is almost undular, but some turbulent mixing due to shear instability occurs downstream (Figure 1.7b). For stronger bores (those which are characterised by a larger increase in fluid depth, where h_1/h_0 is greater than 4), insufficient energy is carried away by waves,

and excess energy is dissipated through turbulence. Turbulent bores advance as a wall of breaking waves. The change in height and velocity associated with the passage of a turbulent bore occurs during a single transition. For very deep bores the leading edge appears very similar to that of a gravity current (Figure 1.7c).

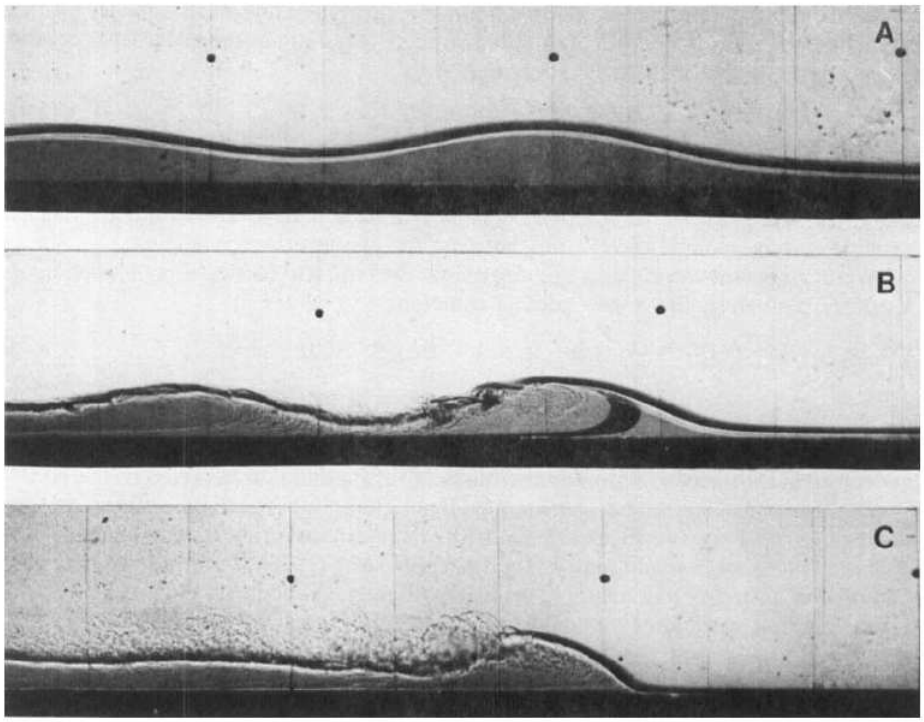

FIGURE 1.7: Photographs of three types of bores: (a) undular; (b) undular becoming turbulent; mixing can be seen downstream of the first crest; (c) a deep turbulent bore that has the appearance of a gravity current. From Rottman and Simpson (1989).

In a two-layer fluid where there is no mixing and the upper layer is very deep, the speed of a bore in terms of its strength, non-dimensionalised as the Froude number $Fr = u/\sqrt{g'h}$, where u is the speed and g' is the reduced gravity, is given by (Wood and Simpson, 1984) as

$$Fr^2 = \frac{1}{2}\frac{h_1}{h_0}\left(1 + \frac{h_1}{h_0}\right). \tag{1.2}$$

Experimental data has shown that Equation (1.2) holds for bore strengths between 1 and 2. For bore strengths greater than about 2, the bore speed is well-predicted by gravity current theory (Simpson, 1997).

Attempts have been made to measure the wavelength of undular bores. For bore strengths between 1.5 and 2.5, the ratio of the wavelength, λ, to the depth of the bore, h_1, has been found to be approximately 10 (Simpson, 1997).

1.7.1.3 Solitary gravity waves

Gravity currents and bores are associated with the transport of mass. The "solitary wave" is closely related to the undular bore, but transports energy rather than mass. A solitary wave consists of a single, rather than periodic, wave (Figure 1.8) that propagates at a uniform velocity. Internal solitary gravity waves can propagate along the interface between two fluids of different densities.

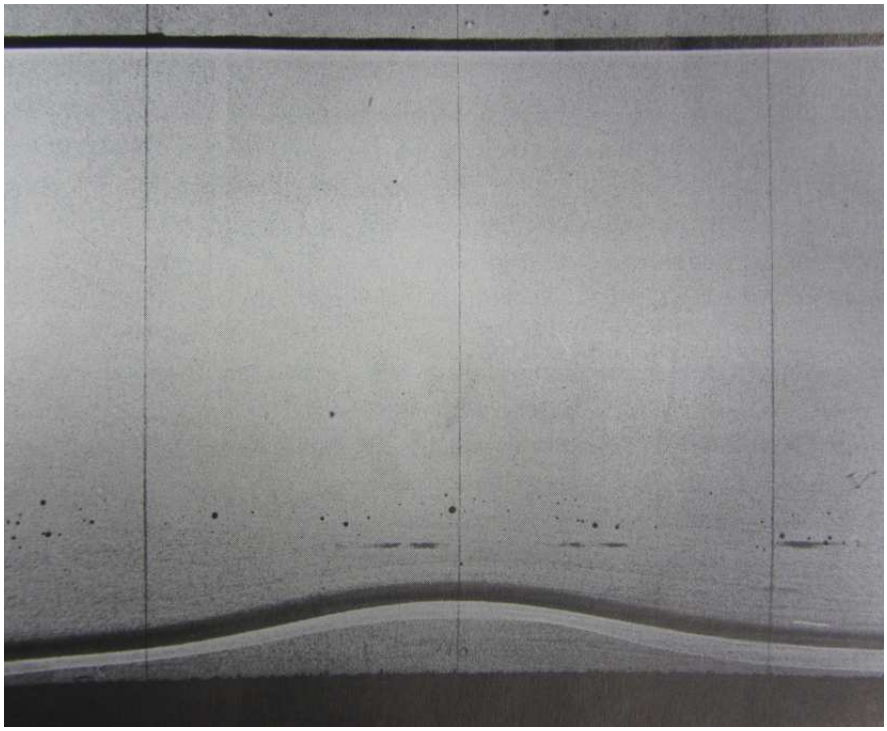

FIGURE 1.8: A solitary wave seen on an interface between two stably stratifed fluids. From Simpson (1997).

1.7.1.4 Evolution

Simpson (1997) showed that a pure gravity current and a pure gravity wave lie at opposite ends of a continuous spectrum of behaviour. Gravity currents, gravity waves and bores can be dynamically distinguished by the way that they transport mass and momentum.

Figure 1.9 is a schematic diagram showing (a) a propagating internal gravity wave train, (b) a solitary gravity wave, (c) a gravity current and (d) a bore. The net upward displacement in the wavetrain equals the net downward displacement, and thus the waves transport momentum but not mass. The solitary wave transports momentum and displaces mass a finite distance. The gravity current transports both mass and momentum. The bore also transports mass and momentum, but the intruding fluid has the same density as the fluid into which it intrudes. The passage of the bore is characterised by a change in fluid depth.

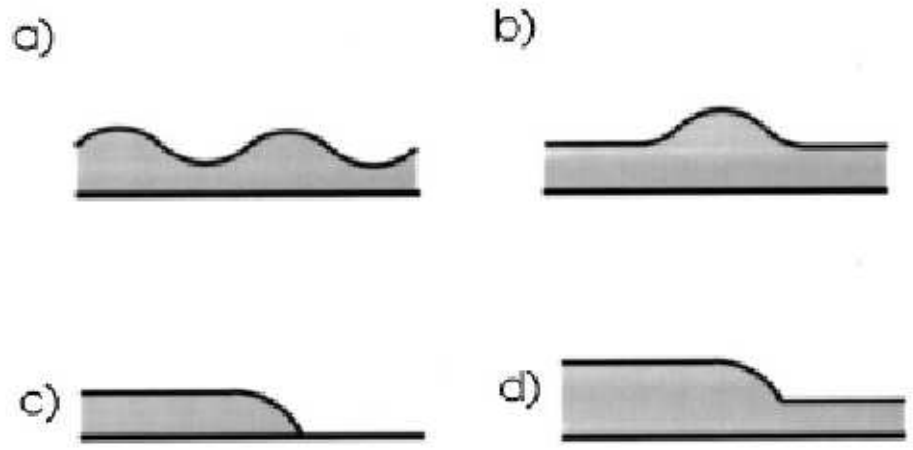

FIGURE 1.9: Schematic diagram of (a) an internal wave train, (b) a solitary wave, (c) a gravity current and (d) a bore. From Sutherland (2002).

The flow of a gravity current into a stable layer (e.g. a thunderstorm outflow into a stable nocturnal boundary layer) can generate an undular bore in the stable layer (Figure 1.10a). The bore moves away from the gravity current and as the gravity current loses its strength and begins to dissipate the disturbance continues to propagate as a series of solitary waves (Figure 1.10b), but no longer meets the classification criteria of an undular bore because the depth of the stable layer returns to its pre-bore value (Locatelli *et al.*, 1998).

1.7.2 Wave trapping

Gravity waves tend to propagate energy vertically. As such, gravity waves decrease in amplitude and decay unless there is an additional energy input or a mechanism to reflect the wave energy. Layers in the atmosphere can sometimes be found where the horizontal propagation of a wave can occur without any loss of energy. These wave trapping layers are referred to as "wave ducts".

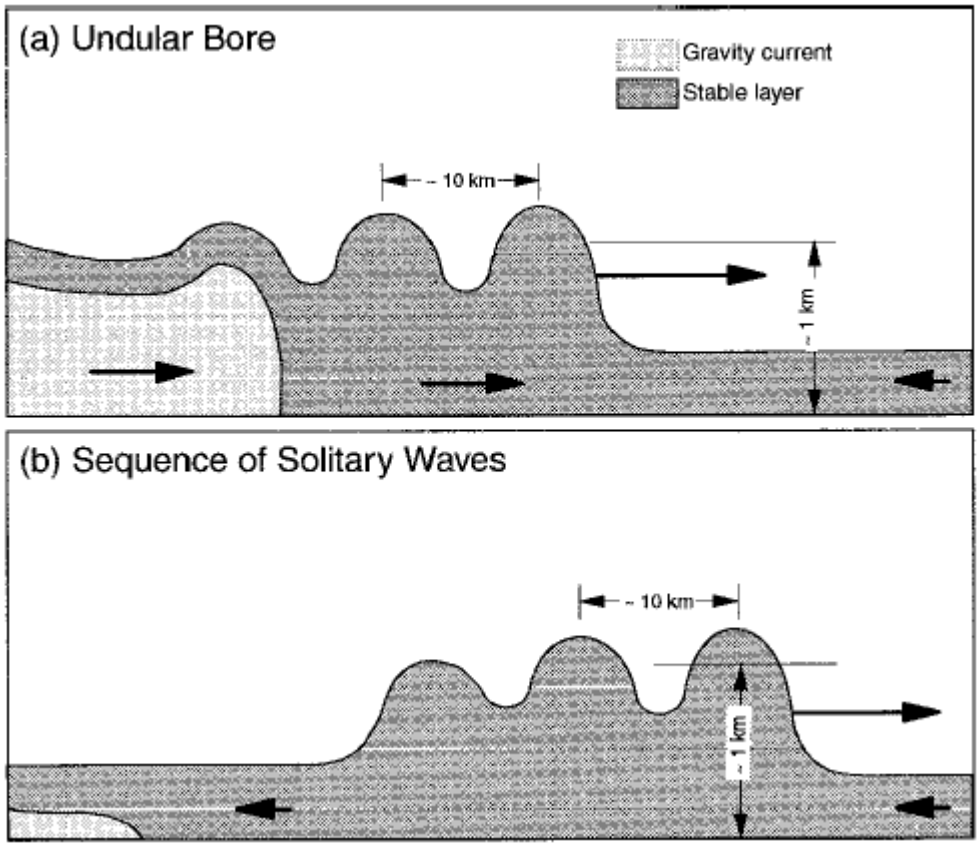

FIGURE 1.10: Schematic diagram of (a) a gravity current propagating into a stable layer and creating a bore; (b) the bore evolving into a series of solitary waves as the gravity current dissipates. From Locatelli *et al.* (1998).

In a two-layer continuously stratified fluid, waves with horizontal wavenumber k and horizontal wave speed c propagating through an atmosphere with Brunt-Väisälä frequency N with base-state winds u satisfy the Taylor-Goldstein equation

$$\frac{d^2w}{dz^2} + m^2 w = 0, \text{where } m^2 = l^2 - k^2. \tag{1.3}$$

The term l^2 is the Scorer parameter, which is given by

$$l^2 = \frac{N^2}{(u-c)^2} - \frac{1}{(u-c)}\frac{\partial^2 u}{\partial z^2}. \tag{1.4}$$

Scorer (1949) examined the upward propagation of energy in gravity waves forced by flow over mountains. If m^2 is positive then an oscillatory solution exists for $w(z)$ in Equation (1.3) and the wave propagates energy vertically. To obtain significant energy

at the ground, Scorer (1949) showed that the term l^2 in Equation (1.3) must decrease with height. If a layer exists where $l^2 < k^2$ (i.e. m^2 is negative) then $w(z)$ decays with height, meaning that the waves decay in the vertical rather than propagate. Energy in those wavelengths is then trapped in the layer below.

1.7.3 Application to thunderstorm outflow

The evaporation of rain and the melting of graupel and hail at low levels in thunderstorms causes the cooling of air. Subsidence occurs near the region of cooling, and divergence occurs near the surface beneath the cooling. The divergence of low-level air is referred to as the thunderstorm outflow (Haertel *et al.*, 2001). The leading edge of the outflow is referred to as the gust front.

Although it might seem initially obvious that a region of cool, dense air should subside and spread, Haertel *et al.* (2001) pointed out that cooling does not alter the total mass above a given area. The surface pressure is thus initially unchanged and the initial motion of the cool air remains unaccounted for. Haertel *et al.* (2001) gave a more complete description of the subsidence and divergence of cooled air: cooling at constant volume immediately produces low pressure via the ideal gas law. An acoustic wave propagates radially outwards from the region of cooling, compressing the cooled air and leaving a hydrostatic high beneath the cooled air. The pressure gradient associated with the hydrostatic high then causes the cooled air to spread.

Thunderstorm gust front outflows can often be described by gravity current theory (e.g. Charba, 1974; Mueller and Carbone, 1987; Simpson, 1969; Wakimoto, 1982). However, not every thunderstorm outflow can be classified as a gravity current. Some thunderstorm outflows have been characterised as combinations of gravity currents and solitary waves or bores (Doviak and Ge, 1984; Fulton and Doviak, 1990; Koch *et al.*, 1991; Locatelli *et al.*, 1998). The solitary waves or bores were generated by a gravity current propagating into a stable layer, as observed by Rottman and Simpson (1989) in laboratory simulations. The solitary waves or bores propagate faster than the gravity current and eventually overtake the disturbance that they were generated by.

The simulations of Haertel *et al.* (2001) showed the vertical structure of the cooling in a storm and the structure of the environment ahead of the storm affected the dynamics of the outflow. In one case the outflow was a gravity current, in another case the outflow was a gravity wave and in a third case the outflow was a combined gravity current and solitary wave. Haertel *et al.* (2001) also found that a solitary wave-bore outflow could be formed directly from the storm, without requiring the interaction of a gravity current with a low-level stable layer. Raymond and Rotunno (1989) performed idealised simulations and also found that the response of a stably-stratified flow to cooling could either be in the form of a gravity current or a gravity wave. They found that a gravity current response only occurred when the cooling was strong enough to produce an outflow that spread faster than gravity waves. These simulations show that the gravity current and wave outflow from a storm lie at either end of a continuous spectrum of behaviour.

1.7.4 Gust front surface signatures

Gravity current gust front

The passage of a gravity current gust front has a surface signature where the temperature decreases and the winds change at nearly the same time, after which a rise in pressure is observed (Engerer *et al.*, 2008; Goff, 1976; Haertel *et al.*, 2001).

Bore gust front

The passage of a bore is characterised at the surface by a pressure rise which lasts for a long time. There is often an accompanying wind shift. Bores initiate long-lasting vertical displacements of air. Temperature changes are infrequently observed and if any occurs at all there tends to be a small increase as warm air is mixed downwards (Knupp, 2006).

Gravity wave gust front

The surface signature of the passage of a gravity wave is characterised by oscillations in winds and pressure with no long-lasting vertical displacement of air. A trough in surface pressure is observed along with weak temperature and wind signals. As the gust front passes, pressure and wind speed both increase, with negligible change in temperature. The surface pressure rise is caused by a temperature perturbation in the lower atmosphere, but this temperature perturbation is elevated and does not have a surface signature: the

material surface bounding the two air masses does not intersect the ground (Haertel *et al.*, 2001).

1.7.4.1 Gravity current – wave hybrid gust front

In the case of an outflow that lies in the middle of the gravity current - gravity wave continuum, Haertel *et al.* (2001) found that the surface signature was a rise in pressure and a change in winds occurring before a fall in temperature. This is consistent with the gravity wave arriving ahead of the gravity current (e.g. as found in the laboratory experiments of Rottman and Simpson, 1989). The arrival of the gravity current is characterised by a sudden change in wind accompanied by a fall in temperature (Haertel *et al.*, 2001).

1.7.5 The gravity current–wave continuum in the atmosphere

In a stratified environment, the gravity current–undular bore–wave family can be viewed as a temporal sequence which has its roots in gravity current dissipation and energy dispersion (Carbone *et al.*, 1990). This sequence was observed to occur by Carbone *et al.* (1990) in a nocturnal squall line in Oklahoma that was initiated by a gust front propagating into a low-level jet. The gust front initially propagated as a gravity current and subsequently as an internal undular bore. Observations of a gravity current gust front in a nocturnal boundary layer in Oklahoma that subsequently evolved into a bore and then a solitary wave were made by Knupp (2006). A strong bore was initiated by a gravity current. The bore initially had similar kinematic properties to the gravity current, but as the initial gravity current dissipated the bore decoupled and became undular. A solitary wave then formed along an inversion ahead of the bore. A second, trailing, solitary wave developed along the surface-based inversion that was the remnant of the bore.

Observations of a bore, generated by a gravity current interacting with a stable surface layer, evolving to a wave were made by Marsham *et al.* (2011) during an elevated convection episode which occurred during IHOP. This behaviour was reproduced by Trier *et al.* (2011) in a simulation of the case study.

The evolution of outflow from a gravity wave to a gravity current has occurred in simulations. Crook and Moncrieff (1988) showed that the flow beneath deep convection in a 2D

model could evolve continuously from a wave, primarily forced by evaporative cooling, to a gravity current.

The evolution of gravity currents and waves can have a significant effect on the convective system. In a series of idealised simulations, Parker (2008) found that a surface-based MCS with gravity current outflow evolved into an elevated MCS above a bore-like feature when it encountered colder low-level air. The propagation speed of the elevated bore-lifted convection was faster than that of the surface-based gravity current-lifted convection. Furthermore, the convective system stalled during the transition from gravity current-lifting to gravity wave-lifting. It is thus clear that accurate prediction of the behaviour of a convective system depends highly on determining the evolution of the lifting mechanism. It also seems that the importance of elevated convection in general is more due to the dynamical effects of the stable layer rather than the intrinsic properties of the elevated source layer.

1.7.6 Wave trapping in the atmosphere

Crook (1986) performed numerical simulations of gravity waves generated by a density current propagating into a low-level stable layer. He found that energy could be trapped in the stable layer when the upper-level winds opposed the wave motion. However, low-level gravity waves have also been observed when the upper-level winds do not oppose the wave motion. Crook (1988) examined a large set of observations of low-level gravity wave events, and found that two further mechanisms were conducive to trapping wave energy at low levels: the presence of a low-level jet that opposes the wave motion, and the presence of an inversion at a height of 3-4 km. The presence of the low-level jet produced a layer above the jet where the Scorer parameter changed sign. This layer enabled the trapping of wave energy below. The inversion did not involve a change in the Scorer parameter, but waves propagated along the inversion and wave reflection was generated off the lower and upper interfaces of the inversion (Crook, 1988). Of the three wave trapping mechanisms discussed by Crook (1988) (opposing upper-level flow, opposing low-level flow, and inversion), opposing low-level flow was found to be the most important. Lindzen and Tung (1976) showed that the most efficient wave ducts form when a layer

of low static stability in which the environmental flow speed equals the wave phase speed occurs over a deep, stable boundary layer.

Modelling studies have shown wave trapping to be an important mechanism in the maintenance of convection. The elevated squall line simulated by Schmidt and Cotton (1990) occurred in an environment where a deep stable boundary layer was surmounted by a deep well-mixed layer. Wave energy was generated in the stable layer and trapped by the mixed layer above. The wave was able to lift low-level air to its level of free convection.

Observations of wave trapping have also been made. The undular bore observed by Koch *et al.* (1991) was generated by a gravity current collapsing into a nocturnal stable layer. The stable layer acted as a wave guide, along which the bore propagated. Marsham *et al.* (2011) found that a stably-stratified boundary layer surmounted by a nearly dry adiabatic layer supported wave trapping. The wave trapping was enhanced by the presence of a low-level jet. The velocity of the gravity wave observed by Marsham *et al.* (2011) was consistent with the theoretical phase velocity for waves in a duct. The lifting provided by the gravity wave was sufficient to initiate convection.

1.7.7 The generation and maintenance of deep convection

Gravity currents

The lifting at the leading edge of a thunderstorm gravity current can generate and maintain deep surface-based convection (Charba, 1974; Goff, 1976). Despite the presence of a low-level stable layer, gravity currents can also provide enough lifting to maintain elevated convection. In numerical simulations, Trier *et al.* (2006) found that even in the presence of a stable boundary layer the strength and organisation of elevated MCSs was influenced by the interaction between the environmental wind shear and the gravity current generated by the MCS. One of the elevated squall lines simulated by Dudhia *et al.* (1987) produced an extensive gravity current that was responsible for the maintenance of the convective updraught.

However, waves or bores generated by storms can also provide the lifting required to initiate or maintain deep convection. This is particularly important in elevated convection, where

the low-level stable layer can both prevent the formation of a gravity current and allow waves and bores to propagate along the interface at the stable layer.

Gravity waves

In simulations of elevated convection, gravity waves have been shown to be able to provide the lifting mechanism necessary to maintain convection. The cold downdraught air in the unicell squall line simulated by Dudhia *et al.* (1987) did not reach the surface and therefore did not produce a density current. The updraught was forced by a solitary gravity wave that lifted boundary layer air. The propagation speed of the elevated 2D squall line modelled by Schmidt and Cotton (1990) was determined by a high-amplitude gravity wave that was able to lift conditionally unstable air above the stable layer to its level of free convection. Buzzi *et al.* (1991) found that the low-level flow in their idealised 2D simulations of elevated convection had the characteristics of a large-amplitude solitary gravity wave. Schumacher and Johnson (2008) found that a low-level gravity wave lifted elevated parcels to their level of free convection, while near-surface parcels ascended and descended over the wave. Schumacher (2009) performed idealised simulations and found that a low-level convectively-generated gravity wave lifted an elevated unstable layer to its level of free convection. Observations have been made of elevated convection maintained by gravity waves. Several of the elevated convection episodes observed by Marsham *et al.* (2011) generated waves which provided enough lifting to initiate further convection. Detailed observations of elevated MCS occurring in the presence of a wave were made by Browning *et al.* (2010) and Marsham *et al.* (2010). These observations are summarised in Chapter 3 and provide the motivation for the modelling studies in Chapters 3 and 4.

Gravity waves can also initiate and maintain surface-based convection. The 2D simulations of Lafore and Moncrieff (1989) found that for certain wind profiles, a wave-like disturbance at low-levels lifted air from the boundary layer to its level of free convection and was responsible for the generation of new cells. A deep, convectively-generated tropospheric gravity wave formed in the simulations of Cran *et al.* (1992) and initiated new convection. Marsham and Parker (2006) showed that deep tropospheric gravity waves observed in a storm during CSIP initiated a secondary storm.

It is possible that a resonance may occur between a wave and the MCS that generated it. The wave observed by Browning *et al.* (2010) and Marsham *et al.* (2010) propagated with the elevated MCS. The estimated phase speed of the wave was comparable with the observed propagation speed of the convective system (Marsham *et al.*, 2010). Based upon this result, Marsham *et al.* (2010) speculated that there may be a resonance between the MCS, which generated the wave and that was travelling with the upper-level winds, and the wave.

Bores

There are many observations of bores initiating surface-based storms. Koch and Clark (1999) observed both a gravity current and a bore developing along a cold front. The bore propagated ahead of the cold front. Although the bore provided insufficient lifting to trigger storms, the combined lifting provided by the bore and the gravity current made it possible for low-level parcels to reach their level of free convection. In an analysis of a tornado outbreak that took place in 1974, Locatelli *et al.* (2002) suggested that the squall line was initiated by updraughts associated with an undular bore that was formed by the propagation of a cold front into a stable air mass. The nocturnal squall line observed by Carbone *et al.* (1990) was initiated by a gust front that propagated into a low-level jet. The gust front initially propagated as a gravity current and then subsequently as an internal undular bore. Karyampudi *et al.* (1995) observed an internal bore initiated by, and propagating ahead of, a cold front. The bore interacted with a lee cyclone, a dryline and a warm front to initiate convection. The bore observed by Knupp (2006) during IHOP had maximum parcel displacements that were just enough for convective initiation.

Bores can also initiate and maintain elevated convection. Downdraughts from the elevated convection observed by Marsham *et al.* (2011) interacted with the low-level stable layer and generated waves and bores that propagated ahead of the system and initiated further convection ahead of the cold pool. During the elevated stage of convection in the idealised simulations of Parker (2008), lifting was provided by a bore propagating on top of a nocturnal inversion.

1.8 Continuous modes of behaviour in convective storms

It is of note that convective storms have two interdependent, continuous forms of behaviour: elevated to surface-based convection, and gravity current to gravity wave lifting. A "phase space" of these two continuums is represented in Figure 1.11. Schematic diagrams show the behaviour at the extrema. Gravity current-lifted, surface-based convection is well understood (e.g. Charba, 1974; Goff, 1976). Gravity current-lifted, elevated convection was discussed by Dudhia *et al.* (1987) and Trier *et al.* (2006). Wave-lifted, elevated convection was observed by e.g. Marsham *et al.* (2011, 2010) and simulated by e.g. Buzzi *et al.* (1991); Schumacher (2009); Schumacher and Johnson (2008). The wave-lifted, surface-based regime is more speculative. Surface-based convection lifted by deep tropospheric gravity waves is well-documented and was discussed above. As mentioned previously, the simulations of Lafore and Moncrieff (1989) showed that a wave-like disturbance at low-levels could lift boundary layer air to its level of free convection. However, in general, a low-level stable layer would be required for a wave to propagate at low-levels. Low-level stability would have to exist within a surface layer that feeds the convection. The wave would also have to propagate across the convective region without being destroyed by the updraught. It is not immediately obvious that these conditions could co-exist.

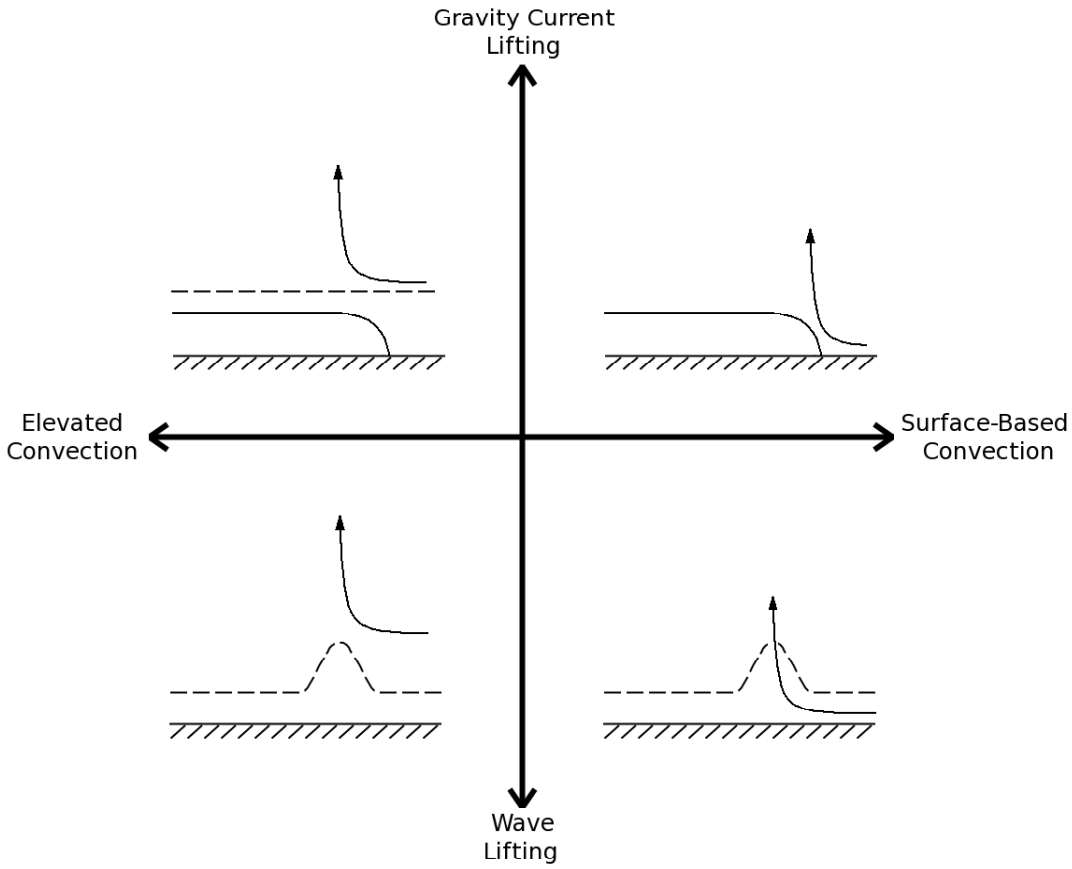

FIGURE 1.11: Schematic diagram of a phase space representing two continuums of convective storm behaviour: elevated to surface-based convection (horizontal axis) and gravity current to gravity wave lifting (vertical axis). Arrows represent convective updraughts. Solid lines represent material surfaces. Dashed lines represent interfaces between layers of different stability.

1.9 Kelvin-Helmholtz billows

1.9.1 Kelvin-Helmholtz instability

The Kelvin-Helmholtz instability is an example of a shear-flow instability in a stratified fluid. Kelvin-Helmholtz instability occurs in a hydrostatically stable flow where there is strong vertical shear. Waves develop perpendicular to the vertical shear vector, travel with the mean horizontal flow, and draw kinetic energy from the mean flow.

1.9.1.1 The Richardson number

The Richardson number (Ri) is a dimensionless number that describes the ratio of buoyancy forces to inertia forces in a fluid. It measures the stabilising effect of stratification compared to destabilising inertia effects. A larger value of Ri implies a more stable flow: as the density gradient of a fluid gets steeper, leading to a greater value of Ri, any disturbance in the fluid requires more energy to lift denser fluid into regions of less dense fluid and to push down less dense fluid into regions of denser fluid.

The Richardson number is defined as (e.g. Tritton, 1985)

$$Ri = \frac{N^2}{\left(\frac{\partial u}{\partial z}\right)^2} = \frac{g}{\theta}\frac{\frac{\partial \theta}{\partial z}}{\left(\frac{\partial u}{\partial z}\right)^2}, \tag{1.5}$$

where N is the Brunt-Väisälä frequency, u the horizontal velocity, z the vertical coordinate, g the acceleration due to gravity and θ the potential temperature. The quantity $\frac{1}{\theta}\left(\frac{\partial \theta}{\partial z}\right)$ is the static stability. The quantity $\frac{\partial u}{\partial z}$ is the (horizontal) shear. It is clear from Equation (1.5) that the value of Ri will be small when flows are statically stable and have strong horizontal shear.

1.9.1.2 The Richardson number criterion for Kelvin-Helmholtz instability

The first studies of the stability of stratified shear flow were made by Taylor (1931) and Goldstein (1931). Kelvin-Helmholtz instability occurs above a critical value of Ri. Taylor (1931) considered a case of a stratified fluid of uniform shear and static stability above a rigid boundary and found the flow to be stable for $\mathrm{Ri} > 0.25$. Goldstein (1931) considered a case of a stratified layer of constant shear and static stability between two semi-infinite homogeneous layers and also found the flow to be stable for $\mathrm{Ri} > 0.25$ and unstable for $0 < \mathrm{Ri} < 0.25$. For the more general case of a shear layer in an unbounded heterogeneous inviscid fluid, Drazin (1958) found the critical value of Ri (the maximum value of Ri for which there can be instability) to be 0.25. Miles (1961) considered the Taylor-Goldstein equation, Equation (1.3), and proved that a necessary condition for stability was $\mathrm{Ri} \geq 0.25$. By considering the Miles-Howard theorem, Scorer (1969) noted that instability is most likely to develop when thin layers with small values of Ri are formed.

1.9.1.3 The relationship between the wavelength of the fastest-growing mode and the thickness of the shear layer

The wavelength λ of the most unstable (i.e. the fastest-growing) mode was shown by Miles and Howard (1964) to depend on the thickness of the shear layer, Δz. The relationship between the thickness of the shear layer and the fastest-growing wavelength is commonly given (e.g. Browning, 1971; Chilson *et al.*, 1997; Fritts and Rastogi, 1985) as

$$\lambda = 7.5\Delta z. \tag{1.6}$$

1.9.2 Laboratory studies of the Kelvin-Helmholtz instability

(Thorpe, 1968) performed a comprehensive series of laboratory studies investigating the nature of shear instability in stratified fluids. His initial experiments used two miscible fluids of different densities (saline solution and fresh water) with a sharp interface in a rectangular tube that could be tilted in order to initiate flow. When the tube was tilted the fluids flowed relative to each other at velocities that depended on their density difference. Waves, or "billows", developed along the interface of the two fluids (Figure 1.12). The wave crests formed normal to the direction of the flow. Eventually, the flow became turbulent and the waves rolled up and developed 3D motions. Investigating this phenomenon for sets of fluids with different density differences (and therefore different values of Ri), Thorpe (1968) only observed instability for values of Ri less than than 0.25.

Further investigation into the nature of the transition of the instability to turbulent flow by Thorpe (1969) led him to conclude that the instability developed through the series of stages shown in Figure 1.13. Figure 1.13a shows the density (ρ) and velocity (u) distributions. The lines in Figure 1.13b mark a fluid of constant density. Figures 1.13c to 1.13j show the development of instability. At first a slight 2D wave forms on the interface between the fluids (Figure 1.13c). As the wave grows and rolls up, the fluid is redistributed and becomes concentrated in the centre, leading to much larger density gradients across the wave than were originally present (Figures 1.13d and 1.13e). The wave overturns (Figure 1.13f) and develops into a spiral (Figure 1.13g). Finally, a transition to

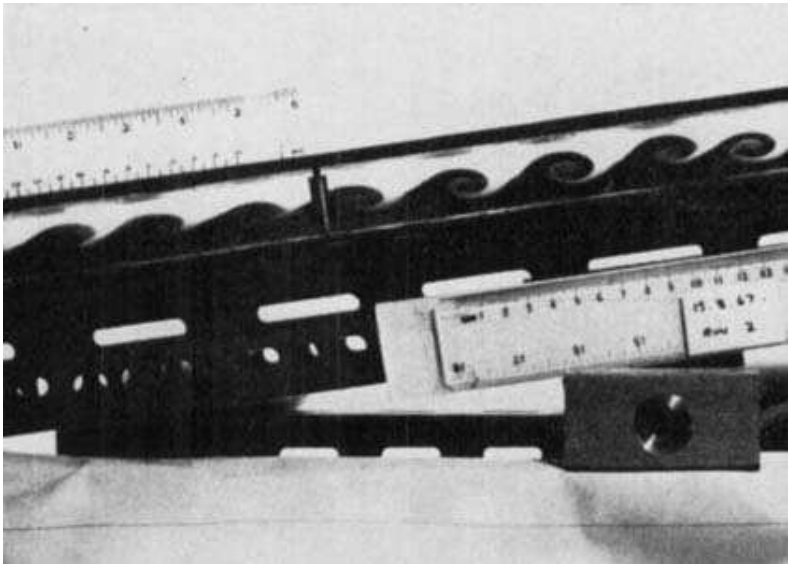

FIGURE 1.12: Waves developing at the interface between two miscible fluids. From Thorpe (1968), Figure 5d.

3D turbulent flow occurs (Figures 1.13h to 1.13j), which Thorpe (1969) was not able to follow in detail.

Thorpe (1971) compared the growth of instability in a stratified shear flow to the theory of Taylor (1931) and Goldstein (1931), and concluded that the wave phenomena that he observed, and the transition to turbulence, were due to the Kelvin-Helmholtz instability. The value of Ri at the onset of instability was found by Thorpe (1968) and Thorpe (1971) to be much less than the critical value of 0.25 predicted by the theory of Miles and Howard (1964). Thorpe (1973b) investigated the turbulent stage of Kelvin-Helmholtz billows in more detail and suggested that the turbulence resulted from gravitational instability near the centre of the billow. This was supported by the results of Thorpe (1973a), who used fixed and moving probes to measure density and horizontal velocity profiles in the billows. The turbulent region was found to quickly spread from the centre to fill the billow and begin to "entrain its surroundings in a process not unlike that at the edge of a thermal or buoyant plume" (Thorpe, 1973b). Entrainment releases potential energy of the entrained fluid, providing the billows with turbulent kinetic energy. This turbulent entrainment process is shown in Figure 1.14, where less dense fluid entrained from the upper layer is carried into the bottom of the billows, and more dense fluid entrained from the lower layer is carried to the top of the billows. This process begins to destroy the density gradients within the billows. In more recent tilt-tank experiments, De Silva *et al.* (1996) found that

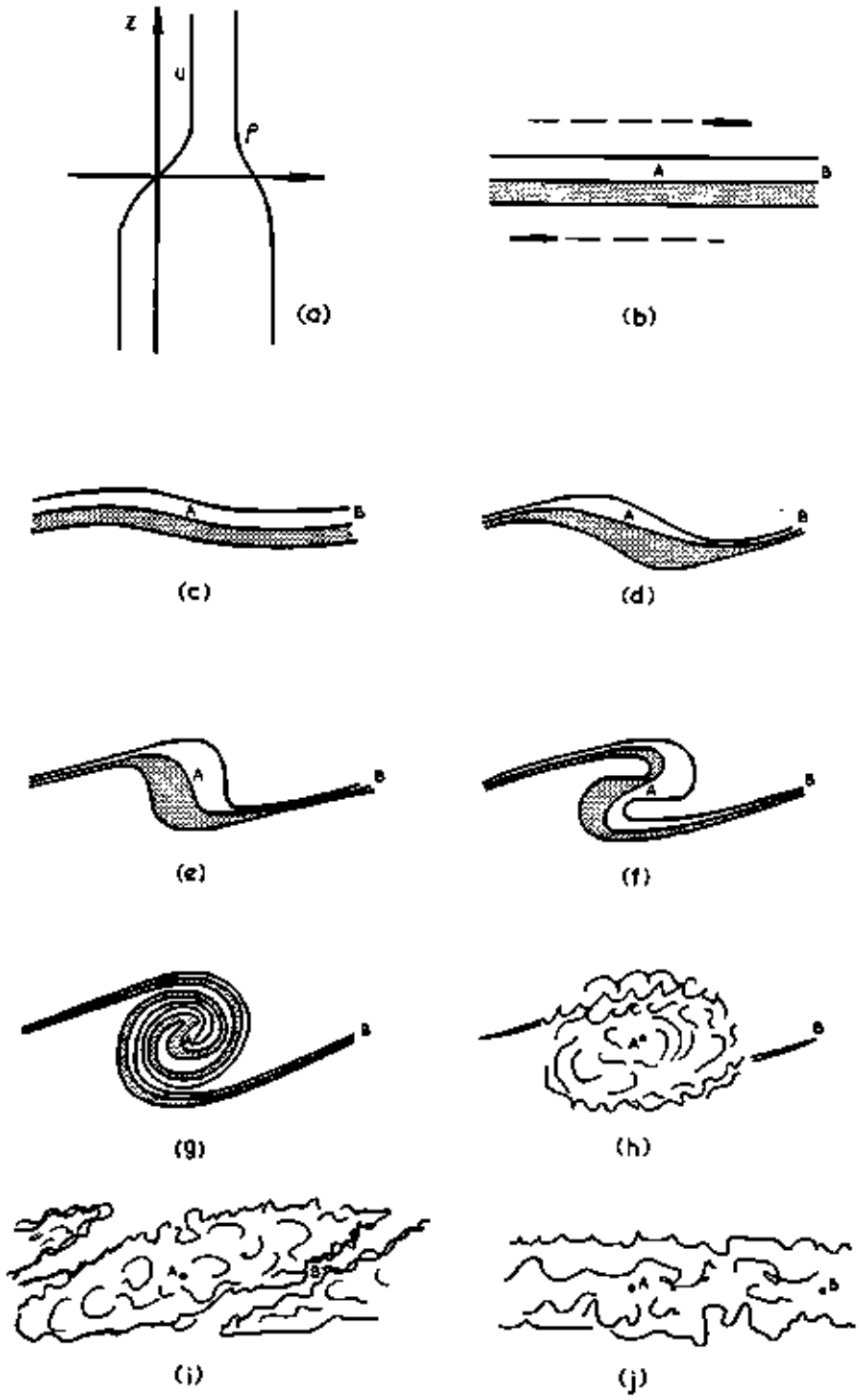

FIGURE 1.13: The growth of disturbances in a stratified shear flow. From Thorpe (1969), Figure 3.

turbulent mixing occurs near the core of a billow from the early stages of its development, from both the bulk roll-up of the billow and from small-scale turbulent motions near the centre.

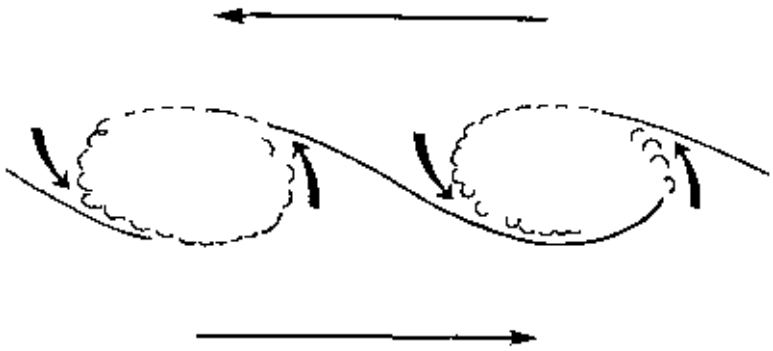

FIGURE 1.14: Turbulent entrainment into billows. From Thorpe (1973b), Figure 7.

Tank experiments are not the only laboratory investigations to have been made into the nature of the Kelvin-Helmholtz instability; wind tunnel experiments have also been performed. Scotti and Corcos (1972) created a statically stable stratified shear layer by uniformly heating one stream of air and merging it with another. A thin wire oscillating in the shear layer was used to introduce small periodic perturbations to the mean flow, and the resulting disturbances were measured over a range of values of Ri. For values of Ri such that $0.45 \leq \text{Ri} \leq 0.76$, the disturbances gradually decayed. For $\text{Ri} < 0.25$, the energy of the disturbances increased. These results were in agreement with the critical value of Ri predicted by theory, and measured in the tank experiments of Thorpe.

1.9.3 Numerical modelling studies of the Kelvin-Helmholtz instability

Numerical modelling investigations of the Kelvin-Helmholtz instability have supported theoretical and laboratory results. Patnaik *et al.* (1976) used a 2D model to investigate the behaviour of a stably-stratified horizontal shear layer. They saw that isopycnic contours (contours of constant density) rolled up into billows (Figure 1.15) much like the waves that were observed in the laboratory studies of Thorpe. Peltier *et al.* (1978) observed similar billow behaviour. Patnaik *et al.* (1976) and Peltier *et al.* (1978) confirmed that the wavelengths of the unstable modes depended on the depth of the shear layer in a way that was in agreement with the theory of Miles and Howard (1964), Equation (1.6).

The computations of Patnaik *et al.* (1976) and Peltier *et al.* (1978) were limited to investigating the early stages of the instability before the transition to turbulence. Sykes and Lewellen (1983) went on to investigate the turbulent nature of breaking Kelvin-Helmholtz waves. Their results showed that when billows break, turbulence is first produced in the core and then spreads to fill the billow. This process was in agreement with the numerous laboratory studies of Thorpe.

The limited nature of 2D studies was highlighted by the results of Fritts *et al.* (1996), who showed that in 2D simulations energy from the breaking billows was dissipated mainly through diffusive transport within the billow cores, but in 3D simulations secondary instabilities developed in the outer regions of the billows which contributed to the mixing of the billow cores.

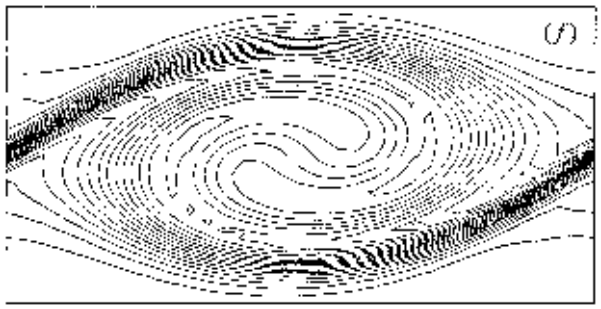

FIGURE 1.15: Isopycnic contours at the time of maximum amplitude in a numerical simulation of Kelvin-Helmholtz waves. From Patnaik *et al.* (1976), Figure 3f.

1.9.4 Kelvin-Helmholtz billows in the atmosphere: observations

The presence of billows in the atmosphere has been widely documented. Visual observations of Kelvin-Helmholtz billow clouds were made by Ludlam (1967), Scorer (1969) and Thorpe (2002). Figure 1.16 shows one such example of a billow cloud. Radar measurements of billows were first made by Browning and Watkins (1970). More recent radar measurements of billows have been made by Luce *et al.* (2010), Houser and Bluestein (2011) and Fukao *et al.* (2011). Aircraft measurements of billows in the atmosphere were made by Browning *et al.* (1973), Hardy *et al.* (1973) and Busack and Brümmer (1988).

FIGURE 1.16: Arched billows in a layer formed by Kelvin-Helmholtz instability; From Scorer (1969), Figure 8, and from the Clarke Collection, Royal Meteorological Society.

Studies have shown that atmospheric billows form in layers of strong shear and have a similar structure to the waves that form in laboratory investigations and numerical modelling studies of the Kelvin-Helmholtz instability. Because the instability patterns formed by some clouds and radar echoes in the atmosphere bear a strong resemblance to the instability patterns seen in laboratory and numerical modelling studies of the Kelvin-Helmholtz instability, such structures in the atmosphere tend to be referred to as Kelvin-Helmholtz waves or billows.

Theoretical and laboratory studies of the Kelvin-Helmholtz instability may not always be directly comparable with observations of billows that develop in the atmosphere. Tank-based laboratory studies of billows use stratified saline solutions, whereas billows that develop in the air are subject to the possible influence of thermodynamic effects through condensation and cloud formation (Thorpe, 2002). The Reynolds number, Re, (which gives a measure of the ratio of inertial to viscous forces in a fluid) at which billows develop is of the order of 10^3 in the laboratory but of the order of 10^7 in the atmosphere (Thorpe, 2002). In a series of numerical simulations performed by Peltier *et al.* (1978), the nature of the Kelvin-Helmholtz instability was found to be very different at high and low Reynolds numbers. However De Silva *et al.* (1996) argued that the Reynolds number of billows produced in the laboratory is sufficiently large to be compared to that of billows that develop in the atmosphere.

Observations have shown the critical value of Ri in the atmosphere to compare well with that predicted by theory and observed in laboratory experiments (i.e. instability occurs for Ri $\leq$ 0.25). Confirming the critical value of Ri for the free atmosphere has been difficult because of the dependence of Ri on the thickness of the shear layer over which it is measured (Browning, 1971). Measuring Ri over a shallow layer can lead to near-critical values, while calculating the bulk value over a deeper layer can lead to values that are well above the critical limit. However, the results of several observational studies appear to support the critical value of Ri = 0.25. Browning (1971) used radar observations to study seventeen events of large-amplitude billows (crest-to-trough amplitudes of 300 to 400 m) and found the minimum Ri for these events to lie in the range of 0.15 to 0.3, i.e. consistent with the critical Ri value predicted by theory. Browning (1971) also found that the billow formation showed a greater dependence on maxima in shear than on maxima in static stability, as might be expected due to the dependence in Equation (1.5) of Ri on the inverse square of the shear, but only the first power of the static stability.

A subsequent aircraft and radar study by Browning *et al.* (1973) found that billows developed in regions of strong shear, high static stability and low Ri (values less than 0.3). The Richardson number of the layer in which the billows observed by Hardy *et al.* (1973) developed was 0.15. Browning and Watkins (1970) found Ri to be less than 0.25 for some time before the onset of Kelvin-Helmholtz instability. Singh *et al.* (1999) calculated a value of Ri of 0.17 in the layer in which their observed billows developed. Fukao *et al.* (2011) reviewed several observations of Kelvin-Helmholtz billows and found the typical values of Ri to range from 0.15 to 0.30 and the average value to be 0.27. They suggested that the fact that the mean value of Ri exceeded 0.25 may have indicated that Ri was typically overestimated due to the lack of vertical resolution of radiosondes and because observational measurements of temperature and winds were rarely co-located.

1.9.4.1 Kelvin-Helmholtz billows in the atmosphere: synoptic environments in which billows can develop

Frontal zones and jet streams are the major synoptic environments that favour the development of Kelvin-Helmholtz instability, due to the enhanced vertical shear of horizontal wind

in such regions. Chapman and Browning (1997) observed billows forming in a strongly-sheared precipitating warm-frontal zone. Hardy *et al.* (1973) found that billows developed in a shear layer between an upper-level frontal zone that had advanced ahead of a surface cold front. Wang *et al.* (1983) observed wave-like rainbands aligned perpendicular to the vertical shear in a cold-frontal zone, and suggested they may have been caused by shear instability. Bryant and Browning (1975) found evidence of turbulence due to billows during the passage of a warm frontal zone with strong surface winds. James and Browning (1981) studied a series of billows that formed in a strongly sheared layer of high static stability associated with an upper tropospheric jet stream. Browning *et al.* (1973) observed billows which formed in a strongly sheared frontal zone beneath a jet axis. Billows were observed by Houser and Bluestein (2011) along a shear interface due to a cold-frontal boundary that separated cold surface air from warmer air above. Luce *et al.* (2008) found that billows developed in the upper part of a jet stream, near the tropopause. These billows were unusually high, and it was suggested that the Kelvin-Helmholtz instability may have been triggered by gravity waves from the jet stream. Klostermeyer and Rüster (1980) observed the formation of billows due to Kelvin-Helmholtz instability in the lower shear layer of a polar front jet stream. Chilson *et al.* (1997) also found that billows developed during the passage of an upper-level jet. Singh *et al.* (1999) observed billows that developed due to Kelvin-Helmholtz instability that formed in association with a jet stream.

1.9.4.2 Kelvin-Helmholtz billows in the atmosphere: billow wavelength and the depth of the shear layer

The relationship between the wavelength of billows that have been observed in the atmosphere and the depth of the layer in which they develop tends to be in agreement with the relationship predicted by linear theory and given in Equation (1.6). From a radar study of 17 Kelvin-Helmholtz billow events, Browning (1971) determined the wavelength of the billows to be between 0.8 and 4.0 km, with a mean value of 1.8 km. Using Equation (1.6), he concluded that the depth of the shear layer in which the billows formed must have been between 100 and 530 m. The maximum depth of the strongly sheared regions with $\mathrm{Ri} < 0.5$ observed by Browning (1971) varied between 400 and 700 m, which was in reasonable agreement with theory. The billows observed by Chilson *et al.* (1997) had a wavelength of 4.0 km, compared to an expected wavelength, based on a calculation using Equation (1.6),

of 4.5 km. For the case discussed by Singh *et al.* (1999), the observed billow wavelength was 7.2 km compared to an expected billow wavelength of 7.5 km. Bryant and Browning (1975) used Equation (1.6) and their observed billow wavelength to calculate the depth of the layer of strong shear, and found the result to compare favourably with observational data of the wind shear.

1.9.4.3 Kelvin-Helmholtz billows in the atmosphere: billow wavelength and crest-to-trough amplitude

The crest-to-trough amplitude of billows observed in the atmosphere tends to be of the order of several hundred metres, while the billow wavelength tends to be of the order of several kilometres. Chilson *et al.* (1997) found the crest-to-trough amplitude of the billows associated with an upper-level jet to be up to 230 m. The wavelength of the primary train of billows studied by Browning *et al.* (1973) was between 1.3 and 2.4 km, with a crest-to-trough amplitude of 230 to 450 m. In their review of several papers discussing observations of Kelvin-Helmholtz billows, Fukao *et al.* (2011) found the typical range of billow depth to be 200-1000 m and the typical range of billow wavelengths to be 1.5-4.0 km. The billows studied by Browning (1971) had wavelengths of between 0.8 and 4.0 km, with a mean value of 1.8 km. The crest-to-trough amplitude of the billows observed by Browning (1971) was between 220 and 450 m, with a mean value of 330 m.

1.9.4.4 Kelvin-Helmholtz billows in the atmosphere: billow duration

Billows in the atmosphere tend to be relatively short-lived. Browning (1971) found that the duration of most of the billow events that he observed was less than 30 minutes. The billows observed by Chilson *et al.* (1997) persisted for an interval of about 10 minutes. The upper-level billows observed by Luce *et al.* (2008) lasted for about 2 hours, but these were observed at an unusual height (16 km) and may have been be an exceptional case. Fukao *et al.* (2011) presented observations of several billow events which each persisted for about 30 minutes.

1.9.4.5 Kelvin-Helmholtz billows in the atmosphere: billow growth and breakdown

Billows that develop in the atmosphere have been observed to undergo some of the same stages of development and breakdown suggested by Thorpe (1969) and shown in Figure 1.13. Browning and Watkins (1970) showed that high power radar could be used to detect billows in clear-air. The turbulence associated with the billows causes small-scale inhomogeneities in the refractive index of the air, which is detectable by radar. However, in clear-air, radars cannot detect billows before they become turbulent, so observations of billows in the early stages of development are lacking. Figure 1.17 is an example of billows seen in the vertical shear field derived from data from high-resolution Doppler radar. The wavelength of the billows in Figure 1.17 is between 4 and 5 km.

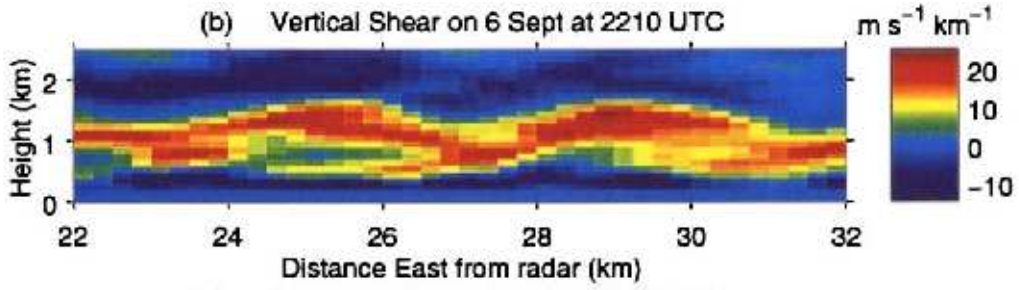

FIGURE 1.17: Vertical shear (m s^{-1} km^{-1}) derived from radar data. From Chapman and Browning (1999), Figure 1b.

Browning and Watkins (1970) studied the evolution of billows in a region of clear-air turbulence and found their life cycle to correspond to that shown in the schematic diagram in Figure 1.18. The following is a summary of the findings of Browning and Watkins (1970): A single shallow unperturbed clear-air echo layer (on the right of the diagram) was embedded in a deeper stable layer with strong shear. The Richardson number was close to the critical value of 0.25, and deep Kelvin-Helmholtz instability developed. The layer echo developed billows by 1243 UTC. The subsequent billow evolution was similar to that seen in the laboratory studies of Thorpe (1969), shown in Figure 1.13, and to the numerical studies of Sykes and Lewellen (1983). The billows rolled up and overturned. By 1250 UTC, turbulent mixing in each billow roll led to the formation of cat's eye patterns in which the static stability was nearly neutral. This had the effect of concentrating the stability into two layers at the top and bottom of the mixed regions. The stable boundaries were detected by the radar, producing a braided echo structure. The cat's eye and braided

structures in the atmospheric billows observed by Browning and Watkins (1970) were reminiscent of the structures seen in the numerical simulations of Patnaik *et al.* (1976), Peltier *et al.* (1978) and Sykes and Lewellen (1983). Finally, when each billow broke, the cells of relatively well-mixed air were stretched out by the wind shear. The edges of these regions were detected by the radar for a while as sloping echo filaments, but by 1258 UTC the regions had merged to produce a homogeneous horizontal layer bounded by two stable layers which the radar detected as a double layer. Browning and Watkins (1970) did not observe an associated splitting of the wind-shear profile.

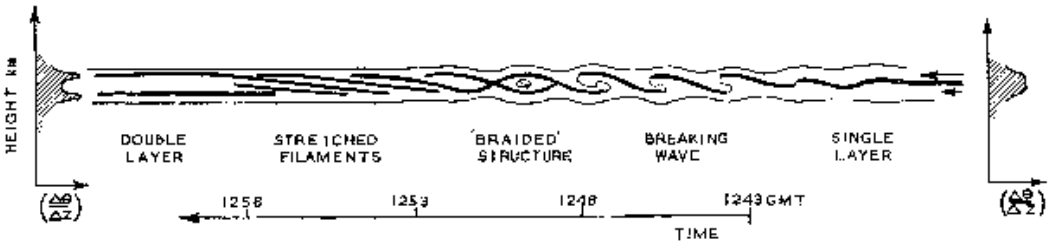

FIGURE 1.18: Schematic representation of the life cycle of an individual Kelvin-Helmholtz billow. Time progresses from right to left. Thick lines correspond to the detectable clear-air radar echo, which started as a single layer at 1243 and finished as a double layer at 1258 UTC. Schematic vertical profiles of $\left(\frac{\Delta\theta}{\Delta z}\right)$ are indicated before and after the occurrence of Kelvin-Helmholtz instability. From Browning and Watkins (1970), Figure 4.

Other studies of billows in the atmosphere have supported the findings of Browning and Watkins (1970). The radar echoes of billows observed by Hardy *et al.* (1973) and Browning *et al.* (1973) showed similar rolling-up behaviour and braided structures to those observed by Browning and Watkins (1970). Chapman and Browning (1997) presented evidence of the wind-shear profile splitting in a similar manner to the splitting of the thermal stratification observed by Browning and Watkins (1970). Luce *et al.* (2010) observed braided structures associated with Kelvin-Helmholtz billows. Fukao *et al.* (2011) detected several billow events with braided structures that showed similar characteristics to those reported by Browning (1971). However, in contrast to the findings of Browning and Watkins (1970) and Chapman and Browning (1997), Fukao *et al.* (2011) rarely observed layer splitting after the breakdown of the billows. Fukao *et al.* (2011) suggested that the large-amplitude billows they observed were generated when the value of Ri fell just below 0.25 and that as such they were not energetic enough to produce efficient mixing.

Billows have been shown to be an important source of clear-air turbulence (Browning, 1971; Browning and Watkins, 1970; Hardy *et al.*, 1973) due to the associated wave breaking, and

therefore present a hazard to aviation. The wave-breaking associated with billows also has meteorological significance in that the resulting turbulence leads to vertical mixing (e.g. of heat, momentum and mass). Chapman and Browning (1999) suggested that this mixing may be substantial enough to alter the structure of a frontal zone. Nappo (1991) reported evidence that the turbulence due to billows was responsible for the transport to the surface not only of heat and momentum, but also of atmospheric pollutants.

1.9.4.6 Kelvin-Helmholtz billows in the atmosphere: billows and convection

As well as being observed in clear-air, billows have also been observed in convective cloud and regions of precipitation. Browning *et al.* (2010) and Browning *et al.* (2012) observed billows in elevated MCSs in the UK, and Houser and Bluestein (2011) observed billows in a winter-time storm in Oklahoma.

Some evidence has been provided that Kelvin-Helmholtz waves can modify precipitation microphysics. In an observational study of a winter storm, Houser and Bluestein (2011) found that Kelvin-Helmholtz waves formed along the shear interface at a cold-frontal boundary between cold surface air and warmer air above, and that enhanced reflectivity was found in the billow updraughts. They hypothesised that the billows caused the increased growth of ice particles by: enhancing riming; supplying moisture and supercooled droplets; opposing the fall speed of the crystals; and prolonging the dwell time of the crystals. The billows also caused the increased generation of ice crystals through the Hallett-Mossop process of splinter production during riming (Hallett and Mossop, 1974).

Cloud may affect the onset of instability. The onset of Kelvin-Helmholtz instability was observed by Luce *et al.* (2010) to occur at a cloud base where cloudy air was advecting over subsaturated air. After the cloud passed, the Kelvin-Helmholtz braids and radar echoes were much weaker, leading Luce *et al.* (2010) to suggest that the presence of cloud was conducive to the onset of instability. The presence of a saturated layer was shown by Chapman and Browning (1999) to affect billow development. They observed billows that formed just ahead of a surface warm front and concluded that ascent at the surface front caused the onset of saturation, which reduced the static stability and lowered the Ri

of a deep sheared layer in the frontal zone from around 1.0 to a value of much less than 0.25. Luce *et al.* (2010) noted that cooling by sublimation could also reduce the stability immediately beneath a cloud.

1.9.5 Modelling studies of Kelvin-Helmholtz billows in the atmosphere

There have been various numerical modelling investigations of Kelvin-Helmholtz instability, as discussed in Section 1.9.3, but not many have been performed with respect to Kelvin-Helmholtz billow events in the atmosphere. Two studies used observed profiles of temperature and wind to produce waves in a model. To support their observational studies of billows that developed below a polar-front jet stream, Klostermeyer and Rüster (1980) used vertical profiles of mean temperature and wind derived from a radiosonde ascent and radar data to initialise a 2D linear model. The frequency, growth rate and velocity profile of the fastest-growing instability that developed in the model was in good agreement with their observational data of the Kelvin-Helmholtz instability. Busack and Brümmer (1988) observed Kelvin-Helmholtz billows in an off-shore stable daytime boundary layer, and used the observed wind and temperature profiles to perform simulations with a linear model. The model produced waves with maximum amplitudes in agreement with the observed waves. The wavelengths produced by the model were 30% shorter than the observed wavelengths, but the model values were still in agreement with the relationship between the wavelength and depth of the shear layer given in Equation (1.6).

1.10 The Convective Storm Initiation Project

The Convective Storm Initiation Project (CSIP) was an international project based in the UK designed to understand why, when and where deep convection breaks out. The main field campaign took place in southern England during June, July and August 2005. A map of the locations of the instruments used during CSIP is shown in Figure 1.19. The Operations Centre was based at Chilbolton, at the centre of the range rings in Figure 1.19. The Chilbolton radar facility (Goddard *et al.*, 1994) was sited here. The main research tool at the Chilbolton Observatory was a 25 m fully steerable antenna. A 3 GHz (S band) Doppler-polarisation radar (CAMRa) [1] and a 1275 MHz (L band) clear-air radar (ACROBAT) [2] were installed on the antenna. A 35 GHz dual-polarisation Doppler cloud radar (Copernicus) was also available at Chilbolton. Other instruments were deployed within range of the CAMRa radar. The instrument systems were provided and operated by scientists at the Universities of Aberystwyth, Leeds, Manchester, Reading, Salford and Bath; the Institute for Meteorology and Climate Research (IMK), Karlsruhe, Germany; the Rutherford Appleton Laboratory; the Met Office; and GeoForschungsZentrum (GFZ) – Potsdam.

During CSIP data were collected from the Chilbolton radars, a UHF wind profiler, three sodars, two Doppler lidars, an ozone lidar, a water vapour lidar, three microwave radiometers, a ceilometer, serial ascents at 1- to 2-hour intervals from six mobile rawinsonde stations, serial ascents from three Met Office operational systems, a network of sixteen automatic weather stations (AWSs), two instrumented light aircraft (a Dornier 128 and Cessna 182), a network of five GFZ GPS integrated water vapour stations and two energy balance stations.

The CSIP instruments were situated in a region of good coverage by the Met Office network of surface stations and the UK operational weather radar network. Composite maps of estimated rainfall intensity were provided every 15 minutes by the network radar. Satellite data from *Meteosat-8* and *Meteosat-6* provided infrared, water vapour and high-resolution visible imagery. The satellite images were used for post-storm analysis and also for nowcasting to guide the deployment of the aircraft and rawinsondes (Browning *et al.*, 2007).

[1] Chilbolton Advanced Meteorological Radar
[2] Advanced Clear-air Radar for Observing the Boundary layer And Troposphere

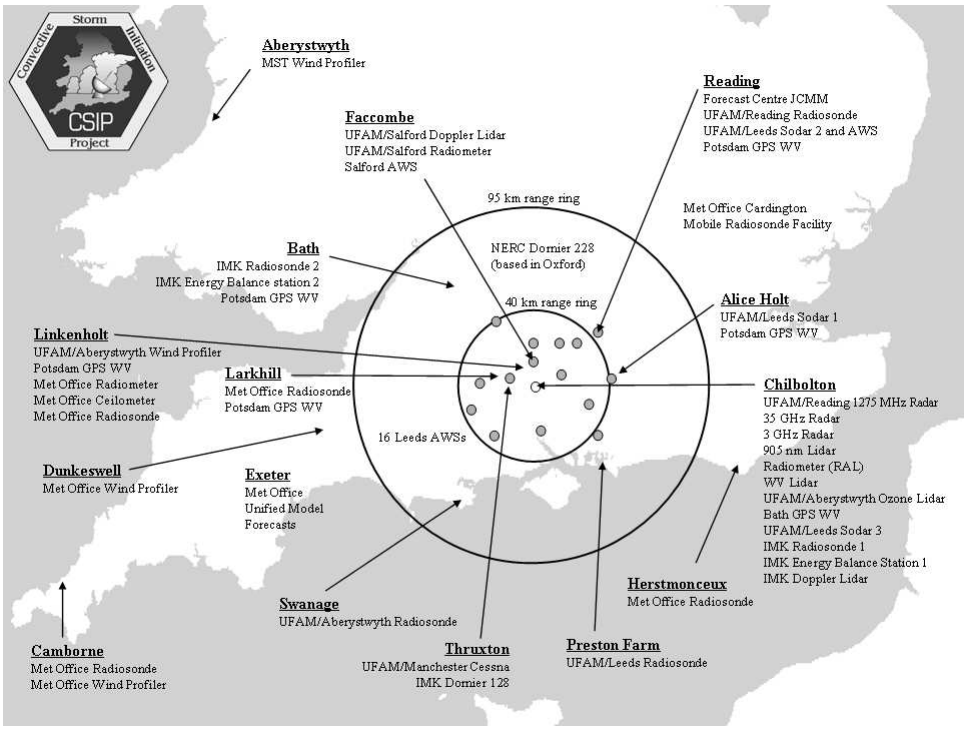

FIGURE 1.19: Map showing the locations of instruments deployed in southern Britain during CSIP in June, July and August 2005. The shaded circles represent the positions of the Automatic Weather Stations (AWSs). From Browning *et al.* (2007).

The Met Office NIMROD system (a fully automated system for weather analysis and nowcasting based on a network of C-band rainfall radars, Golding, 1998) provided hourly surface wind and convergence analyses that were also used to guide the deployment of the aircraft and rawinsondes. The operational mesoscale version of the Met Office Unified Model (12 km horizontal resolution, Cullen, 1993) was used to provide products to forecast convective initiation. A 4 km version of the Unified Model, developed by Met Office staff at the Joint Centre for Mesoscale Meteorology (JCMM) at the University of Reading, was used to provide supplementary runs at higher resolution.

There were eighteen intensive observation periods (IOPs) in June, July and August of 2005. Of these eighteen IOPs, only one involved convection that originated from above the boundary layer (Browning *et al.*, 2007). MCSs were observed during two IOPs. One of these was IOP 3, which was the case of elevated convection. The other was IOP 18, in which an MCS with squall-line structure and an extensive cold pool formed close to the Chilbolton radar (Clark *et al.*, 2012b).

Chapter 2

High-resolution numerical models

2.1 The Weather Research and Forecasting (WRF) model

The Weather Research and Forecasting (WRF) model is a numerical weather prediction (NWP) model that has been designed as a tool for use in both research and operational forecasting situations (Skamarock *et al.*, 2008). The development of WRF was a collaborative effort that was guided by the National Center for Atmospheric Research (NCAR) in the USA. The flexibility and portability of the WRF code allows it to be used in a wide variety of computing environments. The WRF Software Framework (WSF) provides an infrastructure for the dynamics solvers, physics packages, initialisation programs, variational data assimilation and chemistry model. WRF features two dynamical cores: the Advanced Research WRF (ARW) solver, and the Nonhydrostatic Mesoscale Model (NMM) solver. WRF can be used to produce both real and idealised simulations across a range of scales, from Large Eddy Simulations (LES) to the global scale of thousands of kilometres.

2.1.1 An overview of Advanced Research WRF (ARW)

The Advanced Research WRF (ARW) is a subset of the WRF modelling system that uses the ARW dynamics solver to produce a simulation (Skamarock *et al.*, 2008). The ARW solver comprises a set of fully compressible, nonhydrostatic (with a run-time hydrostatic option) Euler equations which are conservative for scalar variables. The prognostic variables are the velocity components u and v in Cartesian coordinates, vertical velocity w,

perturbation potential temperature, perturbation geopotential, and perturbation surface pressure of dry air. The model top is a constant pressure level along a material surface. The bottom boundary condition options are either physical or free-slip.

2.1.2 The ARW governing equations

The ARW dynamics solver integrates the compressible, non-hydrostatic Euler equations in flux form, using variables that have conservation properties. The equations are formulated using a terrain-following hydrostatic-pressure vertical coordinate η which is defined as

$$\eta = (p_h - p_{ht})/\mu, \text{ where } \mu = (p_{hs} - p_{ht}), \tag{2.1}$$

where p_h is the hydrostatic component of the pressure, and p_{hs} and p_{ht} refer to its boundary values along the terrain surface and the top of the model, respectively. The vertical coordinate system is shown in Figure 2.1. The coordinate definition given in Equation (2.1) was first used by Laprise (1992) and is the traditional σ coordinate (also called a mass vertical coordinate) used in many hydrostatic atmospheric models.

The quantity $\mu(x, y)$ represents the mass per unit area in the column at (x, y) in the model domain. The following quantities are used in the flux form variables: $\mathbf{v} = (u, v, w)$, the covariant velocities in the two horizontal (u, v) and vertical (w) directions, $\omega = \dot{\eta}$, the contravariant 'vertical' velocity, and θ, the potential temperature. The following non-conserved variables are also used: $\phi = gz$, the geopotential, p, pressure, and $\alpha = 1/\rho$, the inverse density.

A full description of the dry flux-form Euler equations is given in Skamarock *et al.* (2008). In forming the moist Euler equations, the following principles are used: the dry air mass is coupled to the prognostic variables, dry air is conserved and the coordinate is defined with respect to the dry air mass. The vertical coordinate is then written as

$$\eta = (p_{dh} - p_{dht})/\mu_d, \tag{2.2}$$

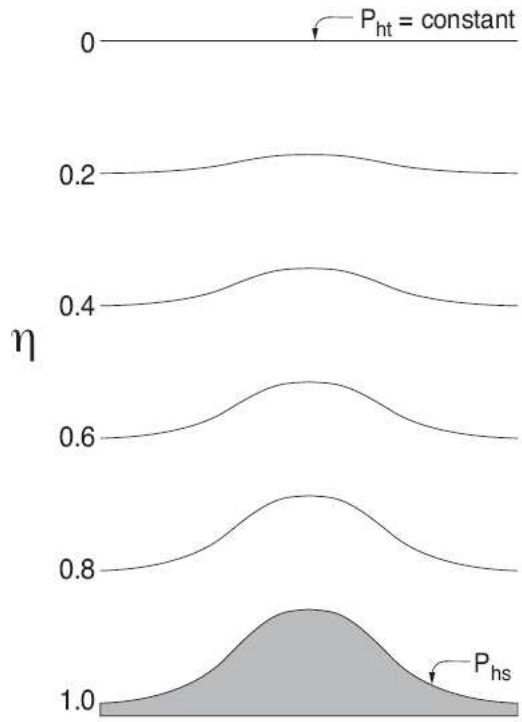

FIGURE 2.1: ARW η coordinate. From Skamarock *et al.* (2008).

where μ_d is the mass of dry air in the column, p_{dh} is the hydrostatic pressure of the dry atmosphere, and p_{dht} is the hydrostatic pressure at the top of the dry atmosphere. The coupled variables are defined as

$$\mathbf{V} = \mu_d \mathbf{v}, \Omega = \mu_d \dot{\eta}, \Theta = \mu_d \dot{\theta}. \tag{2.3}$$

The moist Euler equations are then written as

$$\partial_t U + (\nabla.\mathbf{V}u) + \mu_d \alpha \partial_x p + (\alpha/\alpha_d)\partial_\eta p \partial_x \phi = F_U, \tag{2.4}$$

$$\partial_t V + (\nabla.\mathbf{V}v) + \mu_d \alpha \partial_y p + (\alpha/\alpha_d)\partial_\eta p \partial_y \phi = F_V, \tag{2.5}$$

$$\partial_t W + (\nabla.\mathbf{V}w) - g[(\alpha/\alpha_d)\partial_\eta p - \mu_d] = F_W, \tag{2.6}$$

$$\partial_t \Theta + (\nabla . \mathbf{V}\theta) = F_\Theta, \tag{2.7}$$

$$\partial_t \mu_d + (\nabla . \mathbf{V}) = 0, \tag{2.8}$$

$$\partial_t \phi + \mu_d^{-1}[(\mathbf{V}.\nabla\phi) - gW] = 0, \tag{2.9}$$

$$\partial_t Q_m + (\nabla . \mathbf{V} q_m) = F_{Q_m}. \tag{2.10}$$

In Equations (2.4) to (2.7), the right-hand side (RHS) terms F_U, F_V, F_W, and F_Θ represent forcing terms that arise from the model physics, turbulent mixing, spherical projections and the earth's rotation.

The diagnostic equation for dry inverse density is given by

$$\partial_n \phi = -\alpha_d \mu_d, \tag{2.11}$$

and the diagnostic relation for the full pressure (dry air plus water vapour) is

$$p = p_0 (R_d \theta_m / p_0 \alpha_d)^\gamma, \tag{2.12}$$

where $\gamma = c_p/c_v = 1.4$ is the ratio of the specific heat capacities at constant pressure and volume for dry air, R_d is the gas constant for dry air, p_0 is a reference pressure (typically 10^5 Pa). In Equations (2.4) to (2.12), α_d is the inverse density of dry air ($1/\rho_d$ and α is the full moist inverse density:

$$\alpha = \alpha_d (1 + q_v + q_c + q_r + q_i + ...)^{-1}, \tag{2.13}$$

where q_* are the respective mixing ratios for water vapour, cloud, rain, ice, etc. The moist potential temperature is given by

$$\theta_m = \theta(1 + (R_v/Rd)q_v) \approx \theta(1 + 1.61q_v), \tag{2.14}$$

where R_v is the gas constant for water vapour. Finally, $Q_m = \mu_d q_m$ is the generic coupled moisture variable, where $q_m = q_v, q_c, q_i, ...$ etc.

The full set of governing equations including curvature and Coriolis terms and transformations for projections to the sphere are given in Chapter 2 of Skamarock *et al.* (2008). These governing equations are then rewritten in perturbation form for use with the discrete solver. This has the advantage of reducing truncation errors in calculations of the horizontal pressure gradient and reducing machine rounding errors in calculations of the vertical pressure gradient and buoyancy. New variables are defined as perturbations from a hydrostatically-balanced reference state, and reference state variables are a function of height only and satisfy the governing equations for an atmosphere at rest (Skamarock *et al.*, 2008).

The governing equations are then discretised temporally and spatially (described in full in Chapter 3 of Skamarock *et al.*, 2008). The ARW solver uses a time-split integration scheme, allowing slow or low-frequency (meteorologically significant) modes to be integrated using a third-order Runge-Kutta (RK3) time integration scheme (described by Wicker and Skamarock, 2002), while the high-frequency (but meteorologically insignificant) acoustic modes are integrated on smaller time steps. This maintains numerical stability without severely limiting the main time step. Each time integration consists of two primary loops: an outer loop for the RK3 integration, which uses a large time step, and an inner loop for the acoustic mode integration, using a small time step. The scheme achieves efficiency through the fact that the RK3 time step is much larger than the acoustic time step, and so the more computationally expensive evaluations are only performed during the less-frequent RK3 steps. Both time steps (the RK3 and the acoustic) are limited by Courant numbers. The RK3 time step is limited by the advective Courant number $u\Delta t/\Delta x$ and the choice of advection scheme (which can use 2^{nd} through 6^{th} order discretisation). A table of maximum stable Courant numbers for one-dimensional linear advection was originally given in Wicker and Skamarock (2002) and is reproduced in Skamarock *et al.* (2008) (their Table 3.1). For 3D applications, the time step should satisfy

$$\Delta t_{max} < \frac{Cr_{theory}}{\sqrt{3}}.\frac{\Delta x}{u_{max}}, \tag{2.15}$$

where Cr_{theory} is the Courant number given by Wicker and Skamarock (2002) and u_{max} is the maximum velocity expected in the simulation. For resolutions that allow convection to be explicitly calculated ($\Delta x \leqslant 5$ km), the stability-limiting Courant number is controlled by the vertical velocities in the convective updraughts. The acoustic time step is limited by the speed of sound, c_s as follows:

$$\Delta \tau < 2.\frac{\Delta x}{c_s}. \tag{2.16}$$

In ARW, the ratio of the RK3 time step to the acoustic time step must be an even integer, and the required input in the ARW is in fact the ratio of the RK3 time step to the acoustic time step.

The spatial discretisation in the ARW solver uses Arakawa C grid staggering in the horizontal for the normal velocities and thermodynamic variables (Figure 2.2). The geopotential ϕ is defined at the w points, and the column mass μ and moisture variables q_m are defined at the mass points ((i, j) points). The diagnostic variables (the pressure, p ,and inverse density, α) are computed at the mass points. The vertical grid length $\Delta\eta$ is not a fixed constant but is specified during the initialisation. The user specifies the η values of the model levels, under the constraint that η=1 at the surface and η=0 at the top of the model. Subject to these boundary conditions, η decreases monotonically between the surface and the top of the model. The vertical grid is not regularly spaced but is stretched such that there is a higher resolution of η levels near the surface.

2.1.3 Initial conditions and lateral boundary data

For idealised cases, ARW can be initialised with user-defined initial conditions. For real-data cases, initialisation is from interpolated data that may be from either an external analysis or forecast. Initialisation data for real-data cases are pre-processed by an external package, the WRF Preprocessor System (WPS), that converts the large-scale data into a

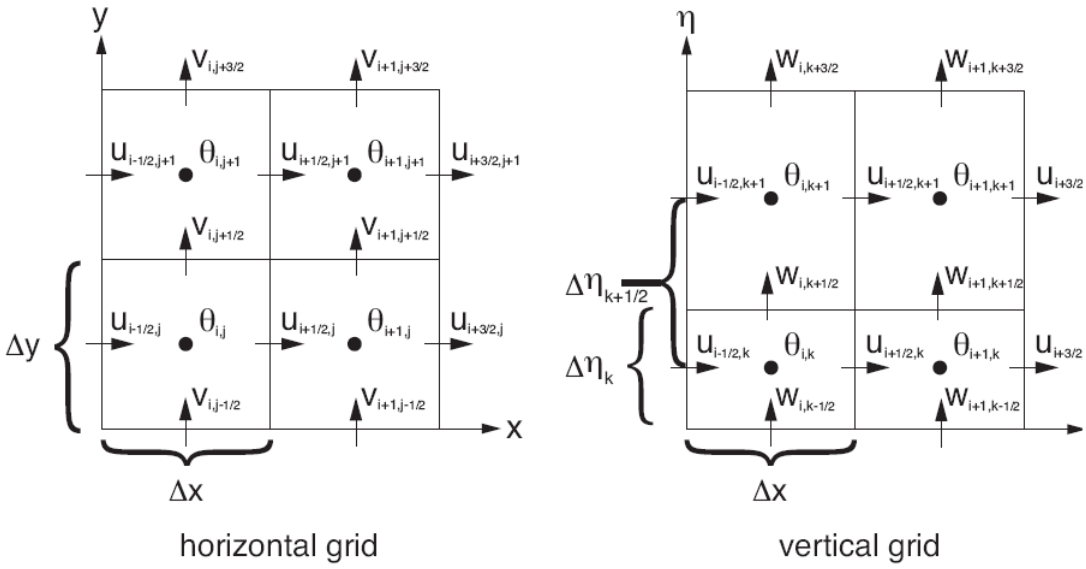

FIGURE 2.2: Horizontal and vertical grids of the ARW. From Skamarock *et al.* (2008).

format that can be used by the ARW real-data processor. The ARW real-data processor then generates initial and lateral boundary conditions from these data.

The following is a brief overview of WPS; a complete description can be found in Chapter 5 of Skamarock *et al.* (2008). WPS first defines a physical grid (including the projection type, location on the globe, number of grid points, nest locations and grid distances). The static fields are then interpolated to this grid. The external analysis or forecast (in GriB [1]format) is processed by the WPS GriB decoder, which diagnoses required fields and reformats the data into an internal binary format. The meteorological data is then horizontally interpolated by WPS onto the projected domain. The output data, which is passed to the ARW pre-processor, completely describes the 3D state of the atmosphere on the horizontal grid staggering at the specified times.

The ARW real-data preprocessor vertically interpolates the input data from WPS using functions of dry pressure. This process is described in full in Chapter 5 of Skamarock *et al.* (2008). Some of the meteorological data are partitioned by the ARW real-data preprocessor into hydrostatically-balanced dry reference states and their associated perturbation fields. The real-data preprocessor generates a separate file containing lateral boundary

[1]GRIdded Binary; a mathematically concise data format standardised by the World Meteorological Organization and used to store historical and forecast weather data

data for the coarse grid. Each lateral boundary field is defined along the four edges of the rectangular grid.

2.1.4 Lateral boundary conditions

For idealised simulations, several choices of lateral boundary conditions are available: periodic lateral boundary conditions (in x, y, or doubly-periodic in (x, y)), open lateral boundary conditions (also called gravity-wave radiating boundary conditions) specified to the west, east, north, south boundary or any combination thereof, and symmetric lateral boundary conditions (again, specified to the west, east, north, south boundary or any combination thereof), located on the normal-velocity planes at the lateral edges of the grids. A specified lateral boundary condition is available and is primarily used for real-data simulations. The specified boundary condition is also called a relaxation, or nudging, boundary condition. The specified boundaries in ARW are used for the outer, most coarse, grid and also for the time-dependent boundaries supplied to a nested grid (described later in Section 2.1.5). For a nested grid, all fine domains use lateral boundary conditions specified from the parent domain even if the coarse grid is using symmetric, periodic or open boundary conditions. The coarse grid specified lateral boundary consists of both a specified and a relaxation zone (see Chapter 6 of Skamarock *et al.*, 2008). The specified zone is determined entirely by an external analysis or forecast (supplied by WPS). The relaxation zone is a region inside the specified zone where the model is nudged or relaxed back to the analysis or forecast fields.

2.1.5 Nesting

Horizontal nesting is supported by ARW, enabling a region of interest to be focused on in high resolution by introducing an additional grid (or grids) to the simulation. The nested grids are rectangular and aligned with the 'parent' (coarse) grid with which they are associated. The nested grids allow the parent grid to be refined temporally and spatially by any integer amount. As described in Section 2.1.4, each nested grid receives its lateral boundary conditions from its respective parent grid. The nest lateral boundary condition behaves in a similar way to the specified lateral boundary condition for real-data cases, but there is no relaxation zone. ARW has the option of both 1-way and 2-way nesting.

In a 1-way nest, the only exchange of information is from the coarse grid to the fine grid in the form of the fine grid lateral boundaries being interpolated from the coarse grid. In a 2-way nest, for all coarse grid points that lie within the fine grid, the fine grid solution replaces the coarse grid solution. Thus, for a 2-way nest the exchange of information is in both directions (from the coarse grid to the fine grid, and from the fine grid to the coarse grid). Multiple inner nested grids may lie within a single outer grid (the parent grid). The finer, nested grids are referred to as 'child' grids. The fine grids may be telescoped to any degree (a parent grid may contain one or more child grids, which subsequently may each contain one or more child grids). At the same nesting level, several child grids may share the same parent grid. Overlapping grids (where more than one child grid at the same nest level contains the same coarse grid point) are not permitted. Also, no grid can have more than one parent. For both 1-way and 2-way nested grid simulations, the ratio of each parent horizontal grid distance to the child horizontal grid distance must be an integer. Nested grids at the same level may have different spatial and temporal ratios.

2.1.6 Physics parameterisations

ARW has five different physics categories, each of which has several parameterisation scheme options. The physics categories are: microphysics, cumulus parameterisation, planetary boundary layer (PBL), land-surface model and radiation. The physics section is isolated from the dynamics solver by physics drivers that perform a pre-physics preparation stage and a post-physics modification stage on the physics tendencies. The pre-physics stage takes the variables required by the physics options (temperature, pressure, heights, layer thicknesses, velocities, and other state variables), converts them to MKS units, de-staggers them and passes them to the physics packages. The physics packages calculate tendencies for the velocity components, potential temperature, and moisture fields. After the physics packages have been called, the post-physics stage re-staggers the tendencies if necessary and converts the output to the variables or units that are required by the dynamics solver. The available physics options for each category are described in full in Skamarock *et al.* (2008); only the parameterisation schemes used for the simulations presented in this thesis will be described here.

Although the physics parameterisations are dealt with in a modular way, there are many interactions between them. These occur via the model state variables (potential temperature, moisture, winds), the tendencies of the state variables, and the surface fluxes. Table 8.6 of Skamarock *et al.* (2008) provides a full summary of the interactions between the physics processes.

2.1.6.1 Microphysics

The microphysics section of the physics parameterisations deals with explicitly-resolved water vapour, cloud, and precipitation processes. Skamarock *et al.* (2008) recommend that for grid sizes less than 10 km (i.e. where updraughts may be explicitly resolved), and in convective or icing situations, mixed-phase schemes should be used. Mixed-phase schemes include processes where ice and water particles interact, such as riming that produces graupel or hail. The Morrison and Tatarskii (2009) two-moment scheme includes both ice-phase and mixed-phase processes. It was developed from the two-moment bulk microphysics scheme described by Morrison and Khvorostyanov (2005) and Morrison and Pinto (2006). Six species of water are included in the scheme, in the form of: vapour, cloud water droplets, cloud ice, rain, snow, and graupel/hail (the user can specify the inclusion of either graupel or hail). A total of ten prognostic variables are available: the number concentrations and mixing ratios of cloud ice, rain, snow, and graupel/hail, and the mixing ratios of cloud droplets and water vapour. The prediction of two-moments (both number concentrations and mixing ratios) enables the particle size distributions to be treated more robustly. The size distributions are treated with gamma functions, of which the intercept and slope parameters are derived from the predicted number concentration and mixing ratios. The calculations of the microphysical process rates and evolution of cloud and precipitation depend strongly on the particle size distributions. Several liquid, ice and mixed-phase processes are included in the scheme. The Morrison two-moment scheme is the most recently developed and sophisticated of all the available microphysics schemes in ARW, and as such has been chosen for use in the coarse-grid simulations presented in this thesis. The fine-grid simulations resolve convection explicitly.

2.1.6.2 Cumulus parameterisation

A cumulus parameterisation scheme deals with the subgrid-scale effects of convective clouds and shallow clouds. The scheme operates on individual columns where updraughts and downdraughts are unresolved. Where the scheme is called, it represents the vertical fluxes in that column. Vertical profiles of heating and moisture are provided by the scheme, along with the convective component of surface rainfall. The employment of a cumulus parameterisation scheme is necessary for grid sizes that are too coarse to explicitly resolve convective eddies (for the ARW, this is when grid sizes are greater than about 10 km). This allows latent heat to be released in the convective columns on a realistic time scale. For fine grid sizes, where the model can explicitly resolve convective eddies (less than or equal to 5 km for the ARW, Skamarock *et al.*, 2008), cumulus parameterisations are not necessary and indeed should not be used because the assumptions about the convective eddies being entirely subgrid-scale break down. For grid sizes of between 5 and 10 km, using a cumulus parameterisation has sometimes been found to help trigger convection (Skamarock *et al.*, 2008). It is therefore evident that the coarser grids of a nested run may require the use of cumulus parameterisation, while the finer grids may be able to explicitly resolve convective eddies.

The Betts-Miller-Janjic (BMJ) scheme (Janjic, 1994, 2000) has variable deep convection profiles and relaxation times. These depend on the cloud efficiency. This is a non-dimensional parameter that characterises the convective region (Janjic, 1994) and which depends on the entropy change, precipitation, and mean temperature of the cloud. The shallow convection moisture profile requires that the entropy change is small and non-negative. The scheme has been refined for use with high horizontal grid resolutions.

2.1.6.3 Surface layer

A surface layer scheme allows surface heat and moisture fluxes to be calculated by the land-surface models and surface stress to be calculated in the planetary boundary layer (PBL) scheme. The surface layer schemes calculate friction velocities and exchange coefficients which are passed to the land-surface model PBL schemes. Over water surfaces, it is the surface layer scheme that computes the surface fluxes and diagnostic fields (Skamarock

et al., 2008). The MM5 similarity theory scheme has been used in the simulations presented in this thesis. This scheme calculates surface exchange coefficients for heat, moisture and momentum using stability functions from Dyer and Hicks (1970), Paulson (1970) and Webb (1970), while the surface fluxes of heat and moisture are enhanced by the calculation of convective velocity following Beljaars (1994).

2.1.6.4 Land-surface model

The land-surface models (LSMs) provide heat and moisture fluxes over land and sea-ice points. They combine information from the surface layer scheme, radiative forcings from the radiation scheme, and precipitation forcing from the microphysics and cumulus schemes with internal information about the land-surface properties and the state variables of the land. The heat and moisture fluxes calculated by the LSM provide a lower boundary condition for the calculation of vertical transport in the PBL scheme (or the vertical diffusion scheme where a PBL scheme is not used). No tendencies are provided by the land-surface model, but the state variables of the land are updated (including the ground temperature, soil temperature and moisture profiles, snow cover and canopy properties). The LSM can be thought of as a 1D column model for each land grid-point; there are no horizontal interactions between neighbouring points (Skamarock *et al.*, 2008). The Noah LSM has been used in the simulations presented in this thesis. It is a 4-layer soil temperature and moisture model that includes canopy moisture, snow cover prediction, root zone, evapotranspiration, soil drainage and runoff, taking into account vegetation categories, monthly vegetation fraction and soil texture. Soil ice and fractional snow cover are also predicted, and surface emissivity properties are considered. The scheme provides sensible and latent heat fluxes to the boundary-layer scheme (Skamarock *et al.*, 2008).

2.1.6.5 Planetary boundary layer and turbulence

The planetary boundary layer (PBL) scheme calculates the vertical subgrid-scale fluxes due to eddy transports in the whole column (i.e. not just in the boundary layer). When a PBL scheme is activated, explicit vertical diffusion is de-activated (Skamarock *et al.*, 2008). A PBL scheme makes the assumption that there is a distinct scale separation between resolved turbulent eddies and subgrid-scale turbulent eddies. At grid sizes where

boundary layer eddies may be resolved (a few hundred metres or less, Skamarock *et al.*, 2008), this assumption may not be valid, and it is recommended that a fully 3D local subgrid turbulence scheme is used in place of a PBL scheme. This method has been employed in the simulations presented in this thesis (i.e. a large-eddy-simulation (LES) boundary layer has been used). A full diffusion scheme has been used for vertical mixing, in which the gradients use full metric terms so that the horizontal gradients in sloped coordinates are computed more accurately. A prognostic equation for 3D turbulent kinetic energy (TKE) has been used, and the eddy viscosities are based on the TKE. A full description of the turbulent mixing in ARW is provided in Chapter 4 of Skamarock *et al.* (2008).

2.1.6.6 Atmospheric radiation

Longwave and shortwave radiation are dealt with in the radiation schemes. The definition of longwave radiation includes infrared or thermal radiation that is absorbed and emitted by surfaces and gases. The upward longwave radiative flux from the ground is determined by the surface emissivity. The surface emissivity depends on the land-use type and the ground temperature (Skamarock *et al.*, 2008). The definition of shortwave radiation includes the visible and surrounding wavelengths that comprise the solar spectrum. The only source of shortwave radiation is the Sun. Shortwave radiation processes include absorption, reflection and scattering in the atmosphere and at surfaces. The upward shortwave radiative flux is the reflection due to surface albedo (Skamarock *et al.*, 2008). The cloud and water vapour distributions predicted by the model affects the radiation, as do the concentrations of carbon dioxide, ozone, and any specified trace gases. All of the available radiation schemes in the ARW are one-dimensional, such that each column is independent of the others. The Rapid Radiative Transfer Model (RRTM) has been used for the treatment of longwave radiation in the simulations presented in this thesis. The RRTM uses pre-set tables to represent the longwave processes arising from the presence of water vapour, ozone, carbon dioxide and trace gases (if chosen by the user). Cloud optical depth is also accounted for. The MM5 (Dudhia) scheme has been used to deal with shortwave radiation in this thesis. Solar flux is integrated downwards accounting for clear-air scattering, water vapour absorption, cloud albedo and cloud absorption (Skamarock *et al.*, 2008).

2.2 The Large Eddy Model

Version 2.4 of the Met Office Large Eddy Model (LEM) is a high-resolution cloud resolving numerical model that performs atmospheric simulations by integrating a Boussinesq set of equations and includes parameterisations for subgrid turbulence, three-phase cloud microphysics and radiation (Gray *et al.*, 2001). A large-eddy simulation is a technique used to model turbulence whereby the larger-scale turbulent eddies are resolved explicitly, while the smaller-scale motions are parameterised. The larger-scale motions are responsible for most of the turbulent energy and transport of the flow, and the smaller-scale motions may only be responsible for the dissipation of kinetic energy (Gray *et al.*, 2001).

The LEM can be run in one, two or three dimensions. The two-dimensional version of the model runs in the y-z plane. The horizontal grid spacing is constant. The vertical grid can vary with height, and higher resolution can be specified in required areas where turbulent scales are smaller (Gray *et al.*, 2001).

The LEM can be run dry, with water vapour and liquid water only, or with cloud physics. Unresolved turbulent eddies are parameterised using a subgrid model . A choice of schemes exist to advect velocities and scalars. Thermal infra-red ("longwave") and solar ("shortwave") radiation can be run in the LEM. The model can also be allowed to respond to prescribed external effects through options which exist to represent large-scale advective (or diabatic) forcing. External forcings can also be time-varying.

2.2.1 Basic equation set

The prognostic variables in the LEM are the three components of the three-dimensional velocity vector, (u,v,w), the potential temperature perturbation , θ', and a set of scalar variables referred to as the Q fields (Gray *et al.*, 2001). The Q fields can be mixing ratios or number concentrations of water species (water vapour, cloud, ice, snow and graupel). The Q fields can also be passive tracers. The LEM solves the following basic equation set, shown in tensor notation:

$$\frac{Du_i}{Dt} = -\frac{\partial}{\partial x_i}\left(\frac{p'}{\rho_s}\right) + \delta_{i3}B' + \frac{1}{\rho_s}\frac{\partial \tau_{ij}}{\partial x_j} - 2\epsilon_{ijk}\Omega_j u_k, \tag{2.17}$$

$$\frac{\partial}{\partial x_i}(\rho_s u_i) = 0, \tag{2.18}$$

$$\frac{D\theta}{Dt} = \frac{1}{\rho_s}\frac{\partial h_i^{\theta}}{\partial x_i} + \left(\frac{\partial \theta}{\partial t}\right)_{mphys} + \left(\frac{\partial \theta}{\partial t}\right)_{rad}, \tag{2.19}$$

$$\frac{Dq_n}{Dt} = \frac{1}{\rho_s}\frac{\partial h_i^{q_n}}{\partial x_i} - \left(\frac{\partial q_n}{\partial t}\right)_{mphys}, \tag{2.20}$$

where χ_s denotes a reference state of χ, χ' denotes a perturbation from the reference state, $\mathbf{u}$ is the vector flow velocity, θ is the potential temperature, q_n represents all other scalar variables, p is the pressure, ρ is the density, B' is the buoyancy, τ is the subgrid stress, h^{θ} is the subgrid scalar flux of θ, h^{q_n} is the subgrid scalar flux of q_n, δ_{i3} is the Kroneker delta function, Ω is the Earth's angular velocity (f-plane approximation), ϵ_{ijk} is the alternating pseudo-tensor, $\left(\frac{\partial \theta}{\partial t}\right)_{mphys}$ is the source term of θ due to microphysics, $\left(\frac{\partial \theta}{\partial t}\right)_{rad}$ is the source term of θ due to radiation, and $\left(\frac{\partial q_n}{\partial t}\right)_{mphys}$ is the source term of q_n due to microphysics. Here, $\mathbf{u}$, θ and q_n describe the quantities of the resolved flow. The subgrid contribution to the flow is dealt with by the subgrid parameterisation. As convention, the material derivative is given by

$$\frac{D}{Dt} \equiv \frac{\partial}{\partial t} + u_i\frac{\partial}{\partial x_i}. \tag{2.21}$$

Equations (2.17) to (2.20) are a Boussinesq-type equation set (Gray *et al.*, 2001). The equation set is linearised about small perturbations from a basic reference state, which must be specified for θ. The mean reference state is defined by ρ_s, θ_s and p_s. Perturbations from the mean state are denoted by a prime superscript and are assumed to be small. For an incompressible Boussinesq system the mean reference state is constant in height, restricting the use of the LEM to boundary layer studies where the vertical derivative of ρ, θ and p can be assumed to be small. To allow the mean reference state to be a function of height only, a quasi-Boussinesq, or anelastic, approximation is used to derive equations (2.17) to (2.20) (Derbyshire *et al.*, 1994; Gray *et al.*, 2001).

In the LEM, θ' is used as the thermodynamic variable (Gray *et al.*, 2001) and so Equation (2.19) is rewritten as

$$\frac{D\theta'}{Dt} + w\frac{d\theta_s}{dz} = \frac{1}{\rho_s}\frac{\partial h_i^{\theta'}}{\partial x_i} + \frac{1}{\rho_s}\frac{\partial h_3^{\theta_s}}{\partial z} + \left(\frac{\partial \theta'}{\partial t}\right)_{mphys} + \left(\frac{\partial \theta'}{\partial t}\right)_{rad}. \tag{2.22}$$

To determine the mean reference state, the universal gas law, Equation (2.23), and the hydrostatic approximation, Equation (2.24), are used to relate the three main state variables ρ_s, θ_s and p_s:

$$p_s = \rho_s R\theta_s \left(\frac{p_s}{p_0}\right)^{R/c_p}, \tag{2.23}$$

$$\frac{dp_s}{dz} = -g\rho_s, \tag{2.24}$$

where R is the gas constant, p_0 is a constant reference pressure, c_p is the specific heat of air at constant pressure, and g is the acceleration due to gravity.

In the LEM the θ_s profile is specified by the user, and the p_s and ρ_s profiles are calculated using Equations (2.23) and (2.24) to form the following first order differential equation:

$$\frac{d}{dz}\left(\frac{p_s}{p_0}\right)^{R/c_p} = -\frac{g}{c_p\theta_S}. \tag{2.25}$$

One set of boundary conditions is required to solve Equation (2.25). In the LEM this is the specification of surface pressure (Gray *et al.*, 2001). The surface density is then calculated from the surface pressure using Equation (2.23).

The buoyancy term, B', is defined in the LEM as

$$B' = g\theta_v'/\theta_s, \tag{2.26}$$

where θ_v is the virtual potential temperature. θ_v.

To compute the momentum equation, Equation (2.17), the pressure perturbation, p' is required. This is calculated through the continuity equation, Equation (2.18). To maximise the timestep permitted by the CFL restriction, Equation (2.15), a Galilean transformation is applied. Newtonian dynamics is invariant under the Galilean transformation, so the model equations are solved in the usual way. The exceptions are the Coriolis terms, which are non-Newtonian, and the surface boundary conditions, which require the velocity relative to the Earth (Gray *et al.*, 2001).

The subgrid model contains parameterisations for the smaller-scale turbulent eddies that cannot be explicitly resolved. The equations which specify the subgrid model in the LEM are described in full in Gray *et al.* (2001), Derbyshire *et al.* (1994) and Brown *et al.* (1994).

2.2.2 Boundary conditions

The LEM uses horizontal periodic boundary conditions for all primed prognostic variables. As such, effects can propagate across the horizontal boundaries. The top and bottom boundary conditions are rigid lids, such that w=0 at the boundary. The other model fields are treated differently at the top and the bottom of the model, as the bottom of the model has to represent the stresses and fluxes due to flow across a surface, while the top of the model has to represent the rest of an unmodelled atmosphere (Gray *et al.*, 2001). The top and bottom boundaries do not permit resolved transport across the interfaces. The surface boundary conditions are derived from Monin-Obukhov similarity theory. For scalar transport from the surface, either sensible and latent heat fluxes, or surface temperature and humidity can be prescribed, both of which can vary in time. The rigid lid at the top of the model can lead to the reflection of gravity waves. In reality this can occur if the upper part of the domain is stably stratified, but in general it is undesirable and may make the simulation sensitive to the depth of the domain (Gray *et al.*, 2001). To prevent vertically-propagating gravity waves from reflecting off the top boundary, a Newtonian damping layer is used on the top model levels. This removes gravity wave perturbations by relaxing the prognostic variables back to their horizontal means above a given height.

2.2.3 Moist processes

The LEM represents moist processes by the use of prognostic variables for water vapour mixing ratio, q_v and liquid water mixing ratio, q_L. The thermodynamic variable is θ. Neglecting terms due to diffusion or precipitation, the equations for θ, q_v and q_L are written as

$$\frac{D\theta}{Dt} = \frac{L_v}{c_p}\frac{C}{\Pi}, \tag{2.27}$$

$$\frac{Dq_v}{Dt} = -C, \tag{2.28}$$

$$\frac{Dq_L}{Dt} = C, \tag{2.29}$$

where C is the rate of change of liquid water due to condensation, L_v is the latent heat of vapourisation, and Π is the Exner function, $(p_s/p_0)^{R/c_p}$. There is no explicit term for C in the LEM, and as such it is calculated diagnostically. Details of this calculation can be found in Section 5.1 of Gray *et al.* (2001).

The LEM contains a bulk-water warm microphysics scheme through the addition of another scalar variable, the rain mixing ratio, q_r. The rain source term, S_r consists of three processes: the autoconversion of cloud droplets to rain, the collection of cloud droplets by rain, and the evaporation of rain into dry air. Autoconversion describes a process that converts particles of solely one species to produce another species. The falling of q_r is represented by advecting q_r vertically downwards with a rain fall speed of w_r (Gray *et al.*, 2001). The LEM has three warm rain parameterisations, developed by Kessler (1974), Lee (1989) and Swann (1996). Tables comparing the autoconversion, collection and evaporation algorithms for these three schemes are given in Section 5.2 of Gray *et al.* (2001).

2.2.4 Three-phase microphysics

The LEM uses a three-phase bulk-water microphysics parameterisation. Water particles are divided into discrete categories: rain (liquid water drops), snow (low-density ice aggregates), graupel (heavily-rimed ice particles), cloud ice (small ice crystals), and liquid water cloud (Gray *et al.*, 2001). A full description of the microphysics scheme used in the LEM is given in Section 6 of Gray *et al.* (2001). Up to six model variables can be used to represent the mass mixing ratios of rain, snow, graupel, cloud ice, cloud water and water vapour. A maximum of three further variables can be used to represent the number concentrations of cloud ice, snow and graupel. One more variable can be used to represent the total graupel particle volume.

If water species are modelled using the mass mixing ratio only, the scheme is referred to as "single-moment" and coefficients are required to determine the particle size as a monotonic function of the mixing ratio. A "double-moment" scheme represents the mass mixing ratio and number concentration of each hydrometeor prognostically. A "triple-moment" scheme can be used for graupel or hail by modelling the total particle volume as a prognostic variable, allowing the density to vary in space and time (Gray *et al.*, 2001).

The microphysics parameterisation determines the conversion rates between the different species of water and the fallspeeds of the bulk hydrometeors. Cloud water droplets in the LEM are assumed to have a constant number density, while all other water species have number densities that are dependent on the diameter of the particle. The mass mixing ratios are calculated as a function of the number density and mass, and the number concentrations are calculated as a function of the number density. In general, each microphysical variable has two source terms: an advective term that corresponds to the fall of each hydrometeor, and a conversion term that corresponds to the change between hydrometeor types due to physical processes. The LEM contains parameterisations for thirty-six conversion processes. The terminal fall velocity of each type of precipitating particle is calculated as a function of the particle diameter. The thirty-six conversion processes are described in full in Section 6 of Gray *et al.* (2001).

2.2.5 Radiation

The radiation scheme used in the LEM is the same as that used in the Met Office Unified Model (Cullen, 1993) and is described in Edwards and Slingo (1996). The radiation code reads in a "spectral" file containing details of the gaseous absorption, impact of aerosols, Rayleigh scattering and treatment of clouds. The LEM is distributed with two basic spectral files, one for the solar spectrum and one for the thermal infra-red spectrum. The radiation scheme is a two-stream radiation scheme that allows absorption lines in the solar and thermal infra-red spectra to be divided up. In the LEM the infra-red spectrum is divided up into eight spectral intervals and the solar spectrum is divided into six spectral intervals. Gaseous absorption and scattering are included in both the solar and infra-red spectra. The radiation code also includes the effect of Rayleigh scattering in the solar spectrum and the effect of the water vapour continuum in the thermal infra-red spectrum. In the two-stream scheme the optical properties of a cloud are expressed in terms of three single scattering parameters: the volume extinction coefficient, the single scatter albedo and the asymmetry factor. The single scattering properties of a cloud are parameterised using the method of Slingo and Schrecker (1982), which describes the single scattering properties in terms of the effective radius of the cloud liquid and cloud ice.

2.2.6 Model grid and numerical methods

The LEM uses an Arakawa C-grid in the horizontal and a Lorenz grid in the vertical, as shown in Figure 2.3. Each velocity component is staggered in its own direction. Scalar quantities (p, θ and q_n) are kept on the centre point. The viscosities, ν, and the diffusivities, ν_h, are located on the w-points. The LEM can be run using forward or centred time-stepping. The timestep must be constrained according to the CFL criterion, Equation (2.15), to maintain numerical stability. Two advection schemes can be used in the LEM, a centred difference scheme or a total variance diminishing scheme. Time-smoothing is applied in the LEM to prevent the risk of two time levels decoupling, as can occur when using a centred difference scheme with first order differential equations. Gray *et al.* (2001) recommended the use of the Asselin/Robert time filter in the LEM.

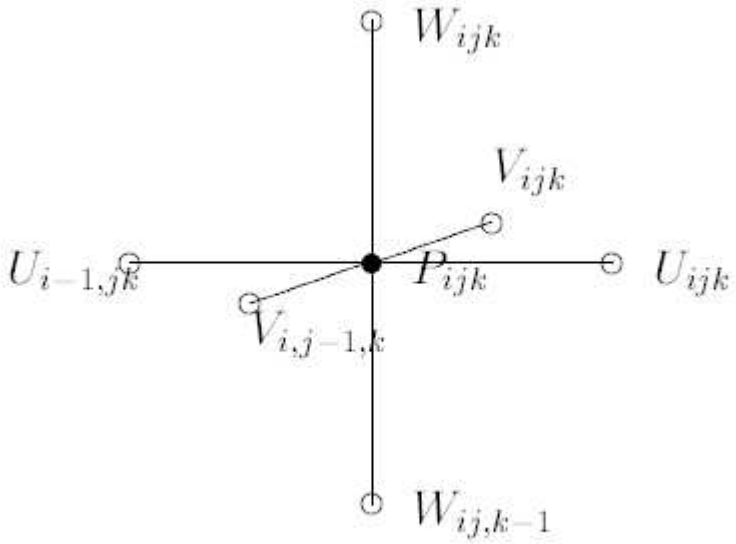

FIGURE 2.3: Staggered grid (Arakawa-C and Lorenz) used in the LEM. From Gray *et al.* (2001).

Chapter 3

Modelling study of an elevated MCS observed during CSIP

3.1 Elevated mesoscale convective systems observed during CSIP IOP 3

The only case of elevated convection encountered during CSIP occurred on 24 June 2005 during IOP 3. Convection was highly organised on this day. Several MCSs remained elevated throughout the observation period. These were studied in detail by Browning *et al.* (2010), Marsham *et al.* (2010) and Browning *et al.* (2012). The detailed analysis performed by these authors is summarised in this Section. The text has been rewritten and has not been taken directly from these papers.

The synoptic situation at 1200 UTC on 24 June 2005 is shown in Figure 3.1. A shallow low pressure system was centred to the south of the CSIP region, over northern France. Isentropic analysis (performed as part of the work contributing to this thesis) of the 32°C potential temperature surface showed that the CSIP region was in a baroclinic zone, with the isentropic surfaces sloping upwards towards the north and west. Back trajectories performed by Browning *et al.* (2010) showed that the air with potential temperature of 32°C originated from northwest Spain four days previously, and had ascended at 1.5 cm s^{-1} during the previous 24 hours.

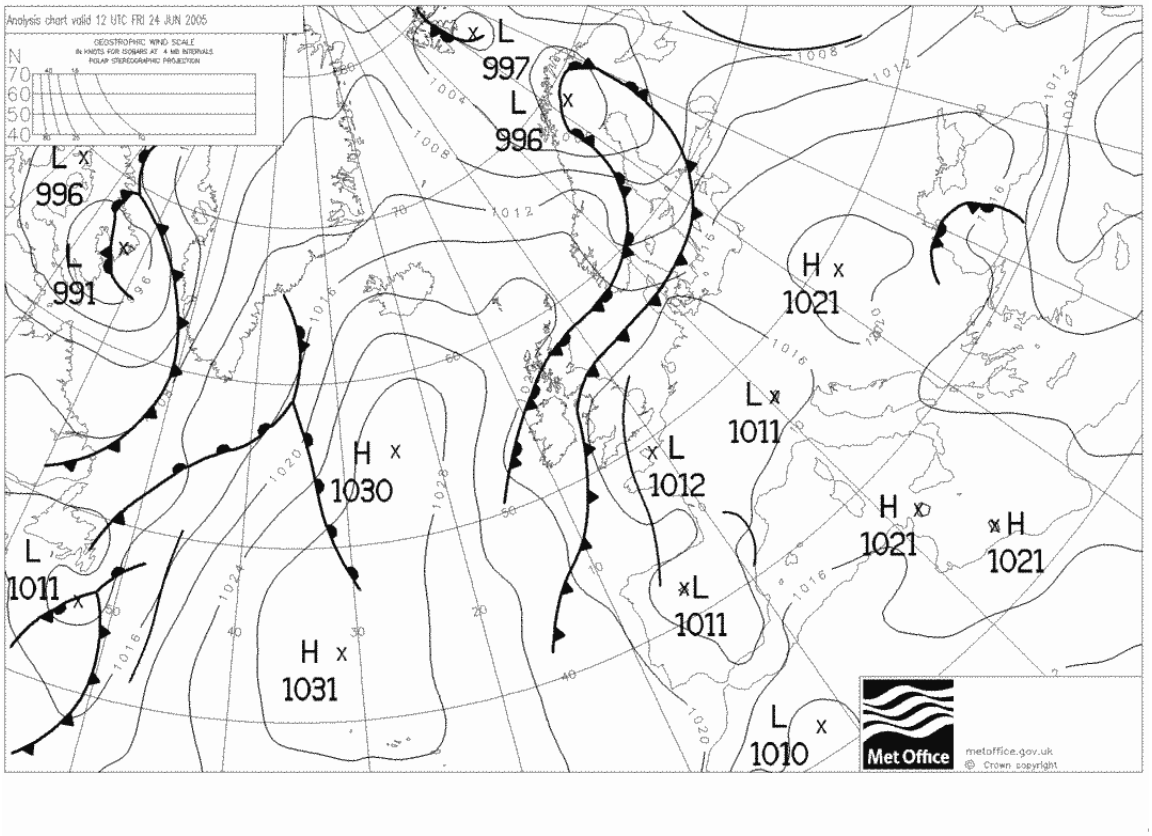

FIGURE 3.1: Met Office surface analysis for 1200 UTC, 24 June 2005. Crown Copyright 2005.

The CSIP region was ahead of a surface cold front that was situated just off the coast of Wales and southwest England (Figure 3.1). The south of England was affected by a cool north to northeasterly flow. Several MCSs formed in the pre-frontal region. They produced heavy, widespread rain. Some of the MCSs are shown in the hourly satellite and network radar images in Figure 3.2. The MCSs labelled B and C are the focus of the work presented in this thesis. Detailed observations of MCS C were analysed by Browning *et al.* (2010) and Marsham *et al.* (2010), and of MCS B by Browning *et al.* (2012).

3.1.1 MCS C

3.1.1.1 The evolution of MCS C

MCS C formed over the sea by 1045 UTC. Figure 3.2a shows MCS C as a new cell of cumulonimbus cloud at this time. The anvil expanded by 1145 UTC (Figure 3.2c). A

convective cell formed just outside the region of subsidence behind the storm (Figure 3.2c), probably due to secondary initiation (Browning *et al.*, 2010). The new convective cell developed and merged with the rest of the MCS. This caused the core of MCS C to propagate to the right of the mid-level wind direction (Browning *et al.*, 2010). The anvil of MCS C had expanded further by 1245 UTC (Figure 3.2e) and the expansion continued through 1345 UTC (Figure 3.2g) and 1445 UTC (Figure 3.2i). Another line of deep convection formed to the south of MCS C by 1445 UTC. This new line developed into a separate MCS, labelled D in Figure 3.2i. MCS D was oriented perpendicular to MCS C.

The equivalent hourly network radar images from 1045 to 1445 UTC are shown in Figures 3.2b, d, f, h, and j. Also shown in these Figures are white outlines showing the parallax-corrected visible anvil of MCS C (Browning *et al.*, 2010). The areal extent of the precipitation increased throughout the lifetime of MCS C, but until 1345 UTC its maximum intensity remained greater than the peak radar threshold of 32 mm hr^{-1}. The maximum precipitation intensity weakened after 1345 UTC (Browning *et al.*, 2010).

The outlines of the anvil canopy of MCS C in the radar images in Figure 3.2 show that MCS C travelled from the southwest to the northeast, along the white line, and moved directly over the Chilbolton radar. However, the anvil was generated and sustained by a line of convection that was oriented north to south. New cells formed at the southern end and decayed towards the northern end (Browning *et al.*, 2010).

3.1.1.2 The structure of the environment near MCS C

A tephigram of data from a radiosonde launched at Swanage at 1100 UTC is shown in Figure 3.3. This ascent was in the inflow to MCS C. The lowest kilometre of the atmosphere was too cool to feed any deep convective updraughts (Browning *et al.*, 2010). This layer was capped by an approximately isothermal layer between 900 to 830 hPa (1.0 to 1.6 km). Above the isothermal layer was a warm, nearly dry-adiabatic layer extending up to about 800 hPa (2.0 km) with a potential temperature of 31°C. Above this layer was a moist layer centred at 770 hPa (2.3 km). This air had modest CAPE of about 405 J kg^{-1} provided it could overcome a layer of CIN of 70 J kg^{-1} centred at 740 hPa. This layer fed the elevated convection (Browning *et al.*, 2010). A second moist layer at 870 hPa (1.3 km) had CAPE of

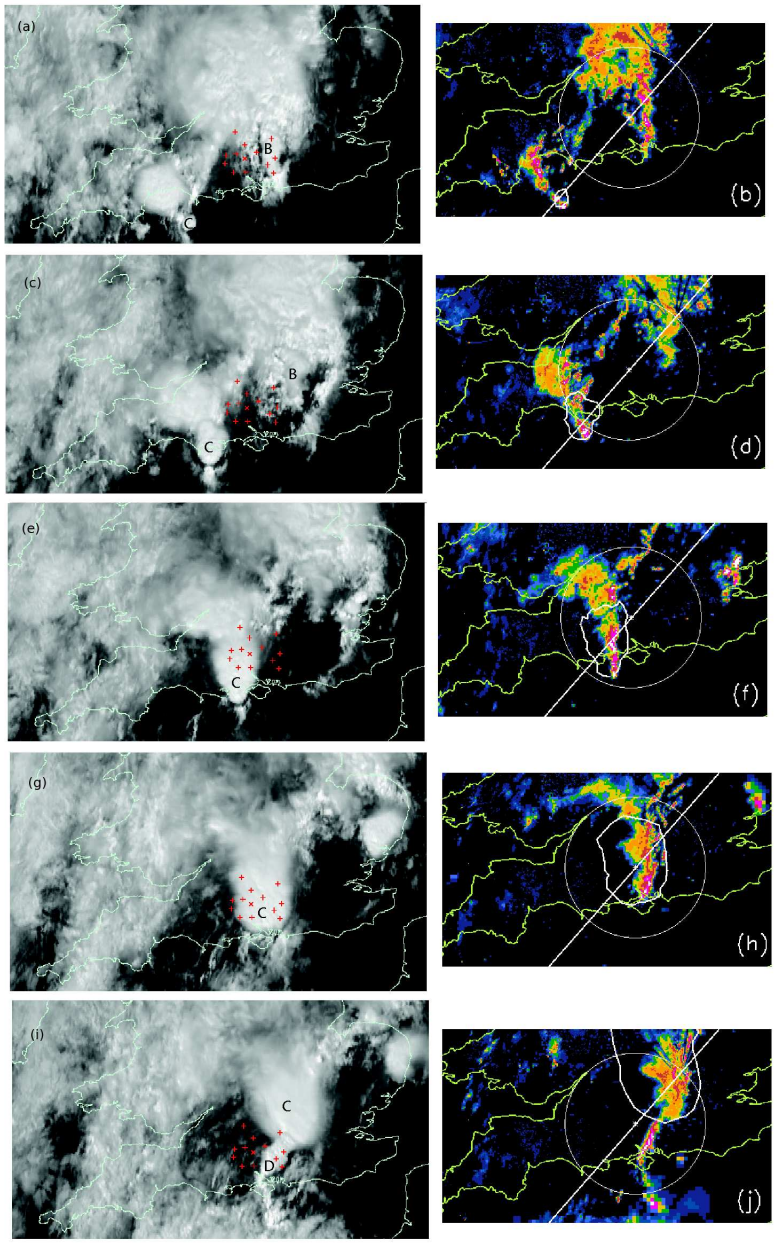

FIGURE 3.2: (a,c,e,g,i) MSG high-resolution visible images and (b,d,f,h,i) rainfall-radar plots from the weather radar network over parts of southern England and Wales at (a,b) 1045, (c,d) 1145, (e,f) 1245, (g,h) 1345 and (i,j) 1445 UTC, 24 June 2005. MCSs B, C and D are labelled on the satellite images, which are not adjusted for parallax. Also shown on the satellite images are the locations of the automatic weather stations set up for CSIP (red +). The radar-network images are composites with resolutions of 1, 2 and 5 km, depending on radar range; colours represent retrieved rainfall intensities as shown by the key. The parallax-corrected outline of the visible anvil from MCS C has been superimposed on the radar plots. The circles show the 95 km range of the Chilbolton Doppler radar (not one of the network radars). The line, through Chilbolton and oriented southwest to northeast, shows the track of MCS C as it first approached and then receded from Chilbolton. From Browning *et al.* (2010). Copyright 2005 EUMETSAT and Crown Copyright 2005.

399 J kg^{-1} and required greater lifting than the other moist layer to overcome 263 J kg^{-1} of CIN before it could undergo deep convection (Browning *et al.*, 2010).

A hodograph of data from the Swanage radiosonde is shown in Figure 3.4. The low-level cool air was associated with northeasterly low-level flow on the northern side of the low pressure system (Figure 3.1). The wind speed in this flow was typically 12 m s^{-1}. Browning *et al.* (2010) referred to this low-level flow as an undercurrent. A similar undercurrent was present in the sounding used by Parker (2008) in his idealised modelling study of elevated convection. The southwesterly winds increased with height and reached speeds of 20 m s^{-1} in the upper troposphere (Figure 3.4). The MCSs observed in the CSIP area travelled from the southwest to the northeast at speeds of about 15 m s^{-1} (Browning *et al.*, 2010). The cool, stable undercurrent flowing beneath the storm had a strong system-relative velocity against the direction of motion of the MCS.

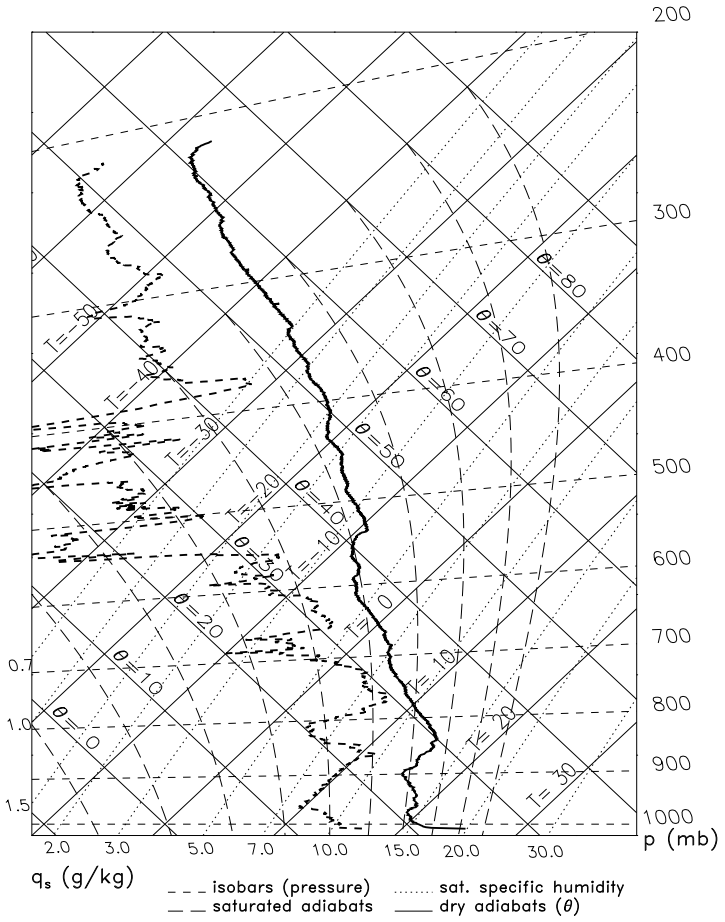

FIGURE 3.3: Tephigram constructed from data from a radiosonde launched from Swanage at 1100 UTC on 24 June 2005.

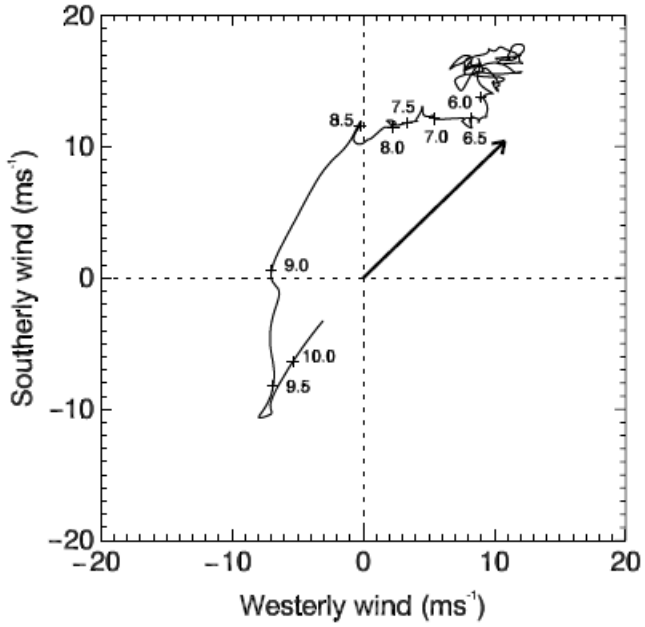

FIGURE 3.4: Wind hodograph constructed from data from a radiosonde launched from Swanage at 1100 UTC on 24 June 2005. Pressure is labelled in hundreds of hPa. The arrow depicts the 15 m s^{-1} velocity of MCS C to the northeast.

3.1.1.3 Surface weather associated with MCS C

Twelve automatic weather stations (AWSs) (Perry, 2008) were operational within a 50 km radius of Chilbolton. All showed very similar data. Traces of pressure, temperature, relative humidity and wind speed and direction from one of the AWS sites are shown in Figure 3.5. MCSs A, B and C are labelled. Each MCS produced a positive pressure anomaly of about 2 hPa. This was accompanied by oscillations of 2 to 5°C in temperature and 20 to 30% in relative humidity (Browning *et al.*, 2010). There were no observations of strong gusts, as would be expected if the MCSs had produced gravity currents.

Marsham *et al.* (2010) analysed data from the Chilbolton AWS and found that the pressure anomaly that accompanied the passage of MCS C could be largely attributed to the hydrostatic effect of variations in the undercurrent depth rather than diabatic cooling. A wind-direction anomaly (WDA) that accompanied MCS C and which approximately corresponded to the lifetime of the surface pressure anomaly was shown by Marsham *et al.* (2010) to be closely associated with, and largely attributable to, a wave in the undercurrent.

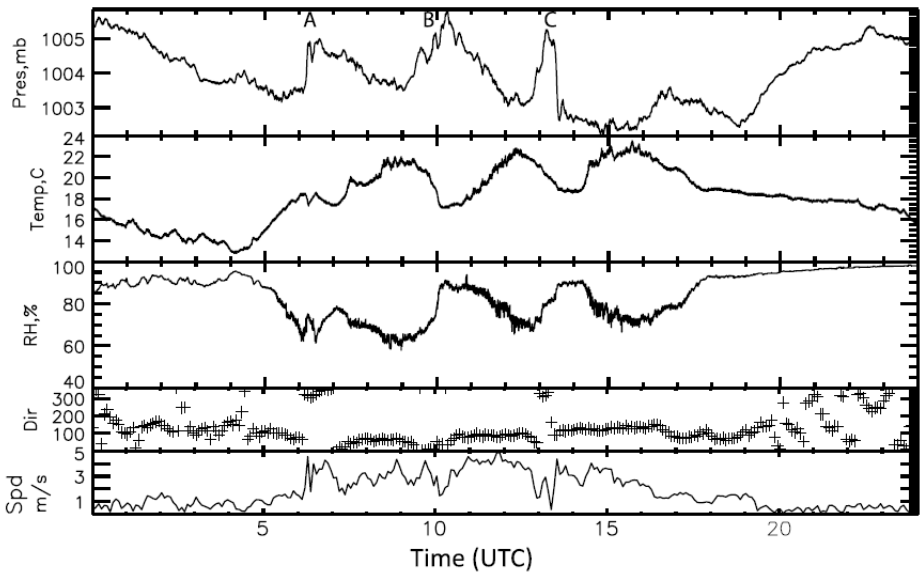

FIGURE 3.5: Traces of pressure, temperature, relative humidity and wind direction and speed for the automatic weather station at Chilbolton on 24 June 2005. Mesoscale pressure maxima associated with MCSs A, B and C occurred at 0630, 1020 and 1315 UTC respectively. From Browning *et al.* (2010).

3.1.1.4 The vertical structure of MCS C

The location and coverage of the Chilbolton Doppler radar was shown in Figure 1.19 in Section 1.10. The radar made low-elevation plan–position indicator (PPI) scans and range–height indicator (RHI) scans at azimuth intervals of about 20°, repeated about every 38 minutes. MCS C travelled nearly directly over the Chilbolton radar (Figure 3.2), which meant that the Doppler scans through the centre of the storm as it approached and moved away from the radar provided information about the component of wind that was parallel to the direction of motion of the storm. As such, the analysis was essentially two-dimensional (Browning *et al.*, 2010).

Vertical structure at 1155 UTC

The RHI scan from the Chilbolton radar along 221° at 1155 UTC is shown in Figure 3.6. This scan was towards the centre of MCS C. A region of intense precipitation was centred near 80 km (Figure 3.6a). The tallest convective plumes were at a range of 80 km (Figure 3.6b). Where they reached heights of more than 10 km they produced divergent anvil outflow. The air in the two source layers (1.2 to 1.6 km and 2.1 to 2.9 km) underwent slantwise front-to-rear ascent and left the storm as a rearward flow at a height of about

(7±1) km (Figure 3.6c). Two layers underwent slantwise rear-to-front descent (red shading in Figure 3.6c). The lower layer (3 to 6 km) corresponded to a rear-inflow jet. The RIJ descended to a height of about 2 km at a radar range of 85 km and did not reach the surface. The upper descending layer was between 8 and 10 km. The speed of the rear-to-front flow increased inside the storm. The maximum storm-relative speed of the rear-to-front flow was about 10 m s^{-1}.

The undercurrent travelled in the opposite direction to the advancing MCS. At the leading edge of the storm, at a radar range of about 75 km, the depth of the cool undercurrent was at least 50% greater than it was ahead of the storm at e.g. 30 km. This increase in depth was a wave in the undercurrent (Browning *et al.*, 2010). Kelvin-Helmholtz billows developed in the undercurrent at ranges beyond 78 km. The billows had a crest-to-trough amplitude of about 400 m and a wavelength of about 2 km. Browning *et al.* (2010) suggested that the billows were triggered by a local increase in shear due to the impact of the RIJ on the top of the stable layer. The descending RIJ increased the depth and decreased the velocity of the undercurrent ahead of it, and decreased the depth and increased the velocity of the undercurrent directly beneath it (Browning *et al.*, 2010). The Kelvin-Helmholtz billows observed in MCS C are not those that are studied in Chapter 5; those billows were associated with MCS B.

The slope of the slantwise circulations decreased by 1423 UTC and the convection weakened significantly. These radar scans are not shown, but are available in Browning *et al.* (2010). However, the system velocity of MCS C increased from 15 m s^{-1} at 1155 UTC to 18 m s^{-1} at 1423 UTC (Browning *et al.*, 2010).

A schematic diagram of the vertical structure of MCS C at 1155 UTC is shown in Figure 3.7. The storm-relative position of the 1100 UTC Swanage radiosonde is indicated in by the label S11. Seven flows are identified in Figure 3.7. These were described by Browning *et al.* (2010) as follows:

Flow 1: The undercurrent. Within the storm, the undercurrent deepened as part of a wave. The undercurrent was capped by a stable lid with elevated near-neutral layers above and below it. This situation is favourable for wave-trapping (Lindzen and Tung, 1976).

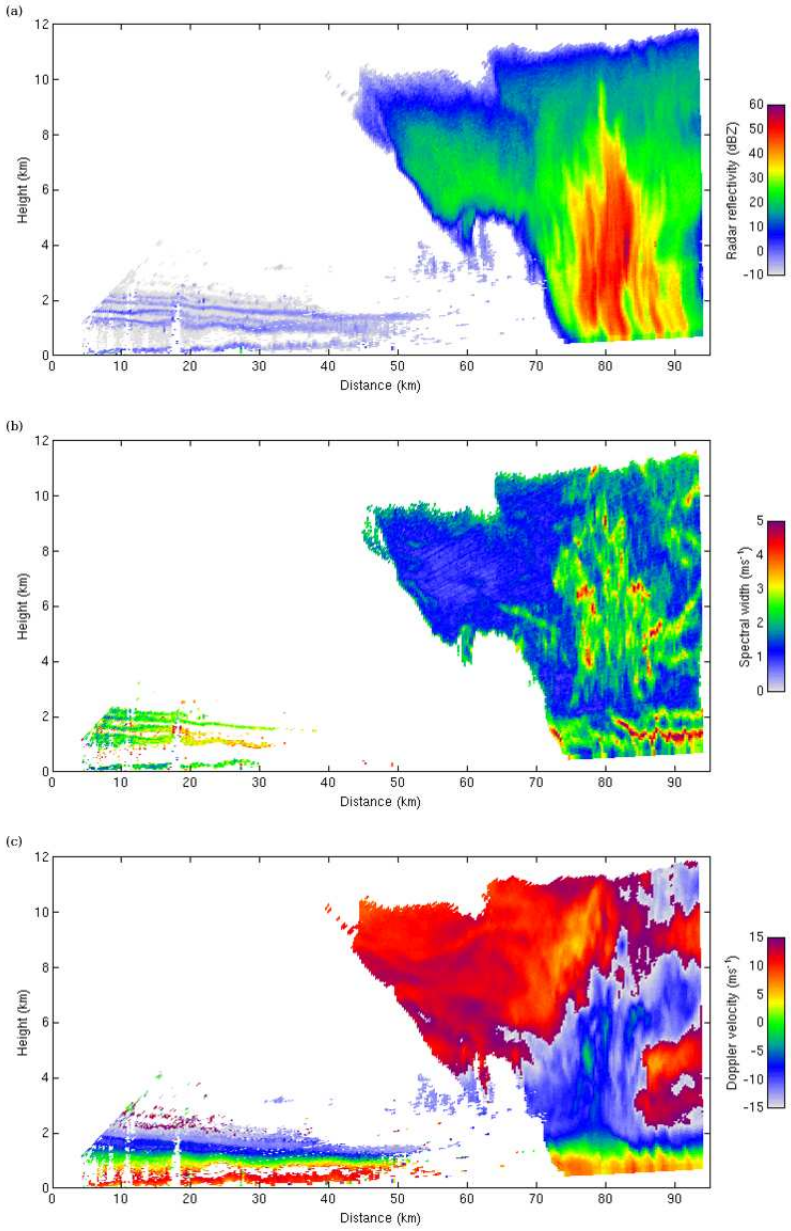

FIGURE 3.6: RHI scan from the Chilbolton radar along 221° at 1155 UTC on 24 June 2005: (a) reflectivity (dBZ), (b) spectral width (m s^{-1}), and (c) Doppler velocity (m s^{-1}) with the colour key labelled in terms of storm-relative velocities; red and orange colours are duplicated, corresponding to negative velocities below 2 km and positive velocities above 2 km. Positive velocities are in the direction the storm is travelling, from right to left. The undercurrent gravity wave was situated between radar ranges 60 and 90 km. From Browning *et al.* (2010).

Flow 2: A very stably-stratified flow with a positive storm-relative velocity and high wet-bulb potential temperature. This was the layer centred at 1.4 km in Figure 3.3. Forced ascent of more than 1.4 km would have been required for Flow 2 to overcome the 263 J kg^{-1} of CIN imposed by Flows 3 and 4.

Flow 3: A shallow layer of warm, dry air with relatively low wet-bulb potential temperature which capped Flow 2.

Flow 4: A second layer of air with high wet-bulb potential temperature. This was the upper layer of high wet-bulb potential temperature in Figure 3.3. Flow 4 required 0.4 km of lifting to overcome to overcome 70 J kg^{-1} of CIN and probably provided the main contribution to the upright convection.

Flow 5: Air fed by Flows 2 and 4 which ascended as upright convection (5a), as rearward-sloping ascent at mid-levels (5b) and as divergent outflow behind (5c) and ahead (5d) of the storm.

Flow 6: A weakly-descending slantwise flow beneath the rear of the divergent anvil outflow.

Flow 7: A RIJ with a storm-relative velocity of up to 10 m s^{-1} near its leading edge.

3.1.1.5 The wave in the undercurrent

The wave in the undercurrent observed during the passage of MCS C was analysed in detail by Marsham *et al.* (2010). Streamline analysis of the Doppler radar data showed that the undercurrent deepened as the air approached the front of the storm, then accelerated and became much shallower beneath the leading edge of the descending RIJ. The action of the RIJ on the top of the undercurrent constricted the undercurrent flow and caused it to accelerate. The increase in shear associated with this process led to the appearance of large-amplitude Kelvin-Helmholtz billows due to shear instability.

The wave that formed in the undercurrent was found by Marsham *et al.* (2010) to be a 'gravity wave without stagnation' (Crook and Moncrieff, 1988), since the air in the undercurrent was nowhere at rest relative to the system. The wave was forced by and

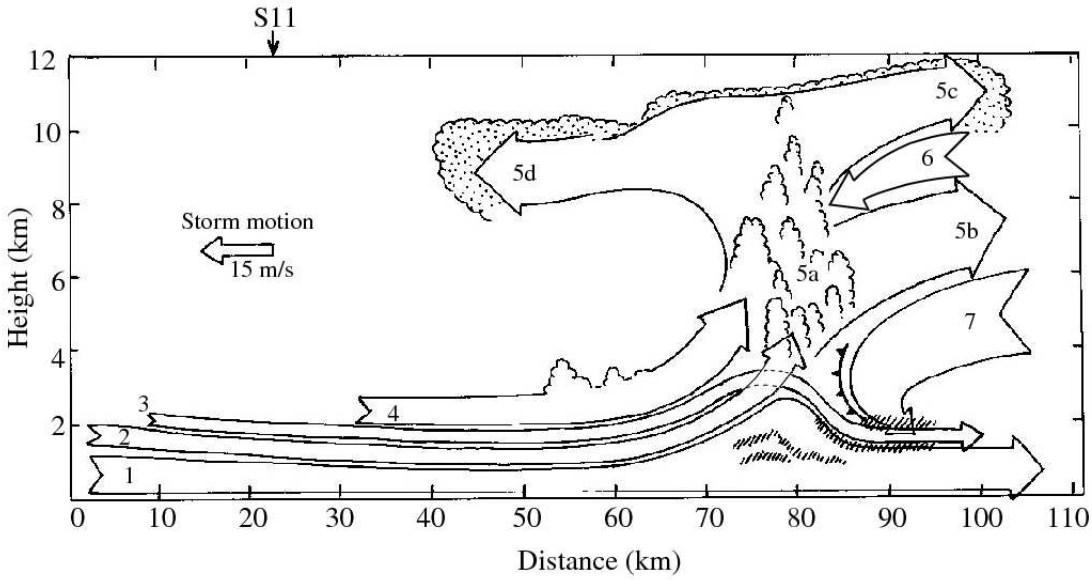

FIGURE 3.7: Synthesis of inferences drawn from Figures 3.6a, b and c and from radiosondes launched from Swanage. The label S11 indicates the storm-relative position of the 1100 UTC sonde. The crenellated lines with dotted shading denote the extent of the anvil cloud, determined from satellite data. Open arrows represent flow relative to the MCS travelling at 15 m s^{-1} from right to left. The arrow labelled 7, approaching from the right, is the RIJ. The leading edge of the RIJ is denoted by cold-frontal symbols. The arrow representing Flow 3 is drawn dotted where it may perhaps have been penetrated by convective parcels fed by Flow 2. From Browning *et al.* (2010).

propagated with the MCS. The wave could be viewed as a response to the propagation of the storm over a shallow inflow layer. The theoretical wave speeds calculated by Marsham *et al.* (2010) were similar to the observed speed of the MCS and RIJ, which both moved with the upper-level winds.

The variations in the depth of the undercurrent were shown by Marsham *et al.* (2010) to be a response to the pressure fluctuations induced by the circulations above. The observed surface pressure maximum was consistent with the hydrostatic effect of the increased depth of the undercurrent. Marsham *et al.* (2010) also considered the non-hydrostatic effects of vertical motions in the RIJ and found that the non-hydrostatic effect of the RIJ impacting on the undercurrent led to a significant constriction of the undercurrent, as observed. The wave would have been affected by both the diabatic convective updraughts and the diabatic cooling that strengthened the RIJ (Marsham *et al.*, 2010).

3.1.2 Summary of the structure and evolution of MCS C and its near-environment

A summary of the main findings of Browning *et al.* (2010) and Marsham *et al.* (2010) is listed below:

1. MCS C formed off the south coast of England. The MCS was associated with elevated convection that was fed by air with high wet-bulb potential temperature travelling from the south to southwest and above a cool northerly undercurrent. IOP 3 was the only case of elevated convection observed during CSIP.

2. The convective updraughts were fed by two layers of air above the cool undercurrent. Both layers required lifting to overcome CIN.

3. There were two outflows. The upper of the two outflows underwent divergent outflow. The lower outflow underwent slantwise front-to-rear ascent.

4. Slantwise downdraughts developed beneath both of the rear updraught outflows. The lower of these was a RIJ.

5. The slope of the slantwise circulations decreased as the convection weakened.

6. The velocity of the MCS increased later in its lifetime, even though the convection had weakened.

7. The RIJ strengthened in the storm. This indicated the importance of physical processes such as the evaporation of precipitation, particularly ice, to the RIJ (Forbes and Clark, 2003).

8. The RIJ descended to the top of the undercurrent. It did not reach the surface.

9. The top of the undercurrent was depressed directly beneath the impacting RIJ and generated a wave.

10. The lifting generated by the wave was sufficient to raise both of the source layers identified by Browning *et al.* (2010) to their levels of free convection.

11. The deepening of the undercurrent under the moist convection could be understood as a response of the undercurrent to the moist convection occurring above it.

12. The observed constriction of the undercurrent was due to non-hydrostatic effects in the RIJ. Marsham *et al.* (2010) speculated that the undercurrent wave may therefore be sensitive to evaporation, sublimation and melting occurring within the RIJ.

13. The wave propagated with the MCS rather than independently of it. The estimated phase speed of the wave was consistent with the observed propagation speed of the system, leading Marsham *et al.* (2010) to speculate that a resonance may occur between the MCS that generated the wave and travelled with the upper-level winds, and the wave that was generated.

14. The absence of strong surface winds was consistent with the failure of the RIJ to reach the surface and produce a strong cold pool.

15. There was no evidence of gravity current outflow associated with the passage of MCS C.

16. Large-amplitude Kelvin-Helmholtz billows formed in a region of strong shear where the RIJ impacted on the top of the undercurrent.

3.1.3 Questions arising from the analysis of MCS C

Browning *et al.* (2010) raised several questions from their analysis of MCS C. Some of these are listed below and are addressed in the rest of this Chapter and in Chapter 4:

- Why did two pairs of slantwise ascent and descent form? One possibility may have been the differing buoyancies of the two source layers, causing them to be detrained from the convective updraughts at different levels.

- The failure of the RIJ to penetrate to the surface was likely to have prevented the formation of a strong gravity current and therefore prevented the enhancement of the MCS by the triggering of new cells along the gust front. How important was this process to the maintenance or otherwise of an intense MCS?

3.2 High-resolution numerical modelling of CSIP IOP 3

To address the questions about the structure and evolution of MCS C that arose from the analyses of Browning *et al.* (2010) and Marsham *et al.* (2010) the WRF model was used to perform a simulation of the CSIP IOP 3 case study.

3.2.1 Model set-up

The WRF model was described in Section 2.1. For the simulations presented in this thesis, version 3.1.1 of WRF was set up with three model nests. The outer domain covered the British Isles and Northern France and contained 173 x 172 horizontal grid points with a horizontal grid spacing of 9 km. Data were output every hour of model time for the outer domain. The inner domain covered southern England and Wales (encompassing the CSIP area) and contained 535 x 409 grid points with a horizontal spacing of 1 km. The use of such a large domain at high horizontal grid resolution meant that the vertical resolution was restricted by the available computational power. 48 vertical levels were chosen on the standard WRF stretched grid. The vertical grid resolution was highest in the lower levels, with a spacing of about 100 m near the ground and increasing above the boundary layer. The observed low-level stable layer occurred in the lowest 2 km, and could therefore be resolved by the chosen vertical grid. At mid-levels (between heights of about 2 and 8 km) the vertical grid spacing was about 250 m. The observed RIJ was about 4 km deep and extended between heights of about z=6 to z=2 km (Figure 3.6c). The vertical grid was therefore able to sufficiently resolve the RIJ. The top of the model was along a constant pressure surface at 5000 Pa. The timestep was 18 seconds. Data were output every 15 minutes of model time for the inner domain. This particular configuration of the WRF model used the Morrison 2-moment microphysics parameterisation scheme, the RRTM longwave radiation scheme, the Dudhia shortwave radiation scheme, the Monin-Obukhov surface-layer scheme and a thermal diffusion land-surface scheme with 4 soil layers. No parameterised boundary layer scheme was used in any of the model nests. Turbulent eddies in the boundary layer may start to be resolved at a horizontal grid resolution of 1 km, and so a fully 3D local subgrid turbulence scheme was used (i.e. an LES-type boundary layer) instead of a PBL scheme. This was because PBL schemes assume that there is a clear scale separation between subgrid eddies and resolved eddies

(Skamarock *et al.*, 2008). The evolution of the 3D turbulent kinetic energy was governed by a prognostic equation with the source and sink terms for the turbulent kinetic energy dependent on shear production, buoyancy, and dissipation (Skamarock *et al.*, 2008). The eddy viscosities were computed by prognostic TKE closure with the length scale dependent on the horizontal and vertical grid spacing (see Chapter 4 of Skamarock *et al.*, 2008, for further details.). The Betts-Miller-Janjic cumulus parameterisation scheme was used in the outer domain. In the middle and inner domains no cumulus parameterisation was used (i.e. convection was explicitly resolved by the model in these domains). No urban physics scheme was used. The model was initialised using initial conditions and lateral boundary conditions from Global Forecast System (GFS) analysis files starting at 0000 UTC on 24 June 2005 and updated every 6 hours. The model required about six hours of spin-up time before realistic convective structures developed. This is discussed in more detail in Chapter 4, Section 4.2.1.

3.2.2 The structure and evolution of the precipitation

The simulated reflectivity field from the inner domain of the model is shown in Figure 3.8. A band of heavy precipitation was oriented north to south over Wales and the south-west of England at 0900 UTC (Figure 3.8a). The heaviest precipitation occurred in the southern part of the band. Behind (to the west of) the northern part of the band there was a broad region of less intense precipitation. This reflectivity structure was suggestive of the 'leading-line, trailing stratiform' type of MCS described by Parker and Johnson (2000), and the structure seen in Figure 3.8a is similar to their Figure 5b. This structure suggests that the simulated convective structures were mature by 0900 UTC. The trailing region of light precipitation was much narrower in the southern part of the band.

The leading line, trailing stratiform structure of the simulated reflectivity field remained at 1000 UTC (Figure 3.8b). The leading line of heavy precipitation had moved to the north-east (the velocity of the simulated MCS is discussed later in Section 3.3). The reflectivity values in the leading line and the trailing region were similar to those at 0900 UTC. A notch developed in the trailing stratiform region in mid-Wales. This may have been due to a flow of relatively dry air into this region.

The simulated MCS began to split into two systems at 1200 UTC (Figure 3.8c). By this time the broad region of trailing stratiform precipitation had moved out of the north of the domain. A few small cells of intense precipitation developed in the east of the domain ahead of the system. These may have been initiated along an outflow boundary from the main MCS.

Two significant changes in the behaviour of the simulated MCS occurred between 1300 and 1400 UTC. The westerly component of the system velocity became greater than at previous times. The system speed also increased. The change in system velocity is discussed in detail in Section 3.3. The original single MCS had fully split into two systems by 1400 UTC (Figure 3.8d). The two MCSs moved at the same speed. By this time the structure of the convection was not as linear as it was during the 0900 to 1200 UTC period. The MCSs no longer had a distinct trailing stratiform structure. There was an area of light rainfall in the north of both MCSs. This structure remained until the MCSs dissipated.

A band of cells of intense precipitation formed in the east of the domain ahead of the MCSs by 1430 UTC (Figure 3.8e). These appeared to be forming along an outflow boundary from the southern MCS. This is discussed in Section 3.5.1. The small precipitation cells moved more slowly than the two MCSs and by 1500 UTC (Figure 3.8f) the northern MCS had merged with the small precipitation cells. After the northern MCS merged with the band of small precipitation cells it stalled and slowed a little. The velocity of the southern MCS did not decrease and it caught up with the northern MCS at 1600 UTC (Figure 3.8g). After this time the two systems merged. The MCS had propagated off the east coast of the UK by 1800 UTC (Figure 3.8h), after which time it dissipated.

Comparison with IOP 3

The simulated MCS differed from the MCSs observed during IOP 3 in several ways, but also shared some similarities. Only one MCS developed in the WRF simulation. This was different from the CSIP observations; several MCSs formed during IOP 3. Like the observed MCSs, the simulated convection moved from the southwest to the northeast and had a similar velocity to MCS C. During the early stages the simulated convection was linear, oriented north to south, and had a trailing stratiform precipitation region (Parker and Johnson, 2004). The structure and orientation of the modelled convection was similar to the observed MCSs, although those did not have as much of a distinct trailing

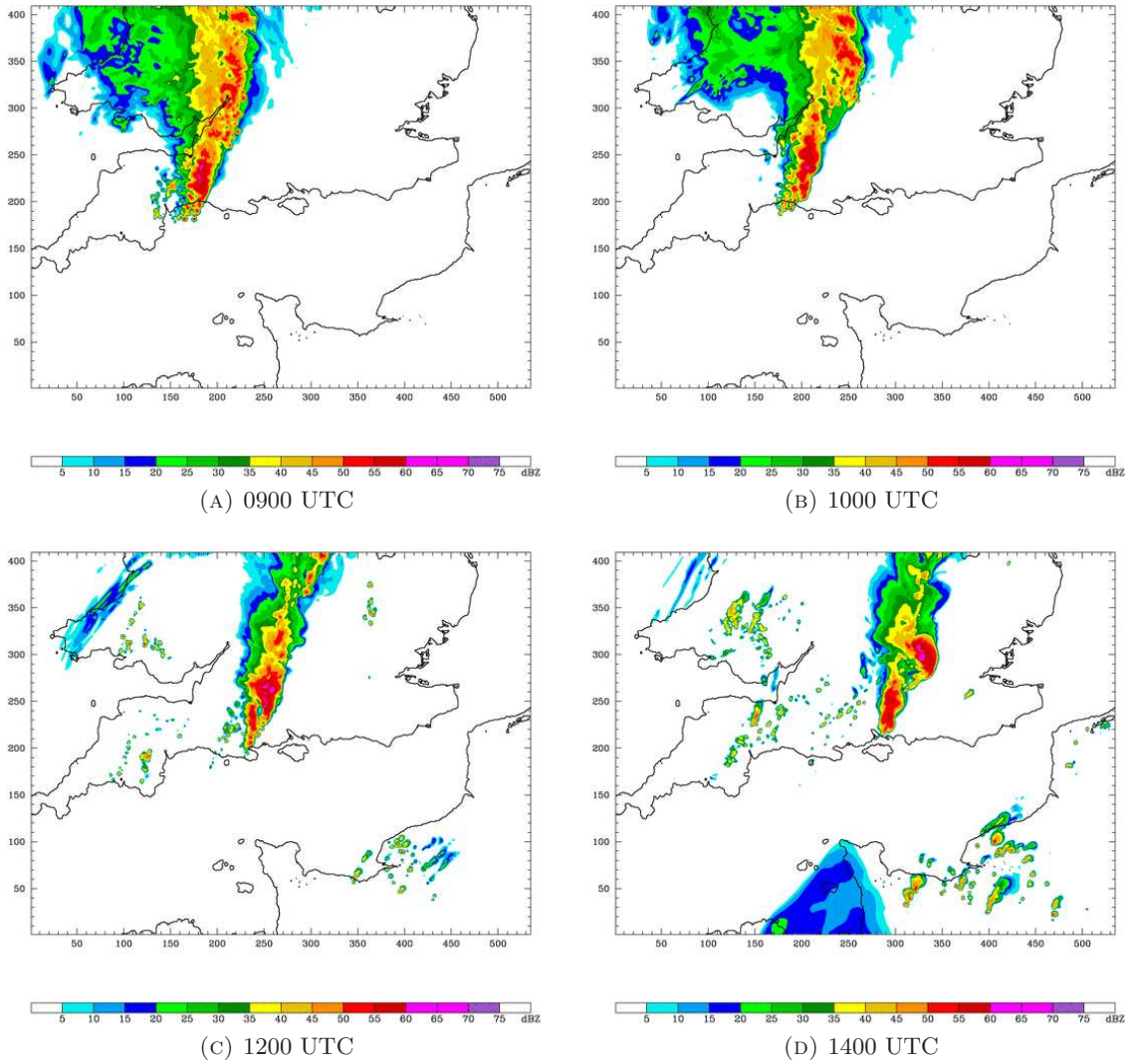

(A) 0900 UTC (B) 1000 UTC

(C) 1200 UTC (D) 1400 UTC

FIGURE 3.8: a-d: Simulated reflectivity (dBZ) field from the inner domain (1km horizontal gridscale resolution) of the WRF model run for 24 June 2005. Data shown at 0900, 1000, 1200 and 1400 UTC model time.

stratiform region. The simulated MCS later split into two systems, both of which moved at the same speed. This system split was not observed during IOP 3. The two resulting simulated MCSs did not have a linear structure or a broad trailing stratiform region and at 1400 UTC the structure of the simulated precipitation (Figure 3.8d) was similar to the observed precipitation at 1345 UTC (Figure 3.2h). The westerly velocity component of the simulated MCS increased between 1300 and 1400 UTC and during this time the system speed also increased. This was similar to the behaviour of MCS C. The velocity of MCS C increased between 1155 and 1423 UTC. A line of cells of intense precipitation formed along an outflow boundary from the southern simulated MCS. These cells moved

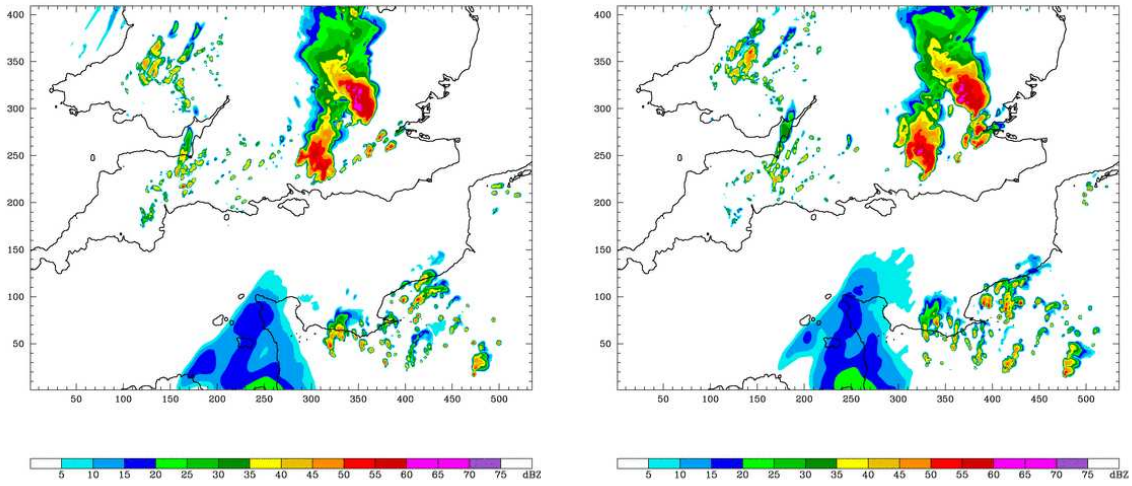

(E) 1430 UTC

(F) 1500 UTC

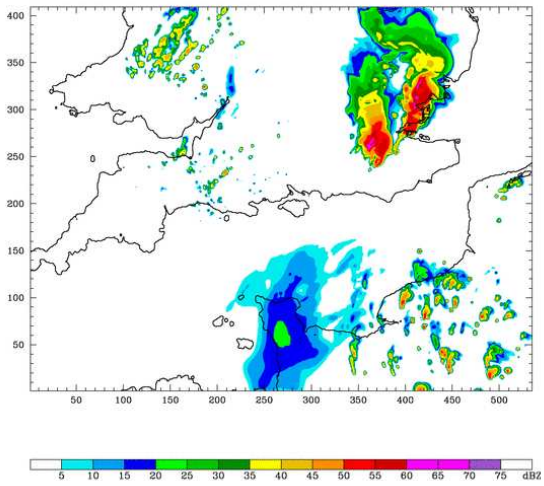

(G) 1600 UTC

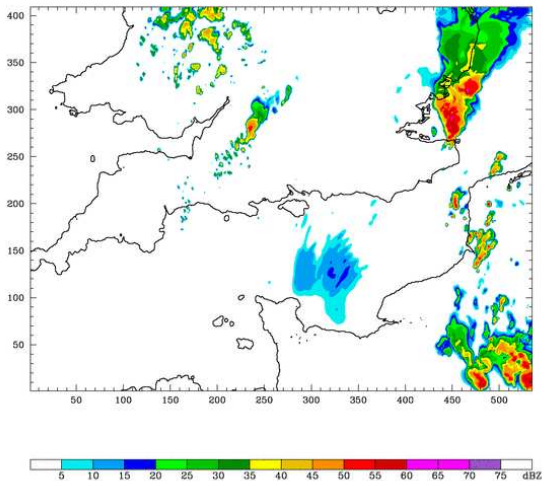

(H) 1800 UTC

FIGURE 3.8: e-h: Simulated reflectivity (dBZ) field from the inner domain (1km horizontal gridscale resolution) of the WRF model run for 24 June 2005. Data shown at 1430, 1500, 1600 and 1800 UTC model time.

more slowly than the MCSs and the northern MCS caught up with and merged with the outflow cells. This caused the northern MCS to stall, and the southern MCS then caught up with the northern system. The two MCSs merged and propagated off the east coast of the UK, after which time the convection weakened and dissipated. No outflow boundary was observed during IOP 3 and neither did any of the observed MCSs merge.

3.3 The velocity of the simulated MCS

The velocity of MCS C increased from 15 m s^{-1} at 1155 UTC to 18 m s^{-1} at 1423 UTC. Browning *et al.* (2010) were unable to explain the increase in system velocity. As mentioned above, the velocity of the modelled MCS increased between 1300 and 1400 UTC (Figure 3.8). In order to determine the system velocities of the simulated MCS, a series of Hovmöller diagrams of vertical velocity were made at several model levels and along several lines in the inner domain of the model. Diagrams were made from west to east across lines of constant y-index, at y-points 240, 260, 280, 300, 320 and 340 (see e.g. Figure 3.8 for the geographical position of these points). There was only a small amount of variation in the system velocity between each line. The system velocity also showed very little variation between model levels. As such, only the diagram from the y-240 line at the model level with the strongest vertical velocity (model level 20) is presented here.

Figure 3.9 is a Hovmöller diagram of vertical velocity and column-integrated cloud at model level 20 along the y-240 line. Cloud formed during the spin-up period of the simulation and consolidated at about 0600 UTC, at which time updraughts and downdraughts (1.5 to 2 m s^{-1}) also began to form at this model level. The convective system propagated across the model domain (from west to east) at a reasonably constant velocity of (6.4±1.3) m s^{-1} until 1300 UTC. A significant increase in system velocity to (10.3±1.3) m s^{-1} occurred between 1300 and 1400 UTC (Figure 3.9). A series of intense (2 m s^{-1}) updraughts and downdraughts developed shortly after the increase in velocity, at 1600 UTC. The increase in system velocity coincided with a transition in the model from elevated, wave-lifted convection to surface-based, gravity current-lifted convection. This is discussed in Section 3.5.1.

The Hovmöller diagrams were used to determine the speed of the simulated convective system before and after the change in velocity. These velocities are shown in Table 3.1. The mean elevated, wave-lifted system velocity was (6.4±1.3) m s^{-1} and the mean surface-based, gravity current-lifted system velocity was (10.3±1.3) m s^{-1}. The difference between the system velocities could not be accounted for by error alone.

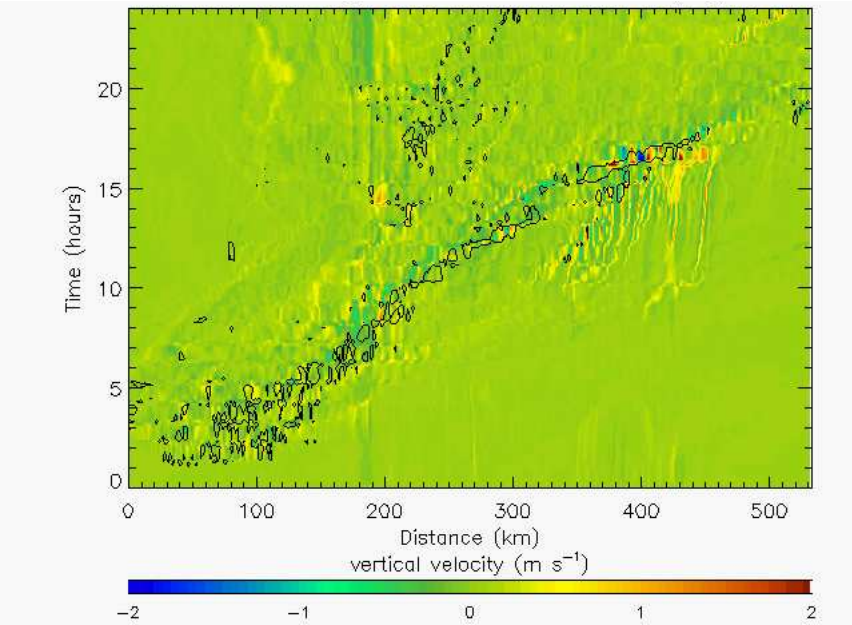

FIGURE 3.9: Hovmöller diagram of vertical velocity (m s^{-1}, colour contour) and column-integrated cloud at 2.0 g kg^{-1} (black line contour) for model level 20 along the y-240 line.

y-index	Velocity 1 (m s^{-1})	Velocity 2 (m s^{-1})
240	5.7± 0.5	12.2 ±0.5
260	5.1± 0.5	12.8 ±0.5
280	4.7± 0.5	9.1 ±0.5
300	7.4± 0.5	8.9 ±0.5
320	7.8± 0.5	10.0 ±0.5
340	7.5± 0.5	8.9 ±0.5
mean	6.4± 1.3	10.3 ±1.3

TABLE 3.1: Table showing the two system velocities of the MCS in the WRF simulation; Velocity 1 is the initial system velocity (during the elevated, wave-lifted phase) and Velocity 2 is the system velocity after the increase occurred (during the surface-based, gravity current-lifted phase).

Comparison with IOP 3

The significant increase in system velocity of the modelled MCS was similar to the behaviour of MCS C. The speed of the simulated MCS was slower than that of MCS C both before (about 6 m s^{-1} compared to 15 m s^{-1} for MCS C) and after (about 10 m s^{-1} compared to 18 m s^{-1}) the increase. This could have been because the upper-level flow was weaker in the model than it was during IOP 3.

3.4 The large-scale environment

The structure of the mean sea-level pressure in the WRF simulation at 1200 UTC was very similar to that of the operational Met Office analysis at this time. The simulated mean sea-level pressure from the outer domain (9 km horizontal resolution) of the model is shown in Figure 3.10. Convection was parameterised in the outer domain of the model. There was a region of low pressure of about 1013 hPa over northern France in the model. A similar low of 1012 hPa occurred over northern France in the Met Office analysis (Figure 3.1). The regions to the west of Ireland and to the east of the UK in the North Sea also had similar pressure distributions.

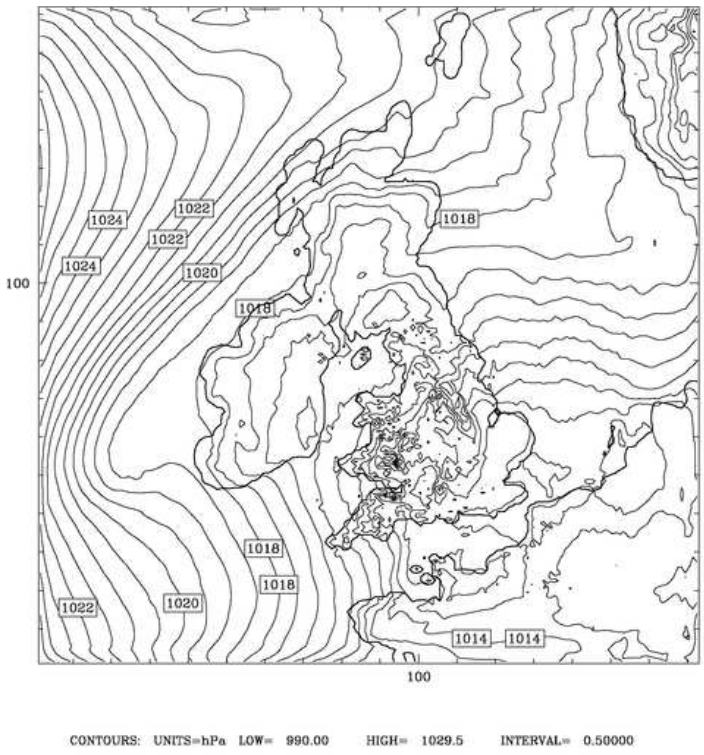

FIGURE 3.10: Mean sea level pressure from the outer model domain at 1200 UTC model time, 24 June 2005. Contours are marked every 0.5 hPa.

In agreement with the Met Office analysis (Figure 3.1), there was also a cold front across Ireland in the WRF simulation. The equivalent potential temperature (θ_e) from the outer domain of the model at 900 hPa and 500 hPa at 0000 UTC is shown in Figures 3.11 and 3.11b. There was a cold front across Ireland at both levels. Ahead of the cold front there was a low-level pre-frontal θ_e gradient across southern England (Figure 3.11a). Values of θ_e were larger in the east and smaller in the west. The simulated storm formed on the

west side of this gradient. At higher levels (500 hPa, Figure 3.11b) high-valued θ_e air was advected from the south of the domain.

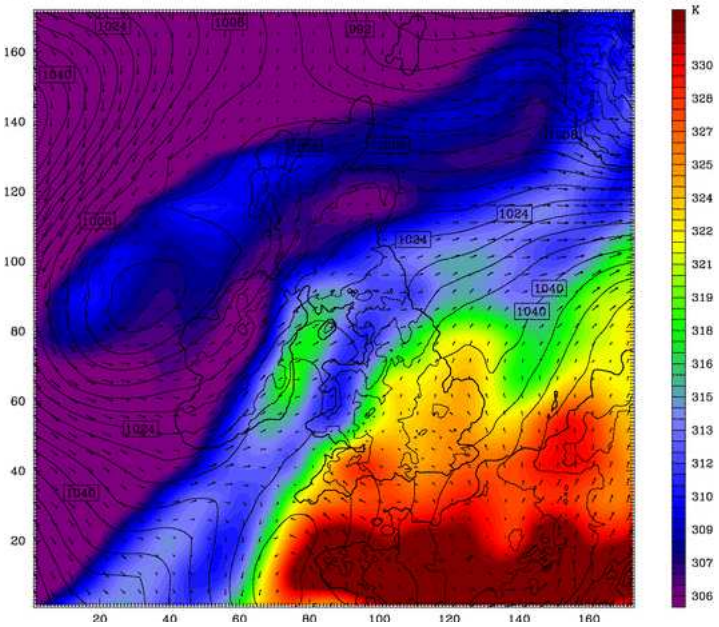

(A) 900 hPa

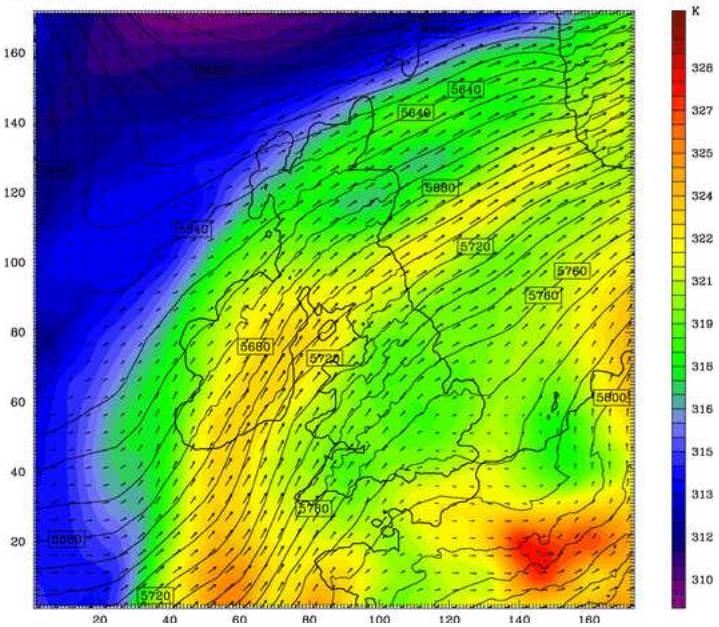

(B) 500 hPa

FIGURE 3.11: θ_e (K, colour contour), horizontal wind vectors and geopotential height (m, black line contour) at 0000 UTC model time. Horizontal distances are in km.

To determine the vertical structure of the large-scale environment in which the simulated MCS formed, two sets of vertical sections of θ_e were made through the outer domain of the model from west to east. These are shown in Figure 3.12. The set labelled 'northern'

were taken through a y-index of 60 and the set labelled 'southern' were taken through a y-index of 40. The geographical location of the y-indices can be seen in Figure 3.11. The convective structures in these vertical sections are not discussed in detail because convection was parameterised in the outer domain of the model. A detailed discussion of the convective structures that developed in the inner domain of the model, where convection was resolved explicitly, is given later in Section 3.5. For the purposes of this analysis, in the early stages of the simulation the boundary layer was determined to be the low-level region of the model that contained the stable layer and that occurred below the elevated source layer and the convective structures, corresponding to approximately the lowest 1 km. In the later stages of the simulation the boundary layer was determined to be the well-mixed region of high-valued θ_e air, corresponding to approximately the lowest 2 km.

The front to the west of the UK (over Ireland and Wales) in the simulated θ_e field (Figure 3.11) had a double-frontal structure. There was a sharp gradient in θ_e at 500 km and another notable gradient in θ_e at 650 km in the north at 0000 UTC (Figure 3.12a). In the south these gradients were at 400 km and 750 km, respectively, at this time (Figure 3.12b). The region of high-valued θ_e air at 700 km in the northern section at 0000 UTC (Figure 3.12a) corresponded to the maximum in θ_e at 900 hPa over the Irish sea (at about 700 km on the x-axis of Figure 3.11a). At low-levels, the values of θ_e from west to east followed a low-high-low-high structure. The wind field along the westernmost frontal gradient (circulation vectors and winds into and out of the plane in Figures 3.12a and 3.12b) showed significant along-front shear that was aligned with the frontal surface. This wind field was suggestive of a large-scale front (with the along-front shear aligned with the ascending frontal surface).

The low-level θ_e gradient across the domain became sharper throughout the model run. Values of θ_e in the lowest 2 km in the east of the domain increased throughout the simulation in both the northern set of vertical sections (Figures 3.12a, 3.12c and 3.12e) and the southern set (Figures 3.12b, 3.12d and 3.12f). This increase in θ_e in the east, combined with the lower-valued θ_e associated with the cold front to the west, led to the sharpening of the θ_e gradient. The simulated MCS propagated through the low-level θ_e field from the west to the east, such that it encountered ever increasing values of θ_e at low levels.

There was an elevated region of high-valued θ_e air initially centred at 800 km between heights of 1.0 and 2.5 km in the south of the domain (Figure 3.12b). Values of θ_e between these heights in the north were not as large (Figure 3.12a). The southern elevated high-valued θ_e air had become a region of inflow to the storm by 1000 UTC (Figure 3.12d). Further to the north the largest values of θ_e at 1000 UTC were near the surface (Figure 3.12c). Values of θ_e in the elevated source air in the north were not as large as they were in the south. In the south the largest values of θ_e were in the near-surface layer by 1200 UTC (Figure 3.12f).

The elevated region of high-valued θ_e had larger values of θ_e in the south than it did in the north (comparing the northern set of vertical sections, Figures 3.12a, 3.12c and 3.12e, and the southern set, Figures 3.12b, 3.12d and 3.12f). As the simulated MCS propagated from the southwest to the northeast it moved through and out of the region of elevated high-valued θ_e air into a region where values of θ_e were greater near the surface than they were at elevated levels.

The increase in depth of the high-valued θ_e source air in the east of the domain may have been due to surface heating. In the southern set of vertical sections, the low-level high-valued θ_e air in the boundary layer between 1200 and 1400 km deepened between 0000 UTC (Figure 3.12b) and 1000 UTC (Figure 3.12d), and further between 1000 UTC and 1400 UTC (Figure 3.12f). The deepening of the low-level high-valued θ_e air was less significant in the north (Figures 3.12a, 3.12c and 3.12e). A greater portion of the region between 1200 and 1400 km was situated over the sea in the northern section (at a y-index of 60) than in the southern section (at a y-index of 40) (Figure 3.11). Less surface heating would therefore have occurred in this region in the northern section. This suggests that a significant cause of the sharpening of the (pre-existing) θ_e gradient was due to surface heating. This is investigated later in this Chapter in Section 3.7 and further in Chapter 4.

The large-scale flow in the lowest 1 km ahead of the simulated MCS was towards the storm in both the north (Figures 3.12a, 3.12c and 3.12e) and the south (Figures 3.12b, 3.12d and 3.12f) of the outer domain. This was similar to the undercurrent observed in MCS C.

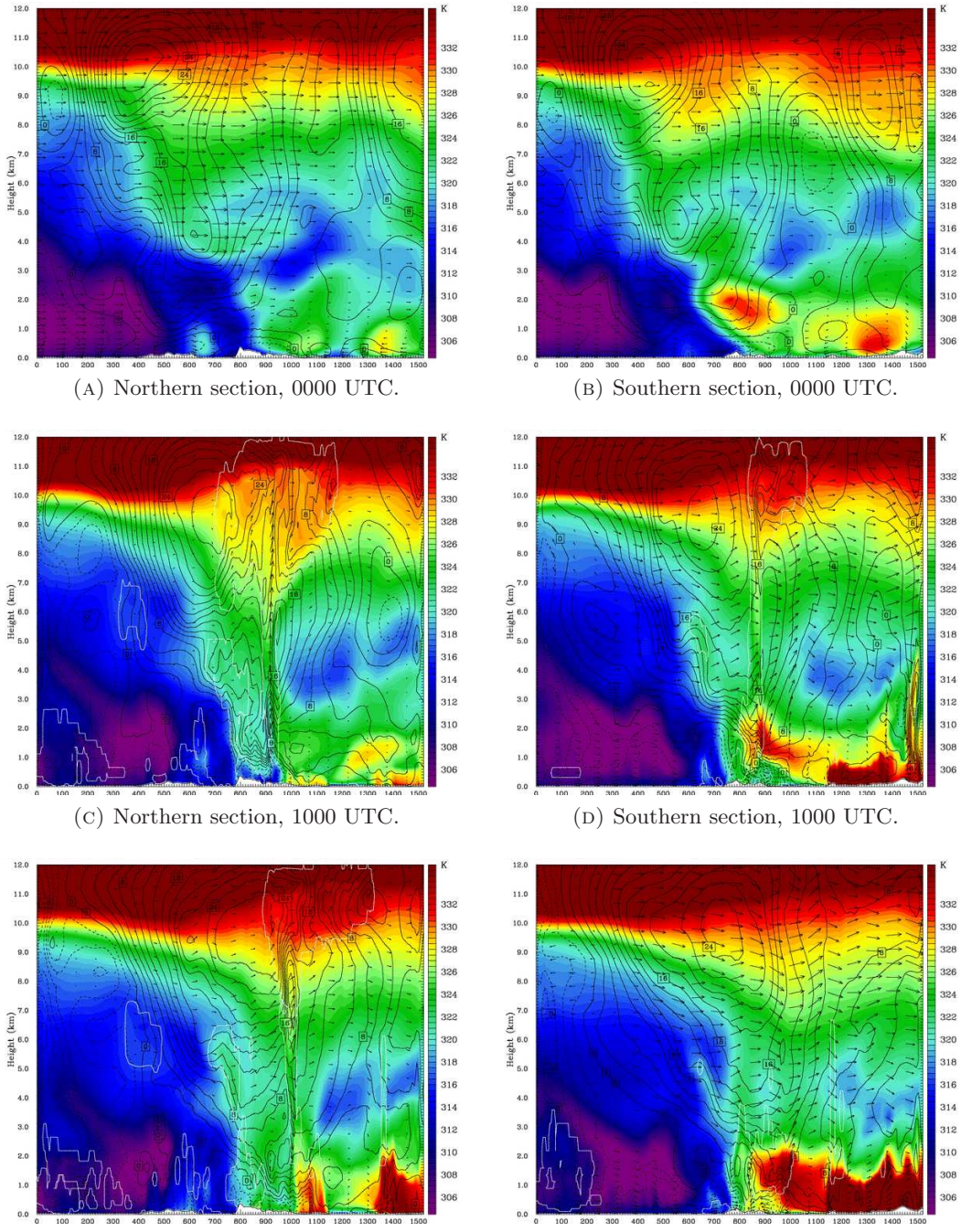

(A) Northern section, 0000 UTC.

(B) Southern section, 0000 UTC.

(C) Northern section, 1000 UTC.

(D) Southern section, 1000 UTC.

(E) Northern section, 1400 UTC.

(F) Southern section, 1400 UTC.

FIGURE 3.12: Vertical sections taken from west to east through the outer domain (9 km horizontal resolution) of the model and showing θ_e (K, colour contour), circulation vectors, horizontal winds in the plane of the cross-section (m s^{-1}, solid black line contour showing winds into the page and dashed black line contour showing winds out of the page) and a single contour of total cloud mixing ratio (5x10^{-3} g kg^{-1}, white line contour). Horizontal distances are in km.

Comparison with IOP 3

The simulated MCS formed in a similar large-scale environment to that of MCS C. Convection developed ahead of a cold front that was in the west of the domain. The large-scale low-level flow was against the direction of the motion of the storm, similar to the observed undercurrent. There was an elevated layer of high-valued θ_e air in the south of the model domain that was the source air for the convection in its early stages. As the simulated MCS propagated from the southwest to the northeast it encountered two significant changes in the large-scale θ_e structure: the low-level values of θ_e increased (due to the sharpening of the θ_e gradient from west to east, with higher values in the east), and the values of θ_e in the elevated source layer decreased to the north. This led to the convection eventually becoming surface-based. The CSIP observations did not show whether there was a west to east θ_e gradient during IOP 3, or whether the elevated source layer was weaker in the north of the UK.

3.4.1 The thermodynamic structure of the pre-convective environment

A tephigram of data taken from the pre-convective environment ahead of the simulated MCS at 1100 UTC is shown in Figure 3.13. At this time the convection in the simulated MCS was fed from the elevated layer of high-valued θ_e (Figure 3.12d). There was a 50 hPa-deep nearly dry-adiabatic near-surface layer. Above this were two moist layers, one centred at 930 hPa and one at 840 hPa. The lower moist layer was nearly isothermal. The low-level nearly dry-adiabatic layer surmounted by two moist layers was similar to the Swanage sounding (Figure 3.3 and also shown in red in Figure 3.13). However, the low-level nearly dry-adiabatic layer in the model was lower than that observed during CSIP, as was the nearly isothermal layer. The two moist layers were lower and shallower than the two moist layers in the Swanage sounding.

Vertical profiles of CAPE and CIN calculated from the model sounding are shown in Figure 3.14. The lower moist layer (at 930 hPa) had modest CAPE of about 50 J kg^{-1} and had to overcome 100 J kg^{-1} of CIN. The upper moist layer (at 840 hPa) had about 350 J kg^{-1} of CAPE. This was less than but comparable to the 405 J kg^{-1} of CAPE of the observed upper source layer (Section 3.1.1.2). There was little CIN for the upper moist layer to overcome. The upper moist layer in the model was the elevated source layer.

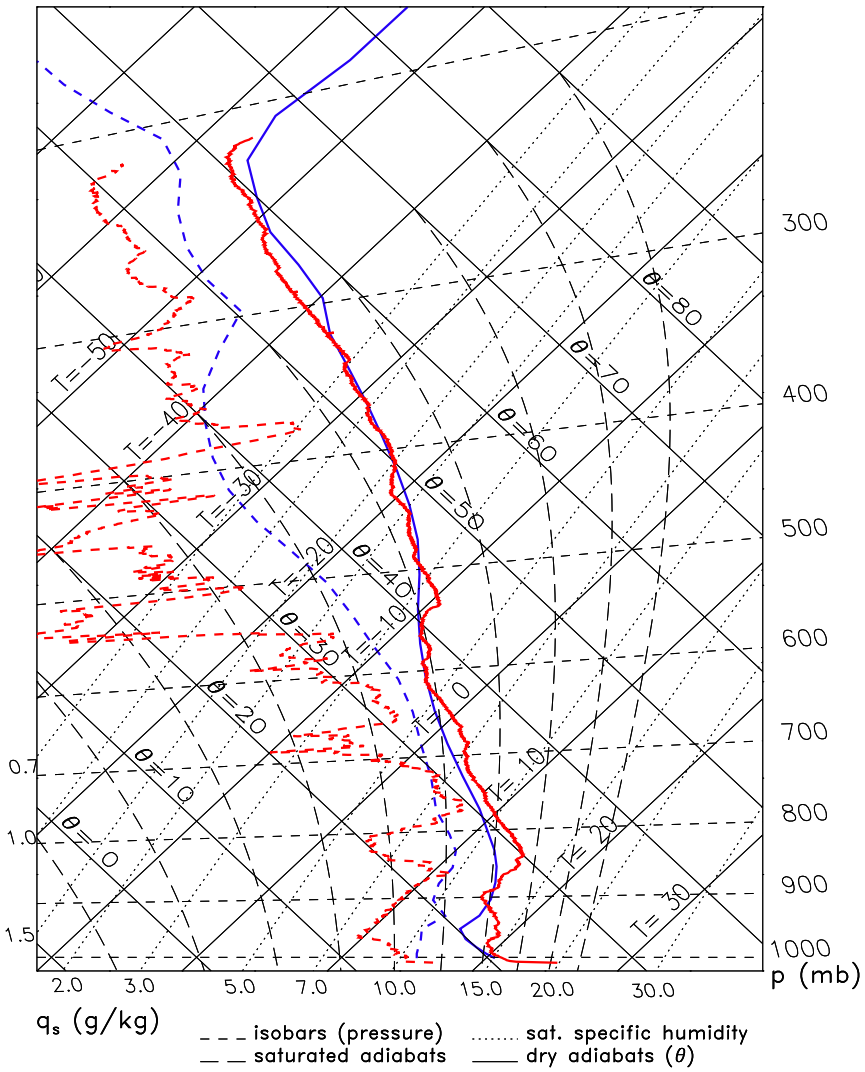

FIGURE 3.13: Tephigram constructed from model data ahead of the MCS at 1100 UTC (blue line). Also shown is the Swanage 1100 UTC sounding from Figure 3.3 (red line).

The elevated source layer in the model was similar, but not as strong, as the observed elevated source layer. The difference between the simulated and observed elevated source layers may have been due to sensitivity to the location of both the observed and modelled soundings.

A hodograph of the winds from the model sounding is shown in Figure 3.15. While the modelled winds were not as strong as the observed winds (Figure 3.4), the low-level flow was northeasterly and the mid- to upper-level flow was southwesterly, which was in agreement with the observations. The northeasterly low-level flow in the model was the undercurrent. The undercurrent extended from the surface to 900 hPa. Although the undercurrent in the simulation was slower and shallower than the observed undercurrent, its temperature was

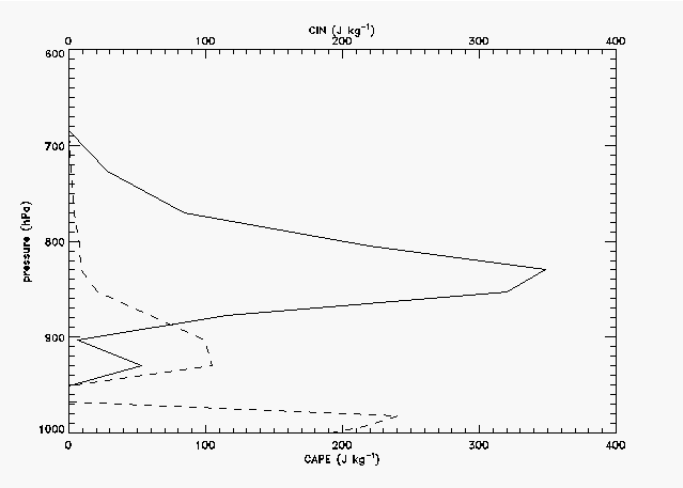

FIGURE 3.14: Vertical profile of CAPE (solid line) and CIN (dashed line) from model data ahead of the MCS at 1100 UTC.

lower than that of the observed undercurrent (Figure 3.13). The upper-level southwesterly winds in the model were also weaker than the observed upper-level southwesterly flow.

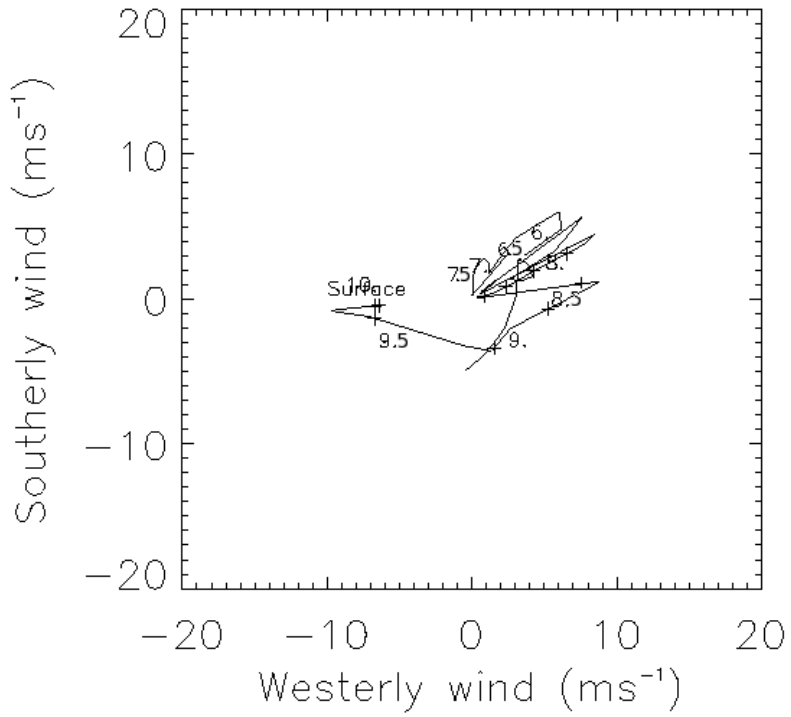

FIGURE 3.15: Wind hodograph constructed from model data ahead of the MCS at 1100 UTC. Pressure is labelled in hundreds of hPa.

3.5 Convective-scale structures

This Section discusses the 3D evolution of the convective structures that developed in the inner domain of the model. The horizontal resolution was 1 km in this domain and convection was resolved explicitly.

3.5.1 The structure and along-line variability of the simulated system

A series of vertical sections of θ_e were made through the model domain to investigate the internal structure of the simulated MCS and its along-line variability. These sections were made approximately normal to the orientation and direction of motion of the storm. The direction and locations of the sections are shown in Figure 3.16. The section that passed through the centre of the MCS (labelled y200 in Figure 3.16) is described in detail below. The ways in which the other sections differed from the central section are also discussed.

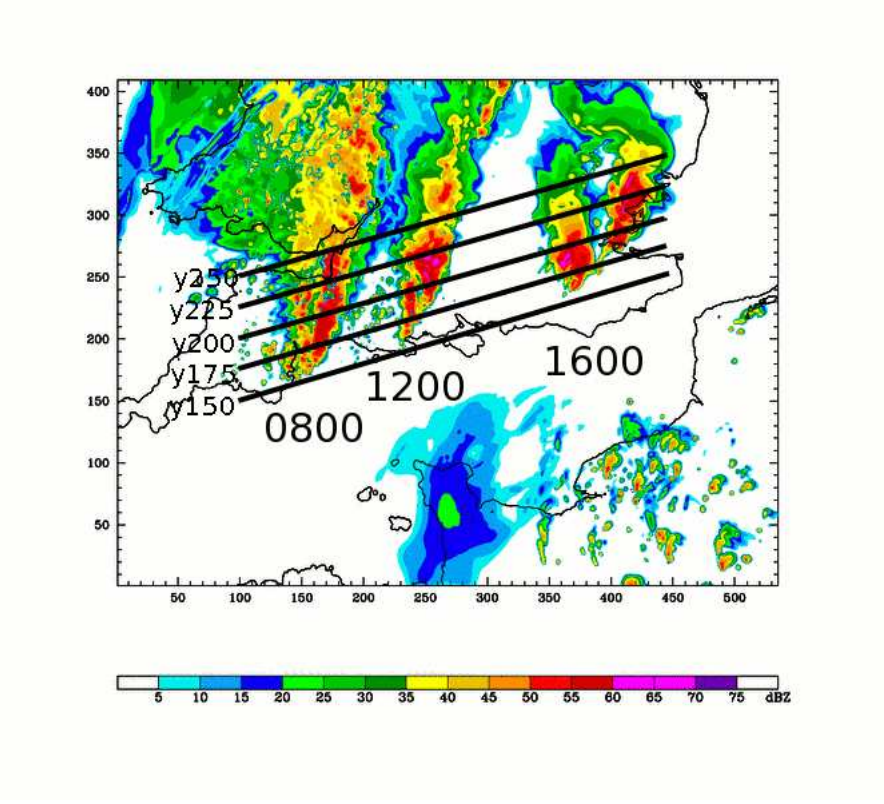

FIGURE 3.16: Reflectivity fields from the WRF simulation overlaid at 0800, 1200 and 1600 UTC (relevant times are labelled under the corresponding reflectivity fields). The black lines are the lines along which the vertical sections through the simulated system were made. Lines are labelled at their far left according to the y-index at which they begin.

3.5.1.1 y200 vertical section

A series of vertical sections of θ_e, system-relative winds and total cloud mixing ratio at different times along the line labelled y200 in Figure 3.16 are shown in Figure 3.17. These sections reveal the vertical structure of the central region of the simulated MCS. In this discussion, 'z' is used as the height coordinate.

Convection formed during the spin-up period of the model. A significant feature of the pre-convective environment was a low-level, low-valued θ_e layer in the lowest 1 km between 0 and 160 km at 0730 UTC (Figure 3.17a). This layer flowed against the direction of motion of the MCS and was similar to the undercurrent associated with MCS C, described by Browning *et al.* (2010) and earlier in this Chapter in Section 3.1. Above the cold undercurrent and ahead of the MCS there was an elevated, high-valued θ_e layer centred at z=2 km. This air was the source air for the convection. There was a RIJ of low-valued θ_e air to the rear of the convective system between z=3.5 and z=6.0 km at 0730 UTC (Figure 3.17a). In the analysis of the simulation the RIJ was determined to be a region of low-valued θ_e that entered the rear of the storm, underwent descent, and which had positive system-relative velocity at all times. Under adiabatic conditions θ_e is a conserved quantity and as such was used as a tracer to determine the position of the RIJ. The RIJ entered the rear of the storm beneath the cloud (e.g. Figure 3.17) and below the melting level (Figure 3.13), and so this assumption was generally valid. However, it should be noted that if any evaporation, sublimation or melting did occur within the RIJ then θ_e would no longer be conserved and it would no longer be appropriate to treat it as a passive tracer. Behind the MCS, the RIJ was penetrated by two updraughts of high-valued θ_e air at 30 and 45 km. The RIJ descended under the trailing stratiform region to z=1 km at 65 km. The RIJ did not descend to the surface. The descending RIJ brought low-valued θ_e air underneath the main convective region and the elevated source layer. The descending RIJ constricted the cold undercurrent to z=400 m between 50 and 75 km. The constriction of the undercurrent caused a wave to form at the top of the undercurrent and in the elevated source layer between z=2.0 and z=3.5 km at 80 km. There was cloud associated with the wave, indicating that the wave lifted air in the elevated source layer to its condensation level. Far ahead (to the east) of the MCS, there were greater values of θ_e in the near-surface layer of the cold undercurrent between 165 and 235 km. This caused

the horizontal low-level θ_e gradient to sharpen, and was due to a combination of advection (discussed previously in Section 3.4) and surface heating (discussed later in Section 3.7).

There were four waves at the top of the undercurrent and in the elevated source layer at 0815 UTC (Figure 3.17b), caused by the constriction of the undercurrent by the RIJ. There were wave peaks at 100, 92, 88 and 85 km, giving an average wavelength of about 4 km. Each of the wave peaks had shallow cloud associated with it between z=2 and z=4 km. Ahead of the MCS, between 175 and 235 km, the layer of increasing θ_e in the cold undercurrent had deepened to 300 m.

The RIJ descended to z=750 m at 115 km at 1015 UTC (Figure 3.17c). The cold undercurrent was constricted by the RIJ to z=300 m between 95 and 115 km. There was a single wave at 130 km at the top of the undercurrent and in the elevated source layer. The values of θ_e in the elevated source layer had increased since 0815 UTC. Because this layer was centred at z=2 km the increased values of θ_e could not have been due to surface heating and were therefore due to advection (Figure 3.11 in Section 3.4). Values of θ_e had also increased in the low levels and affected the cold undercurrent (70 to 190 km, Figure 3.17c). Values of θ_e in the undercurrent were about 322 K at 1030 UTC, compared to 318 K at 0815 UTC.

The layer of increasing θ_e ahead of the MCS between 230 and 330 km had deepened to z=1.5 km by 1130 UTC (Figure 3.17d). The top of the high-valued θ_e boundary layer air (in the east) reached the bottom of the high-valued θ_e elevated source layer (in the west) and the two regions began to merge. This indicated the potential for a transition from elevated to surface-based convection to occur as the MCS propagated through the model domain from the southwest to the northeast. The storm was sufficiently behind the region of high-valued θ_e boundary layer air at this time that most of the inflow to the convection would have been from the elevated layer. The RIJ descended to z=1 km at 150 km. The descent of the RIJ constricted the undercurrent to z=500 m or less between 100 and 150 km.

The MCS continued to propagate through the model domain and the inflow to the convection became surface-based by 1330 UTC (Figure 3.17e). The MCS had passed through the region of elevated high-valued θ_e air and into the region of high-valued θ_e boundary-layer

air at 230 km. The transition from elevated to surface-based convection occurred at the same time as the system velocity increased (Section 3.3). The RIJ was no longer visible along the y200 section at this time.

The MCS was cut off from the surface-based source layer along the y200 section at 1445 UTC (Figure 3.17f). The MCS formed gravity current outflow, creating a region of low-valued θ_e at the surface between 220 and 280 km. The RIJ did not descend to the surface along the y200 section and therefore the gravity current had probably formed due to diabatic cooling in the convective region. The gravity current flowed into the high-valued θ_e boundary layer air. There were (system-positive) gust front winds at the head of the gravity current at 275 km. A new convective cell formed above the head of the gravity current at 290 km between z=1.0 and z=1.75 km. The new convection was surface-based and was initiated by the gravity current. Comparing Figure 3.17f with the line along which the y200 section was taken (Figure 3.16) and the reflectivity field at 1445 UTC (Figure 3.18) shows that the new convective cell was associated with intense precipitation. The cells of intense precipitation ahead of the MCS in Figure 3.18 were therefore new convective cells that formed along a gravity current outflow boundary from the southern MCS.

The new convection rapidly deepened to reach z=12 km at 300 km at 1500 UTC (Figure 3.17g). The cells of convection that formed along the outflow boundary began to merge with the northern MCS by this time (Figure 3.8f). The low-valued θ_e air in the RIJ may have mixed with the low-valued θ_e air in the convective downdraughts along the y200 section at this time. However, the system-relative winds did not show the RIJ reaching the surface.

Summary and comparison with MCS C

The structure of the simulated convection and its near-environment shared a number of similarities with MCS C. There was a cool undercurrent in the model, above which was an elevated layer of high-valued θ_e air. Both of these features were observed during IOP 3. The simulated convection was initially elevated and the source air was the elevated high-valued θ_e layer. MCS C was a case of elevated convection. The simulated MCS developed a RIJ which descended to the top of the undercurrent (about z=1 km). Along the y200 section the RIJ did not reach the surface. The RIJ of MCS C was not observed to descend to the

surface. The descent of the RIJ in the model constricted the low-level stable undercurrent and caused a series of waves to form ahead of the RIJ at the top of the undercurrent. The waves lifted the elevated source layer to at least its condensation level. A similar wave was observed in the undercurrent below MCS C caused by the RIJ descending and constricting the undercurrent. The wave observed during IOP 3 was shown by Marsham *et al.* (2010) to have lifted both of the observed source layers to their levels of free convection.

There were some differences between the simulated and observed convection. There was only one elevated, high-valued θ_e layer in the simulation. There were two elevated source layers observed during IOP 3. The simulated MCS eventually developed gravity current outflow. The observations of MCS C did not show that it formed a gravity current. New convection was initiated in the model along the outflow boundary associated with the gravity current. The undercurrent in the model was shallower than the observed undercurrent (about 1 km compared to 2 km). The values of θ_e at low-levels in the model increased throughout the simulation, weakening the undercurrent and contributing to the transition from elevated to surface-based convection. This was due to a combination of advection and surface heating (discussed later in Section 3.7). It is not known whether this occurred during IOP 3. The shallower, weakening undercurrent in the model would have been more susceptible to penetration by downdraughts than the observed undercurrent. Even though the RIJ did not penetrate the undercurrent along the y200 section in the model, convective downdraughts were able to reach the surface and form a gravity current. The slope of the RIJ in the model did not change along the y200 section. The observations of MCS C showed that the slope of the RIJ decreased over time. Browning *et al.* (2010) were unable to explain the decrease in slope of the RIJ.

3.5.1.2 y250 vertical section

The northernmost section of the pre-convective environment (y250, Figure 3.16) had the same structure as the central section (y200). The values of θ_e in pre-convective environment were about 2 K less than those in the y200 section. This affected the undercurrent, the elevated source layer and the region of increasing θ_e in the east of the domain. The RIJ penetrated to the surface at 1000 UTC (Figure 3.19a). This formed an early gravity current that flowed ahead of the MCS into the low-level region of high-valued θ_e air.

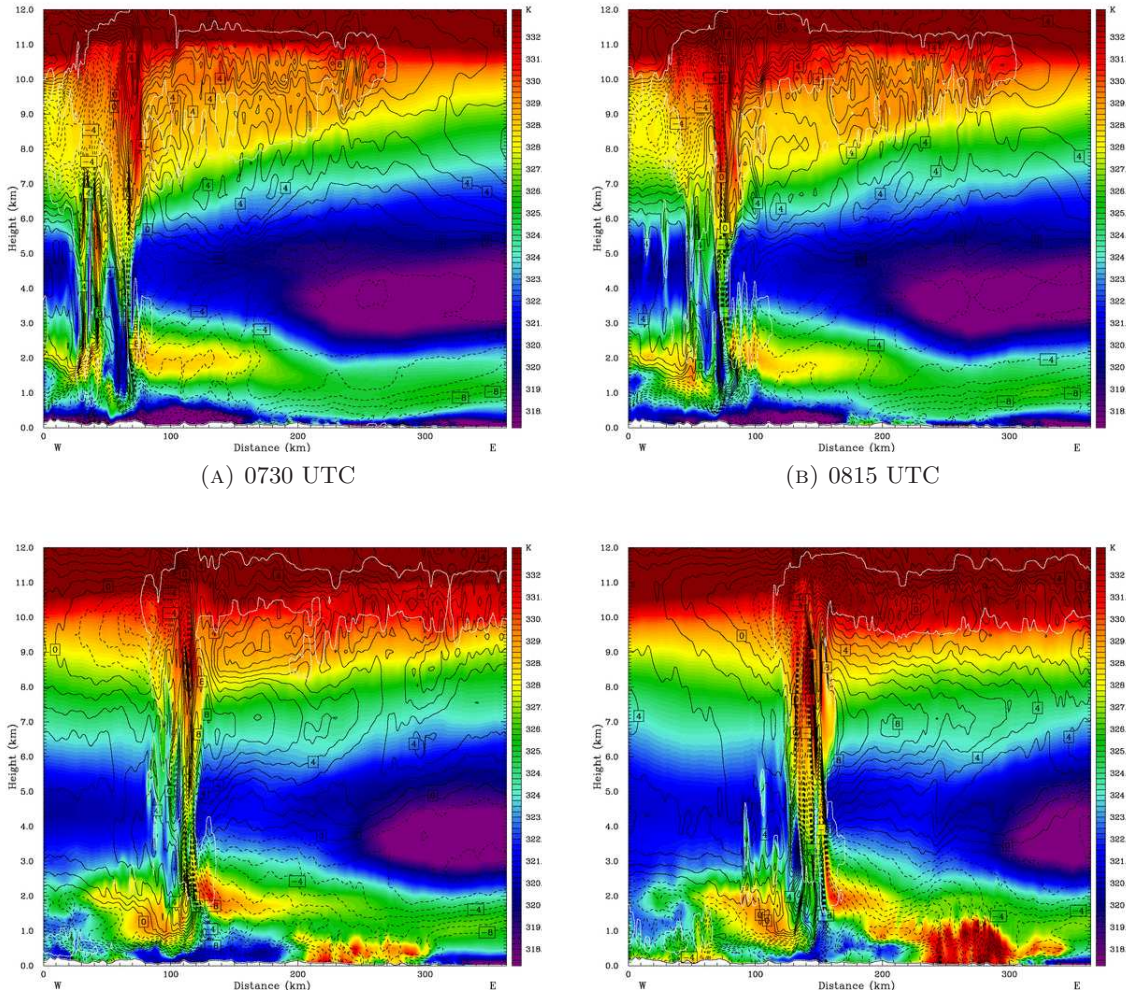

(A) 0730 UTC (B) 0815 UTC

(C) 1015 UTC (D) 1130 UTC

FIGURE 3.17: a-d: Vertical sections taken through the inner domain (1 km horizontal resolution) of the model along the line labelled y200 in Figure 3.16, showing θ_e (K, colour contour), system-relative winds (m s^{-1}, solid black line contour showing positive system-relative winds and dashed black line contour showing negative system-relative winds) and a single contour of total cloud mixing ratio (5x10^{-3} g kg^{-1}, white line contour).

The gravity current may also have been strengthened by diabatic cooling. After reaching the surface the RIJ rose back above the undercurrent and did not descend to the surface again along the y250 section. The RIJ generated a wave at the top of the undercurrent that lifted the elevated source air. No change in system velocity occurred when the early gravity current formed. The gravity current did not initiate new convection. The gravity current dissipated by 1330 UTC (Figure 3.19b). By this time the MCS had propagated through the elevated source layer and the convection became surface-based as the MCS encountered the high-valued θ_e air at low levels at 250 km. No gravity current formed

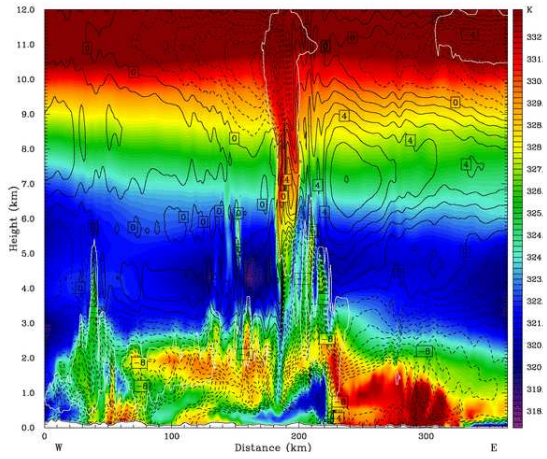

(E) 1330 UTC

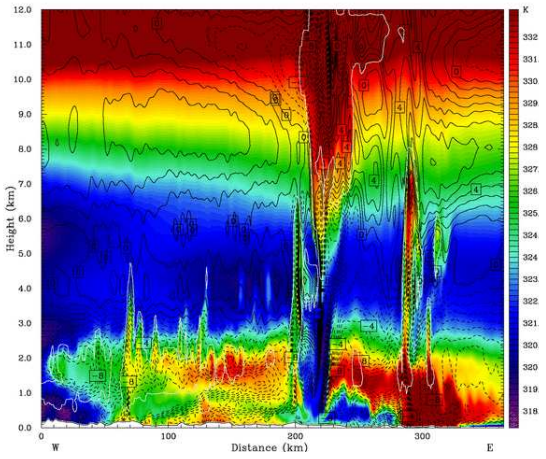

(F) 1445 UTC

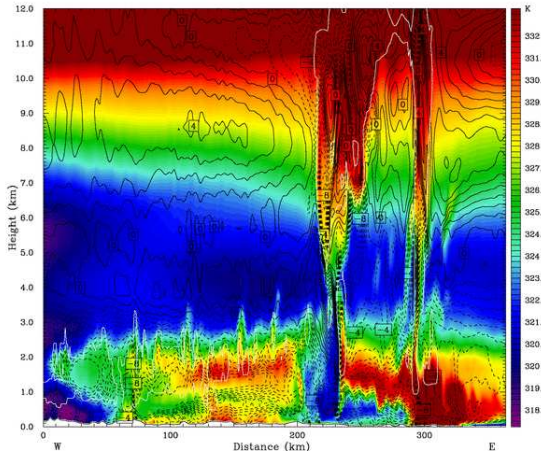

(G) 1500 UTC

FIGURE 3.17: e-g: Vertical sections taken through the inner domain (1 km horizontal resolution) of the model along the line labelled y200 in Figure 3.16, showing θ_e (K, colour contour), system-relative winds (m s^{-1}, solid black line contour positive system-relative winds and dashed black line contour showing negative system-relative winds) and a single contour of total cloud mixing ratio (5x10^{-3} g kg^{-1}, white line contour).

along the y250 section after the transition to surface-based convection. Both of the simulated MCSs (that developed from the split of the original storm) were visible along the y250 section by 1600 UTC (Figure 3.19c). There was no source of high-valued θ_e air along the y250 section at this time, suggesting that the inflow to the MCS was further to the south.

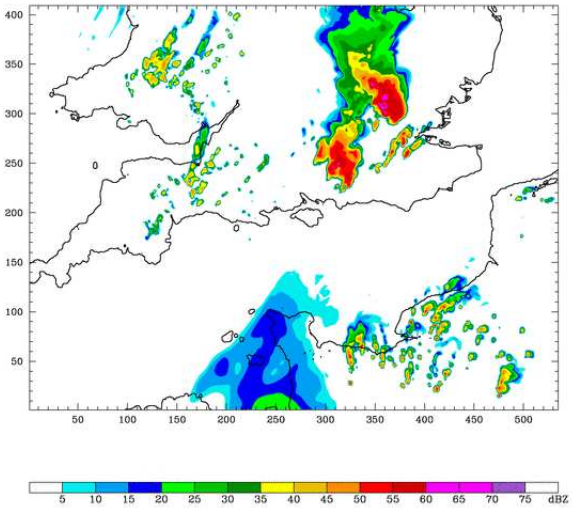

FIGURE 3.18: Simulated reflectivity (dBZ) field from the inner domain of the WRF model run for 24 June 2005 at 1445 UTC model time.

3.5.1.3 y225 vertical section

The structure of the pre-convective environment along the y225 section was similar to that along the y250 section. The values of θ_e in pre-convective environment were about 1 K less than those in the y200 section. The RIJ remained elevated and did not descend to the surface. The descent of the RIJ constricted the undercurrent and caused a wave to form at the top of the undercurrent. A gravity current formed at about 1015 UTC (Figure 3.20a). The RIJ did not reach the surface along the y225 section and therefore the gravity current was formed by the RIJ reaching the surface further to the north (the y250 section, discussed above). The gravity current may also have been strengthened by diabatic cooling. The convection became surface-based at about 1330 UTC. Both of the simulated MCSs were visible along the y225 section at 1600 UTC (Figure 3.20b). There was no source of high-valued θ_e air along the y225 section at this time.

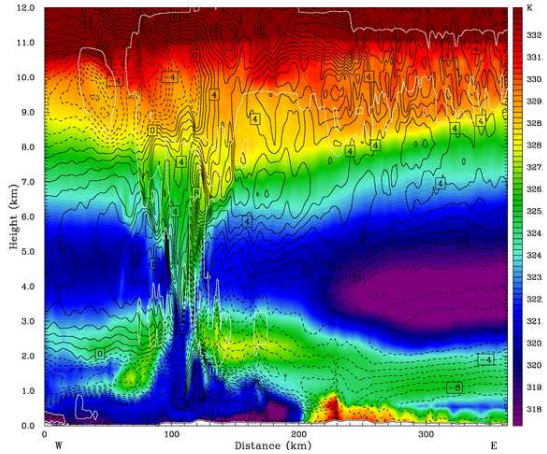

(A) 1000 UTC

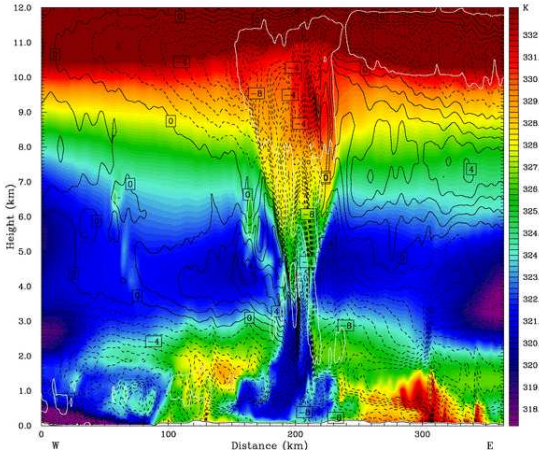

(B) 1330 UTC

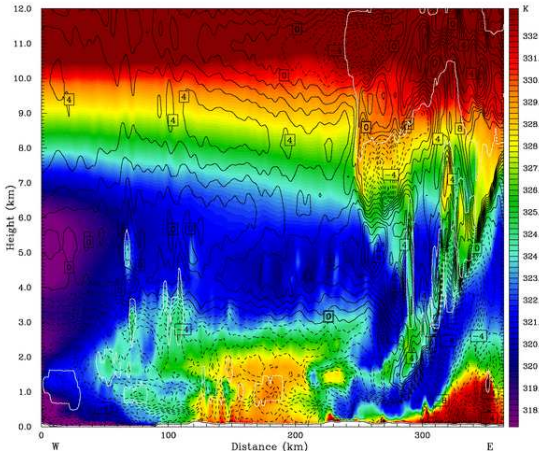

(C) 1600 UTC

FIGURE 3.19: As Figure 3.17 but for the y250 vertical section.

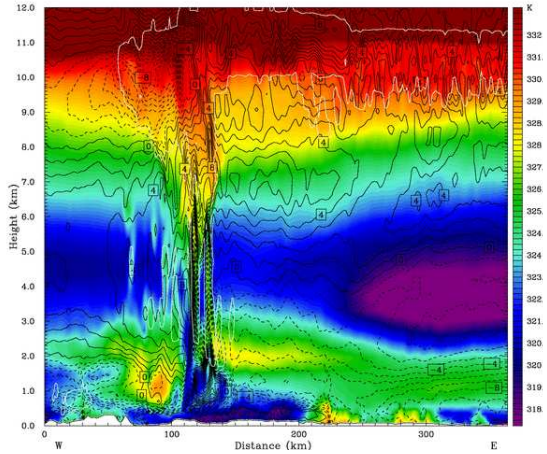

(A) 1015 UTC

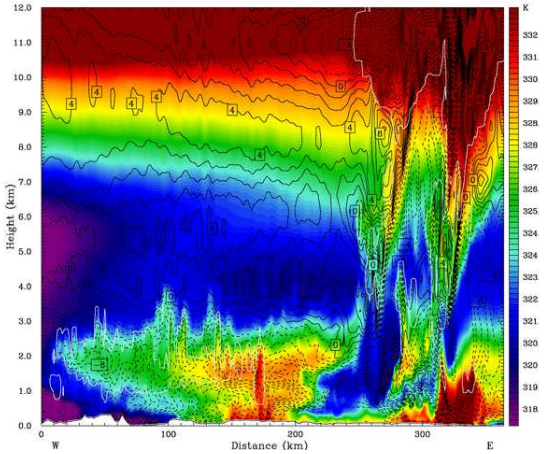

(B) 1600 UTC

FIGURE 3.20: As Figure 3.17 but for the y225 vertical section.

3.5.1.4 y175 vertical section

The y175 section was to the south of the y200 section that has been discussed in detail above in Section 3.5.1.1. The structure of the pre-convective environment along the y175 section was similar to that of the other sections. The values of θ_e in the elevated source layer were about 2 K greater than those along the y200 section. The RIJ descended, constricted the undercurrent and caused a wave to form at the top of the undercurrent at 0715 UTC (Figure 3.21a). The RIJ weakened and consisted of nearly horizontal mid-level inflow by 0900 UTC (Figure 3.21b). The RIJ remained nearly horizontal for the rest of the simulation. After the split of the original MCS at 1200 UTC, the y175 section passed through the southern system. The convection became surface based at about 1330 UTC. A gravity current formed at 1345 UTC and flowed into the high-valued θ_e air in the boundary layer (Figure 3.21c). Cloud formed above the gravity current, between 190 and 230 km.

3.5.1.5 y150 vertical section

The y150 section passed through the southern end of the simulated MCS (Figure 3.16). It did not pass through any regions of intense convection but nevertheless it revealed some important aspects of the interaction between the RIJ and the convective environment. The RIJ remained horizontal and did not descend (e.g. at 0730 UTC, Figure 3.22a). The undercurrent was not constricted under the MCS and there was no wave in the undercurrent and elevated source layer. This suggests that wave in the undercurrent in the rest of the MCS was caused by the descending RIJ constricting the undercurrent.

3.5.1.6 The along-line variability of the convective structures

The RIJ followed a continuum of behaviour along the MCS. In the north of the MCS it initially descended through the undercurrent to the surface and formed a gravity current. After this time the RIJ rose back above the undercurrent and did not descend to the surface again. The RIJ constricted the undercurrent and a wave formed at the top of the undercurrent. The convection remained elevated and the gravity current eventually dissipated. In the centre of the MCS the RIJ descended but did not penetrate through the undercurrent. This constricted the undercurrent and formed waves at the top of the

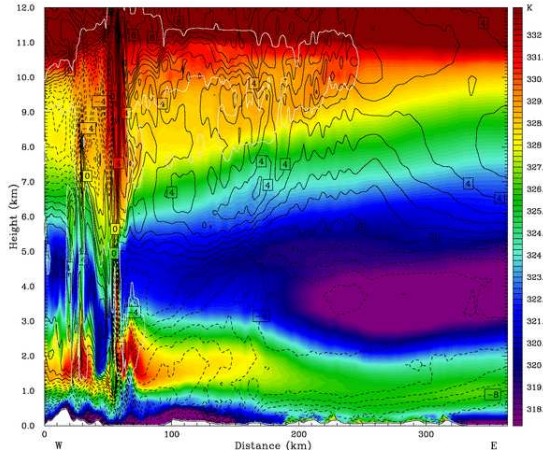

(A) 0715 UTC

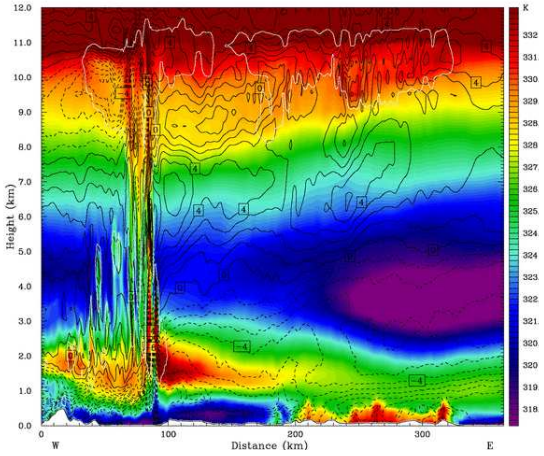

(B) 0900 UTC

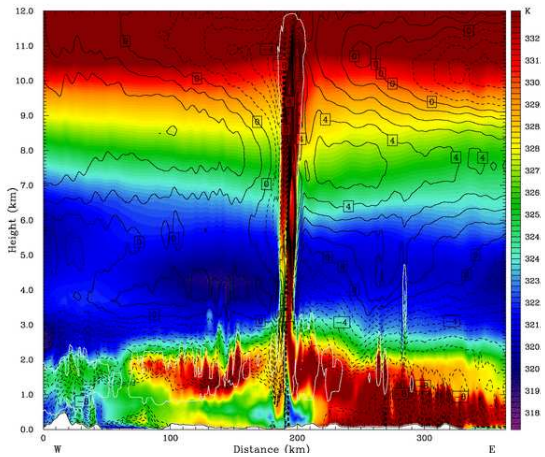

(C) 1345 UTC

FIGURE 3.21: As Figure 3.17 but for the y175 vertical section.

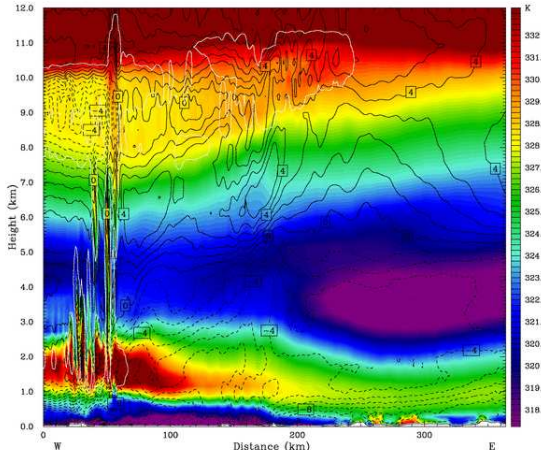

(A) 0730 UTC

FIGURE 3.22: As Figure 3.17 but for the y150 vertical section.

Section	Time of RIJ to surface (UTC)	Time of waves in elevated source layer (UTC)	Subsequent behaviour of RIJ	Time of transition to surface-based convection (UTC)	Time of gravity current in surface-based phase (UTC)
y250	1000	0815-1215	descended to surface at 1000 then remained elevated	1330	
y225		0800-1300	remained elevated	1330	
y200		0815-1230	remained elevated	1330	1345
y175		0715-0815	weakened and became horizontal	1330	1345
y150		no wave	remained horizontal	1330	

TABLE 3.2: Table showing the timing and along-line variability of the MCS and its near-environment in the WRF simulation of IOP 3.

undercurrent and in the elevated source layer. The waves lifted air in the elevated source layer to its level of free convection. In the south of the MCS the RIJ remained horizontal and did not descend. The undercurrent was not constricted in this region. No waves formed in the undercurrent or elevated source layer. This behaviour was different from MCS C. The RIJ associated with MCS C never penetrated to the surface and also never became horizontal. However, the radar observations of MCS C only provide information about its structure along one plane and were not able to provide information about the 3D structure of the convective system.

After the convection became surface-based there was no source of high-valued θ_e air in the north of the MCS. The inflow to the convection was further to the south. In the centre and south of the MCS a gravity current formed when the convection became surface-based. The gravity current lifted high-valued θ_e air from the boundary layer to its level of free convection. This behaviour differed from the observations. A gravity current was never observed in association with MCS C.

A summary of the timing and behaviour of the simulated MCS is shown in Table 3.2.

It is important to note that without analysing trajectories or using tracers it is not possible to tell with absolute certainty whether the simulated convection was elevated or surface-based. The presence of an elevated layer of high-valued θ_e (or an elevated layer with high-valued CAPE) is a strong indication of elevated convection, but strong surface outflow may be able to lift surface-based parcels with low CAPE to their level of free convection even in the presence of an elevated unstable layer. Purely elevated and purely surface-based convection represent the extreme ends of a continuous spectrum of behaviour. There is also a temporal aspect to the definition; air parcels in an elevated layer of high-valued θ_e may have originated from the boundary layer several hours earlier. The dynamically significant aspect of elevated convection is the presence of a low-level stable layer and the associated potential for features such as waves and bores (e.g. Marsham *et al.*, 2011) to provide a lifting mechanism for the convection. The wave-lifted MCS in this simulation moved through an elevated layer of high-valued θ_e to a region with high values of θ_e at low levels. After this time a gravity current formed and lifted air from the boundary layer to its level of free convection. The change in lifting mechanism from the wave to the gravity current clearly coincided with the change in system velocity discussed in Section 3.3. Tracers or trajectory analysis to determine the origin of the air in the convection has not been performed as it would not add significant further insight into the dynamics of the simulated MCS.

3.5.2 The cloud-scale structure of the MCS and the effects of microphysical processes

The analysis of the structure and evolution of the simulated MCS presented in Section 3.5 revealed that there was along-line variability in the behaviour of the RIJ. The cloud-scale structure of the simulated MCS and the interaction between the RIJ and microphysical processes are investigated in this Section. A series of vertical sections were made through the MCS. One of these went through the centre of the storm, where the RIJ was well-developed but did not reach the surface, and closely followed the y200 line shown in Section 3.5. The other line was to the north of the central line, where the RIJ reached the surface, and closely followed the y225 line shown in Section 3.5.

3.5.2.1 Central region of the MCS

The front edge of the RIJ descended under the cloud and reached z=1 km at 0715 UTC (Figure 3.23a). Behind the main MCS, two updraughts penetrated the RIJ, at 25 and 35 km (Figures 3.23a and 3.23b). There were two maxima in the horizontal wind speed in the RIJ. One was centred at z=5.3 km at 50 km (Figure 3.23a) and had a maximum system-relative speed of 7 m s^{-1}. Air in the maximum descended at about 2 m s^{-1} (Figure 3.23b). The position of the maximum corresponded to the RIJ entering the back (western) edge of the main MCS under the stratiform region where there was snow and graupel at 50 km (Figure 3.23c). The second maximum in the horizontal wind speed was centred at z=1.4 km at 58 to 61 km and had a magnitude of 5 m s^{-1} (Figure 3.23a). There was a 3 m s^{-1} downdraught at the rear of the maximum (Figure 3.23b), showing that this air was flowing RTF. The second RIJ maximum was associated with a maximum rain mixing ratio of 1.25 g kg^{-1} beneath the liquid convective cloud (Figure 3.23c). The main updraught in the MCS was located just above the front edge of the second RIJ maximum. The updraught had a magnitude of about 2 m s^{-1} (Figure 3.23b). There was a wave in the high-valued θ_e elevated source layer ahead of the main updraught and the descending RIJ at 65 km (Figure 3.23a). Air in the wave ascended at 2.5 m s^{-1} (Figure 3.23b). Although most of the convective cloud was composed of snow, ice and graupel, the cloud associated with the wave was liquid (Figure 3.23c). Graupel fell through the wave and its associated cloud (Figure 3.23c). The base of the convective cloud was at z=2.8 km. The base of the liquid cloud associated with the wave was at z=1.6 km.

The RIJ was intersected by a region of system-negative flow between 63 and 68 km at 0745 UTC (Figure 3.24a). The system-negative flow descended at about 5 m s^{-1}. The origin of this flow may have been air that ascended in the wave but did not undergo convection and left the wave to the rear of the MCS. The RIJ descended beneath the cloud between 65 and 80 km at 0745 UTC (Figure 3.24a). A significant amount of precipitation fell through this region. A maximum value of rain mixing ratio of 1.65 g kg^{-1} was located behind the MCS at z=2.3 km at 67 km. Figures 3.24a, 3.24b and 3.24c suggest that cooling due to the evaporation of rain caused a region of relatively strong descent to develop. This will be studied later in Chapter 4. Under the descending RIJ the undercurrent was constricted to about z=500 m. The main updraught in the MCS was neither particularly

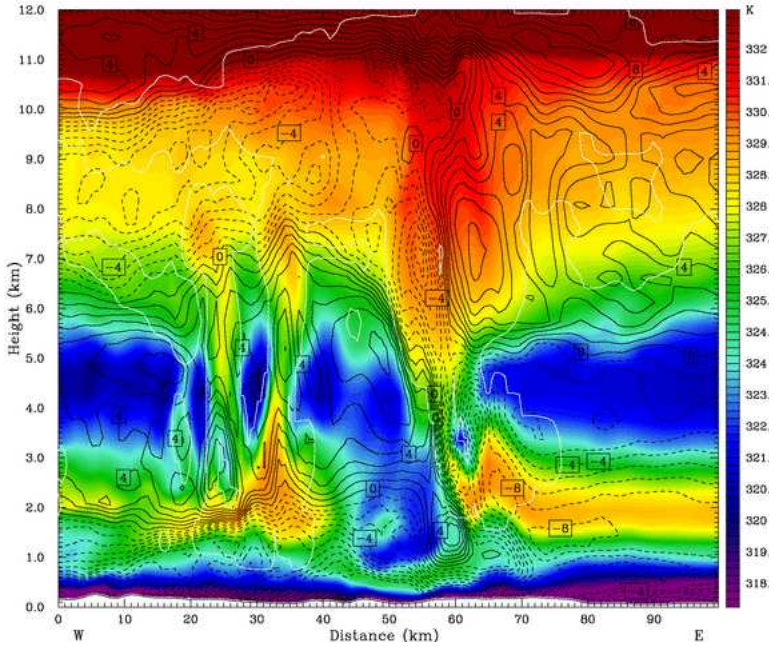

(A) θ_e (K, colour contour), system-relative winds (m s^{-1}, solid black line contour showing positive system-relative winds and dashed black line contour showing negative system-relative winds) and a single contour of total cloud mixing ratio (5x10^{-3} g kg^{-1}, white line contour).

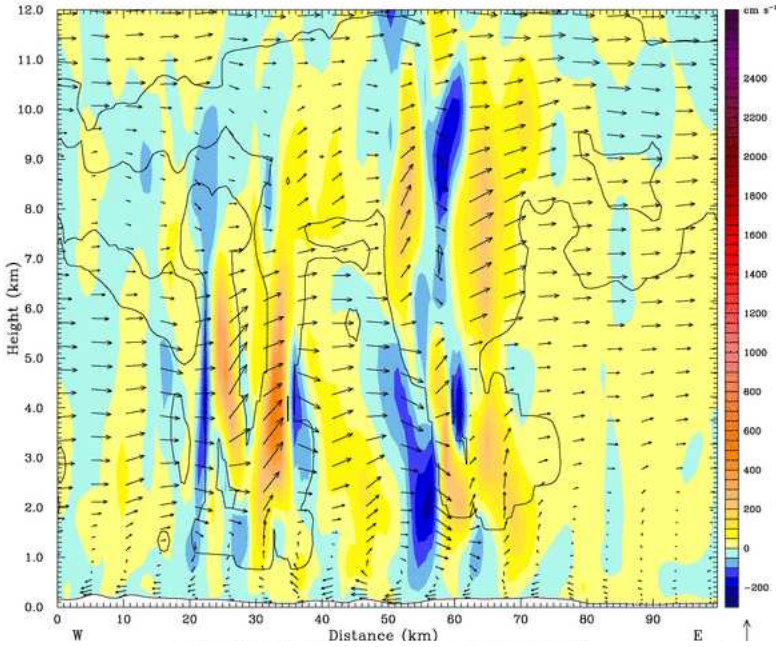

(B) Vertical velocity (m s^{-1}, colour contour), circulation vectors (not system-relative) and a single contour of total cloud mixing ratio (5x10^{-3} g kg^{-1}, black line contour).

FIGURE 3.23: a-b: Central section, 0715 UTC.

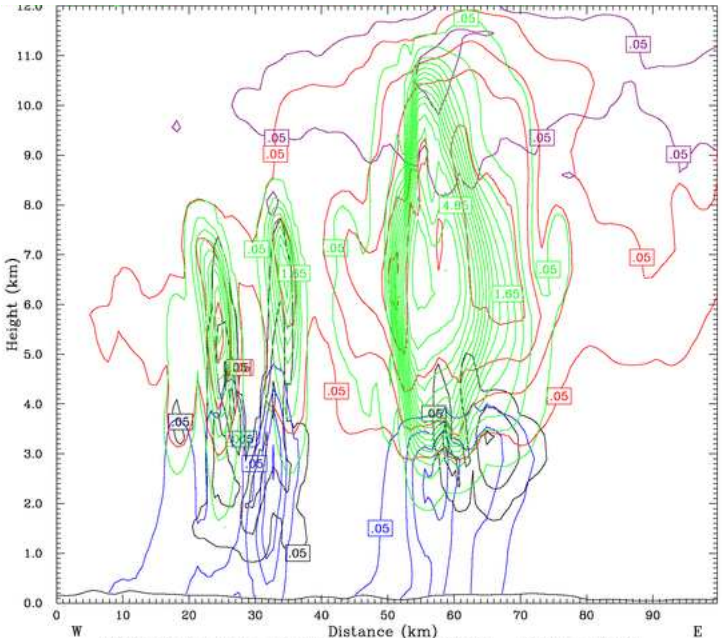

(c) Contours of hydrometeor mixing ratios (g kg^{-1}, contour interval 0.4 g kg^{-1}): cloud water (black), cloud ice (purple), snow (red), graupel (green) and rain (blue).

FIGURE 3.23: c: Central section, 0715 UTC.

strong at 0745 UTC, having a maximum of about 7 m s^{-1}, nor particularly deep, reaching z=7 km.

There were two maxima in the horizontal wind speed in the RIJ at 0745 UTC. One was between z=3.7 and z=5.2 km at 53 to 58 km and had a maximum system-relative speed of 6 m s^{-1} (Figure 3.24a). The maximum was associated with the acceleration of the RIJ under the back edge of the main MCS where it encountered a region of snow and falling graupel (Figure 3.24c). The second horizontal wind speed maximum was at z=1.5 km between 70 to 75 km and had a maximum system-relative speed of 4 m s^{-1} (Figure 3.24a). The maximum horizontal wind speed was associated with a maximum rain mixing ratio of 1.65 g kg^{-1} at 67 km (Figure 3.24c). The base of the convective cloud was at 1.3 km beneath the main updraught.

Waves formed in the elevated source layer ahead of the descending RIJ by 0815 UTC (see e.g. Table 3.2 in Section 3.5). There were peaks in the elevated high-valued θ_e source layer in Figure 3.25a at 62, 67, 73, 80 and 85 km. Air in the waves ascended at about 0.5 m s^{-1} (Figure 3.25b). Cloud formed on the wave peak at 62 km and had a small amount of rain (0.05 g kg^{-1}) associated with it. The main upright updraught in the MCS was at

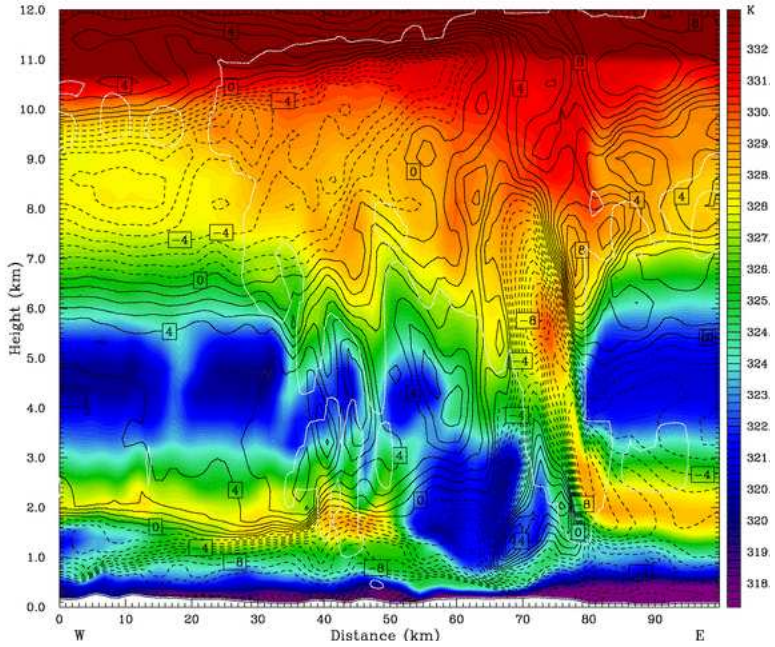

(A) As Figure 3.23a.

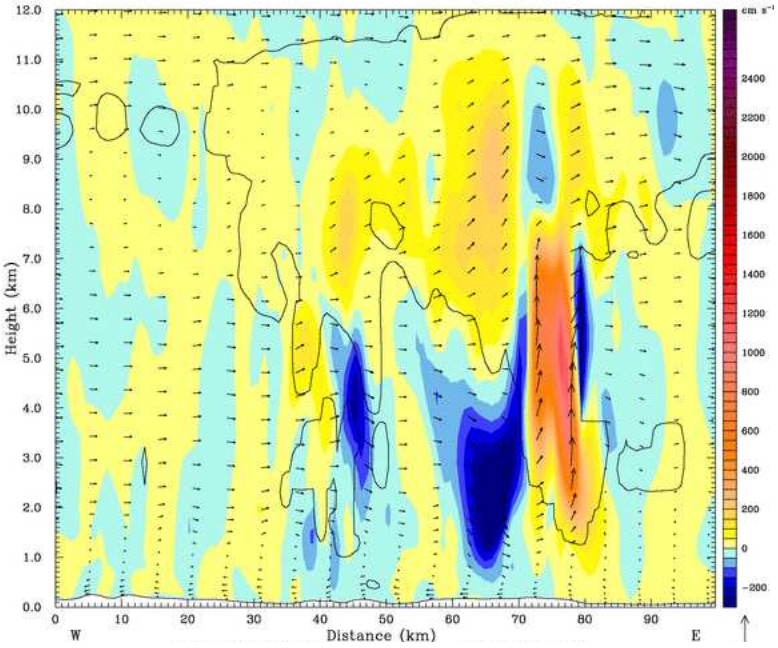

(B) As Figure 3.23b.

FIGURE 3.24: a-b: Central section, 0745 UTC.

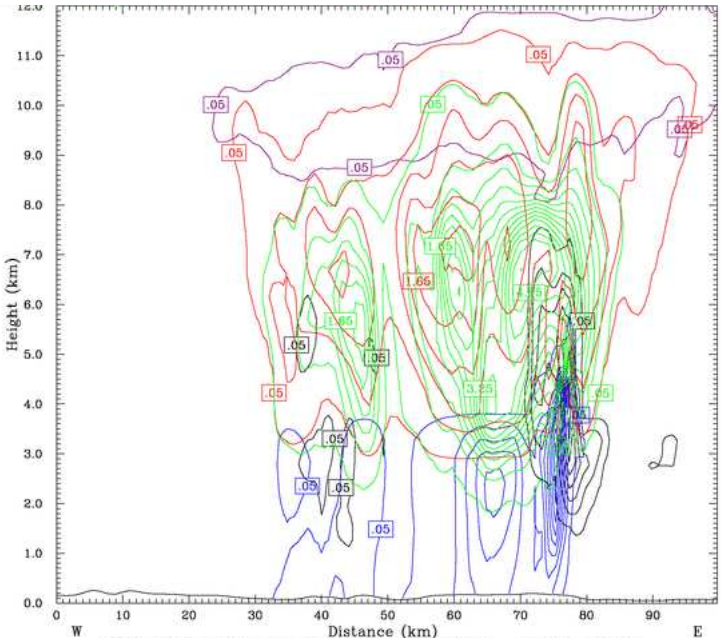

(c) As Figure 3.23c.

FIGURE 3.24: c: Central section, 0745 UTC.

56 km (Figure 3.25b). It was weaker than it was at this location at 0745 UTC with a maximum of about 4 m s^{-1}. It was also weaker than the updraught of 12 m s^{-1} located at about 28 km. However, it was considerably deeper than 30 minutes before, reaching z=12 km. The region of descent behind and beneath the cloud at 50 km (Figure 3.25b) had a similar strength of 5 m s^{-1} to that at 0745 UTC, but comparison of Figures 3.24b and 3.25b shows that the region was narrower at this location and time. The region of descent corresponded to the RIJ (Figure 3.25a), which reached z=1 km and was undercutting the convective cloud. There was rain between 27 and 68 km (Figure 3.25c). There were two maxima in the horizontal wind speed in the RIJ at 0815 UTC (Figure 3.25a). One was at z=1.5 km at 53 km and had a maximum system-relative speed of 7 m s^{-1}. The horizontal wind speed maximum corresponded to a maximum in rain mixing ratio of 1.25 g kg^{-1} (Figure 3.25c). The other horizontal wind speed maximum in the RIJ of 8 m s^{-1} was at 3.7 km at z= 33 km (Figure 3.25a). This corresponded to the RIJ entering the back of the MCS and under the stratiform region where there was graupel and snow.

The stratiform region, consisting mainly of snow particles and graupel, extended to about 25 km at z=5 km. There was strong inflow from z=3.5 to z=6 km (Figure 3.25a). However, the picture is complicated. Figure 3.25c indicates that there was a convective cloud with strong updraughts and significant graupel embedded within the stratiform region at 28 km,

intercepting the RIJ. The RIJ (region of low-valued θ_e) descended just after the convective clouds, on average from z=4.5 to z=2.5 km in a distance of about 12 km. The horizontal wind speed was about 8 m s^{-1} and the vertical wind speed about 1 m s^{-1}, so the angle of descent (about 7°) is consistent. Interestingly, at least in this location, the low-valued θ_e air then ascended to z=3.5 km. This lifting also formed a small, surface-based cloud at 55 km. The RIJ then experienced a 3-4 m s^{-1} downdraught at 52 km and the low-valued θ_e air descended to z=1.5 km. The downdraught is likely to have been produced by the rain (Figure 3.25c) and melting graupel.

The vertical sections shown in Figure 3.26 intersected a region of strong convection at 0945 UTC. There were two horizontal wind speed maxima in the RIJ (Figure 3.26a). One was at z=2.0 km at 59 km and had a horizontal wind speed of 8 m s^{-1}. The other was at z=1.6 km at 67 km and had a horizontal wind speed of 4 m s^{-1}. Both horizontal wind speed maxima were associated with local maxima in the rain mixing ratio (Figure 3.26c). It is not clear from Figure 3.26 whether there was a horizontal wind speed maximum associated with the RIJ passing under the back edge of the stratiform region. The RIJ did not reach the surface and remained elevated throughout the rest of the simulation at this location. Within the RIJ there were cloudy regions of higher-valued θ_e at 35, 43 and 47 km at 0945 UTC (Figure 3.26a) which were associated with maxima in the graupel mixing ratio (Figure 3.26c) and downdraughts of about 2 m s^{-1} (Figure 3.26b). The strongest updraught in the cloud was at 68 km and reached z=12 km (Figure 3.26b). The stratiform cloud extended for 25 km behind the convection. Most of the stratiform cloud was composed of snow, graupel and ice. The base of the convective cloud was about z=1.6 km (Figure 3.26c). The lower cloud base in this region could have been due to moistening from precipitation. The convective cloud contained liquid water and graupel, as well as ice particles and snow at the upper levels (Figure 3.26c). There was evidence of significant rain at z=4 km, but the rain at the ground was relatively light at this time and location.

The MCS was in the transition to becoming surface-based at 1315 UTC (Section 3.5). The RIJ began to weaken in this location at this time (Figure 3.27a). There were two maxima in the horizontal wind speed. One was at z=4.2 km at 35 km and corresponded to the RIJ crossing under the back edge of the stratiform region where graupel and snow mixing

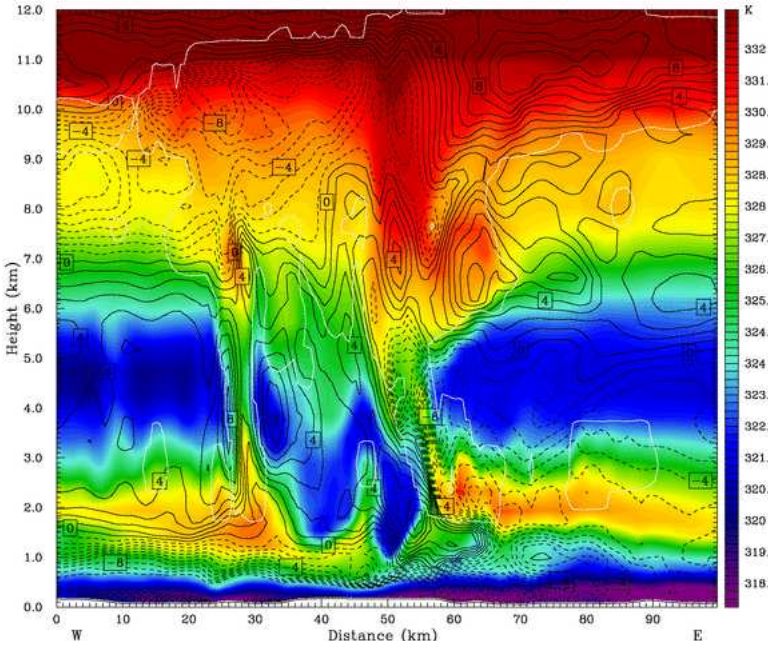

(A) As Figure 3.23a.

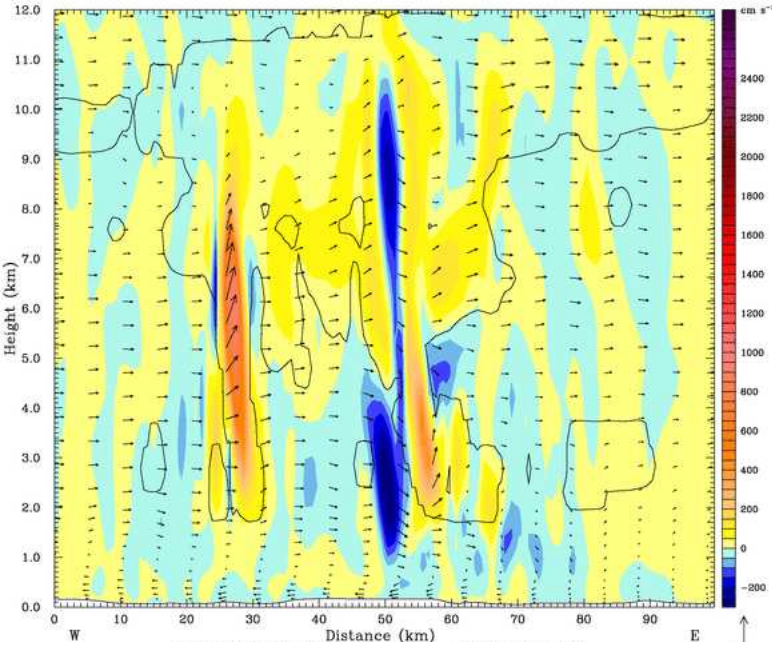

(B) As Figure 3.23b.

FIGURE 3.25: a-b: Central section, 0815 UTC.

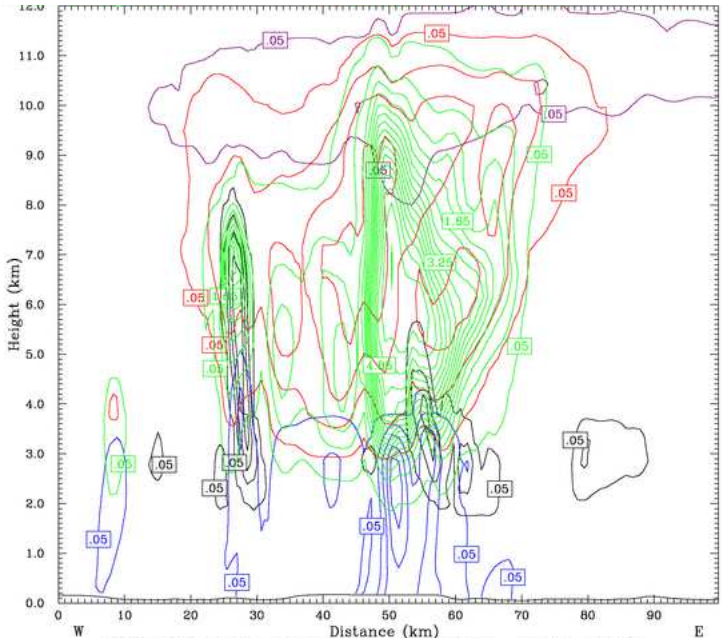

(c) As Figure 3.23c.

FIGURE 3.25: c: Central section, 0815 UTC.

ratios were about 1.65 and 0.05 g kg^{-1}, respectively (Figure 3.27c). The other horizontal wind speed maximum was at z=2.7 km at 43 km and corresponded to a maximum in rain mixing ratio of 0.85 g kg^{-1}. The RIJ remained elevated above the low-level undercurrent. The cloud was about 30km wide at this location, considerably narrower than at previous times. The base of the convective cloud was at about z=3 km (Figure 3.27c). Ahead of the MCS, between 55 and 85 km there was a region of liquid cloud that had a cloud base at z=1.0 km and which extended to z=5.5 km (Figure 3.27c). The liquid cloud formed in the region where the surface-based high-valued θ_e air began to mix with the elevated high-valued θ_e air (Figure 3.27a). Thus it is likely that the lower, liquid cloud was associated with the transition of the system to surface-based convection, when near-surface air parcels began to be lifted. There were updraughts of up to 6 m s^{-1} in the liquid cloud, at 60 and 65 km in Figure 3.27b.

In summary, there were two horizontal wind speed maxima in the RIJ in the central region of the MCS. One was associated with the acceleration of the RIJ under the stratiform region where it encountered snow and falling graupel, the melting of which cooled the air in the RIJ and strengthened its descent. The RIJ then descended gradually through the stratiform region. When the RIJ reached the convective region it tended to encounter a maximum in rain mixing ratio, which was associated with another horizontal wind speed

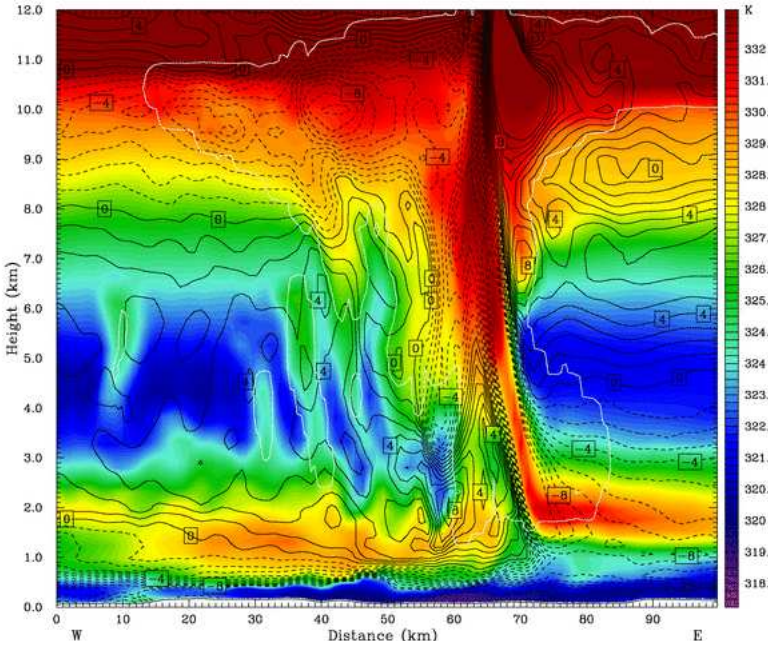

(A) As Figure 3.23a.

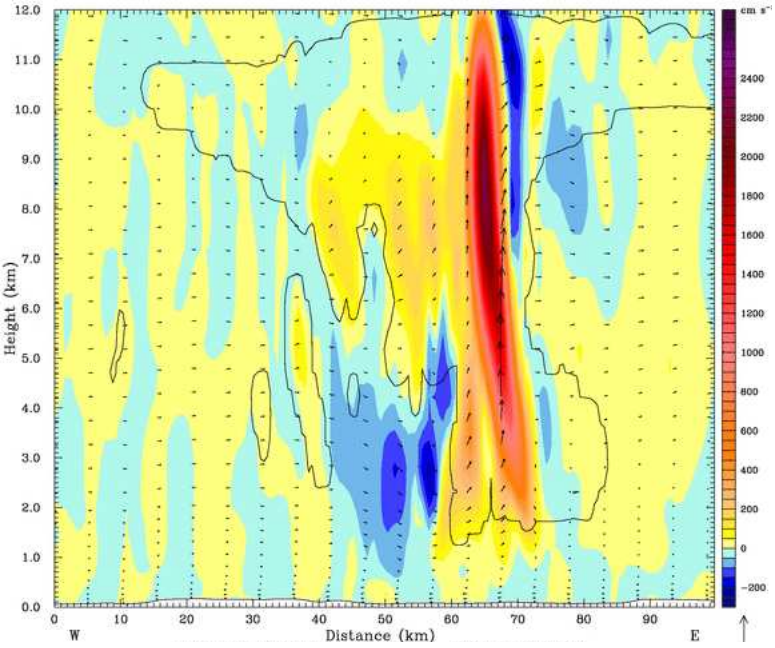

(B) As Figure 3.23b.

FIGURE 3.26: a-b: Central section, 0945 UTC.

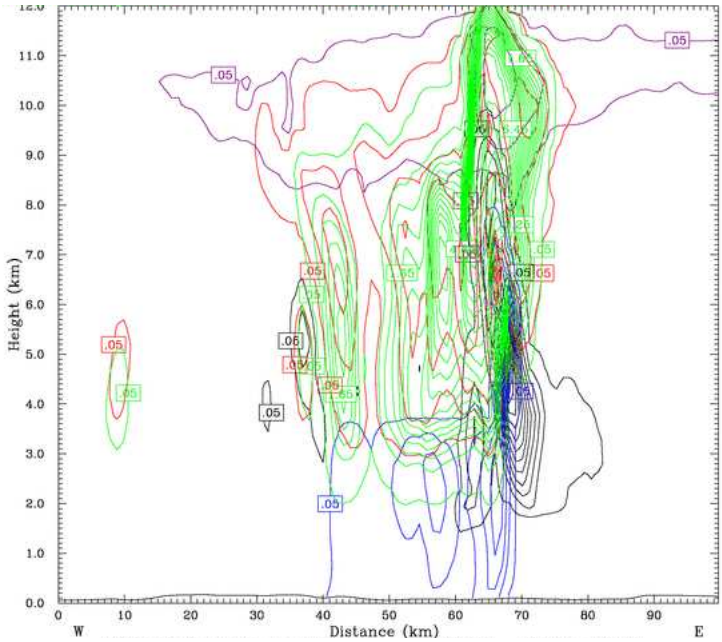

(c) As Figure 3.23c.

FIGURE 3.26: c: Central section, 0945 UTC.

maximum in the RIJ. Along the central region of the MCS, the cooling associated with the microphysical processes was not sufficient to cause the RIJ to penetrate through the low-level stable undercurrent. The RIJ remained elevated along this region. The RIJ generated a wave at the top of the undercurrent and in the elevated high-valued θ_e source air ahead of the storm. Liquid cloud formed on this wave. The convective cloud consisted almost entirely of snow, graupel and ice. As the MCS became surface-based, the convective cloud base became lower. The cloud along the central section became considerably narrower over time. This may have had a significant impact on the behaviour of the RIJ, exposing it to less cooling by melting as it passed through the narrower stratiform region.

3.5.2.2 Northern region of the MCS

The analysis of the structure and evolution of the simulated MCS presented in Section 3.5.1 showed that in the north of the convective system the RIJ descended through the low-level stable undercurrent to the surface, whereas in the centre and to the south it did not reach the surface. The two horizontal wind speed maxima in the RIJ were found in Section 3.5.2.1 to correspond to local maxima in graupel and snow mixing ratios in the stratiform region and a maximum in rain mixing ratio near the convective region. It is

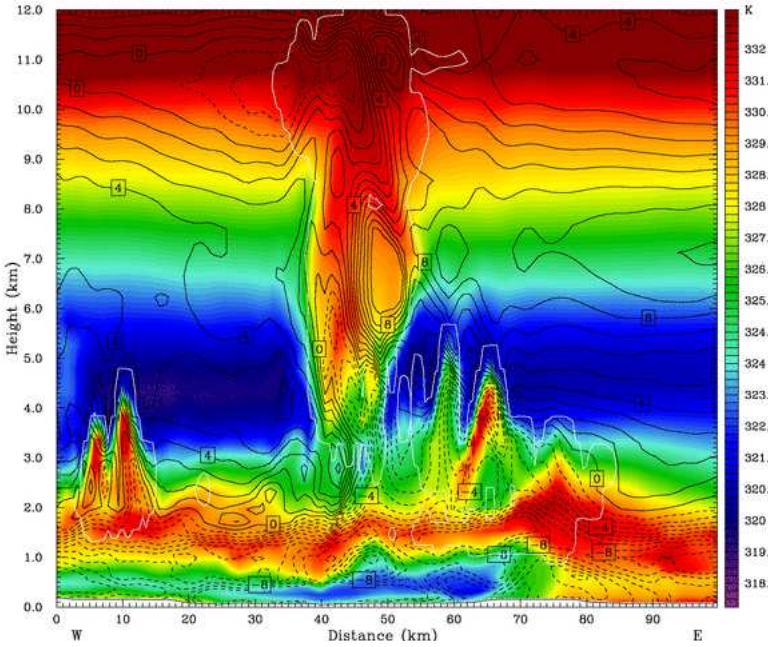

(A) As Figure 3.23a.

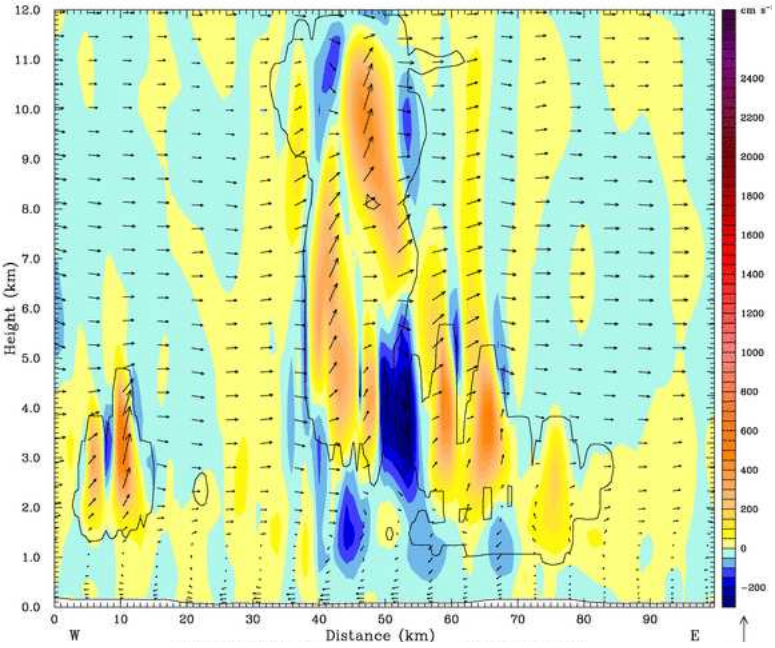

(B) As Figure 3.23b.

FIGURE 3.27: a-b: Central section, 1315 UTC.

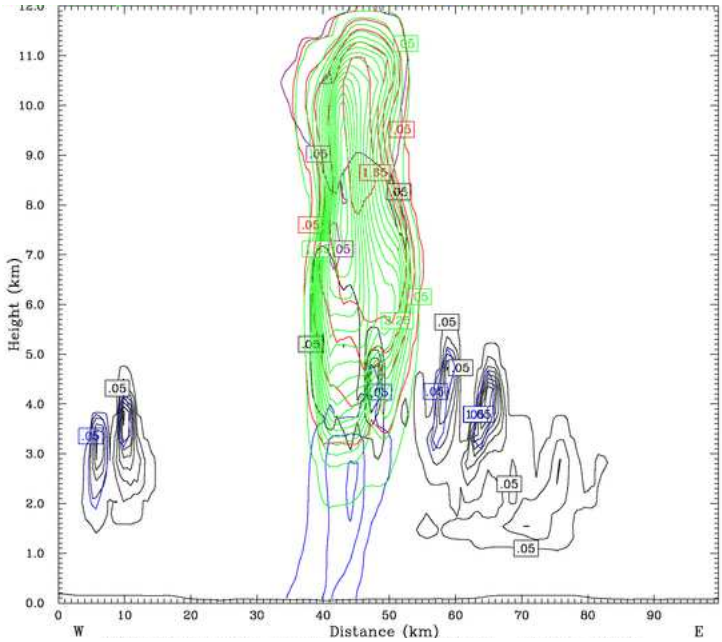

(c) As Figure 3.23c.

FIGURE 3.27: c: Central section, 1315 UTC.

therefore of interest to investigate whether a difference in microphysics in the north of the system caused the RIJ to descend to the surface.

There were two maxima in the horizontal wind speed in the northen section of the MCS at 0745 UTC. One was at z=3.5 km at 38 km and had a maximum horizontal wind speed of 10 m s^{-1} (Figure 3.28a). The horizontal wind speed maximum corresponded to the RIJ entering a region in the back edge of the stratiform region where there was a significant amount of graupel falling. There was maximum in the graupel mixing ratio of 1.65 g kg^{-1} at 40 km (Figure 3.28c) which was associated with a downdraught of 1.5 m s^{-1} (Figure 3.28b). The other horizontal wind speed maximum in the RIJ was at z=1.6 km at 65 km and had a maximum horizontal wind speed of 11 m s^{-1} (Figure 3.28a). The horizontal wind speed maximum occurred just ahead of a maximum in rain mixing ratio of 1.65 g kg^{-1} at z=2.4 km at 58 km (Figure 3.28c). A downdraught of 4 m s^{-1} occurred at the location of the rain mixing ratio maximum (Figure 3.28b). The RIJ did not descend to the surface at 0745 UTC, but began descending under the stratiform region at about 40 km (Figure 3.28a) and reached z=750 m between 60 and 78 km. Ahead of the RIJ there was a wave in the elevated high-valued θ_e source layer. There were peaks in θ_e at 72 and 77 km (Figure 3.28a). The wave peaks were associated with updraughts of about 4 m s^{-1} (Figure 3.28b). Liquid cloud formed on the waves (Figure 3.28c). The convective cloud

mostly consisted of graupel, ice and snow in the northern region of the MCS at 0745 UTC. The extent of the cloud was about 80 km at this time and at this location.

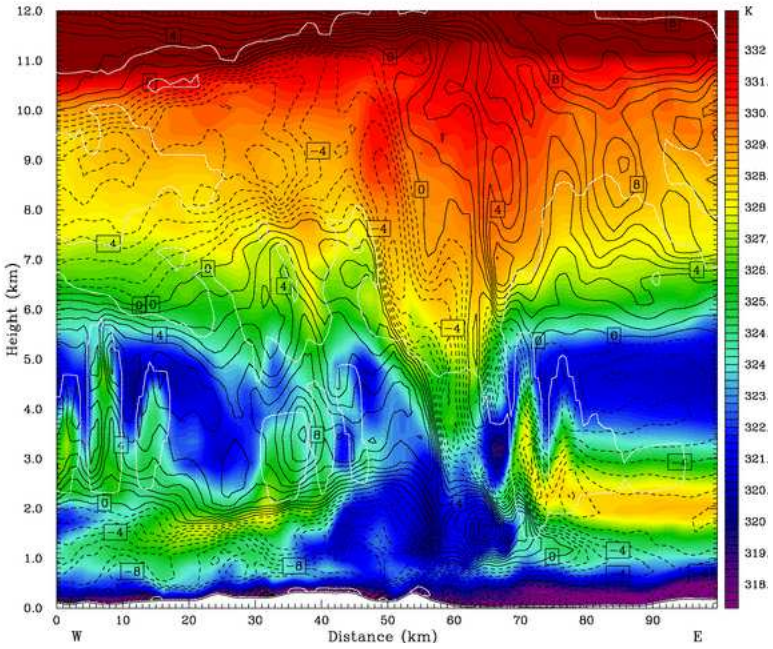

(A) As Figure 3.23a.

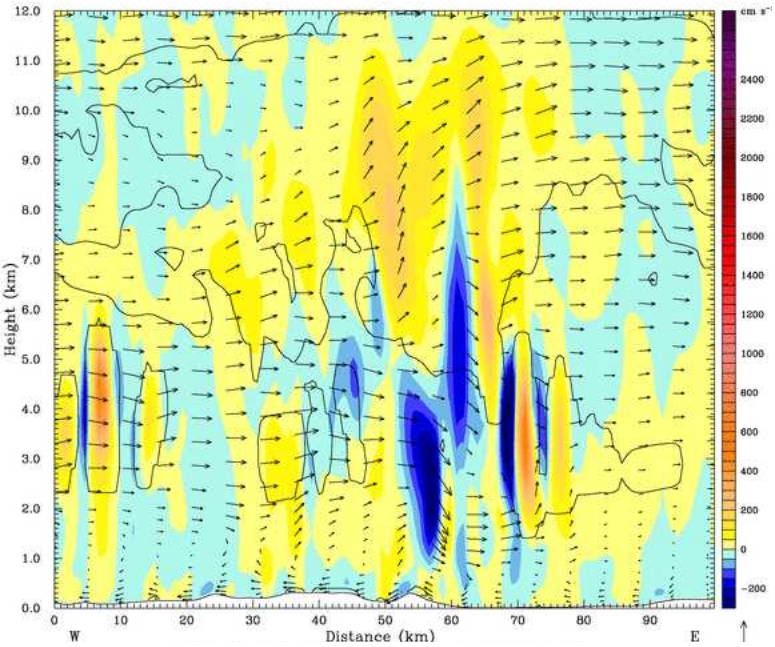

(B) As Figure 3.23b.

FIGURE 3.28: a-b: Northern section, 0745 UTC.

The descending RIJ reached the surface at 77 km at 1245 UTC in the northern region of the MCS (Figure 3.29a). A significant amount of rain fell through the RIJ at this

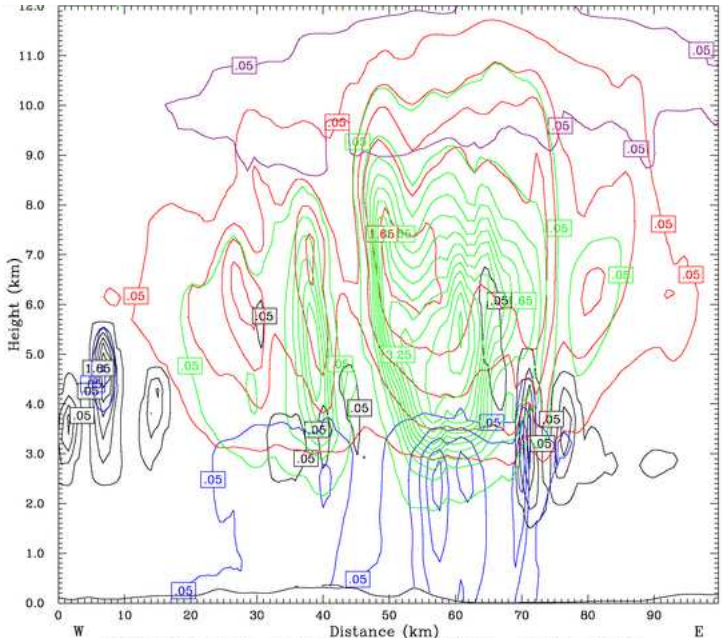

(c) As Figure 3.23c.

FIGURE 3.28: c: Northern section, 0745 UTC.

time. There was a maximum in the rain mixing ratio of more than 3.22 g kg^{-1} at 78 km (Figure 3.29c). Above the region where the RIJ penetrated to the surface, and underneath the intense rain, there was a maximum in the horizontal wind speed in the RIJ of 10 m s^{-1} (Figure 3.29a). Above and just ahead of the region where the RIJ penetrated to the surface there was an updraught of more than 4 m s^{-1} (Figure 3.29b). The updraught lifted air from the elevated layer of high-valued θ_e into the MCS (Figure 3.29a). The extent of the cloud was about 45 km at this time and at this location. The convective cloud consisted mostly of snow, graupel and ice at 1245 UTC. The base of the convective cloud was at z=2.3 km. In the updraught ahead of the RIJ there was a liquid cloud which had a base at z=1.3 km. There was a second horizontal wind speed maximum of 8 m s^{-1} in the RIJ at z=4.0 km at 54 km (Figure 3.29a). The horizontal wind speed maximum corresponded to a region where the RIJ entered the back edge of the stratiform region and encountered graupel mixing ratios of up to 1.25 g kg^{-1} (Figure 3.29c).

In summary, there were also two horizontal wind speed maxima in the RIJ in the northern region of the MCS. Like the central section, one was associated with the acceleration of the RIJ across the back edge of the stratiform region where it encountered snow and falling graupel. It is probable that the cooling associated with the snow and graupel in this region strengthened the descent of the RIJ. The second horizontal wind speed maximum

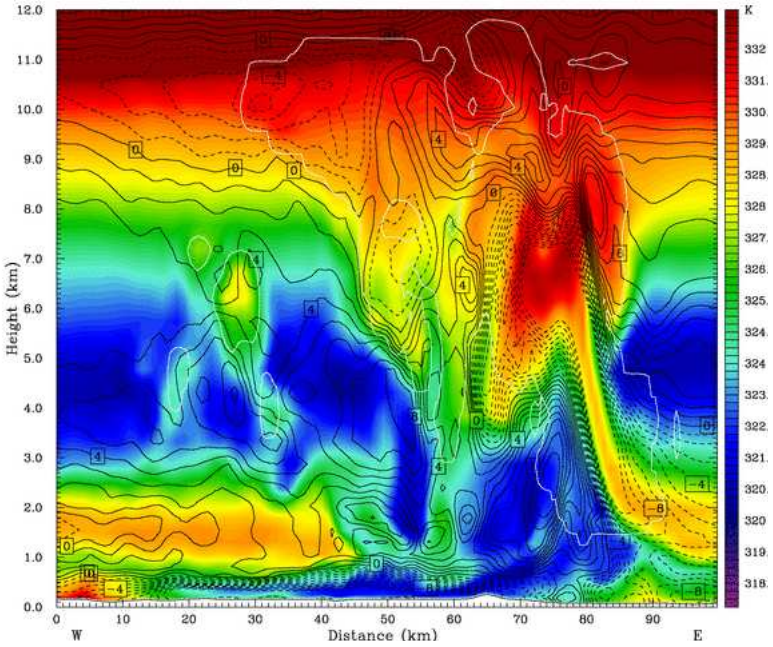

(A) As Figure 3.23a.

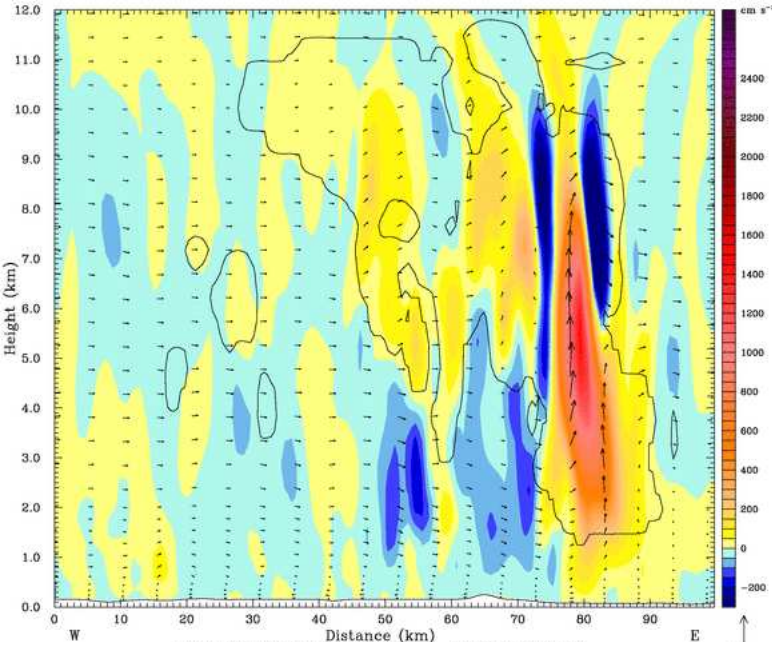

(B) As Figure 3.23b.

FIGURE 3.29: a-b: Northern section, 1245 UTC.

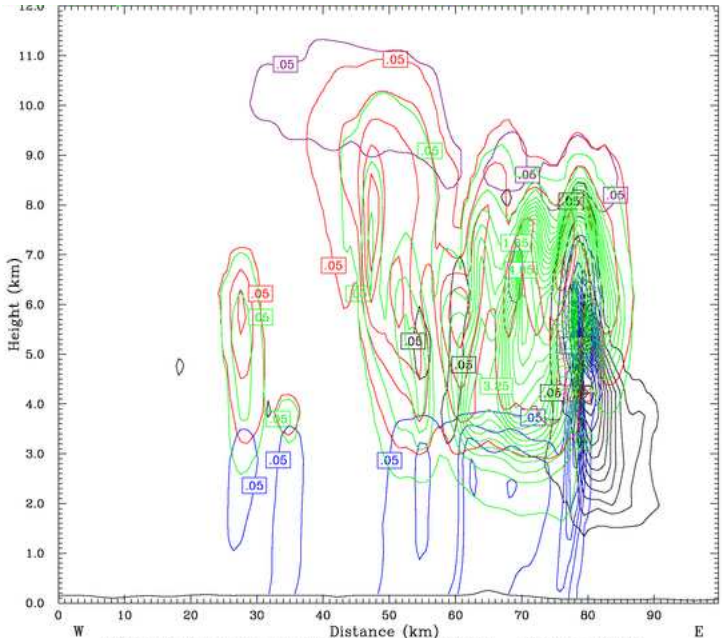

(c) As Figure 3.23c.

FIGURE 3.29: c: Northern section, 1245 UTC.

in the RIJ was associated with a maximum in the rain mixing ratio and was probably caused by cooling associated with the rain. In the northern region of the MCS the cloud did not narrow as much as it did in the central region. The RIJ was able to penetrate to the surface. The wider cloud may have strengthened the RIJ by exposing it to cooling for a longer period. The rain mixing ratios in the northern region of the MCS were also considerably larger than those in the central region. This also may have contributed to the strengthening of the RIJ in the north by exposing it to more cooling. The combined effects of the increased cooling in the northern region of the MCS may have strengthened the RIJ enough for it to be able to penetrate through the low-level undercurrent to the surface.

3.5.2.3 Summary of the cloud-scale structure of the MCS and the effects of microphysical processes

Two horizontal wind speed maxima in the RIJ were observed throughout the MCS. One maximum occurred when the RIJ entered the stratiform region at the back of the MCS. The cooling associated with graupel and snow in this region strengthened the descent of the RIJ. The other horizontal wind speed maximum occurred in the convective region where there was intense rainfall. Here the cooling associated with the rain strengthened

the descent of the RIJ. Microphysical processes were more vigorous in the northern region of the simulated MCS, where the cloud was wider. The RIJ penetrated to the surface in this region. The wider cloud with more intense rain meant that the RIJ was exposed to cooling over a larger region, and thus it was strengthened. The stronger RIJ was able to penetrate through the undercurrent and descend to the surface.

Where the RIJ did not descend to the surface it caused a wave at the top of the undercurrent and in the elevated high-valued θ_e source layer of ahead of the MCS. A positive feedback process may exist which strengthens the RIJ: the RIJ is initially unable to penetrate the low-level stable layer and causes a wave to form at the top of the undercurrent. The wave lifts the elevated high-valued θ_e air and causes a new convective updraught to develop. The strength of the updraught depends on the instability of the elevated source layer and the amount of lifting provided by the wave. A strong updraught will lead to vigorous microphysical processes which can strengthen the RIJ by cooling.

One possible outcome of this positive feedback process is that the RIJ is strengthened sufficiently enough that it can penetrate the low-level stable layer and reach the surface. In the case of elevated convection, this could eventually lead to the system becoming surface-based and gravity current-lifted. However, in the simulated MCS analysed in this Chapter the transition from elevated to surface-based convection did not depend on the RIJ reaching the surface but instead was caused by the MCS propagating through the elevated region of high-valued θ_e air to a region where a combination of surface heating and advection had increased the values of θ_e in the boundary layer.

3.6 The effect of the gravity current on the simulated MCS

The results discussed above showed that the simulated MCS formed a gravity current outflow in the later stage of its lifetime, when the convection became surface-based. It is known that lifting at the gust front of a gravity current can initiate deep convection (e.g. Lin *et al.*, 1998). RKW theory (Rotunno *et al.*, 1988; Weisman and Rotunno, 2004) states that an optimal state for the maintenance of deep convection in a shear environment exists when the strength of the cold pool is balanced by the shear. RKW theory has been described in Section 1.5.1. The pre-convective environment was characterised by strong

shear: the flow at low-levels was towards the MCS, while that at mid- and upper-levels was away from the MCS. When the simulated MCS developed a gravity current the system velocity of the storm increased from (6.4±1.3) m s^{-1} to (10.3±1.3) m s^{-1}. It is therefore of interest to see whether the RKW optimal state criteria were met. RKW theory says that the optimal state for upright convection occurs when the ratio of the gravity current speed to the shear in the lowest 5 km, $c/\Delta u$, is between 1 and 1.5.

In calculating the cold pool buoyancy for use in Equation 1.1 (in Section 1.5), it was noted that the air was not saturated at low levels, either inside or ahead of the gravity current, so the contribution from the condensate could be ignored. The virtual potential temperature, θ_v, is given by $\theta_v = \theta\,(1 + 0.61q)$, where q is the water vapour mixing ratio. The water vapour mixing ratio inside the gravity current was the same as that in the environment, so when calculating θ'_v the q term could be ignored, and the value of θ_v could be assumed to be the same as θ. Equation (1.1) was therefore reduced to:

$$c^2 = -2g \int_{z=0}^{z=H} \frac{\theta'}{\overline{\theta}} dz. \tag{3.1}$$

The gravity current formed in the centre of the simulated MCS (Figure 3.17). The depth of the gravity current at 1330 UTC was about 650 m (Figure 3.30). The potential temperature perturbation between the gravity current and the environment ranged between 4 and 7 K, depending on the height at which it was defined. The environmental potential temperature was between 298 and 299 K. These values gave a range of gravity current strengths, c, from 13.1 to 17.3 m s^{-1}. The vertical shear of the horizontal velocity in the lowest 5 km was 13 m s^{-1} (Figure 3.30). This gave a range of $c/\Delta u$ values from 1.3 to 1.0. This was consistent with the "optimal state" criteria of Weisman and Rotunno (2004) for deep lifting at the leading edge of the gravity current and indicated that the ratio of the gravity current strength to the environmental shear was optimal for the maintenance of deep convection.

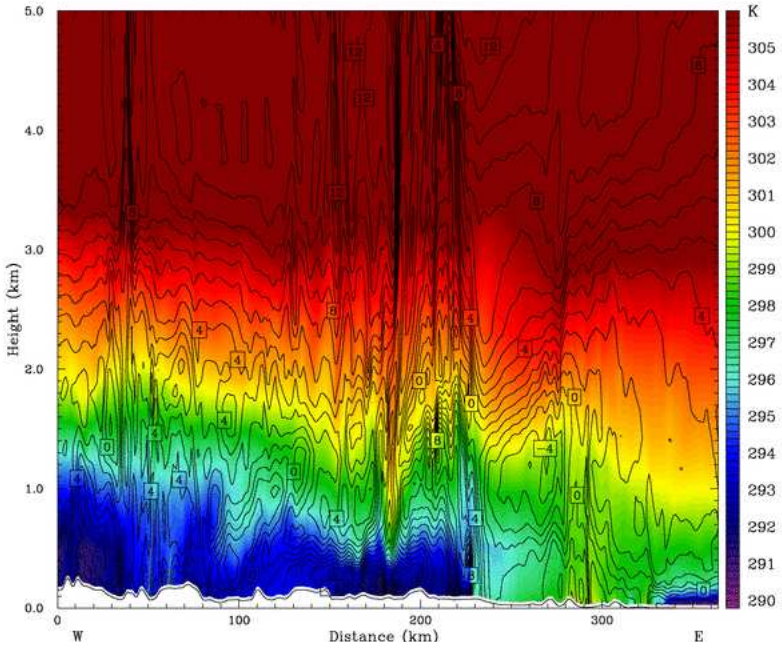

FIGURE 3.30: Vertical section taken through the inner domain (1 km horizontal resolution) of the model along the line labelled y200 in Figure 3.16, showing θ (K, colour contour) and system-relative winds (m s^{-1}, solid black line contour showing positive system-relative winds and dashed black line contour showing negative system-relative winds) at 1330 UTC.

3.7 The rôle of surface fluxes in the evolution of the convection

The analysis of the vertical structure of the simulated MCS and its pre-convective environment discussed in Section 3.5.1 showed that the transition from elevated to surface-based convection occurred when the convective system moved through the elevated layer of high-valued θ_e air into a region where the values of θ_e in the boundary layer air had increased considerably. The transition to surface-based convection began when the high-valued θ_e boundary layer air became incorporated by some means into the elevated inflow, and was complete when the inflow was sourced entirely from the boundary layer. The transition from elevated to surface-based convection completed at about 1330 UTC and was accompanied by the development of a gravity current and an increase in system velocity (discussed previously in Section 3.3). This Section discusses the rôle of the surface sensible and latent heat fluxes in controlling the transition from elevated to surface-based convection.

3.7.1 The surface latent heat flux

A Hovmöller diagram of the latent heat flux at the surface, made west-east through the y-280 point, is shown in Figure 3.31. The values of the surface latent heat flux began to increase at 0700 UTC, which was associated with the start of solar heating after sunrise in the model. This was consistent with the time when values of θ_e began to increase at low-levels in the east of the domain (Figure 3.17a). Note that due to the interpolation of model data along the vertical sections in Section 3.5.1 the horizontal distance scale in Figure 3.17a does not have a one-to-one correspondence with the horizontal distance scale in Figure 3.31. The maximum value of the surface latent heat flux was about 400 W m^{-2}. The passage of the cloud associated with the MCS caused the surface latent heat flux to decrease to zero, presumably due to shading the surface from solar radiation (Marsham *et al.*, 2007). A delay of approximately 30 minutes occurred after the passage of the MCS before the surface latent heat flux recovered. The surface latent heat flux decreased to zero after 1730 UTC, coinciding with the reduction in solar heating in the model in the evening and towards sunset. The latent heat flux was zero at all times between 155 and 190 km and between 320 and 380 km (Figure 3.31). This is explained later. When the simulated MCS reached 320 km (where the latent heat flux was zero at the surface) along this y-index at about 1330 UTC the system velocity increased. When the MCS reached 380 km (where the latent heat flux became non-zero) at about 1500 UTC there was a small decrease in system velocity. It was still greater than the system velocity between the start of the simulation and 1330 UTC, but was less than the system velocity between 1330 and 1500 UTC. This result clearly indicates that there was a significant interaction between the simulated MCS and the surface latent heat flux.

The boundaries of the region of zero surface latent heat flux between 320 and 380 km (Figure 3.31) were too sharp to have been caused by cloud shading due to the passage of the MCS. The region must have therefore been caused by the surface type, orography or soil moisture. A map of the surface latent heat flux, orography and column-integrated cloud is shown in Figure 3.32. The region of zero latent heat flux along y280 between 155 and 190 km corresponded to a region that was over the Severn channel (i.e. not over land). The region of zero latent heat flux between 320 and 380 km corresponded to the location of London. The terrain height was less than 100 m in this region in the model. The lack of

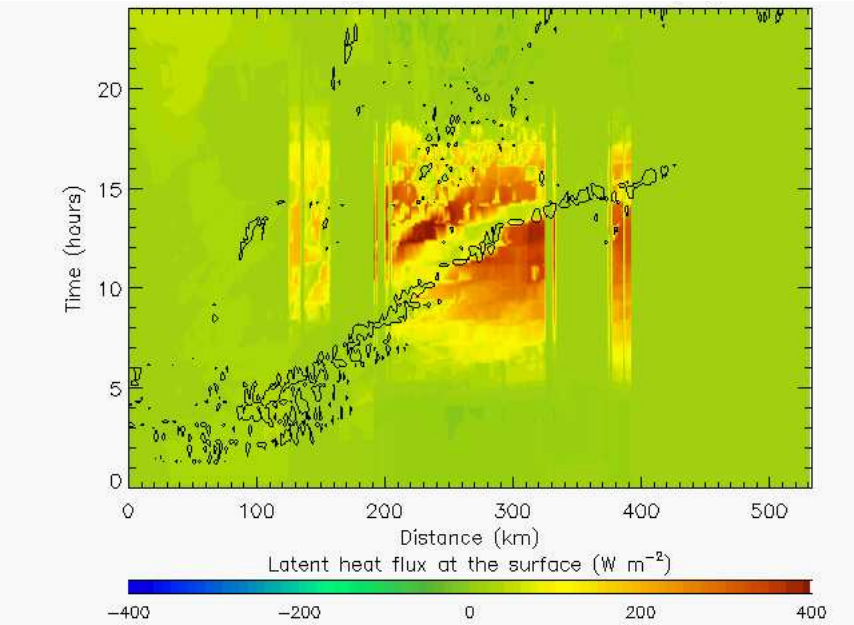

FIGURE 3.31: Hovmöller diagrams of the surface latent heat flux (W m^{-2}, colour contour) and column-integrated cloud contoured at 2.0 g kg^{-1} (black line contour) from the inner domain of the model.

significant orographic features suggests that the change in surface forcing in the London region was therefore due to either a change in surface type or a change in soil moisture. The MCS (the white line contour) was centred at an x-distance of about 310 km at 1330 UTC (Figure 3.32a), just to the west of the region of zero latent heat flux. The transition of the MCS from elevated to surface-based convection and the increase in system velocity occurred at 1330 UTC when the MCS encountered the zero latent heat flux in this region. The MCS left the region of zero latent heat flux at about 1500 UTC (Figure 3.32b) and propagated east of London, where the surface latent heat flux values were non-zero. The analysis of the Hovmöller diagram in Figure 3.31 showed that this corresponded to a small decrease in system velocity even though the convection had already become surface-based by this time.

3.7.2 The surface sensible heat flux

The sensible heat flux is the flux of heat into the air from the ground. A Hovmöller diagram of the surface sensible heat flux through y280 is shown in Figure 3.33. Values of the surface sensible heat flux began to increase in the model at about 0700 UTC. The maximum value of the sensible heat flux was about 400 W m^{-2}. The surface sensible heat flux was zero at

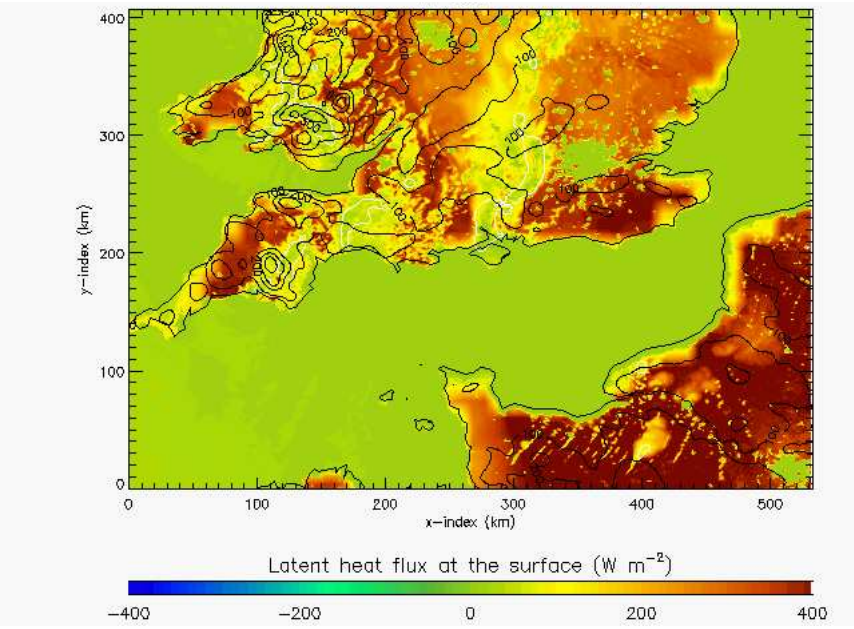

(A) 1330 UTC

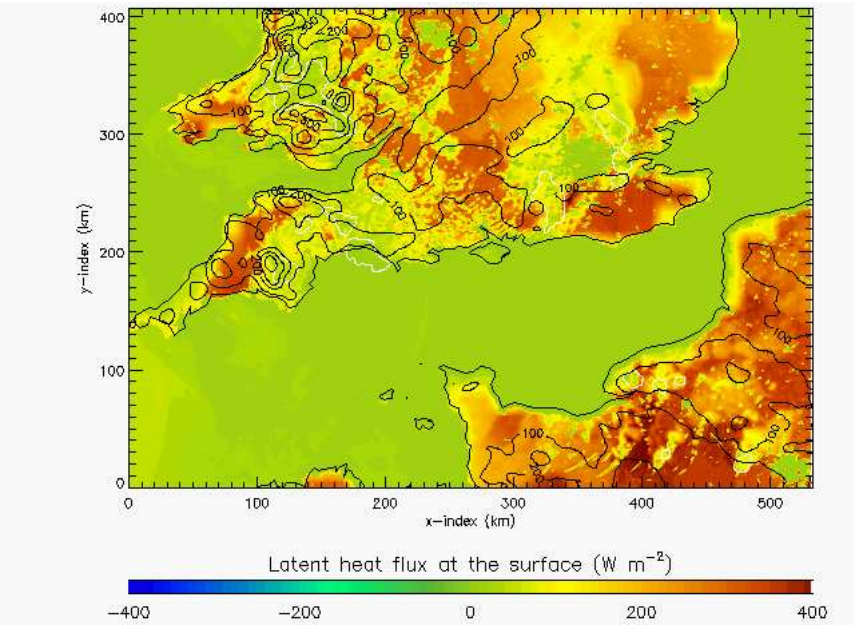

(B) 1500 UTC

FIGURE 3.32: Map of the surface latent heat flux from the inner domain of the model (W m^{-2}, colour contour), orography (m, black line contour) and column-integrated cloud contoured at 2.0 g kg^{-1} (white line contour).

all times between 155 and 190 km (Figure 3.33). This region was over the Severn Channel (Figure 3.34). Strong sensible heat fluxes occurred in the region between 320 and 380 km (Figure 3.33). This region corresponded to the location of London (Figure 3.34). From 1100 UTC onwards the value of the sensible heat flux was nearly twice as strong (about 400 W m^{-2}) in this region than in the rest of the domain. The passage of the MCS caused the values of the surface sensible heat flux to decrease. Between 0700 and 1330 UTC the values decreased to about zero. When the MCS passed into the region of strong sensible heat fluxes the values decreased to 200 W m^{-2} but not to zero.

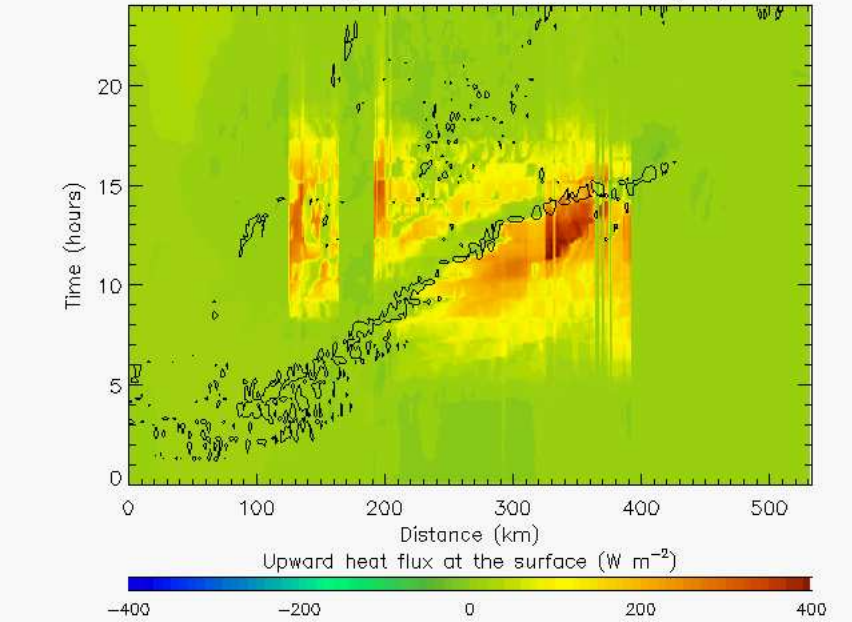

FIGURE 3.33: As Figure 3.31 but for the surface sensible heat flux.

Significantly greater values of surface sensible heat flux were associated with London at 1330 UTC than the rest of the country (Figure 3.34a). The values of the surface sensible heat flux in and behind the MCS were small, and were associated with cloud cover. These two effects caused a strong west-east gradient in the surface sensible heat flux. The values of the surface sensible heat flux increased ahead of the MCS in a region running northeast through London from the Isle of Wight at 1330 UTC (Figure 3.34a). This may have been an outflow boundary from the MCS. The MCS passed over the region of large values of sensible heat flux near London by 1500 UTC and into a region where the values of the sensible heat flux were less (Figure 3.34b).

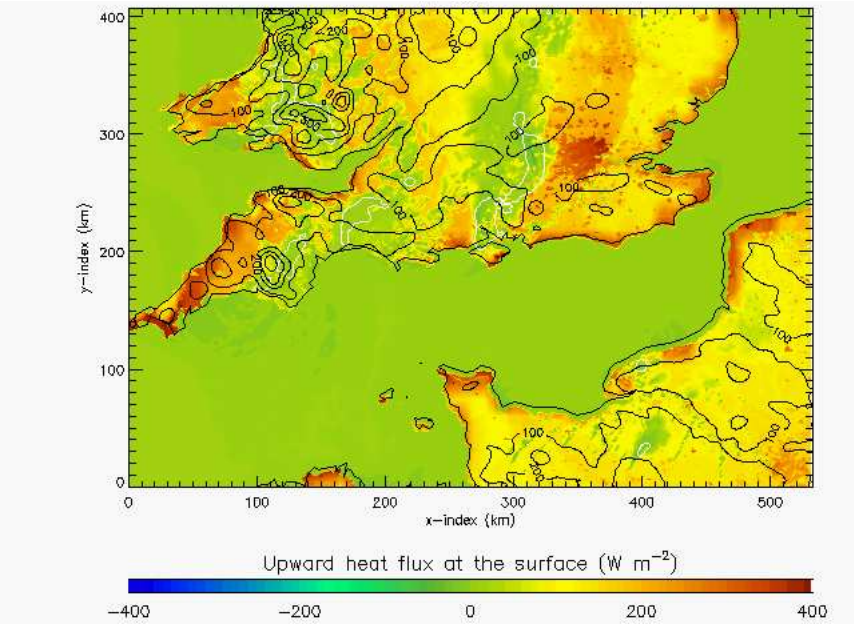

(A) 1330 UTC

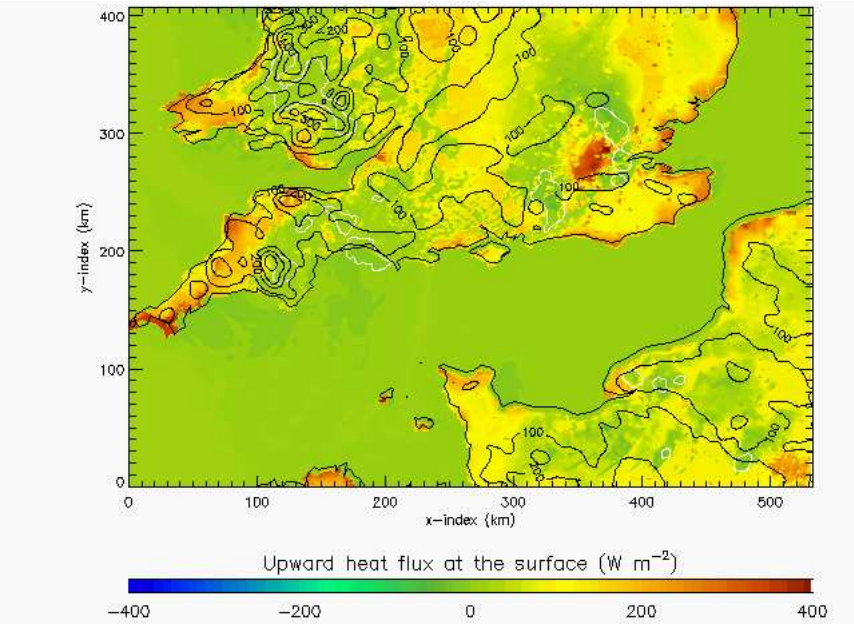

(B) 1500 UTC

FIGURE 3.34: As Figure 3.32 but for the surface sensible heat flux.

3.7.3 The effect of the surface heat fluxes on the MCS

The analysis of the vertical sections of θ_e shown in Section 3.5.1 showed that the transition from elevated convection to surface-based convection occurred gradually as the simulated MCS passed through a region of elevated high-valued θ_e air into a region where the values of θ_e in the boundary layer had increased throughout the simulation. The transition to surface-based convection was fully complete at 1330 UTC. This time coincided with the passage of the MCS into the London region, where the surface latent heat flux was zero and the surface sensible heat fluxes were strong. The change in surface latent and sensible heat fluxes over London could be attributed to either a change in surface type or a change in soil moisture. At 1330 UTC the system velocity of the MCS increased. When the MCS passed out of the London region a small decrease in system velocity occurred (e.g. Figure 3.31). It is therefore possible that a component of the increase in system velocity that occurred at 1330 UTC was attributable to the change in surface fluxes as the system passed into the London region. The surface sensible heat flux (Figure 3.34) suggests that part of the strong west to east gradient in convective boundary layer growth seen in the vertical sections of θ_e in Section 3.5.1 was due to the combined effect of cloud cover in the west of the UK and London in the east. Observations of surface heat fluxes in the London region were not made during CSIP, so these results could be compared to the IOP 3 data.

3.8 The deepening of the pre-convective boundary layer in the east of the UK

The analysis of the vertical structure of the simulated MCS and its pre-convective environment discussed in Section 3.5.1 showed that the pre-convective boundary layer deepened significantly in the east of the domain. The large-scale flow at 0000 UTC (Figure 3.11) suggested that the increase in θ_e at low-levels in the east of the domain was partly attributable to the advection of high-valued θ_e air from the south. It can also be seen that the y250 and y150 vertical sections discussed in Section 3.5.1 were out of the range of influence of London (Figure 3.16), where the surface sensible and latent heat fluxes were shown to have affected the behaviour of the simulated MCS. However, the values of θ_e in

the pre-convective boundary layer nevertheless increased throughout the simulation in the y250 and y150 vertical sections.

Maps of θ_e, maximum reflectivity and horizontal wind vectors on the 950 hPa surface are shown in Figure 3.35. The west-east gradient in θ_e across the UK was obvious at 0830 UTC (Figure 3.35a), with lower values in the west and higher values in the east. Values of θ_e were large (330 K or greater) in northern France and in the far south-east of the UK. The winds on the 950 hPa surface show that at 0830 UTC there was flow from the south-east towards the UK. This would have advected high-valued θ_e air towards the south-east of the UK. Values of θ_e in the UK between the Isle of Wight and the east coast began to increase from about 325 K to 328 K at this time. Comparing Figure 3.35a with the orography in e.g. Figure 3.34a, the increase in θ_e in the south of the UK at 0830 UTC occurred over regions where the terrain height was greater than its surroundings.

The values of θ_e in the south-east of the UK at 950 hPa continued to increase, especially over orographic features. The wind field in the region of increasing θ_e showed that high-valued θ_e air from the south-east was also being advected towards the south-east of the UK at 1000 UTC (Figure 3.35b). The MCS was in the south-west of the UK at 1000 UTC, but low-valued θ_e air flowed out from the MCS west of the Isle of Wight. This outflow of low-valued θ_e air in the west, combined with the increase in θ_e in the east, sharpened the pre-existing west-east gradient in θ_e (as previously discussed in Section 3.4).

The transition from elevated to surface-based convection was fully complete by 1330 UTC. Figure 3.35c shows that by this time the combination of surface heating and the advection of higher-valued θ_e air from the south-east had increased the values of θ_e at 950 hPa in the east of the UK to 330 K or greater. The eastern boundary of the convective system had reached the high-valued θ_e air in the east. By 1330 UTC the large-scale wind field had changed such that the flow from the south-east towards the UK had decreased. However, the combination of surface heating and the earlier advection of high-valued θ_e air towards the UK had increased the values of θ_e in the east of the UK sufficiently enough for the convection to become surface-based (Section 3.5.1).

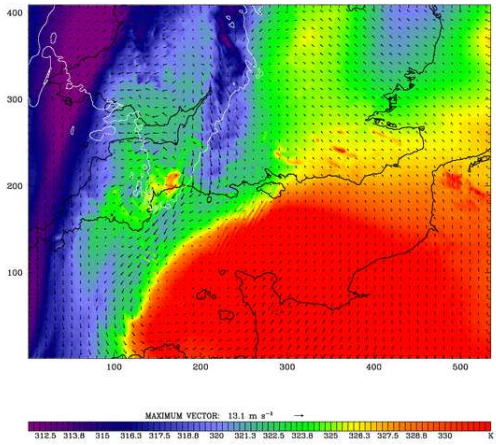

(A) 0830 UTC

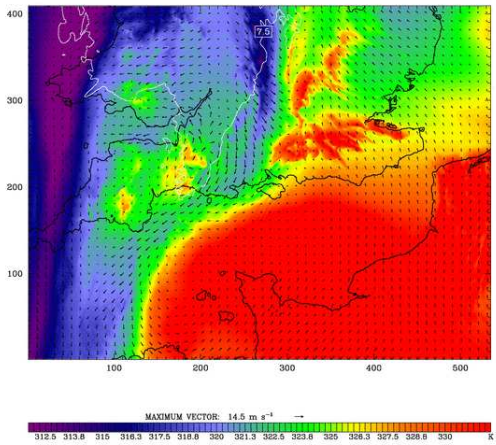

(B) 1000 UTC

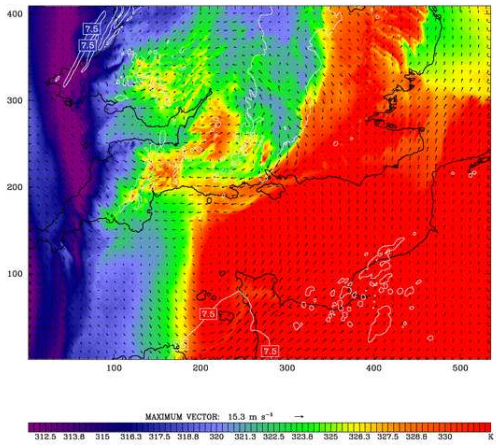

(C) 1330 UTC

FIGURE 3.35: θ_e (K, colour contour), horizontal wind vectors and maximum reflectivity (white line contour) at 950 hPa from the inner domain (1km horizontal resolution) of the WRF run for 24 June 2005.

3.9 The lack of a gravity current associated with MCS C

The observations of MCS C never showed evidence of any gravity current outflow from a cold pool (Browning *et al.*, 2010; Marsham *et al.*, 2010). However, the MCS in the WRF simulation of IOP 3 developed a gravity current in the late stages of the storm. The surface station data analysed by Marsham *et al.* (2010) was limited to four AWS sites in the CSIP area. If MCS C formed a gravity current late in its lifetime after it passed out of the CSIP region, this may not have been noted by Browning *et al.* (2010) and Marsham *et al.* (2010).

By 1600 UTC, MCS C had moved out of the CSIP area and into East Anglia (Figure 3.36). The work of Browning *et al.* (2010) and Marsham *et al.* (2010) has been extended in this thesis by analysing data from all of the Met Office MIDAS land surface stations in southern England for 24 June 2005. If MCS C developed gravity current outflow after it moved out of the CSIP region and into East Anglia a cold pool signature (a temperature decrease accompanied by a pressure increase and wind speed increase) may have been evident in the land surface station data. A limitation of the land surface station data was that some stations did not successfully record full sets of pressure, temperature and wind data. Another limitation was that the data was recorded at hourly intervals. The rapid movement of MCS C meant that hourly data may have been insufficient to provide significant information about the structure of the outflow. Only surface stations in East Anglia that contained full datasets of temperature, pressure, wind speed and wind direction were selected for analysis. Three stations met these requirements: Coltishall, Weybourne and Marham.

Coltishall is marked on the map in Figure 3.37. MCS C was to the west of Coltishall at 1600 UTC. Coltishall would have been affected by MCS C between 1600 and 1700 UTC. During this period a 2°C decrease in temperature was observed (second panel down in Figure 3.38), from about 21 to 19°C. The temperature decrease in this period was accompanied by an increase in pressure from about 1013.6 to 1014.2 hPa (top panel in Figure 3.38). Although a temperature decrease was accompanied by a pressure increase during this period, the changes were small and were accompanied by a decrease in wind

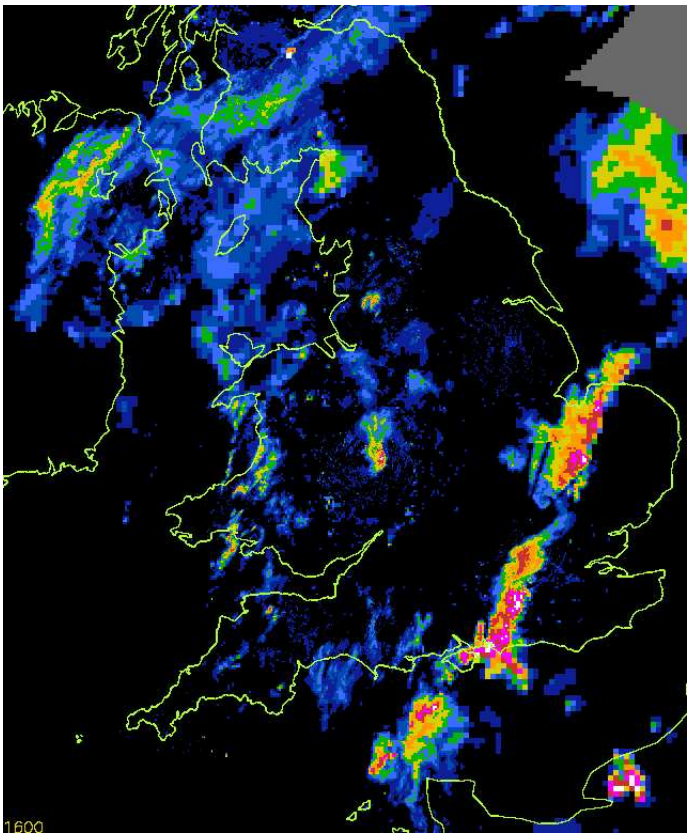

FIGURE 3.36: Radar-rainfall plot from the weather radar network over parts of southern England and Wales as for Figure 3.2, but at 1600 UTC.

speed from 13 to 7 knots (fourth panel down in Figure 3.38), rather than an increase in wind speed as would be expected from the passage of a gravity current.

MCS C was to the west of Weybourne at 1600 UTC (Figures 3.36 and 3.37). Weybourne would have been affected by MCS C between 1600 and 1700 UTC. During this period the temperature increased from 16.5°C to 17.0°C (second panel down in Figure 3.39) and the pressure increased from 1015.2 to 1015.4 hPa (top panel in Figure 3.39). The wind speed also decreased slightly from 6 to 5 knots (fourth panel down in Figure 3.39). The increase in temperature and pressure accompanied by a decrease in wind speed at Weybourne was not indicative of a cold pool.

Compared to Coltishall and Weybourne, the Marham station was closer to MCS C at 1600 UTC (Figures 3.36 and 3.37). Between 1600 and 1700 UTC the temperature at Marham decreased from 18.5 to 18.0°C (second panel down in Figure 3.40). During this period the pressure increased from 1014.3 to 1014.5 hPa (top panel in Figure 3.40) and

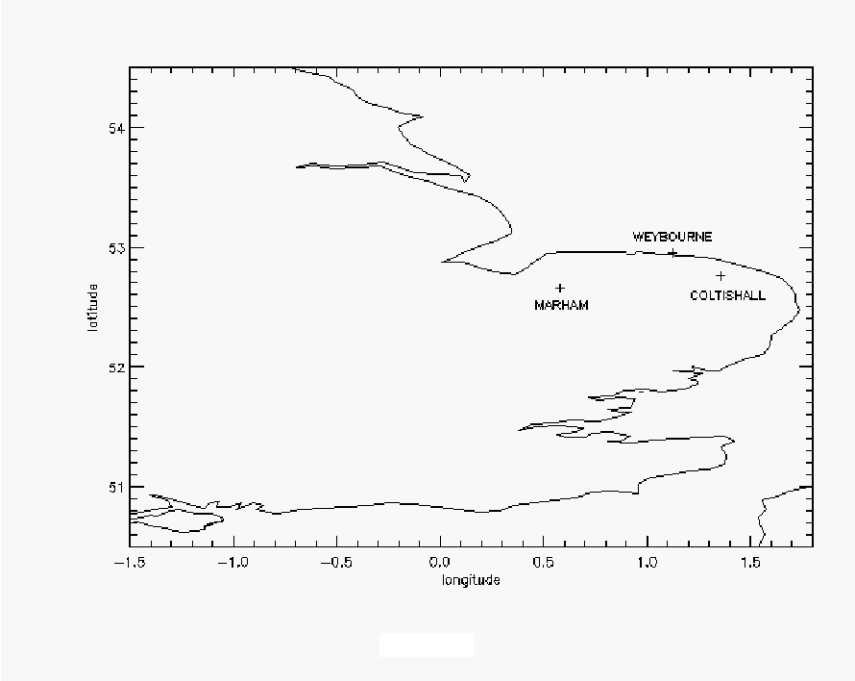

FIGURE 3.37: Location of the three MIDAS land surface stations.

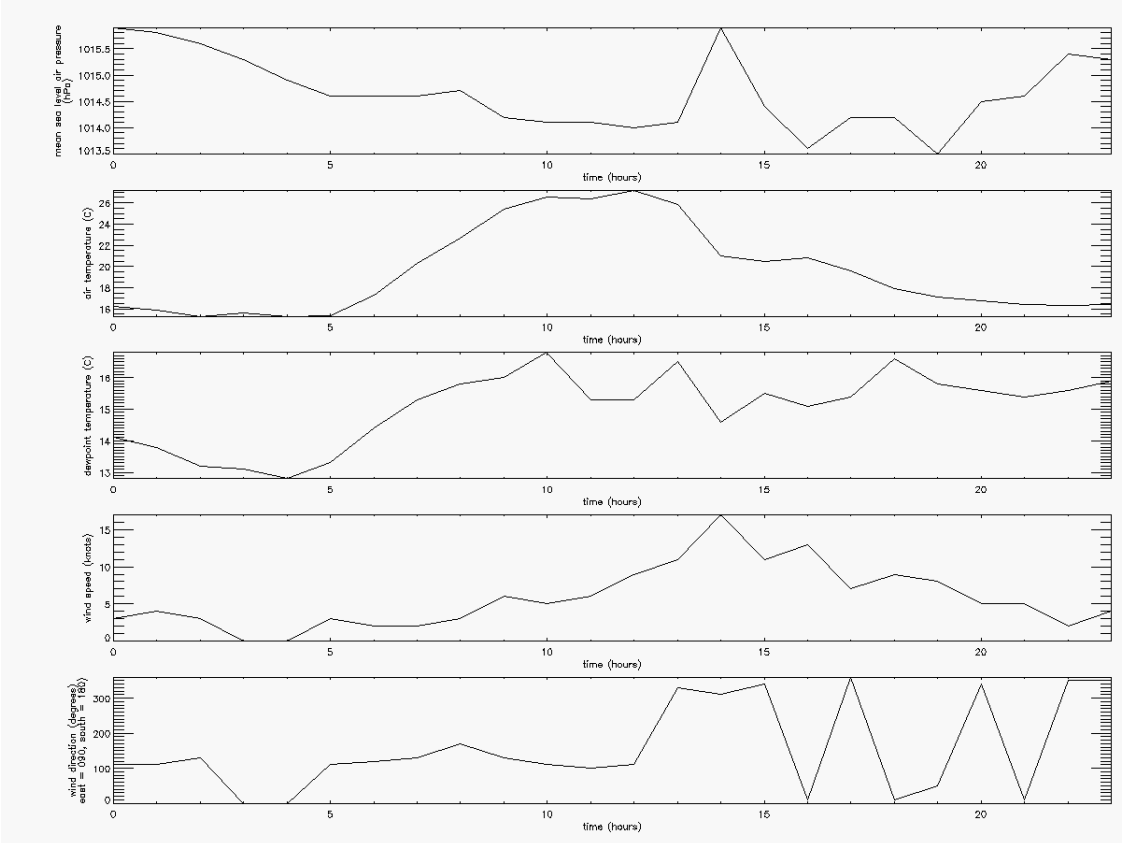

FIGURE 3.38: Timeseries of mean sea level pressure (hPa), temperature (°C), dewpoint temperature (°C), wind speed (knots) and wind direction (degrees) at the Coltishall surface station on 24 June 2005.

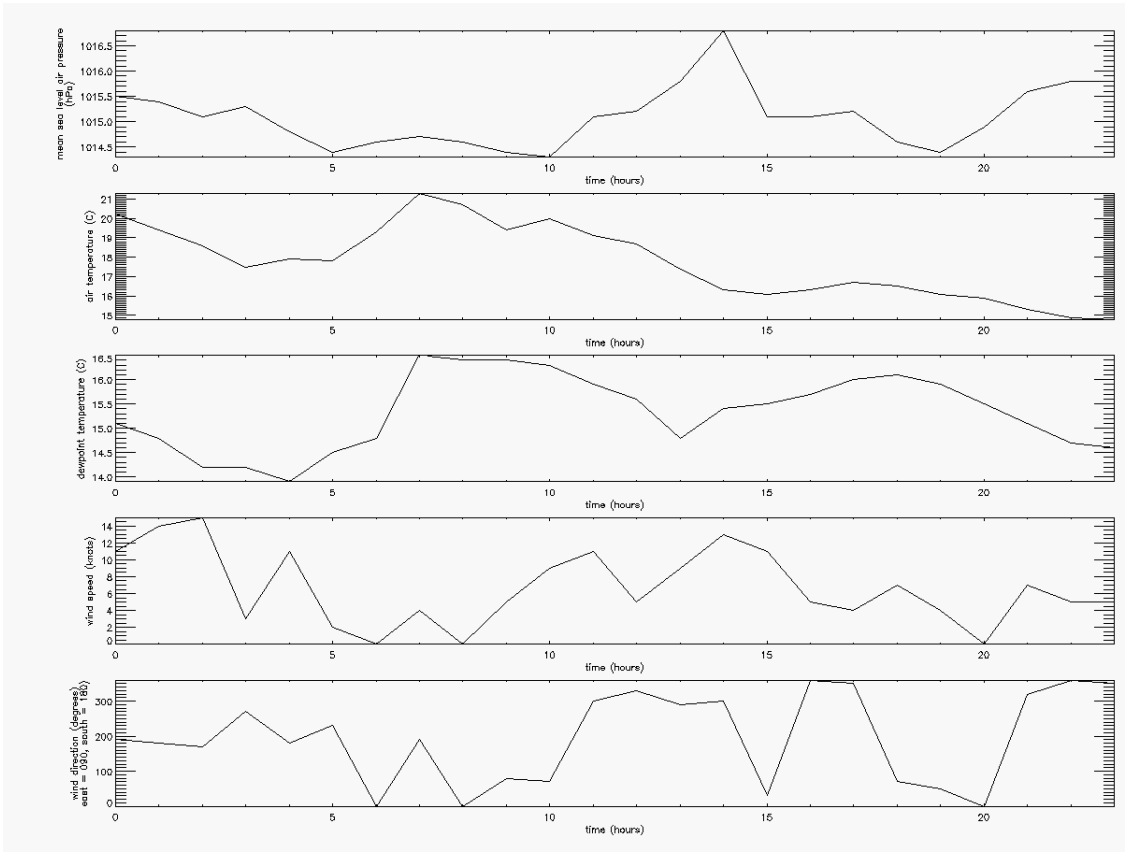

FIGURE 3.39: As Figure 3.38 but for the Weybourne surface station.

the wind speed decreased from 9 to 6 knots (fourth panel down in Figure 3.40). The small temperature decrease accompanied by a pressure increase and wind speed decrease at Marham was not indicative of a cold pool.

No significant cold pool signature from MCS C was observed at Coltishall, Weybourne or Marham during the 1600 to 1700 UTC period. This period corresponded to the later stage of MCS C. Browning *et al.* (2010) found that MCS C did not develop a cold pool during the earlier stage of its lifetime, while it remained within the CSIP area. These results suggest that MCS C never developed any significant gravity current outflow. Because of the hourly resolution of the surface station data and the fast speed of MCS C during its later stages, it is possible that the passage of a gravity current was not resolved by the stations. However, analysis of the network radar images between 1045 and 1600 UTC (not shown) did not reveal a line of rainfall associated with a cold pool, such as that observed by Clark *et al.* (2012b) during CSIP IOP 18.

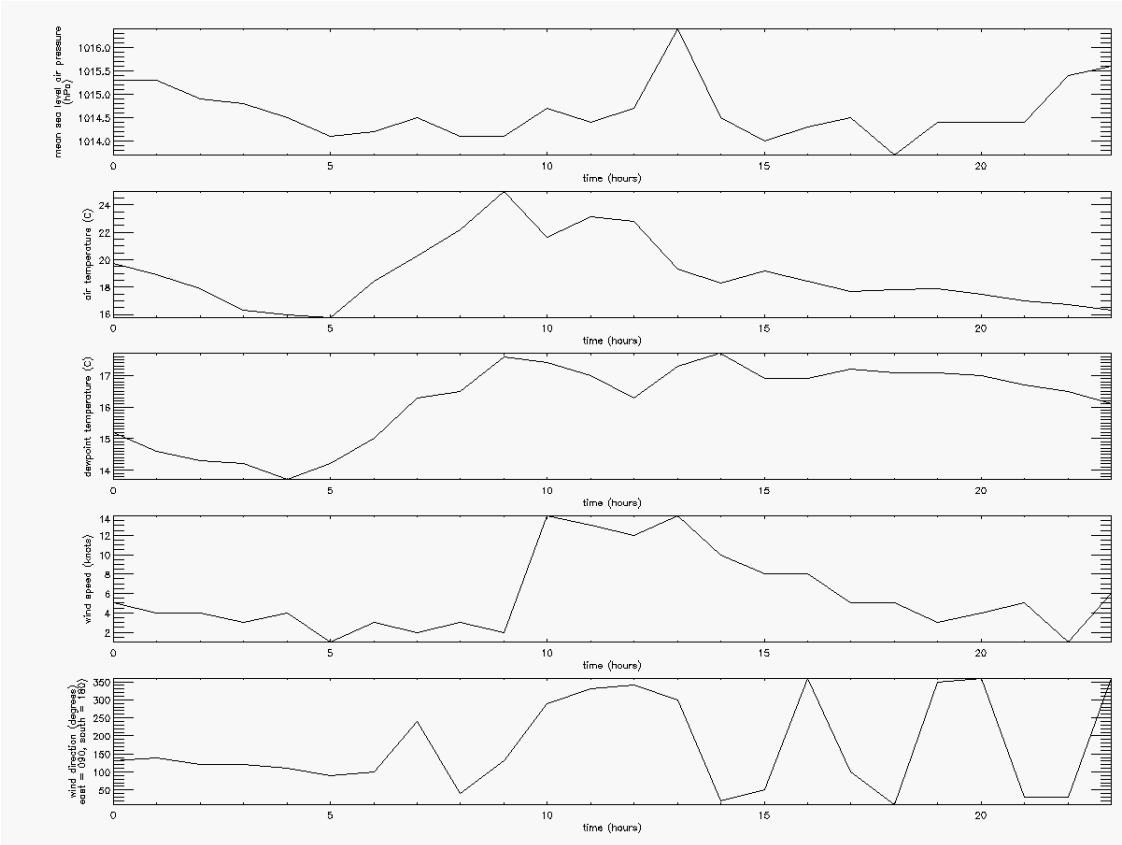

FIGURE 3.40: As Figure 3.38 but for the Marham surface station.

The stable undercurrent observed during IOP 3 was about twice as deep as the undercurrent in the simulation. The deeper undercurrent would have been less susceptible to penetration by downdraughts in the RIJ and in the convective region. The difference between the observed and simulated undercurrents may explain why a gravity current never formed during IOP 3 but did form in the simulation.

3.10 Summary of the simulated MCS

The simulation of IOP 3 generated an MCS that shared several similarities to MCS C that was observed by Browning *et al.* (2010) and Marsham *et al.* (2010). Unlike the MCSs observed during IOP 3, the WRF simulation only generated one MCS. The simulated MCS split into two storms late in its lifetime. This did not occur in any of the MCSs observed during IOP 3. The convection formed during the spin-up period of the model and as such it was not possible to investigate the mechanisms responsible for the initiation of convection during IOP 3. The RIJ also formed during the early stages of the simulation, probably due to the broad region of stratiform precipitation that developed in the early stages. Early in its lifetime, the simulated MCS had a trailing stratiform structure similar to that described by Parker and Johnson (2000). A stratiform region of precipitation is required for the development of a RIJ (e.g. Houze, 2004). Due to the formation of the RIJ during the spin-up period, it was also not possible to verify the processes responsible for its generation. However, the proximate cause of the generation of RIJs is not disputed to be dynamic (e.g. Pandya and Durran, 1996; Schmidt and Cotton, 1990).

The simulated MCS formed in a similar environment to that of MCS C. Convection developed ahead of a cold front that was in the west of the domain. There was an undercurrent that flowed in the opposite direction to the MCS. However, the undercurrent in the simulation was about 1 km deep and was about half the depth of the observed undercurrent, which was about 2 km deep. The mid- to upper-level flow in the simulation was south-westerly, which was in agreement with the observations. Initially, the simulated convection was elevated, like the convection that was observed during IOP 3. The elevated source layer in the simulation was centred at about 840 hPa. The source layer had little CIN to overcome and had about 350 J kg^{-1} of CAPE. This was comparable to the elevated source layer in the observations, which had about 405 J kg^{-1} of CAPE. However, unlike the inflow to MCS C, which was observed to have two source layers, there was only one source layer in the model. This could have been because the vertical resolution of the simulation, 48 levels, smoothed the two elevated source layers into one. This is a limitation of the simulation. Due to the large domain size and high horizontal resolution of this simulation, the vertical resolution was limited. Future simulations would benefit from the use of a higher vertical resolution if the necessary computing power is available. Another

explanation for the difference between the simulated and observed source layers could be the sensitivity of both the observed and modelled soundings to the location at which they are made.

The propagation of the modelled MCS was similar to that of MCS C. Both storms moved from the southwest to the northeast and an increase in velocity occurred in both the simulated and observed storms. The speed of the simulated MCS was slower than that of MCS C both before (about 6 m s^{-1} compared to 15 m s^{-1} for MCS C) and after (about 10 m s^{-1} compared to 18 m s^{-1}) the increase. This may have been because the southwesterly upper-level flow was weaker in the simulation than it was during IOP 3.

Throughout the duration of the simulation the values of θ_e at low-levels in the east of the domain increased. This was due to a combination of surface heating and advection. As the simulated MCS propagated from the southwest to the northeast it encountered two significant changes in the large-scale θ_e structure: the low-level values of θ_e increased and the values of θ_e in the elevated source layer decreased to the north. This contributed to the transition of the convection in the simulation from elevated to surface-based. The CSIP observations did not show whether there was a west to east θ_e gradient during IOP 3, or whether the elevated source layer was weaker in the north of the UK. MCS C remained elevated throughout the duration of the observations. The transition of the simulated MCS from elevated to surface-based convection was more similar to the behaviour of the elevated nocturnal squall line observed by Marsham *et al.* (2011), and modelled by Trier *et al.* (2011).

The RIJ in the simulated MCS behaved similarly to the RIJ observed in MCS C. The notable difference was that early in the simulation the RIJ descended to the surface in the north of the MCS and formed a gravity current. However, the convection remained elevated and the gravity current dissipated. The early gravity current outflow did not affect the propagation speed of the storm. After the penetration of the simulated RIJ to the surface, the RIJ rose back up above the undercurrent, and did not descend to the surface again. The RIJ did not descend to the surface anywhere else in the simulated MCS. The descent of the RIJ to the top of the undercurrent, and its failure to penetrate to the surface, constricted the undercurrent and caused a wave to form at the top of the undercurrent ahead of the RIJ and the convective region. The wave lifted air in the

elevated source layer. This was similar to the wave observed during IOP 3. Marsham *et al.* (2010) showed that the observed wave lifted both of the observed source layers to their levels of free convection. In the south of the simulated MCS the RIJ remained horizontal and did not descend. The undercurrent was not constricted in this region and no waves formed in the undercurrent or elevated source layer. This behaviour was different from MCS C. The RIJ associated with MCS C never penetrated to the surface and also never became horizontal. However, the radar observations of MCS C only provided information about its structure along one plane. As such, full details of the 3D structure of MCS C were not known.

There were two horizontal wind speed maxima in the simulated RIJ, similar to those reported by Smull and Houze (1987) and Klimowski (1994). One maximum occurred near the back edge of the trailing stratiform region, and the other occurred within and behind the leading convective region. This was the same as the findings of Smull and Houze (1987) and Klimowski (1994). The velocity maximum in the stratiform region was associated with a local maximum in the graupel and snow mixing ratios. The velocity maximum in the convective region was associated with a local maximum in the graupel, snow and rain mixing ratios. In the north of the simulated MCS, where the RIJ penetrated to the surface during the early stages of convection, the areal extent of the stratiform cloud was greater. It is therefore likely that the diabatic cooling processes caused the velocity maxima in the RIJ. The descent of the RIJ may also have been strengthened by diabatic cooling in the north of the MCS due to the wider stratiform cloud in this region, exposing the RIJ to cooling for a longer period and strengthening its descent enough that it could penetrate through the undercurrent to reach the surface.

Gravity current outflow formed from the simulated MCS once the convection was fully surface-based. Deep convection was initiated at the leading edge of the gravity current. The ratio of the strength of the gravity current to the strength of the shear in the lowest 5 km was optimal for the generation of deep convection (Weisman and Rotunno, 2004). The significant increase in the velocity of the simulated MCS coincided with the development of the gravity current. However, the increase in velocity of MCS C was not associated with a gravity current. No gravity current was evident in the observations of MCS C during any stage of its lifetime. This was a significant difference between the simulation and

the observations. This may have been due to differences in the low-level stable layers: the undercurrent in the simulation was about half as deep as the undercurrent that was observed during IOP 3. The simulated undercurrent would therefore have been more susceptible to penetration by downdraughts. Another difference was the increasing values of θ_e in the pre-convective boundary layer that occurred in the simulation due to a combination of surface heating and advection. This was responsible for the transition from elevated to surface-based convection in the simulation. The increased values of θ_e in the simulated pre-convective boundary layer would also have been susceptible to penetration by downdraughts. MCS C remained elevated throughout the observation period, although it is not known whether the convection became surface-based later in the day, after MCS C had left the CSIP area.

The behaviour of the simulated MCS during its surface-based phase was more similar to the behaviour of the only other MCS observed during CSIP, which occurred on 25 August 2005 during IOP 18 (Clark *et al.*, 2012b), than it was to MCS C. The MCS observed during IOP 18 formed a cold pool and the ratio of the propagation speed of the gravity current outflow from the cold pool to the low-level shear was shown to be approximately within the RKW optimal range (Clark *et al.*, 2012b).

This simulation has provided a comprehensive study of an elevated MCS with a RIJ. It is clear from these results that the development of a RIJ in an elevated MCS is of dynamical importance to the convective system as it provides a mechanism that aids the maintenance of convection, via the generation of a wave in the stable layer.

Although there were some differences between the simulated MCS and MCS C that was observed during IOP 3, the behaviour of the modelled and observed storms was in reasonable agreement during the elevated phase of the simulation. The transition of the simulated MCS from elevated to surface-based convection was similar to the evolution of the nocturnal squall line observed by Marsham *et al.* (2011) and its subsequent simulation by Trier *et al.* (2011). However, the results of those authors showed that the transition to surface-based convection occurred after sunrise, due to boundary layer warming. In the simulation presented here, the evolution of the convection was more dependent on the evolution of the large-scale environment than it was on the diurnal cycle. The undercurrent in the simulation was not a nocturnal feature and persisted throughout the day. Although

the undercurrent was partly weakened by surface heating, the advection of high-valued θ_e air from the south of the model domain was an important factor that contributed to the transition to surface-based convection.

A schematic diagram of the evolution of the simulated MCS and the pre-convective environment is shown in Figure 3.41. In the initial stages of the convection (Figure 3.41a) there is a stable undercurrent of low-valued θ_e air surmounted by a layer of high-valued θ_e air. The RIJ descends beneath the stratiform cloud and in the convective region but does not penetrate through the stable layer. The undercurrent is constricted beneath the RIJ and a wave forms ahead of the convection at the top of the undercurrent. The wave lifts air in the elevated high-valued θ_e layer, enabling it to overcome the CIN. Cloud forms above the wave. The MCS propagates via new convection initiated by the wave. In the pre-convective environment (to the east), a combination of advection and surface heating cause the values of θ_e in the boundary layer to increase (Figure 3.41b). As the MCS propagates eastwards the RIJ remains elevated and the storm remains wave-lifted. The transition from elevated to surface-based convection occurs gradually: the origin of the air lifted by the wave is a combination of air from the elevated high-valued θ_e layer and high-valued θ_e from the boundary layer. The high-valued θ_e pre-convective boundary layer continues to deepen. When the MCS reaches this region, the RIJ remains elevated but convective downdraughts descend to the surface and form a gravity current (Figure 3.41c). The speed of the MCS increases when the gravity current forms. The gravity current flows ahead of the storm. New convection is initiated via the lifting of high-valued θ_e from the boundary layer by the gravity current.

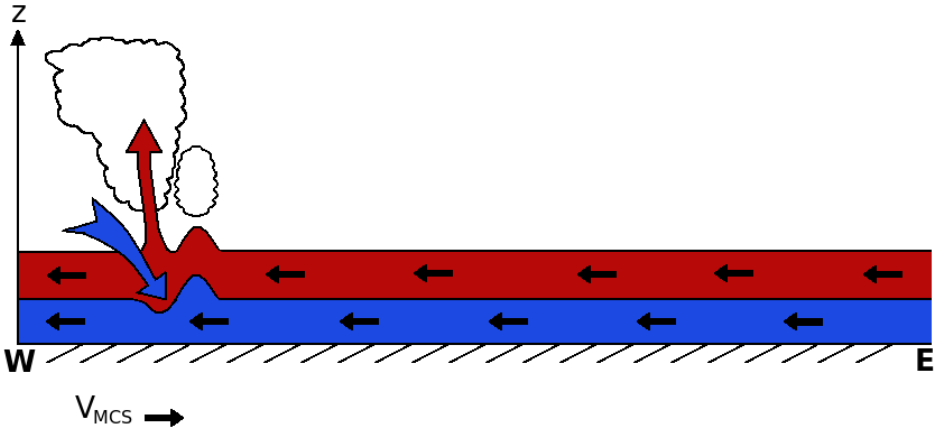

(A) Elevated phase: wave-lifted.

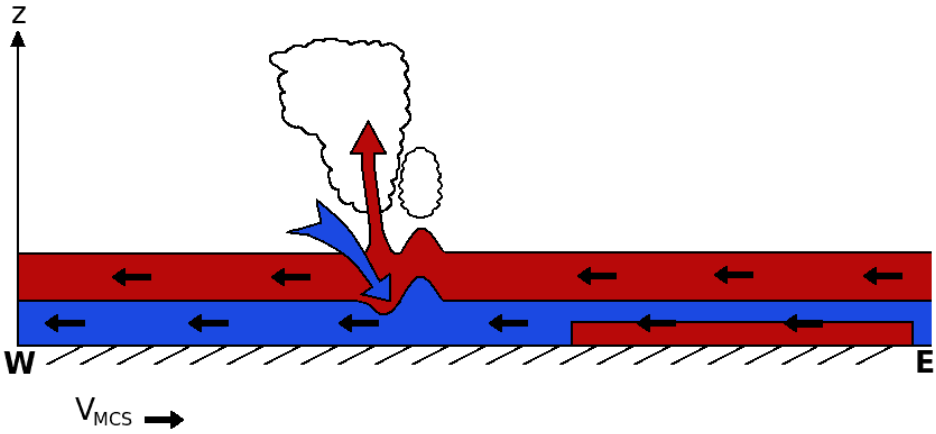

(B) Transition phase: wave-lifted.

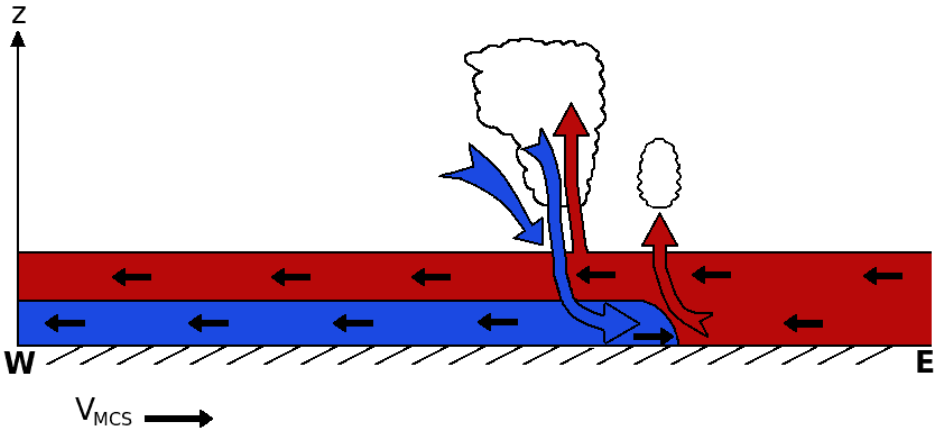

(C) Surface-based phase: gravity current-lifted.

FIGURE 3.41: Schematic diagram of the evolution of the simulated MCS and the pre-convective environment. Blue and red colours represent low-valued and high-valued θ_e air, respectively. Arrows show the direction of the flow.

Chapter 4

Sensitivity studies of the simulated MCS

The results presented in Chapter 3 showed that surface heating contributed to the increased values of θ_e at low-levels and therefore to the weakening of the undercurrent in the simulation. It was also suggested that diabatic cooling processes affected the strength and descent of the simulated RIJ. The results of e.g. Braun (1995); Braun and Houze (1997); Franklin *et al.* (2006) also showed that microphysical processes were important to the development and evolution of the RIJ. The interaction between the RIJ and the undercurrent was responsible for the generation of a wave in the undercurrent that acted to maintain the convection during the elevated phase. The increased values of θ_e at low-levels, from a combination advection and surface heating, were responsible for the transition from elevated to surface-based convection. As such, the sensitivity of the simulated MCS to surface heat fluxes and to diabatic cooling was investigated. Five sensitivity runs were performed in total.

The first sensitivity run investigated the rôle of surface fluxes on the transition from elevated to surface-based convection. The surface latent and sensible heat fluxes were removed from the model by setting every instance of them in the WRF code to zero. The simulation was repeated using the modified model. The same analysis fields and boundary conditions that were used in the original simulation were used to initialise the sensitivity simulations.

There are two possible approaches to performing microphysics sensitivity studies. The first is to remove the entire microphysical process from the model, altering both the temperature and moisture fields simultaneously. This preserves conservation of energy in the model, but allows unphysical processes to occur. The second approach is to alter the temperature field alone, removing the contribution to the latent heating from the required microphysical process. Altering the temperature field without adjusting the moisture field accordingly means that energy is no longer conserved, even though the physical processes may be more realistic. The second approach has been used in these simulations with the caveat that the studies looked at cooling processes only. Removing coolings from the model without altering the moisture field led in every case to a dissipation rather than an intensification of the system, and as such the effects due to the violation of energy conservation were deemed to be insignificant. If, however, an intensification of the system had been observed when the cooling processes were removed the approach would not have been valid and it would have been more appropriate to remove the entire process from the model and preserve energy conservation.

A set of four microphysics sensitivity runs were performed in which the individual diabatic coolings from microphysical processes were removed from the model. In one, the contribution to the temperature tendency equation in the Morrison microphysics scheme (Morrison and Khvorostyanov, 2005) from cooling by evaporation was set to zero. A similar run was performed with cooling by sublimation set to zero. In a third run the contribution to the temperature from cooling by melting was removed. Cooling by melting is an instantaneous process in the Morrison microphysics scheme and therefore there is no melting term in the temperature tendency equation. A final run was performed with all cooling processes removed (evaporation, sublimation and melting). In each of these cases, the physical processes were allowed to occur, but the contribution to the temperature tendency and/or the temperature was removed. The same analysis fields and boundary conditions that were used in the original simulation were used to initialise the sensitivity simulations.

In the following analysis of the sensitivity runs, each of the modified models has been abbreviated as follows:

- CTL: The control run using the unmodified WRF model. The results from this run were described in detail in Chapter 3

- NOSFX: No surface latent or sensible heat fluxes.
- NOEVP: No contribution to the temperature tendency from evaporative cooling.
- NOSUB: No contribution to the temperature tendency from sublimational cooling.
- NOMLT: No contribution to the temperature from cooling by melting.
- NOCOOL: No contribution to the temperature tendency from evaporative or sublimational cooling, and no contribution to the temperature from cooling by melting.

4.1 The sensitivity to the surface latent and sensible heat fluxes

The following Section discusses the effects on the simulated MCS of removing the surface latent and sensible heat fluxes from the model.

4.1.1 The structure and evolution of the precipitation

The initial development of the MCS in the NOSFX simulation was similar to that of the CTL simulation. There was a band of intense precipitation oriented north to south in the southwest of the UK in both simulations at 0800 UTC (Figures 4.1a and 4.1b). The precipitation was less intense in the north of the bands and in both runs there was a broad trailing region of lighter rainfall that extended over most of Wales.

The structure and location of the simulated MCS in the NOSFX and the CTL runs remained similar until 1200 UTC. At this time the MCS in the CTL run began to split into two (Figure 4.2a) and subsequently the more northerly of the two resulting systems propagated ahead of (and slightly faster than) the southerly system (Chapter 3). In contrast, the MCS in the NOSFX run did not split at this time (Figure 4.2b) and its position remained roughly halfway between that of the two split systems in the CTL run (Figure 4.2b).

A region of small trailing cells of intense precipitation formed in the NOSFX simulation. This did not occur in the CTL run. The cells began to develop at 1330 UTC and persisted until the system dissipated. The trailing cells were greatest in number and had the heaviest

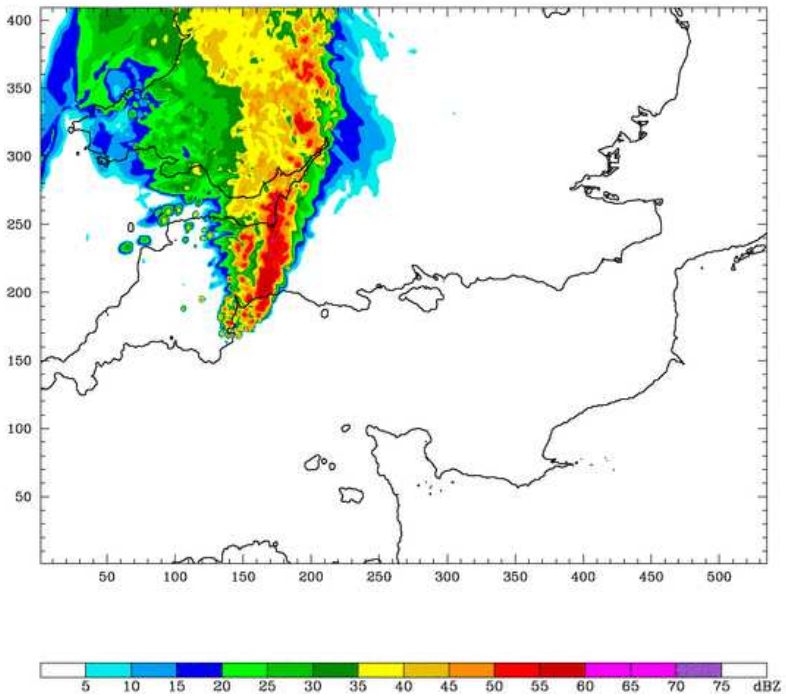

(A) CTL

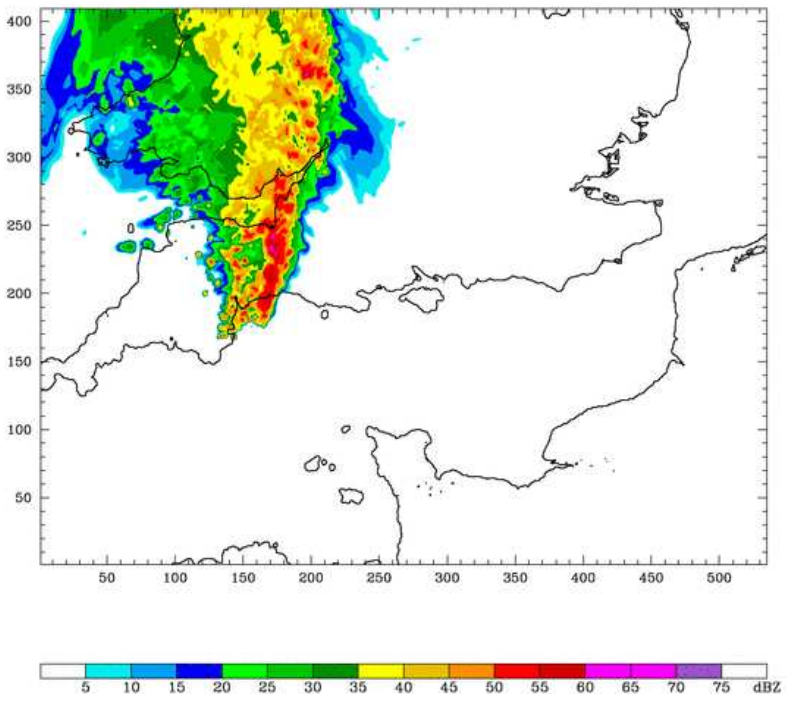

(B) NOSFX

FIGURE 4.1: Simulated reflectivity (dBZ) field at 0800 UTC from the inner domain of the CTL and NOSFX runs.

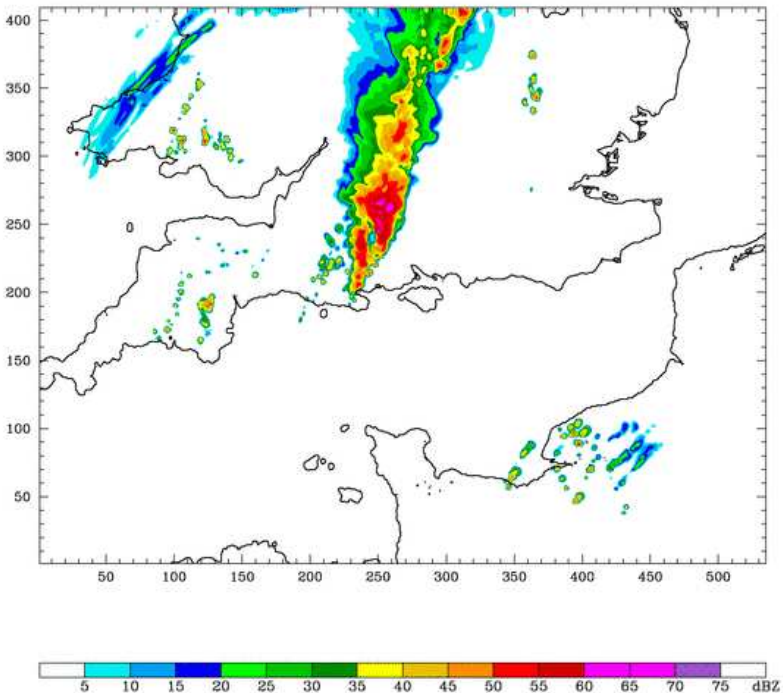

(A) CTL

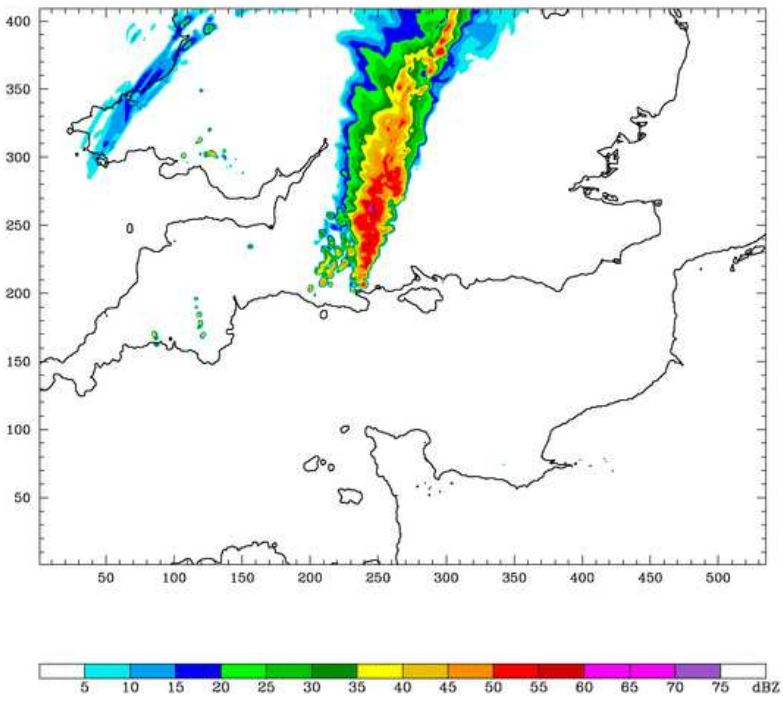

(B) NOSFX

FIGURE 4.2: As Figure 4.1 but at 1200 UTC.

rainfall at 1430 UTC (Figure 4.3b). The CTL run had no equivalent structure at this time, but did have a series of cells of heavy rainfall that developed along an outflow boundary ahead of the storm (Figure 4.3a).

The simulated MCS in the NOSFX run eventually split into two, but the process began at 1500 UTC (Figure 4.4b), much later than in the CTL run. In comparison, the two MCSs in the CTL run had fully decoupled from each other by this time (Figure 4.4a). The location of the system when it began to split in the NOSFX run was roughly half way between the location of the two systems in the CTL run. This time was also when the heavy precipitation in the NOSFX run began to cover a much narrower region than the heavy precipitation in the CTL run, and marked the beginning of the dissipation of the NOSFX system. The two systems in the CTL run did not begin to dissipate at this time.

The simulated MCS in the NOSFX run dissipated much earlier than the MCS in the CTL run. There was no heavy precipitation in the NOSFX run at 1800 UTC and only a small area of light precipitation remained over the east of the UK (Figure 4.5b). In contrast, heavy precipitation associated with the MCSs persisted in the CTL run at 1800 UTC (Figure 4.5a), where the two systems began to merge as they moved off the east coast. At no point in the later stages of its lifetime did any cells of heavy precipitation develop ahead of the simulated MCS in the NOSFX run as they did in the CTL run. This suggested that no gravity current developed in the NOSFX run. It is therefore likely that the MCS in the NOSFX run dissipated earlier than the MCS in the CTL run because convection was not maintained via the generation of new convective cells at the leading edge of a gravity current.

4.1.2 The velocity of the simulated MCS

To determine the effect of surface fluxes on the system velocity of the simulated MCSs, several Hovmöller diagrams of vertical velocity and column-integrated cloud were made from west to east through the model domain along lines of constant y-index for each run, as for the CTL run in Section 3.3. The system velocities were determined from each Hovmöller diagram, and the resulting set of system velocities for the NOSFX run were averaged to give a mean value. Like the CTL run, the simulated MCS in the NOSFX run had two

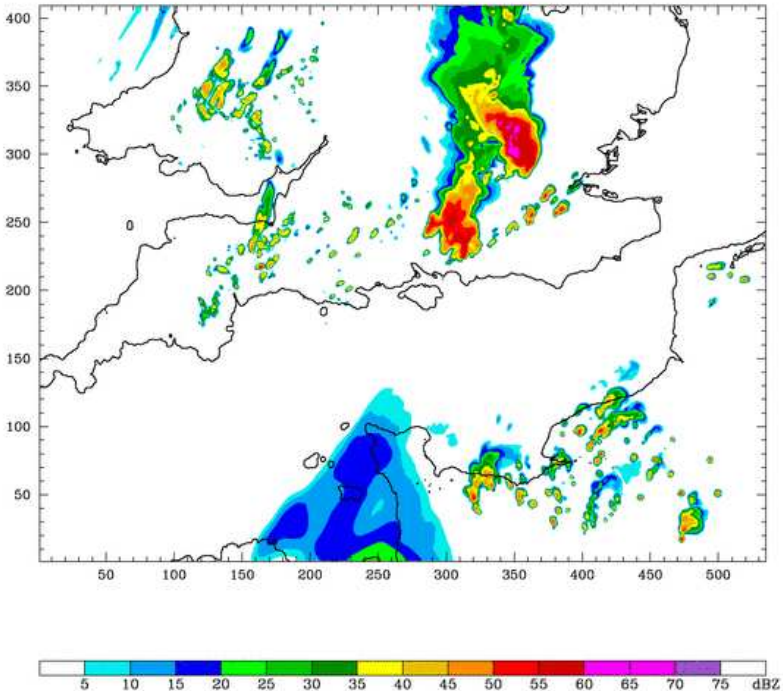

(A) CTL

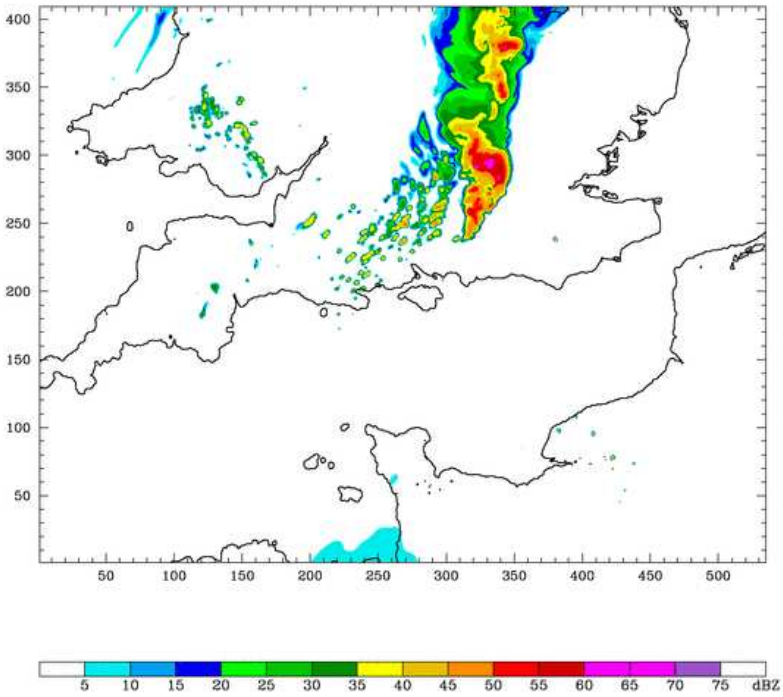

(B) NOSFX

FIGURE 4.3: As Figure 4.1 but at 1430 UTC.

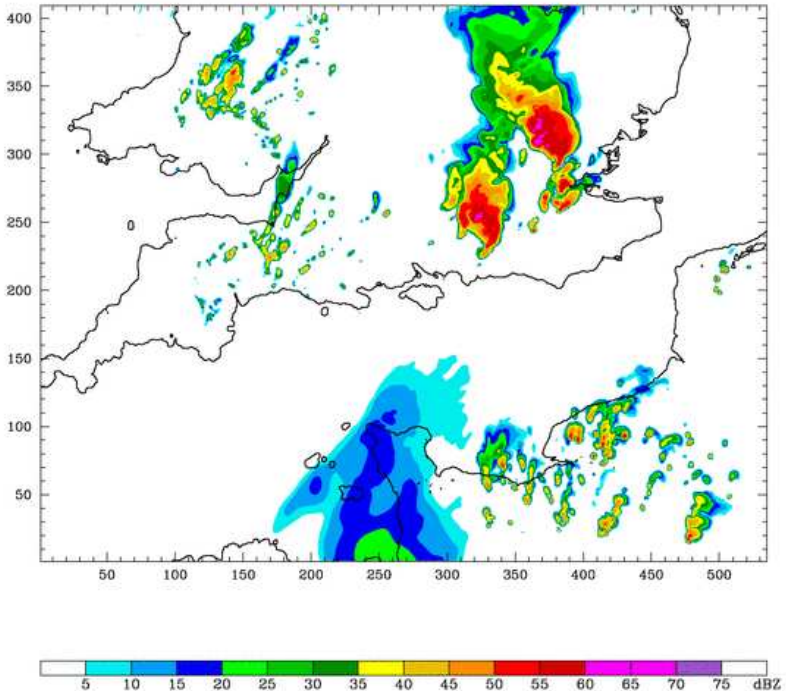

(A) CTL

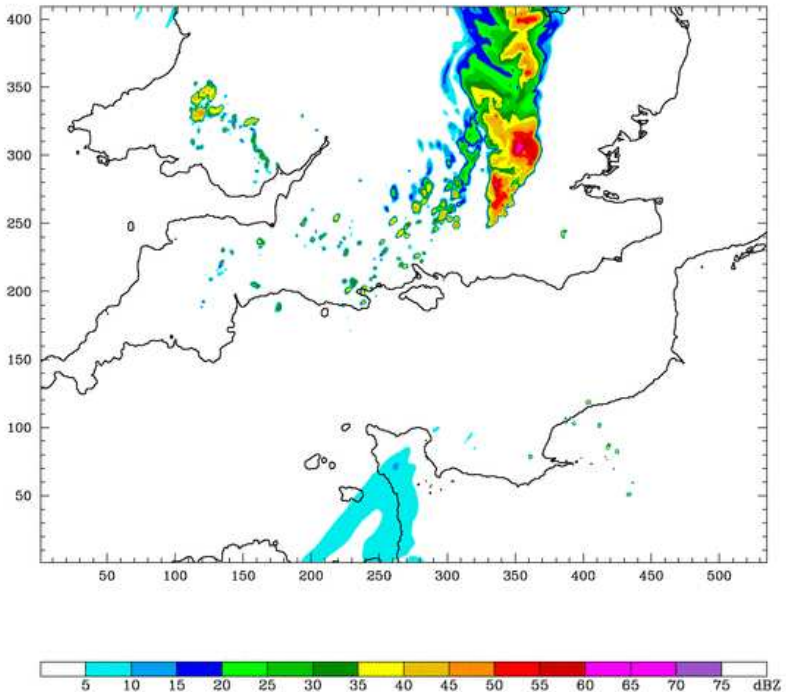

(B) NOSFX

FIGURE 4.4: As Figure 4.1 but at 1500 UTC.

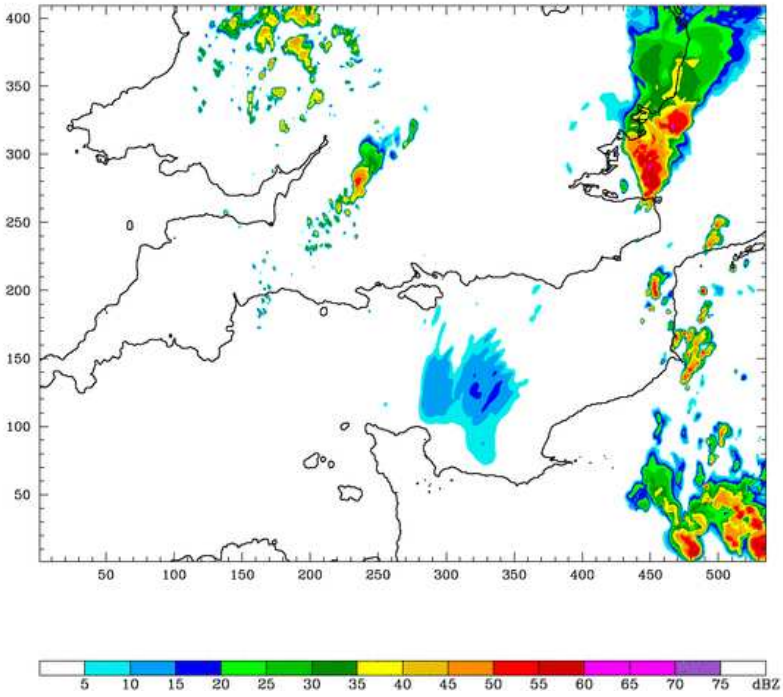

(A) CTL

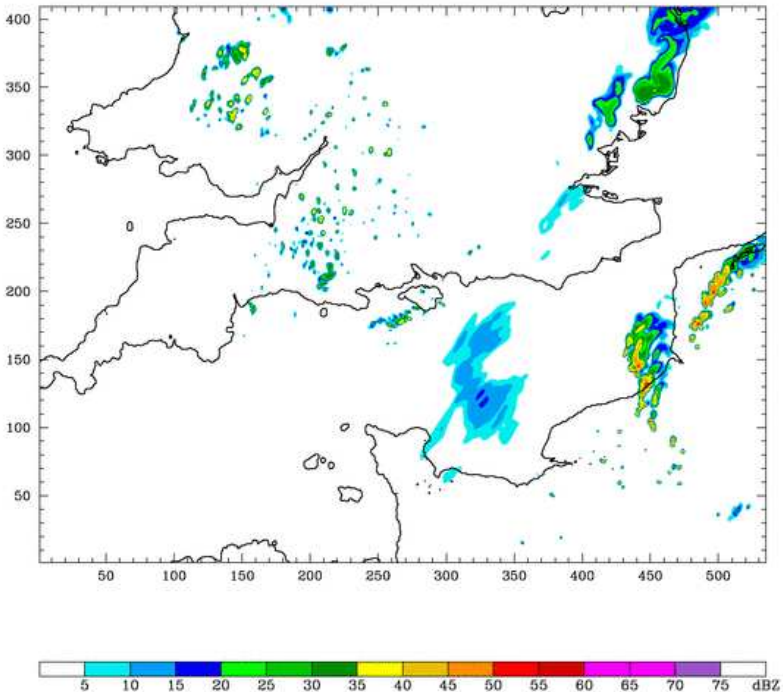

(B) NOSFX

FIGURE 4.5: As Figure 4.1 but at 1800 UTC.

distinct velocities (Figure 4.6). These will be shown later in Section 4.1.4 to correspond to the periods when the convection was elevated and wave-lifted and surface-based and gravity current-lifted. The change in system velocity occurred between 1300 and 1400 UTC (Figure 4.6). The initial speed of the MCS in the NOSFX run was (5.8±1.2) m s^{-1} and its subsequent speed was (9.4±1.3) m s^{-1}. These system velocities were, within the error limits, the same as the system velocities of the MCS in the CTL run. Both system velocities were slower than those of MCS C, which was observed to have an initial speed of 15 m s^{-1} and a subsequent speed of 18 m s^{-1}.

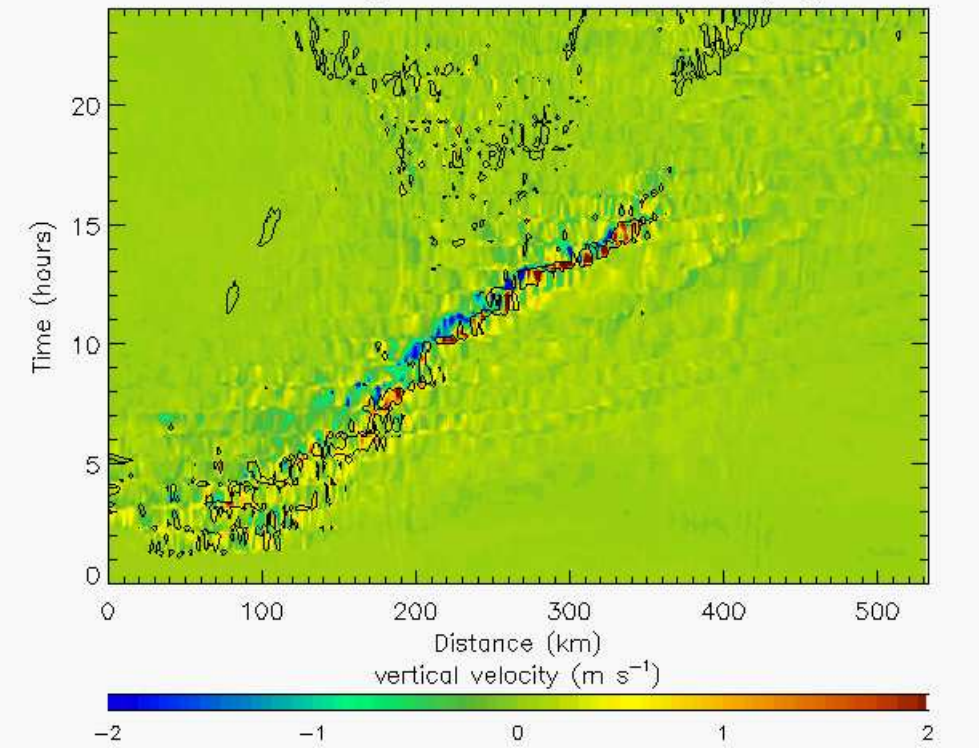

FIGURE 4.6: Hovmöller diagram of vertical velocity (m s^{-1}, colour contour) and column-integrated cloud at 2.0 g kg^{-1} (black line contour) for model level 24 and y-index point 260 for the NOSFX run.

4.1.3 The large-scale effect of the surface latent and sensible heat fluxes

The surface latent and sensible heat fluxes affected the transition to surface-based convection. Values of θ_e began to increase at low-levels in the east of the domain at 0900 UTC (Figure 4.7a). This also occurred in the NOSFX run at this time (Figure 4.7b). The increasing values of θ_e in the NOSFX run could not have been due to surface heating

and were therefore due to advection from the south. This result confirms that the low-level values of θ_e in the CTL run increased due to a combination of surface heating and advection.

As already discussed in Chapter 3, the simulated elevated MCS in the CTL run encountered the region of high-valued θ_e air at low-levels in the east which led to the convection becoming surface-based by 1330 UTC (Figure 4.8a). In comparison, the lack of surface heating in the NOSFX run meant that at 1330 UTC the convection was not fully surface-based. Values of θ_e had increased at low-levels due to advection, but not as strongly as in the CTL run (Figure 4.8b). The leading edge of the convection in the NOSFX run encountered relatively low-valued θ_e air at low-levels at 1330 UTC. However, an increase in the system velocity was observed in the NOSFX run during this period (Section 4.1.2). This suggests that although the convection was not fully surface-based, a change in the lifting mechanism had occurred. This is shown later to be due to the development of a gravity current.

The MCS in the NOSFX simulation reached the region of high-valued θ_e air at low-levels in the east at 1500 UTC (Figure 4.9b) and the transition to fully surface-based convection began. By this time the inflow to the MCS in the CTL simulation had been surface-based for some time (Figure 4.9a).

The surface latent and sensible heat fluxes had a significant effect on the vertical structure of the synoptic scale environment in the outer domain of the model (which had a horizontal resolution of 9 km and in which convection was parameterised). The vertical structure was similar in the NOSFX and CTL simulations until about 0800 UTC, when surface heating began in the CTL run. The boundary layer began to deepen in the east in the CTL run from 0900 UTC onwards (Figure 4.10a). At this time, high-valued θ_e air also started to arrive in the east in the NOSFX run (Figure 4.10b), which was advected from the south (Figure 4.7b). This shows that the increasing values of θ_e at low-levels in the east in the CTL run were not only caused by surface heating but were also due to advection.

The depth of the high-valued θ_e boundary layer in the east of the domain in the NOSFX run (Figure 4.11b) was about half of that in the CTL run (Figure 4.11a). The deeper boundary layer in the CTL run meant that convection became fully surface-based several

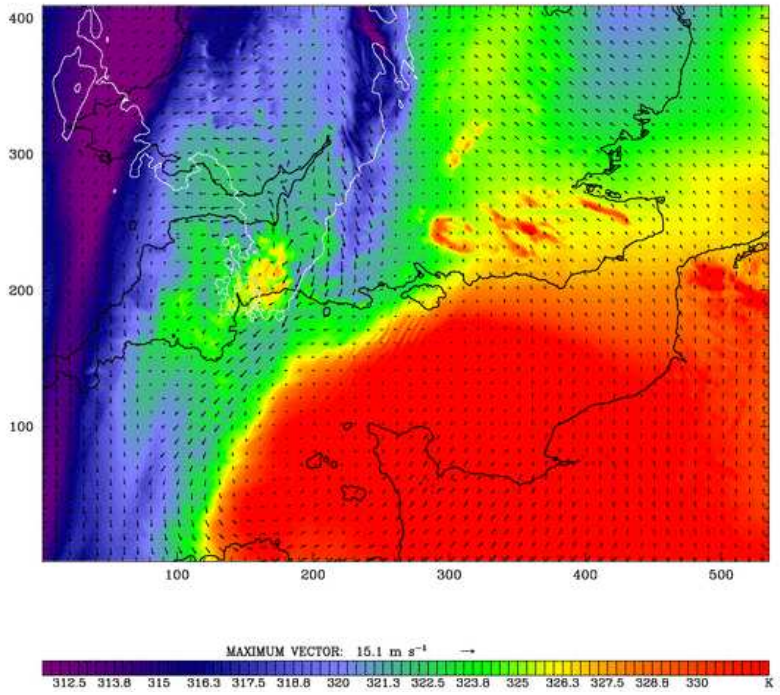

(A) CTL

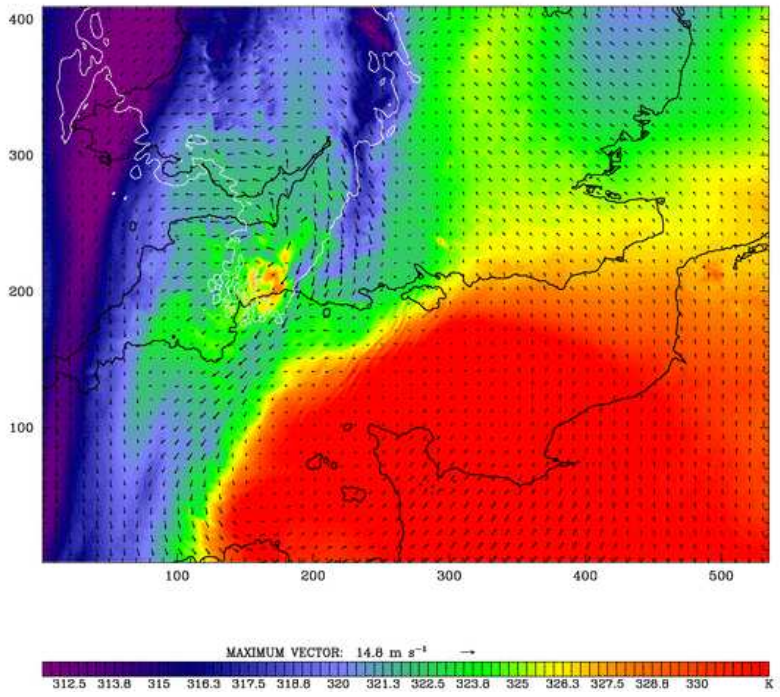

(B) NOSFX

FIGURE 4.7: θ_e (K, colour contour) and horizontal wind vectors on the 950 hPa surface at 0900 UTC from the inner domain of the CTL and NOSFX runs.

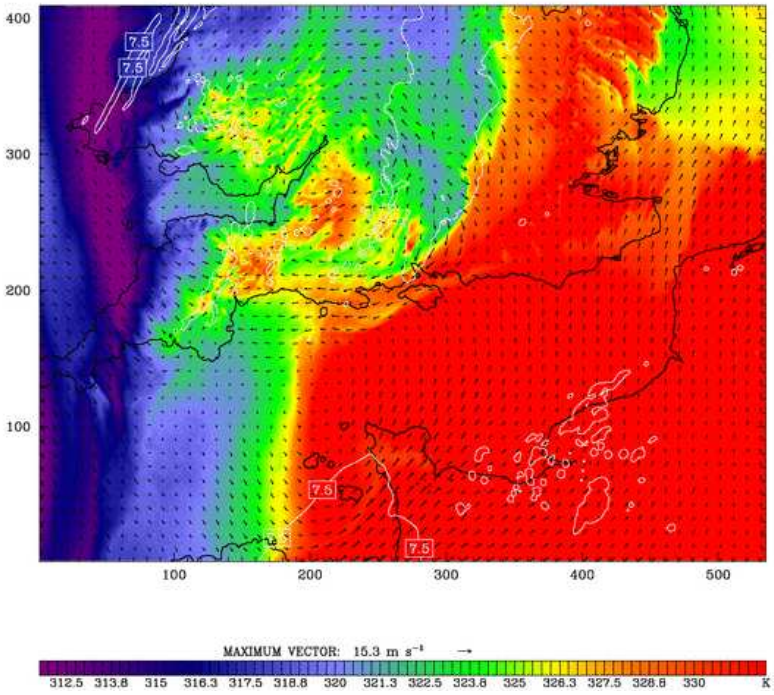

(A) CTL

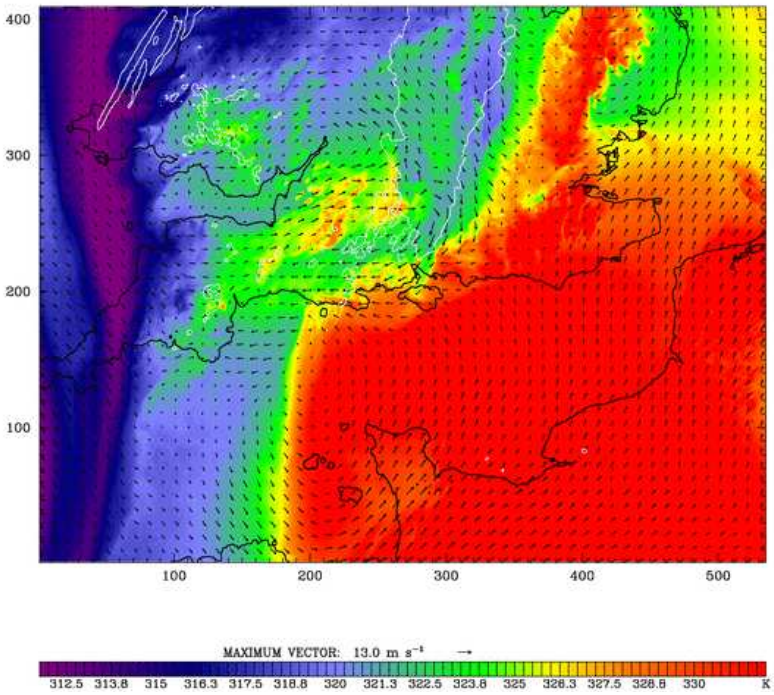

(B) NOSFX

FIGURE 4.8: As Figure 4.7 but at 1330 UTC.

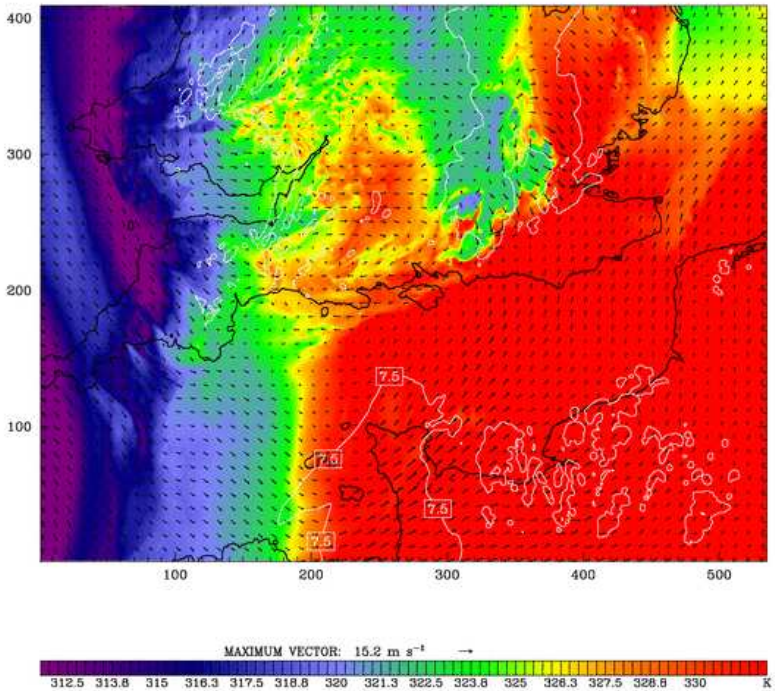

(A) CTL

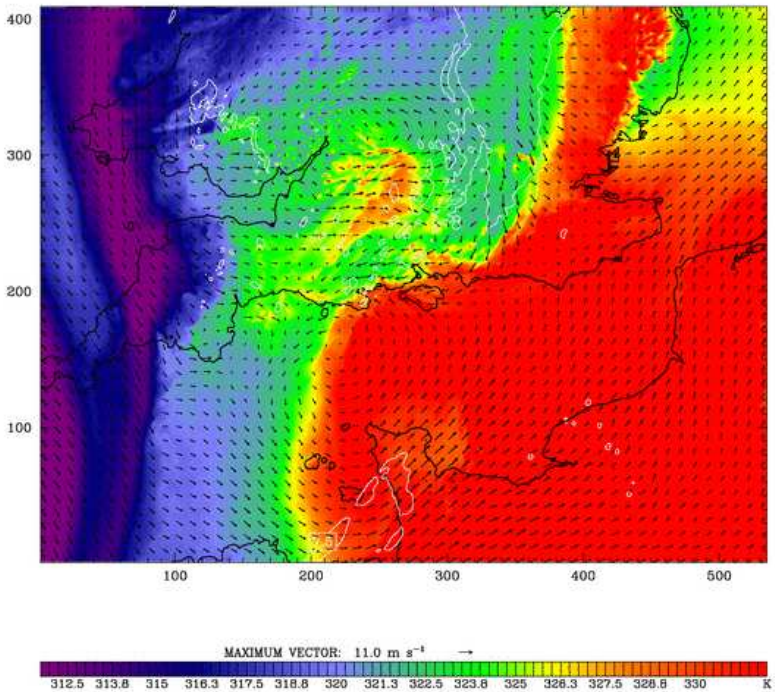

(B) NOSFX

FIGURE 4.9: As Figure 4.7 but at 1500 UTC.

hours earlier than it did in the NOSFX run. In both runs the values of θ_e in the elevated source layer were also greater at 1200 UTC than they were at 0900 UTC (Figure 4.11). This was due to advection, because the elevated layer was not coupled to the surface.

The convection had become fully surface-based in both runs by 1800 UTC, but the high-valued θ_e boundary layer was about twice as deep in the CTL run, where it reached about 2 km (Figure 4.12a), than it was in the NOSFX run, where it reached about 1 km (Figure 4.12b). The increased values of θ_e in the boundary layer in the NOSFX run were purely due to advection of high-valued θ_e air from the south. In the CTL run the increased values of θ_e in the boundary layer were due to a combination of surface heating and advection.

4.1.4 The vertical structure of the convection and its near-environment

The effect of surface latent and sensible heat fluxes on the 3D structure of the convection was investigated by analysing a series of vertical sections of θ_e and system-relative winds for the NOSFX simulation. Sections were made along several lines through the simulated MCS, oriented perpendicular to its direction of propagation, in a similar manner to the vertical sections taken through the CTL run, discussed in Chapter 3. The differences between the NOSFX run and the CTL run along the section that passed through the centre of the simulated MCS (along the y200 line) are described in detail. The along-line variability of the behaviour of the MCS in the NOSFX run was the same as that in the CTL run, so the other vertical sections are not shown.

The initial structure of the MCS and the pre-convective environment in the centre of the NOSFX run was similar to the CTL run. There was a low-level, low-valued θ_e undercurrent in the lowest 1 km ahead of the MCS between 0 and 160 km at 0830 UTC in the NOSFX run (Figure 4.13a). The undercurrent in the NOSFX run had a similar structure to the undercurrent in the CTL run at 0830 UTC (Figure 4.13b). The undercurrent in the NOSFX run was surmounted by an elevated layer of high-valued θ_e air centred at z=2 km (Figure 4.13a). This air was the source air for the convection. The extent and depth of the source layer in the NOSFX run at 0830 UTC was about the same as that in the CTL run at the same time (Figure 4.13b). There was a RIJ of low-valued θ_e air between

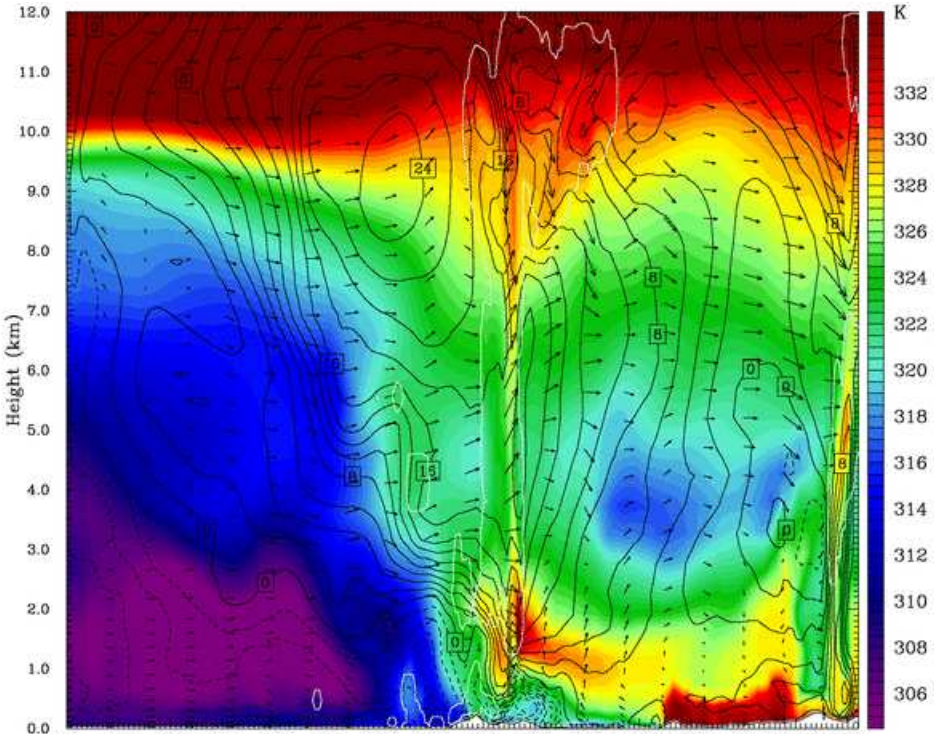

(A) CTL

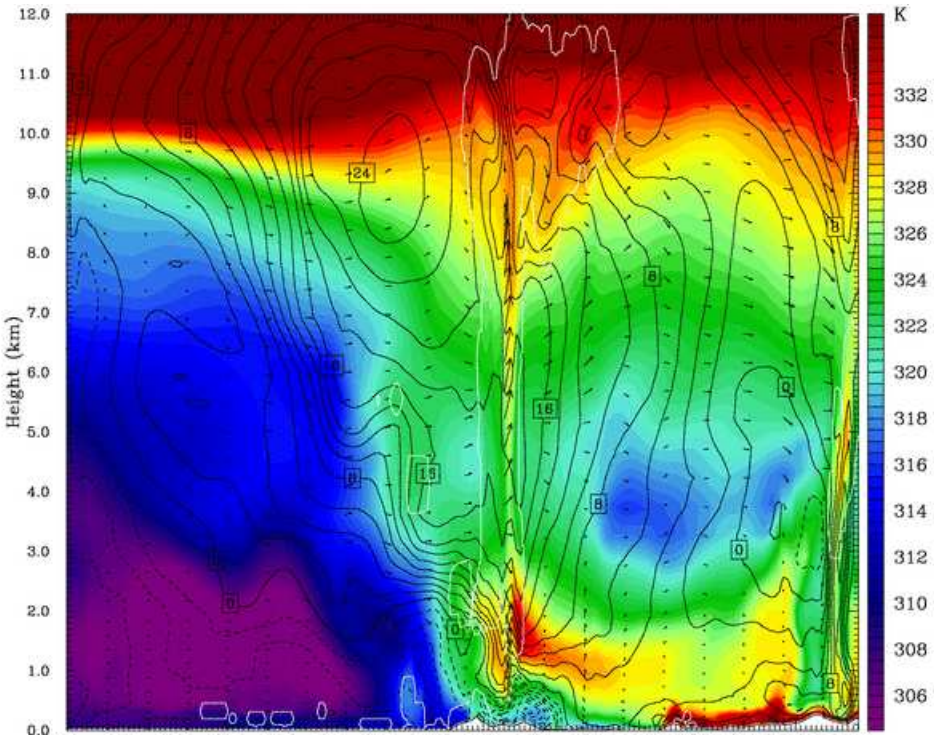

(B) NOSFX

FIGURE 4.10: θ_e (K, colour contour), circulation vectors, horizontal winds into/out of the page (m s^{-1}, solid/dashed black line contour) and total cloud mixing ratio (5x10^{-3} g kg^{-1}, white line contour) at 0900 UTC from the outer domain of the CTL and NOSFX runs. Horizontal distances are in km.

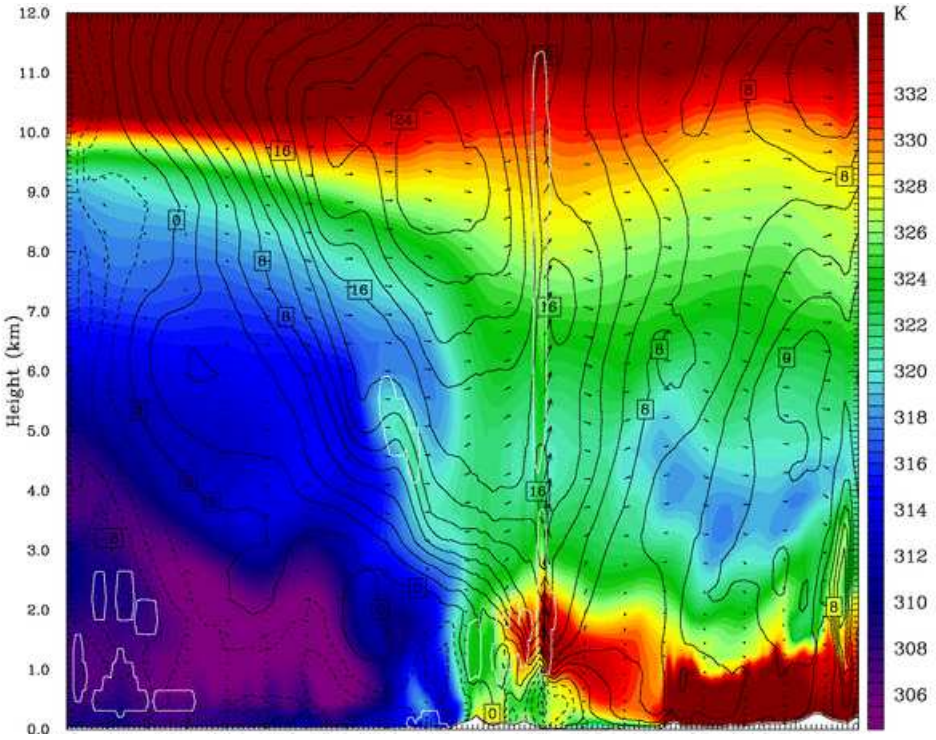

(A) CTL

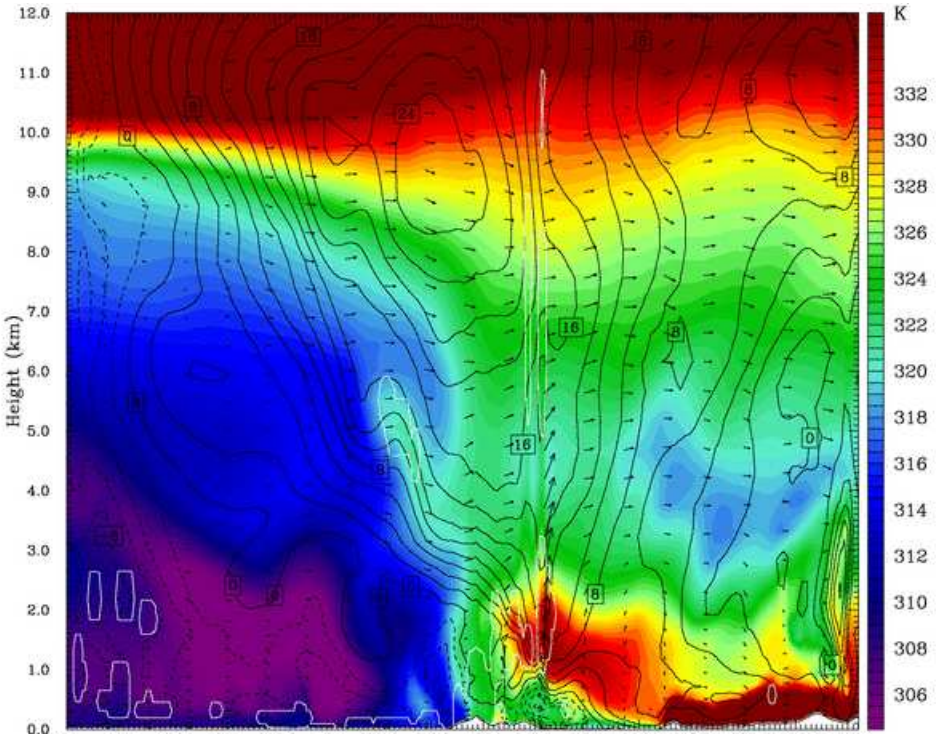

(B) NOSFX

FIGURE 4.11: As Figure 4.10 but at 1200 UTC.

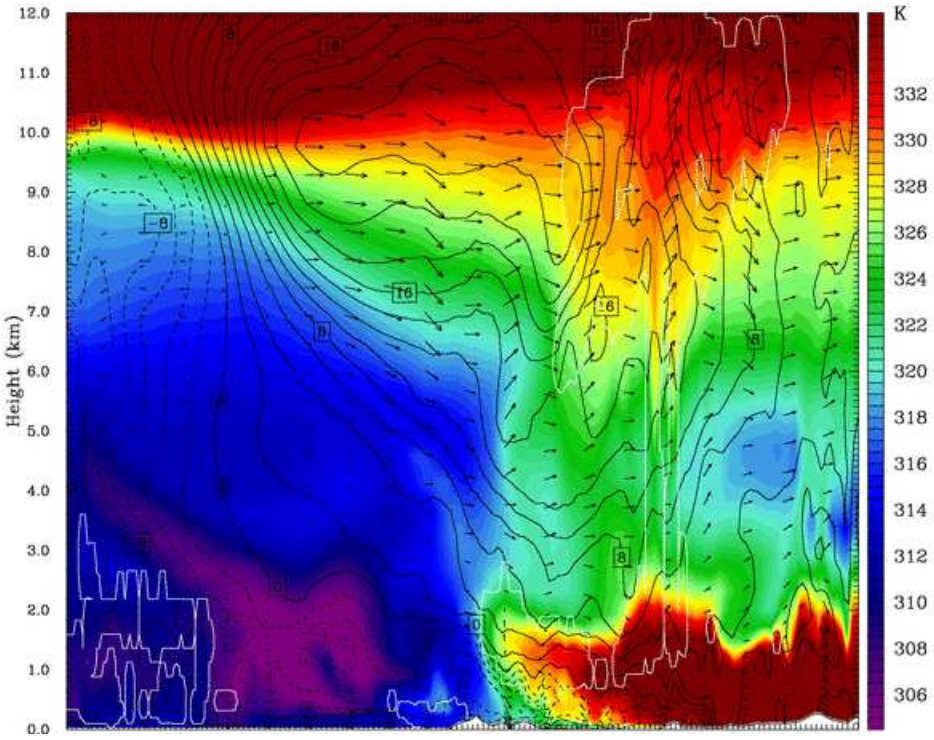

(A) CTL

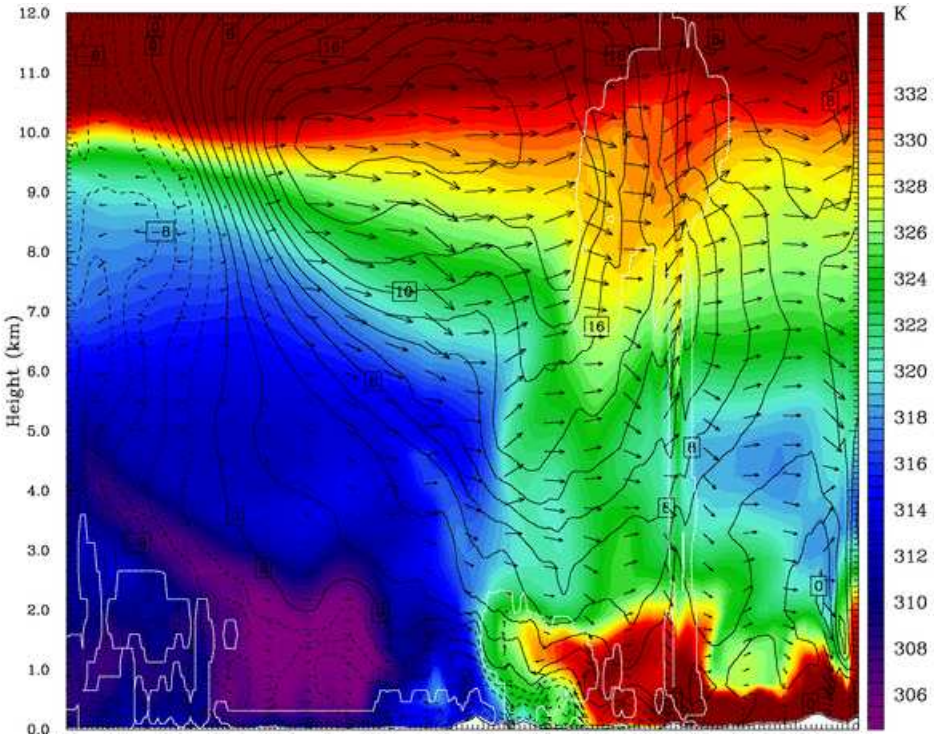

(B) NOSFX

FIGURE 4.12: As Figure 4.10 but at 1800 UTC.

3.0 and 6.0 km in the NOSFX run at 0830 UTC (Figure 4.13a). The RIJ descended under the stratiform region of the MCS but did not reach the surface. The RIJ never reached the surface along this section in the NOSFX run. The descending RIJ constricted the undercurrent and caused a wave to form in the elevated source layer ahead of the convection in the NOSFX run (Figure 4.13a). Similar behaviour occurred in the CTL run at this time (Figure 4.13b). However, the low-valued θ_e air in the RIJ only descended to about z=1.5 km in the NOSFX run (Figure 4.13a), compared to z=1 km in the CTL run (Figure 4.13b). The undercurrent had a similar structure in both the NOSFX and CTL runs at 0830 UTC, and at this early time the effects of surface heating in the CTL run would have been minimal. The difference in the height to which the RIJ descended was therefore probably due to small differences in the 3D structure of the convection in the two runs at this time and not due to a fundamental difference in the dynamics of the system caused by the surface heat fluxes. The RIJ in the NOSFX run was penetrated by an updraught of high-valued θ_e air at 35 km at 0830 UTC (Figure 4.13b). This did not occur at this time in the CTL run, however this was likely to be due to small differences in the structure of the convection between the two runs. The values of θ_e began to increase at low-levels in the NOSFX run between 180 and 240 km at 0830 UTC (Figure 4.13a); this was due to the advection of air from the south. In the CTL run this region was deeper due to the additional effects of surface heating (Figure 4.13b).

The MCS in the NOSFX simulation propagated in a similar direction to the MCS in the CTL simulation (as discussed in Section 4.1.1). The low-level values of θ_e in the east of the NOSFX run did not increase as much as they did in the CTL run because there was no surface heating. A low-valued θ_e undercurrent was still present ahead of the MCS in the NOSFX run at 1330 UTC (Figure 4.14a). At this time in the CTL run there was no undercurrent; the low-level flow towards the storm had high values of θ_e (Figure 4.14b). The inflow to the MCS in the NOSFX run was from the elevated layer of high-valued θ_e air at 1330 UTC (Figure 4.14a). In contrast, the inflow to the MCS in the CTL run at this time was from the high-valued θ_e boundary layer (Figure 4.14b). The removal of the surface latent and sensible heat fluxes delayed the transition from elevated to surface-based convection in the NOSFX run. The removal of the surface heat fluxes also caused the undercurrent to persist in the NOSFX run. Low-valued θ_e air reached the surface at 1330 UTC in the NOSFX run (Figure 4.14a). The system-positive winds in the RIJ did not

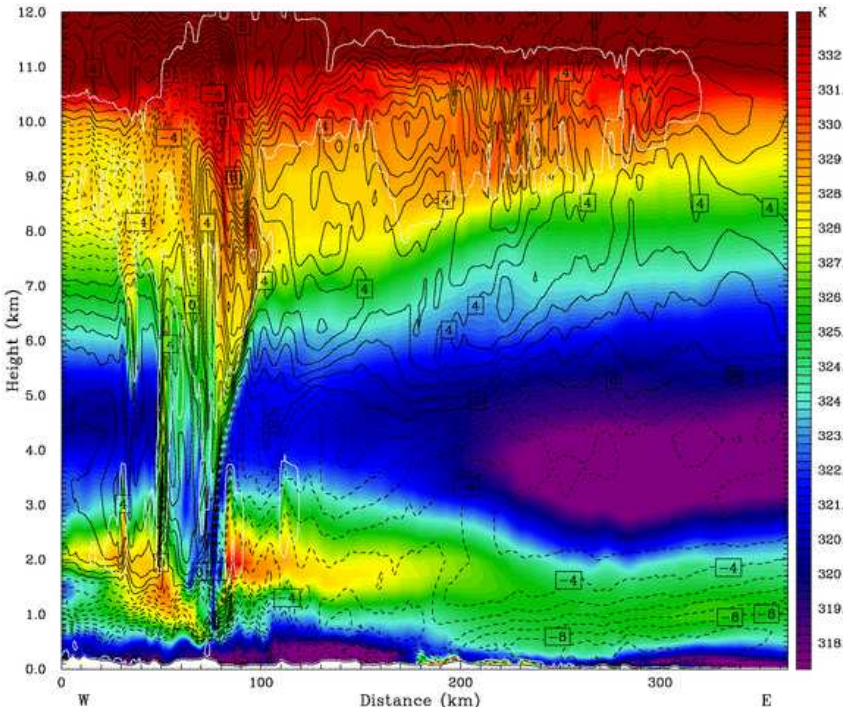

(A) NOSFX

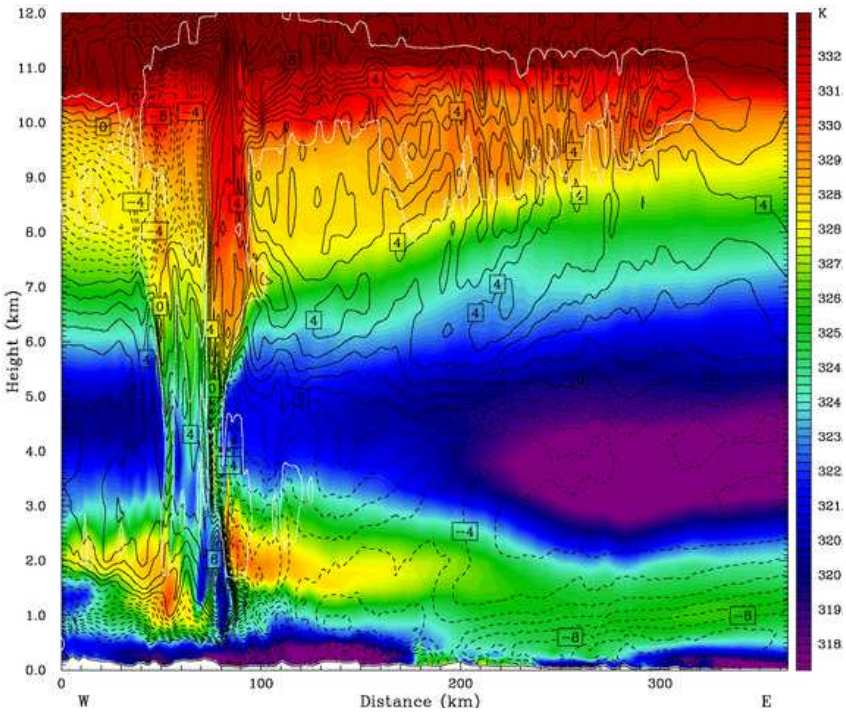

(B) CTL

FIGURE 4.13: y200 vertical section of θ_e (K, colour contour), system-relative horizontal winds (m s^{-1}, black line contour, solid positive and dashed negative) and total cloud mixing ratio (5x10^{-3} g kg^{-1}, white line contour) at 0830 UTC from the inner domain of the NOSFX and CTL runs.

reach the surface along the y200 section in the NOSFX run so the origin of the low-valued θ_e air was probably from the convective downdraughts. A gravity current formed from the outflow of low-valued θ_e air and, like the CTL run, this coincided with an increase in the speed of the MCS in the NOSFX simulation (Figure 4.6). However, the gravity current in the NOSFX run flowed into a region where the environmental air had much lower values of θ_e than in the CTL run (Figure 4.14). This was because the undercurrent still existed in the NOSFX run, whereas surface heating in the CTL run had increased the values of θ_e at low-levels.

The undercurrent in the NOSFX run had dissipated by 1500 UTC (Figure 4.15a). Ahead of the MCS the values of θ_e at low-levels and in the boundary layer in the NOSFX simulation at this time had increased significantly from previous times. The convection in the NOSFX run was in the transition to becoming fully surface-based (Figure 4.15a). In contrast, the convection in the CTL run had been surface-based for some time by 1500 UTC (Figure 4.15b). The convection was much weaker in the NOSFX run at 1500 UTC than it was in the CTL run: the cloud was narrower (Figure 4.15) and the precipitation was lighter (Figure 4.4). Although a gravity current formed in the NOSFX run, the lower environmental values of θ_e into which it flowed meant that it was weaker than the gravity current that formed in the CTL run. This is shown by Equation (1.1) in Chapter 1. It is likely that the weaker gravity current in the NOSFX run was unable to initiate new convection for as long as the gravity current in the CTL run, leading to the earlier dissipation of the NOSFX convective system. Deep convection was initiated at the leading edge of the gravity current in the CTL run at 1500 UTC (300 km in Figure 4.15b). There was no deep convection associated with the leading edge of the gravity current in the NOSFX run at this time (Figure 4.15a). The RIJ in the NOSFX run did not descend below 2.5 km at 1500 UTC (Figure 4.15a), whereas the RIJ in the CTL run descended to 1 km (Figure 4.15b). The RIJ in the NOSFX run was probably weaker than the RIJ in the CTL run at 1500 UTC because the narrower cloud and lighter rain due to the weaker convection meant that there was less cooling by evaporation, sublimation and melting. The effects of the diabatic cooling processes on the simulated MCS are explored later in this Chapter in Section 4.2.

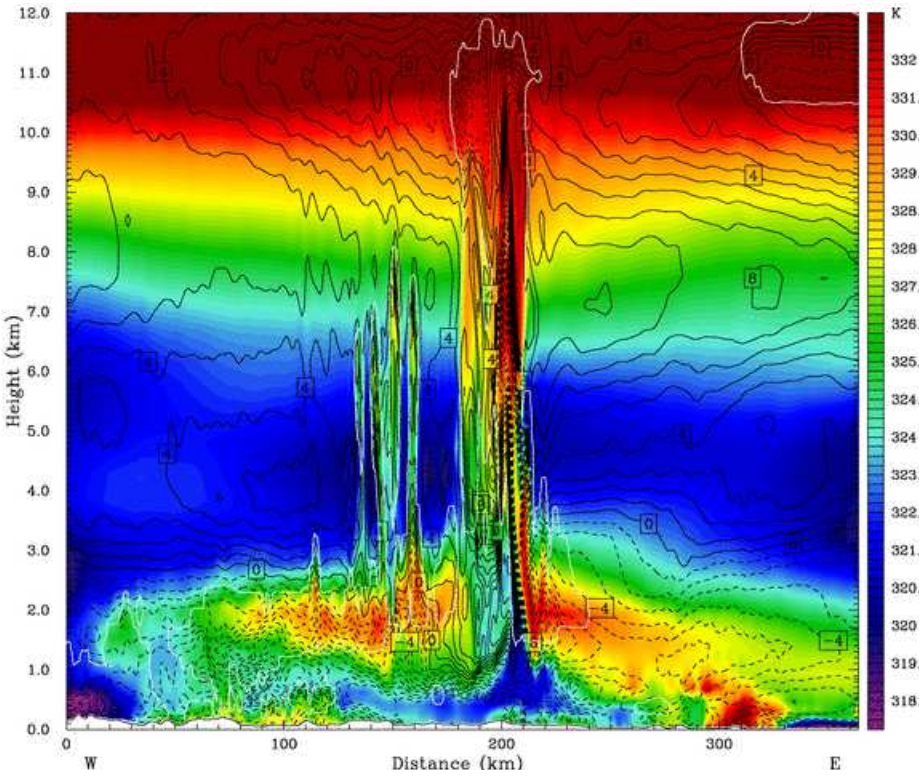

(A) NOSFX

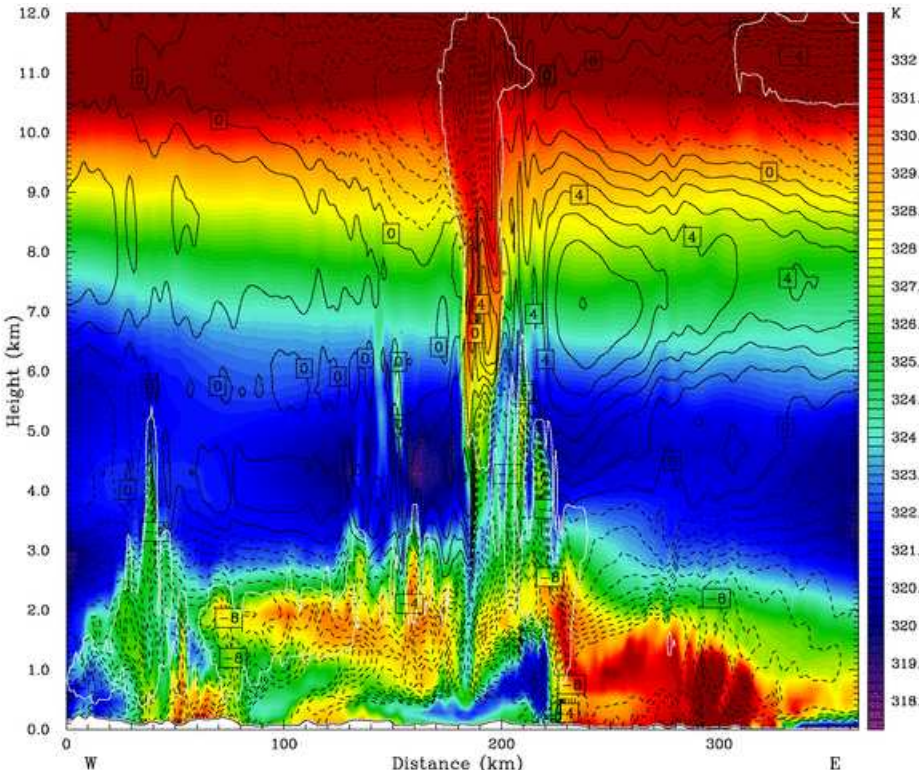

(B) CTL

FIGURE 4.14: As Figure 4.13 but at 1330 UTC.

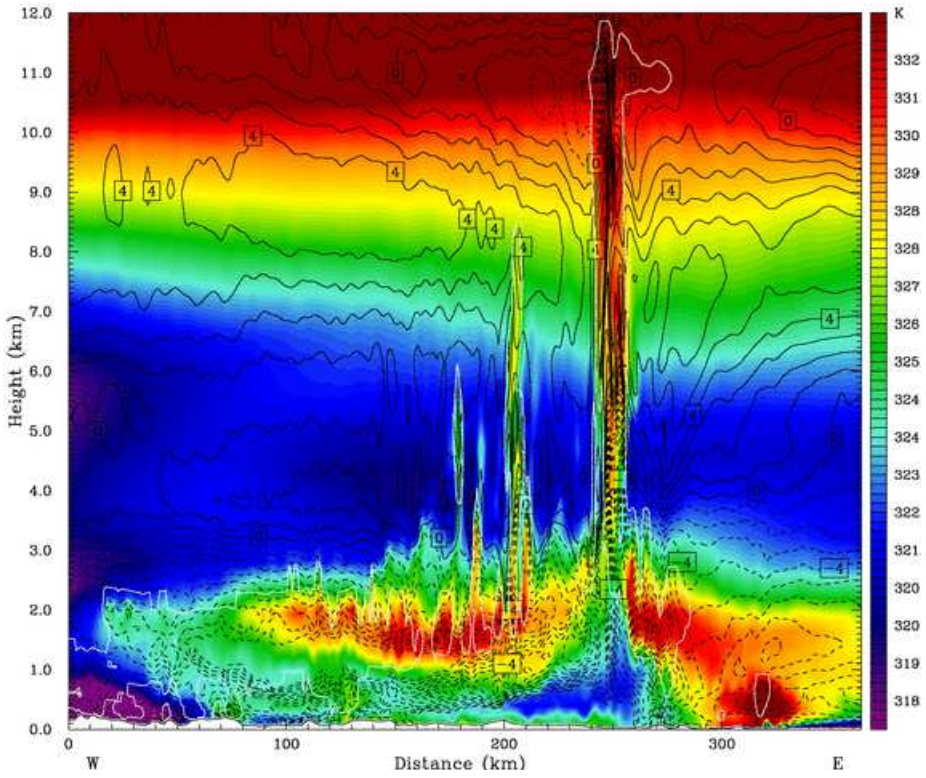

(A) NOSFX

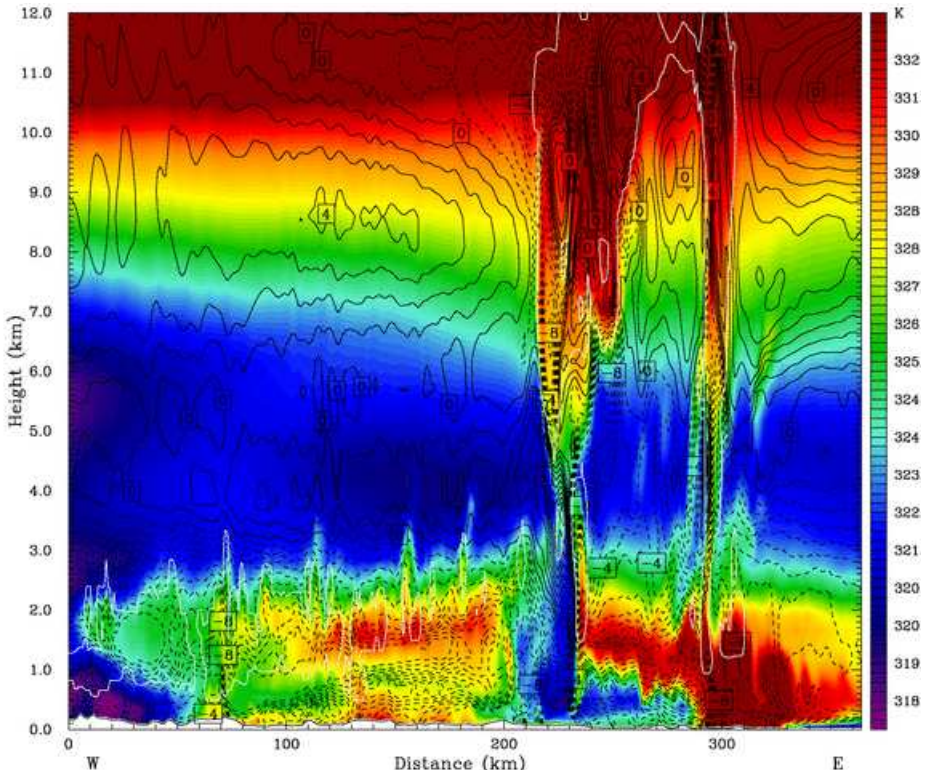

(B) CTL

FIGURE 4.15: As Figure 4.13 but at 1500 UTC.

4.1.5 Summary of the effect of the surface latent and sensible heat fluxes on the simulated MCS

The surface latent and sensible heat fluxes did not have a significant effect on the structure of the convection or the RIJ. This was similar to the results of Trier *et al.* (2011), who found that surface warming had little effect on the strength or structure of their simulated elevated nocturnal MCS until late morning, when the convection had become primarily surface-based. The along-line variability of the MCS in the NOSFX run was the same as that of the CTL run: in the north of the MCS the RIJ penetrated through the undercurrent to the surface and formed a gravity current at about 1000 UTC. After this occurred the RIJ rose back up above the undercurrent and did not penetrate to the surface again. The convection remained elevated and the gravity current eventually dissipated. In the rest of the MCS the RIJ did not reach the surface at any time. The undercurrent was constricted by the RIJ and waves formed at the top of the undercurrent and in the elevated source layer.

Although the surface heat fluxes did not have a significant effect on the internal structure of the convection, they did, however, have a significant effect on the thermodynamic structure of the pre-convective environment. Removing the surface heat fluxes from the model meant that the pre-convective boundary layer did not deepen as much as it did in the CTL run: the values of θ_e in the lowest 1 km ahead of the MCS in the NOSFX run were significantly lower than they were in the CTL run. The lack of surface heating in the NOSFX run also meant that the low-valued θ_e undercurrent persisted for longer than it did in the CTL run. This prolonged the period of elevated, wave-lifted convection in the NOSFX run. When the source of inflow to the MCS in the CTL run was from the region of high-valued θ_e boundary layer air, the source of inflow in the NOSFX run was still from the elevated layer of high-valued θ_e air.

The surface heat fluxes also affected the way in which the simulated MCS interacted with the pre-convective environment. The convective downdraughts formed a gravity current in both the CTL and the NOSFX simulations at about 1330 UTC. The gravity current in the CTL run initiated new deep convection, but this did not occur in the NOSFX run. This was because the gravity current in the NOSFX run was weaker than the gravity current in the CTL run. The values of θ_e in the lowest 1 km of the NOSFX run were

lower than those in the CTL run, so the difference between the values of θ_e in the gravity current and its environment was much less. The lower-valued θ_e air near the surface in the NOSFX run was also more stable than the higher-valued θ_e air near the surface in the CTL run and would have required deeper lifting to reach its level of free convection. The MCS weakened and began to dissipate much earlier in the NOSFX run than it did in the control run. This was because no new cells of deep convection were initiated by the gravity current in the NOSFX run.

It is difficult to determine exactly when convection became surface-based and gravity current-lifted in the NOSFX run, as the shallow layer of high-valued θ_e air ahead of the system had values of θ_e up to 4 K greater than in the elevated layer of high-valued θ_e close to the storm (332 compared to 328 K). Gravity current dynamics could therefore have dominated even though the storm still appeared to be in the elevated source layer.

4.2 The sensitivity of the simulated MCS to diabatic cooling processes

The following Section discusses the effects on the simulated MCS of removing the diabatic coolings from microphysical processes from the model.

4.2.1 The model spin-up period

Figure 4.16 is a timeseries of the maximum vertical velocity in the CTL, NOEVP, NOSUB, NOMLT and NOCOOL runs, which shows that there was a similar spin-up period, where the vertical velocity undergoes an overshooting period before stabilising, of about 6 hours for all runs. The intensities of the simulated MCSs were reasonably similar in the early stages and only began to show significant divergence from 14 hours onwards. It is not possible to tell whether the divergence of the models after 14 hours was due to the differences in the microphysics or the carrying forward of small differences from the spin-up period.

4.2.2 The structure and evolution of the precipitation

The diabatic cooling processes had a significant effect on the structure and evolution of the precipitation associated with the simulated convection. In the following discussion of the structure and evolution of the precipitation, each Figure shows the reflectivity field from all of the model runs at a given time, although the effect of each cooling process is discussed individually.

Removing evaporative cooling from the model caused little change to the initial structure of the precipitation. Initially the reflectivity field of the NOEVP run (Figure 4.17b) was similar to that of the CTL run (Figure 4.17a). Intense precipitation covered a slightly greater area in the NOEVP run. Like the CTL run, the MCS in the NOEVP run propagated from the southwest to the northeast. Its structure was less elongated than that of the MCS in the CTL run at 1200 UTC (Figure 4.18b compared with Figure 4.18a). At 1200 UTC the MCS in the CTL run began to split into two; this behaviour did not occur in the NOEVP run. There were trailing cells of precipitation behind the MCS in

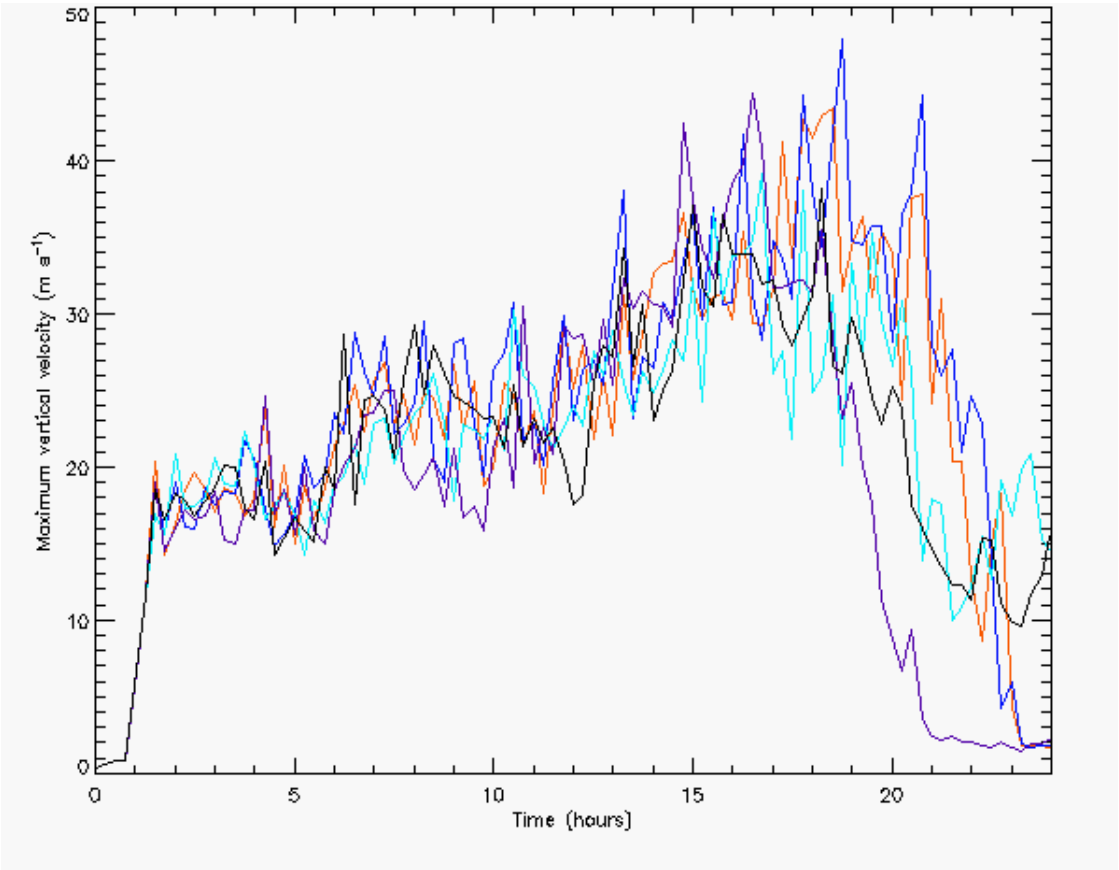

FIGURE 4.16: Timeseries of maximum vertical velocity (m s^{-1}) for the CTL (black), NOEVP (red), NOSUB (dark blue), NOMLT (light blue) and NOCOOL (purple) runs.

both the CTL and NOEVP runs at 1400 UTC (Figures 4.19a and 4.19b). However, in the NOEVP run there was deep convection from the trailing cells at 1600 UTC (Figure 4.20b), which did not occur in the CTL run (Figure 4.20a). The MCS in the NOEVP run had propagated out of the model domain by 2000 UTC (Figure 4.21b), as had the MCS in the CTL run (Figure 4.21a), but in the NOEVP run deep convection from the trailing cells remained. This convection propagated more to the east than the initial MCS.

Removing sublimational cooling from the model had a very similar effect on the structure of the precipitation to the removal of evaporative cooling. Initially the reflectivity field of the NOSUB run (Figure 4.17c) was similar to that of the CTL run (Figure 4.17a) and that of the NOEVP run (Figure 4.17b). The MCS in the NOSUB run also propagated from the southwest to the northeast. Similarly to the NOEVP run, its structure was less elongated than that of the MCS in the CTL run at 1200 UTC (Figure 4.18c compared to Figure 4.17a). The MCS in the NOSUB run did not split into two. There were trailing cells

of precipitation behind the MCS in the NOSUB run at 1400 UTC (Figure 4.19c). There was deep convection from the trailing cells in the NOSUB run at 1600 UTC (Figure 4.20c). The MCS in the NOSUB run propagated out of the domain by 2000 UTC, but deep convection from the trailing cells remained and propagated more to the east than the initial MCS (Figure 4.21c).

Removing cooling by melting from the model did not have as significant an effect on the precipitation as the removal of cooling by evaporation or sublimation. Initially the reflectivity field of the NOMLT run (Figure 4.17d) was similar to that of the CTL run (Figure 4.17a). The intense precipitation associated with the convective system in the NOSUB run propagated from the southwest to the northeast and had the same elongated structure at 1200 UTC (Figure 4.18d) as the CTL run (Figure 4.18a). Although at 1200 UTC there was some evidence of the MCS in the NOMLT run splitting, the process did not fully establish. There was a single MCS in the NOMLT run at 1400 UTC (Figure 4.19d), compared to two MCSs in the CTL run at this time (Figure 4.19a). There were cells of intense precipitation ahead of the system in the NOMLT run at 1400 UTC. These formed along what will be shown later to be an outflow boundary associated with a gravity current. The MCS in the NOMLT run caught up with and merged with these cells by 1600 UTC (Figure 4.20d). Similarly to the CTL run, the MCS in the NOMLT propagated off the east coast of the UK and dissipated by 2000 UTC (Figures 4.21a and 4.21d).

Removing all diabatic cooling processes from the model had a similar effect on the precipitation to the removal of cooling by evaporation and sublimation. Initially the reflectivity field of the NOCOOL run (Figure 4.17e) was similar to that of the CTL run (Figure 4.17a). The MCS in the NOCOOL run propagated from the southwest to the northeast. Similarly to the NOEVP and NOSUB runs, its structure was significantly less elongated than that of the MCS in the CTL run at 1200 UTC (Figure 4.18e compared to Figure 4.17a). The MCS in the NOCOOL run did not split into two. Trailing cells of precipitation developed behind the MCS in the NOCOOL run at 1400 UTC (Figure 4.19e). Deep convection developed from the trailing cells in the NOCOOL run by 1600 UTC (Figure 4.20e), which continued to deepen. By 2000 UTC there was a significant amount of intense precipitation in the NOCOOL run (Figure 4.21e).

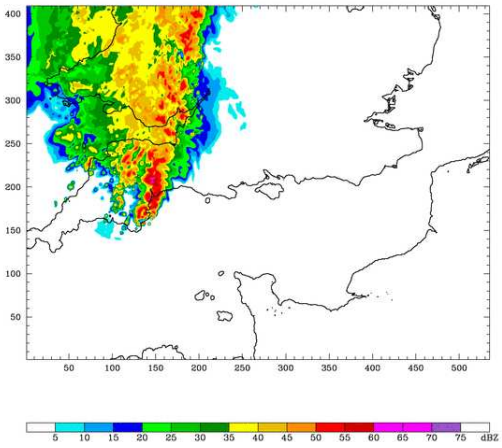

(A) CTL

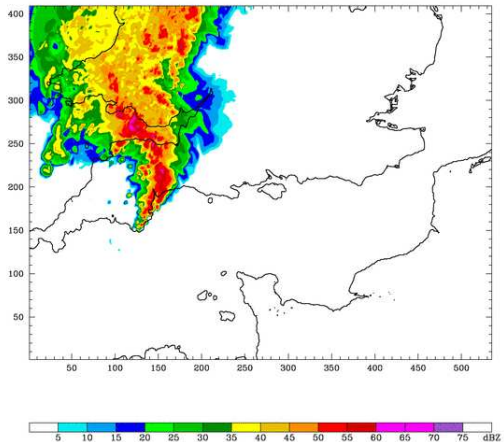

(B) NOEVP

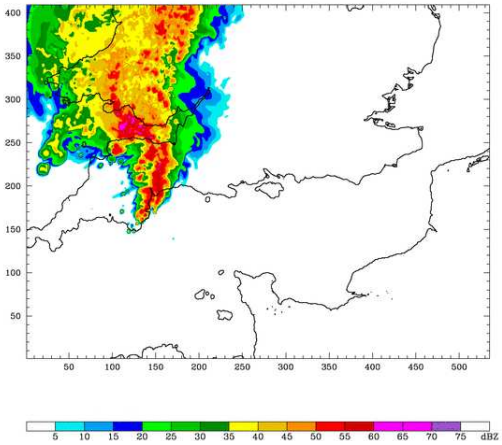

(C) NOSUB

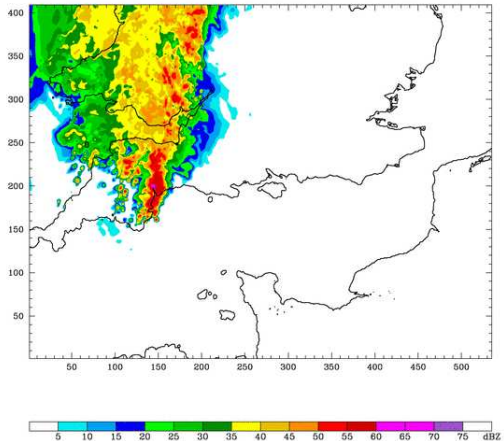

(D) NOMLT

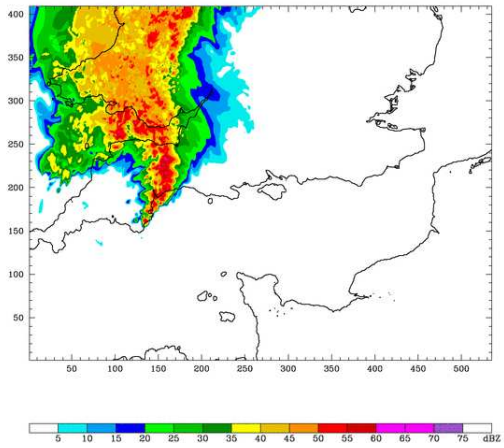

(E) NOCOOL

FIGURE 4.17: Simulated reflectivity (dBZ) field at 0700 UTC from the inner domain for the CTL, NOEVP, NOSUB, NOMLT, and NOCOOL runs. Distances are in km.

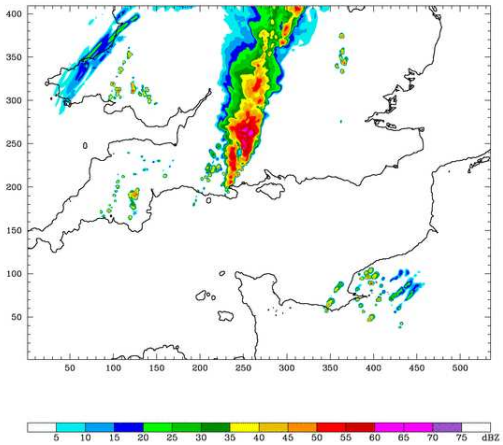

(A) CTL

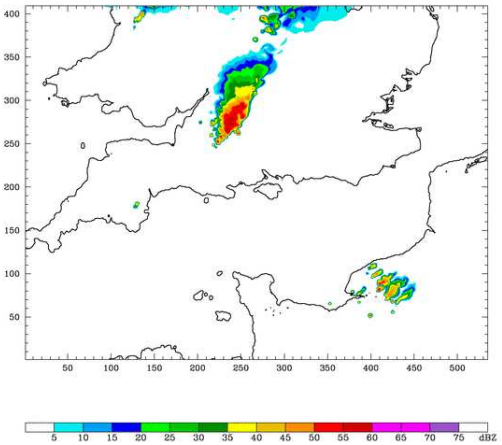

(B) NOEVP

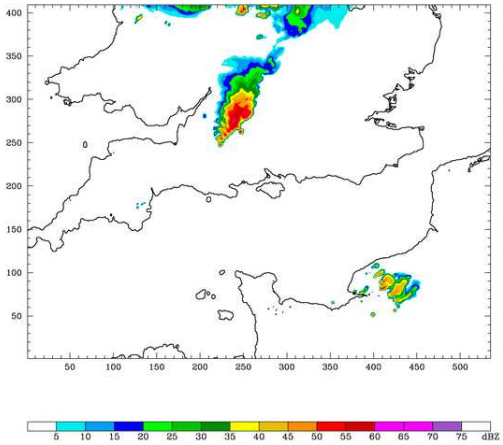

(C) NOSUB

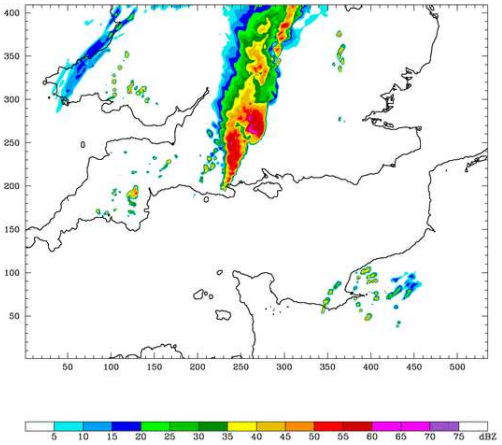

(D) NOMLT

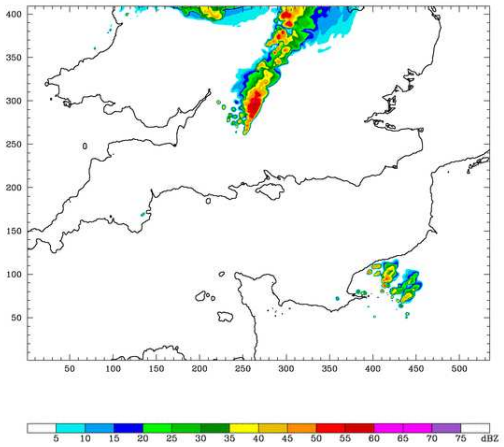

(E) NOCOOL

FIGURE 4.18: As Figure 4.17 but at 1200 UTC.

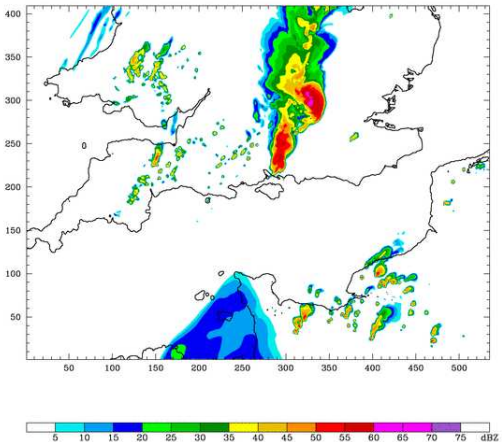

(A) CTL

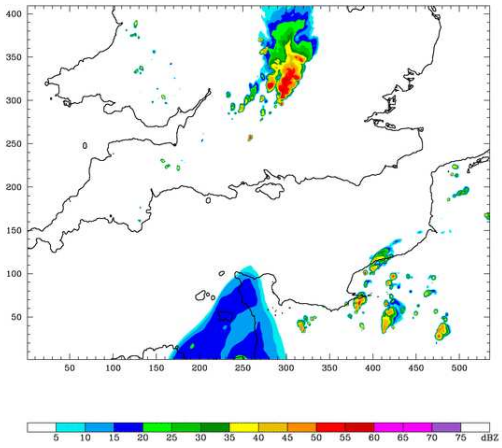

(B) NOEVP

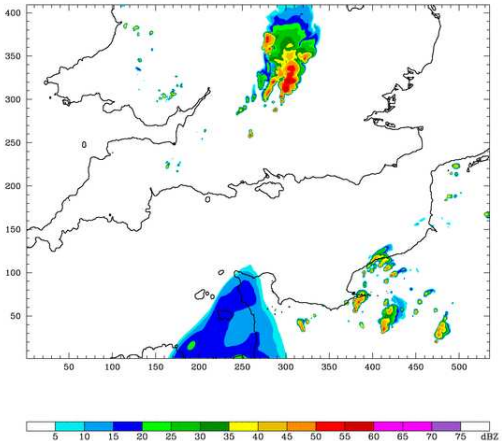

(C) NOSUB

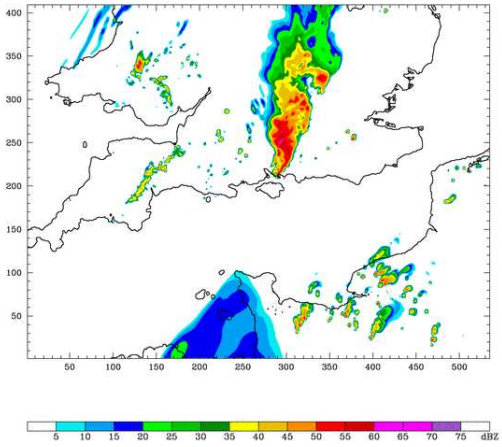

(D) NOMLT

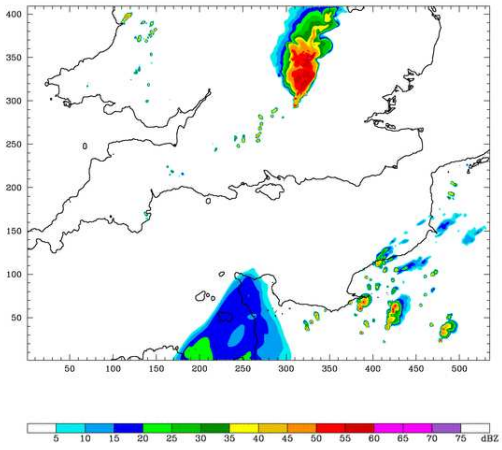

(E) NOCOOL

FIGURE 4.19: As Figure 4.17 but at 1400 UTC.

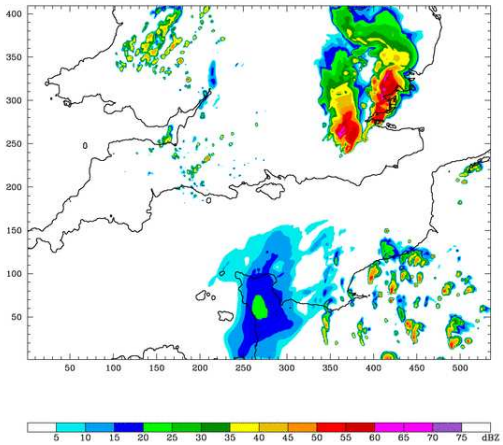

(A) CTL

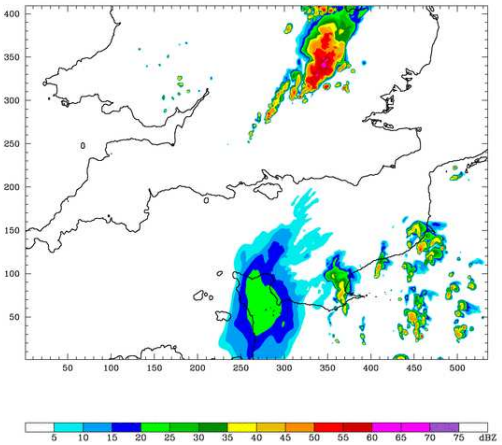

(B) NOEVP

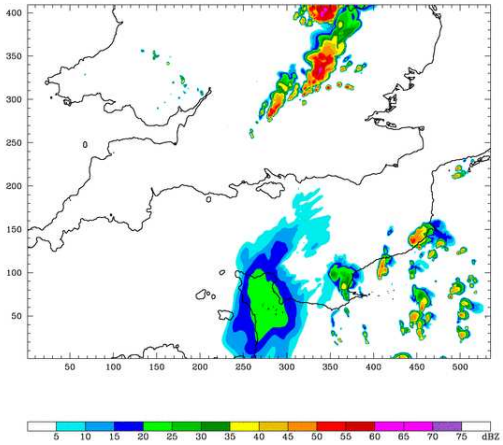

(C) NOSUB

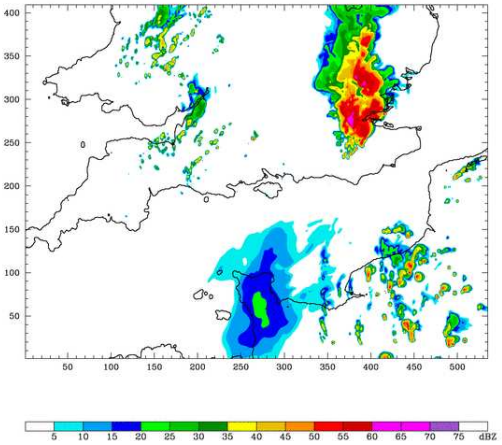

(D) NOMLT

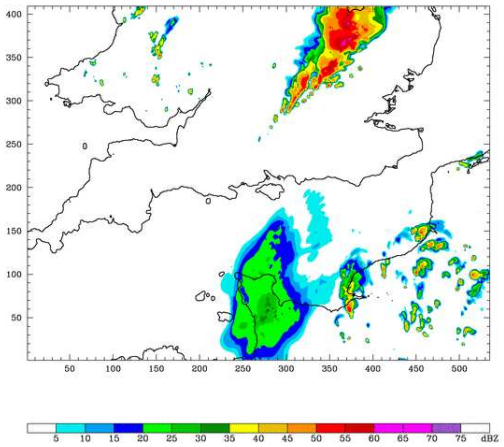

(E) NOCOOL

FIGURE 4.20: As Figure 4.17 but at 1600 UTC.

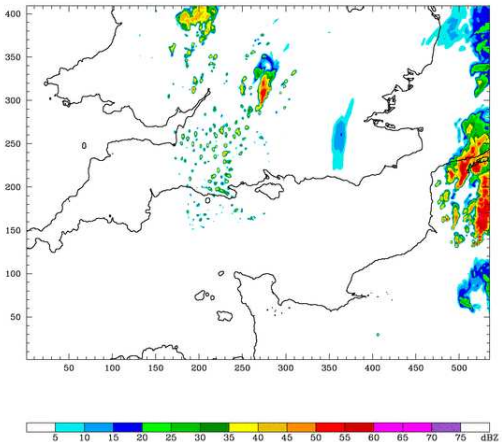

(A) CTL

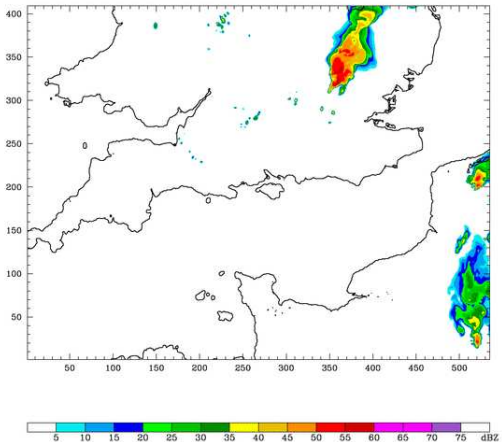

(B) NOEVP

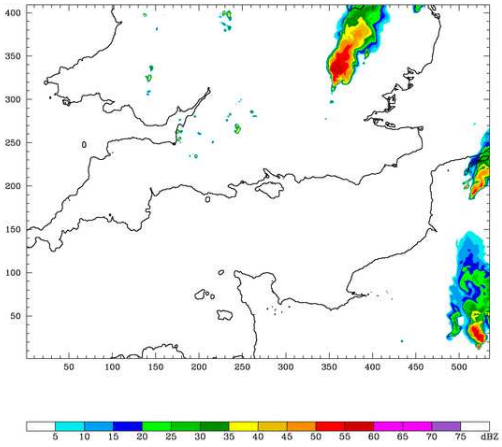

(C) NOSUB

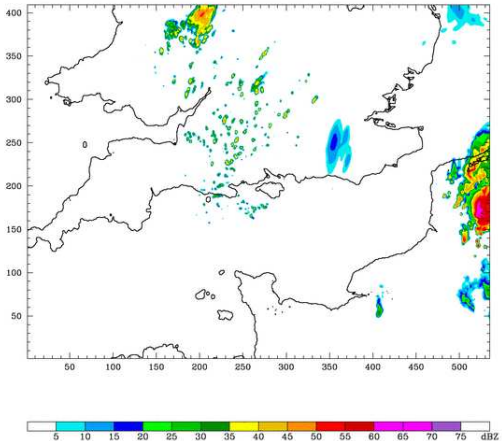

(D) NOMLT

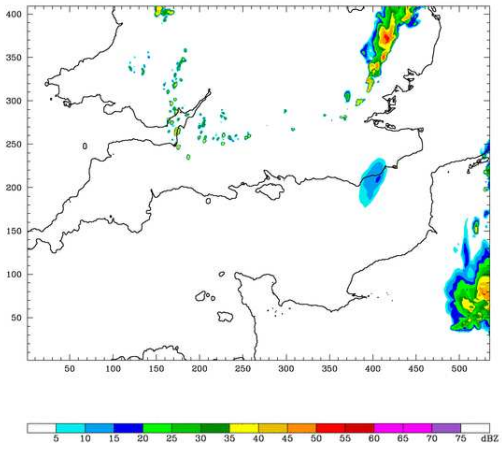

(E) NOCOOL

FIGURE 4.21: As Figure 4.17 but at 2000 UTC.

In summary, diabatic cooling processes affected the propagation of the simulated MCS and the initiation of new convective cells. Evaporative and sublimational cooling had a much greater effect on the structure and evolution of the precipitation than cooling by melting. This is perhaps not surprising, as the values of the latent heats of evaporation and sublimation are of the same order of magnitude, while the value of the latent heat of melting is an order of magnitude smaller (List, 1984). When cooling by melting was removed from the model, the structure and evolution of the precipitation was very similar to that of the CTL run. The MCS in the NOMLT run was elongated to the south, similar to the MCS in the CTL run. Intense precipitation formed ahead of the MCS in both the CTL and NOMLT runs. In the CTL run this was shown to be along a gravity current outflow boundary (Chapter 3); this will later also be shown to be true for the NOMLT run. In contrast, removing cooling by evaporation and sublimation caused the precipitation to propagate more to the northeast. In the NOEVP, NOSUB and NOCOOL runs the MCS was not elongated to the south in the way that it was in the CTL and NOMLT runs. No leading cells of precipitation formed when cooling by evaporation and sublimation were removed. This will later be shown to be because no gravity current outflow formed in these runs. Instead, trailing cells of precipitation formed behind the MCSs in the NOEVP, NOSUB and NOCOOL runs. One particularly notable feature was that the diabatic cooling processes all seemed to favour the split of the system: only in the CTL run did the MCS split into two.

4.2.3 The velocity of the simulated MCS

To determine the effects of the diabatic cooling processes on the system velocity of the simulated MCS, several Hovmöller diagrams of vertical velocity and column-integrated cloud were made from west to east through the model domain along constant y-indices for each run, as for the CTL run in Chapter 3. A system velocity (or velocities, in the runs where the MCS had two distinct system velocities) was determined from each Hovmöller diagram, and the resulting set of system velocities for each run were averaged to determine a mean system velocity. One Hovmöller diagram for each run is shown in this Section.

The MCS in the NOEVP run (Figure 4.22) had a single system velocity of (6.1±1.5) m s^{-1}. Trailing cells developed along the y320 line at about 1600 UTC, but the velocity of these

cells was the same as the velocity of the main MCS. Similar behaviour occurred along the y320 line in the NOSUB run (Figure 4.23), which had a system velocity of (5.1±1.7) m s^{-1}. The NOMLT run (Figure 4.24) had a system velocity of about (6.5±1.3) m s^{-1} from the development of convection until about 1500 UTC, after which time the system velocity increased to about (12.4±1.6) m s^{-1} No trailing (or outflow) cells developed along the y320 line in the NOMLT run. The NOCOOL run (Figure 4.25) showed similar behaviour to the NOEVP and NOSUB runs: only one system velocity was observed along the y320 line, (7.2±1.7) m s^{-1}. The system stalled for about 2 hours along this y-index at about 1500 UTC, but after this time the system velocity was the same as its initial value.

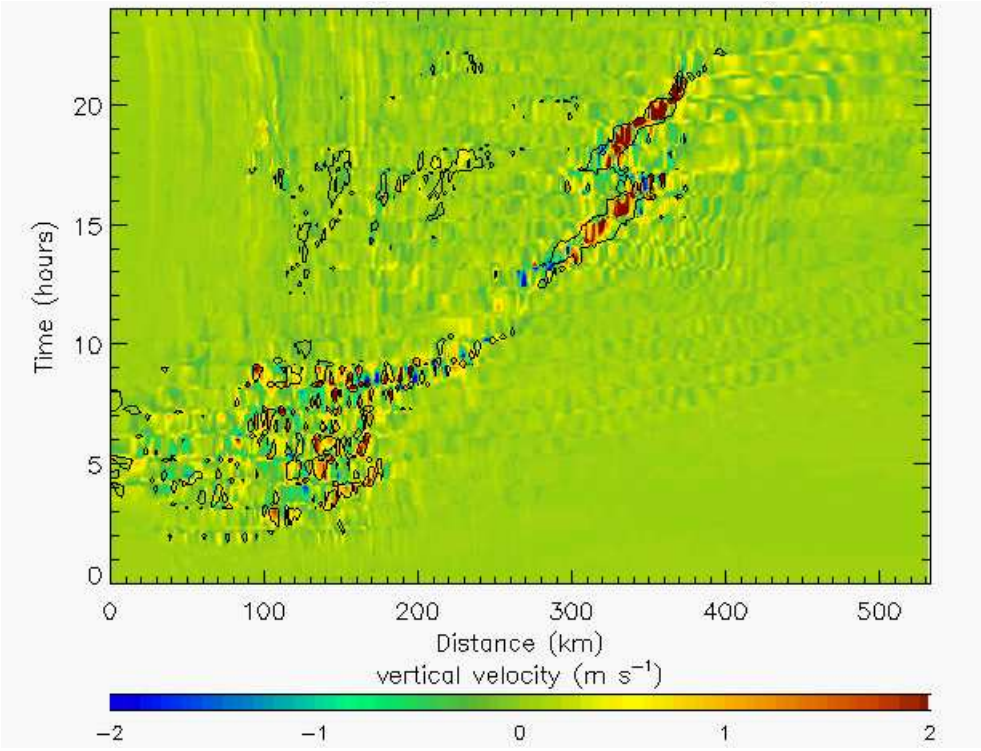

FIGURE 4.22: NOEVP: Hovmöller diagram of vertical velocity (m s^{-1}, colour contour) and column-integrated cloud at 2.0 g kg^{-1} (black line contour) along the y320 y-index at model level 24.

A comparison of the system velocities in each of the sensitivity runs (including the NOSFX run, discussed previously in Section 4.1) is shown in Figure 4.26. Of the diabatic cooling sensitivity runs, only the MCS in the NOMLT run was similar to the CTL run in having two distinct system velocities. Unlike the CTL run, the simulated MCS in the NOEVP, NOSUB and NOCOOL runs only had one system velocity. The system velocity was, within the error limits, the same in each of these runs and was also the same as the initial system velocity in the CTL and NOMLT (and NOSFX) runs. This system velocity was about

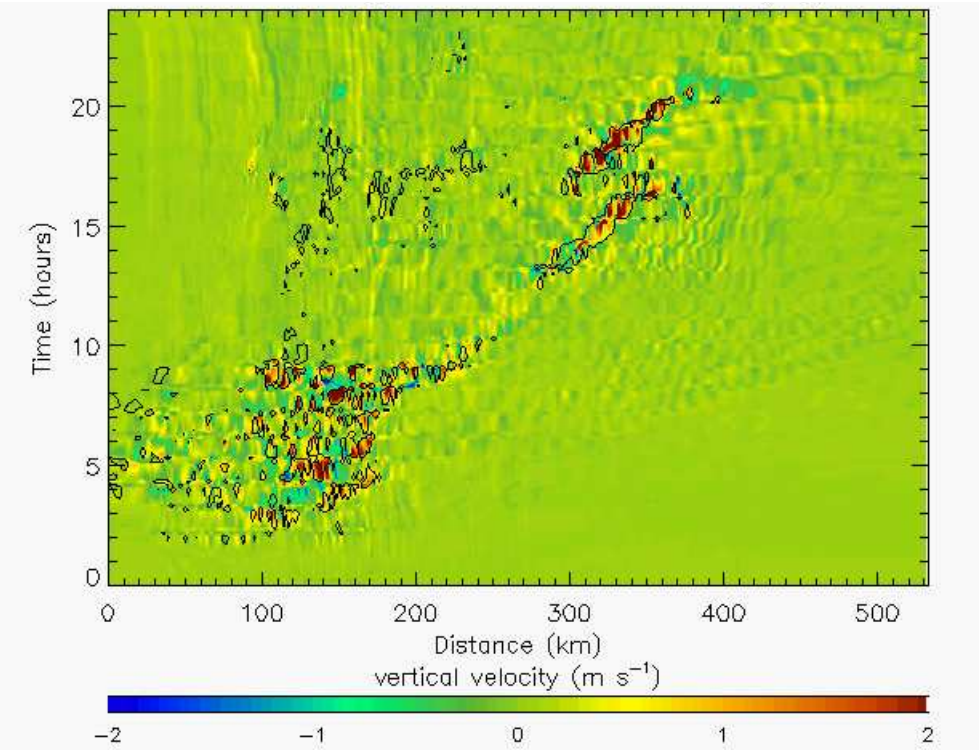

FIGURE 4.23: As Figure 4.22 but for the NOSUB run.

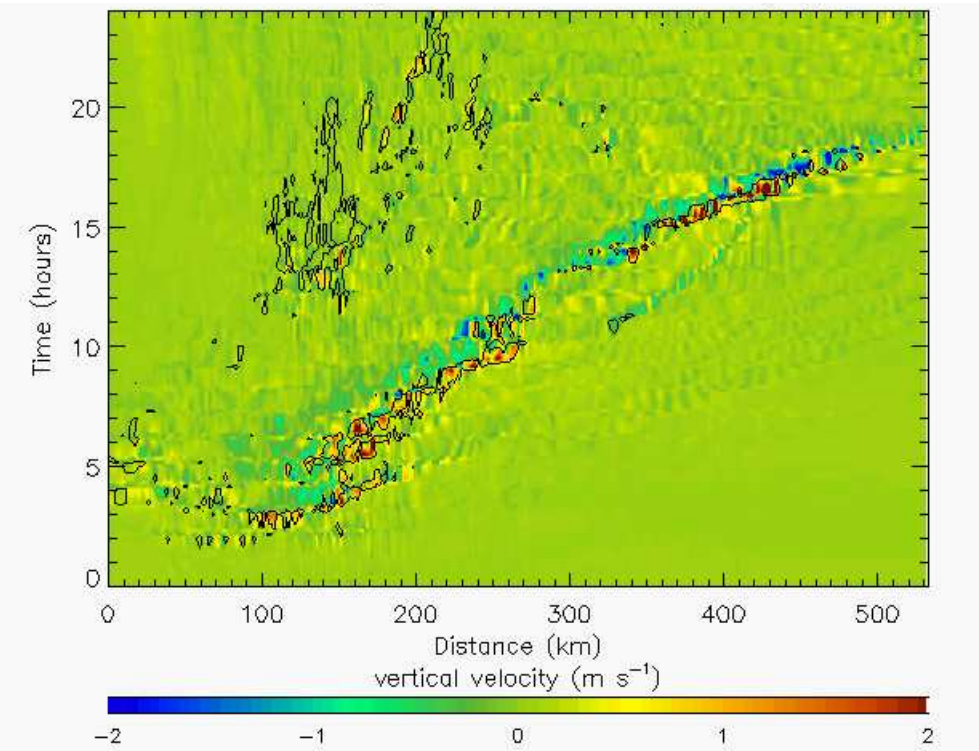

FIGURE 4.24: As Figure 4.22 but for the NOMLT run.

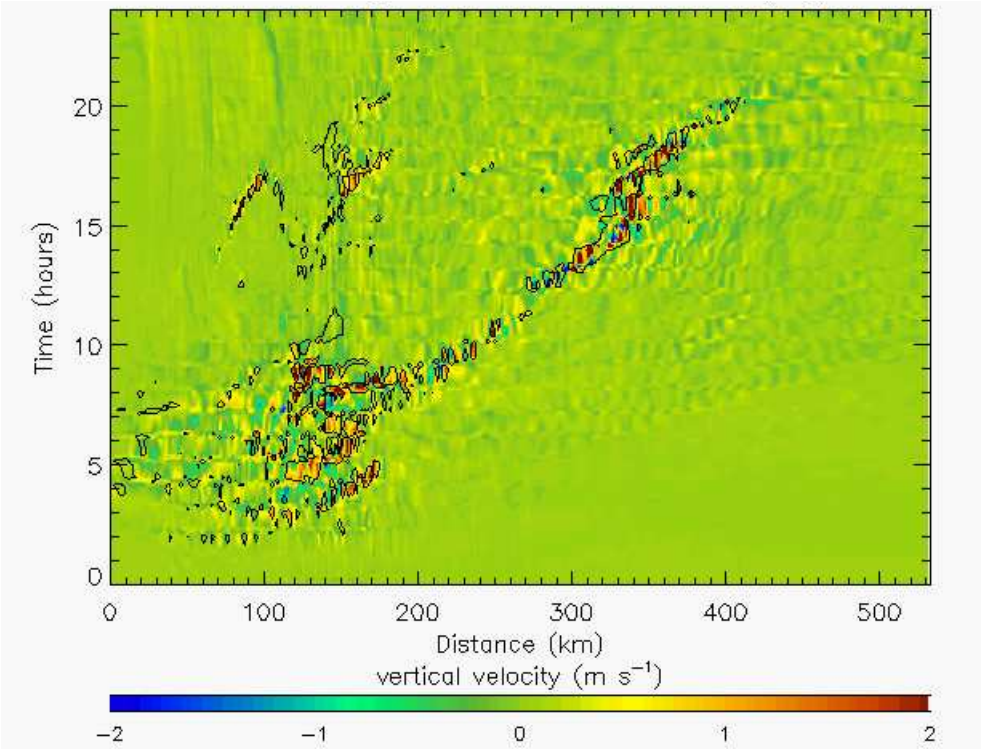

FIGURE 4.25: As Figure 4.22 but for the NOCOOL run.

6.5 m s^{-1}. The second system velocity in the NOMLT run was, within the errors, the same as the second system velocity in the CTL (and NOSFX) runs and was about 10.5 m s^{-1}. It is also clear from Figure 4.26 that for the three runs in which the simulated MCS had two system velocities (the CTL, NOMLT and NOSFX runs), the two different velocities were distinct features of the system and could not be accounted for by error alone.

4.2.4 The effect of diabatic cooling processes on the low-level flow

A cold pool developed in the early stages of the CTL and NOMLT runs. Low-valued θ_e air flowed out of the area of intense precipitation and ahead of the storm at 950 hPa at 0700 UTC in the CTL and NOMLT runs (centred at x=230 and y=220 km in Figures 4.27a and 4.27d) but was absent in the NOEVP, NOSUB and NOCOOL runs at this time (Figures 4.27b, 4.27c and 4.27e). The low-valued θ_e air in the cold pool flowed from the north to the south within, and as it left, the storm. To the south of the MCS the flow of low-valued θ_e air turned to the west, back towards the storm. This strengthened the southern region of the undercurrent in the CTL and NOMLT runs, providing an additional source of low-valued θ_e air that flowed against the direction of motion of the MCS. Without cooling

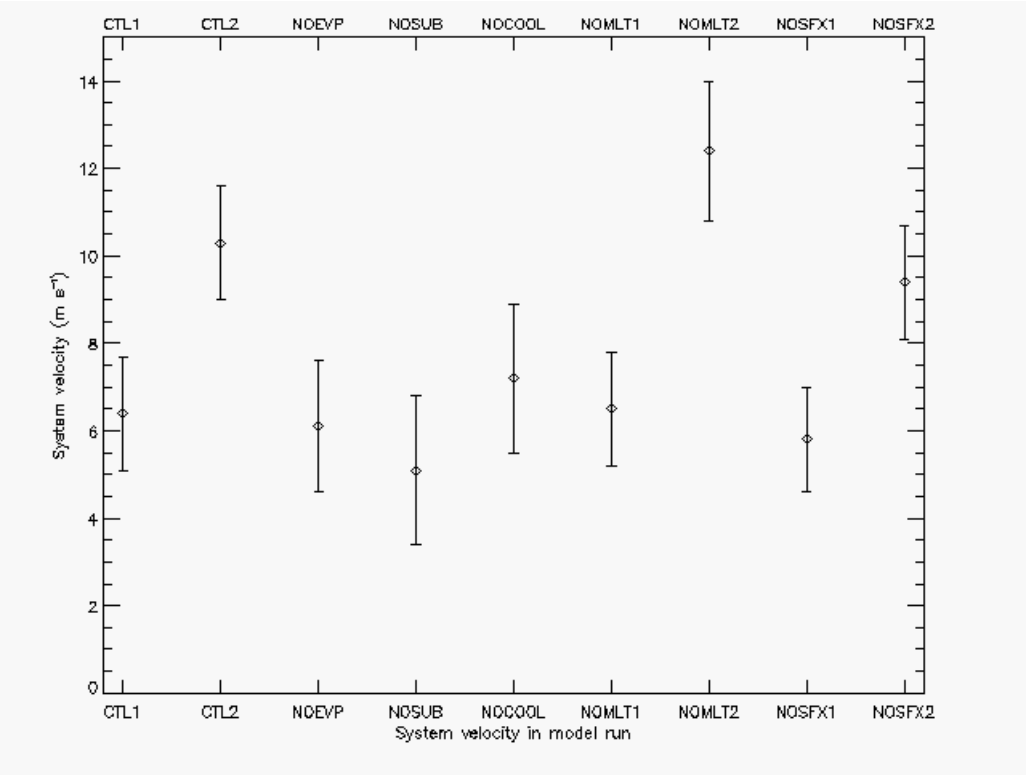

FIGURE 4.26: System velocities (m s^{-1}) for each of the sensitivity runs. Runs that had two system velocities are marked by the name of the run and the number 1 or 2, representing the initial and subsequent system velocities, respectively.

by evaporation or sublimation the undercurrent at 950 hPa at 0700 UTC had values of θ_e that were about 5 K greater and the flow had a southerly rather than northerly velocity component. This result shows that the early cold pool that formed in the north of the MCS in the CTL and NOMLT runs was driven by cooling by evaporation and sublimation, and that the cold pool outflow from the north acted to strengthen the undercurrent in the south.

The strengthening of the undercurrent by the flow of low-valued θ_e air from the north caused the elongation of the MCS. In the CTL and NOMLT runs, new cells initiated to the south of the MCS. The area of intense precipitation in these runs (Figures 4.28a and 4.28d) extended much further to the south at 1200 UTC than it did in the NOEVP, NOSUB and NOCOOL runs at this time (Figures 4.28b, 4.28c and 4.28e). The new cells were initiated by lifting from the gravity current outflow from the cold pool.

The flow of low-valued θ_e air from the north, cooled by evaporation and sublimation, also delayed the transition from elevated to surface-based convection. The region of intense

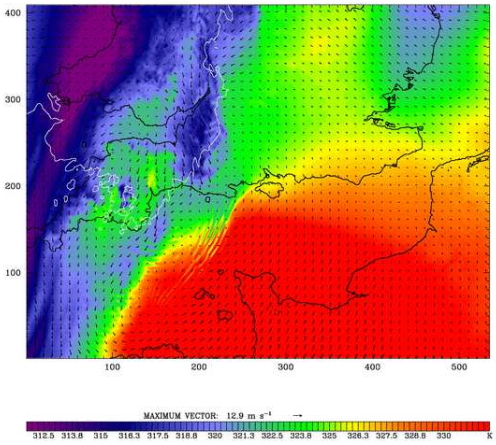

(A) CTL

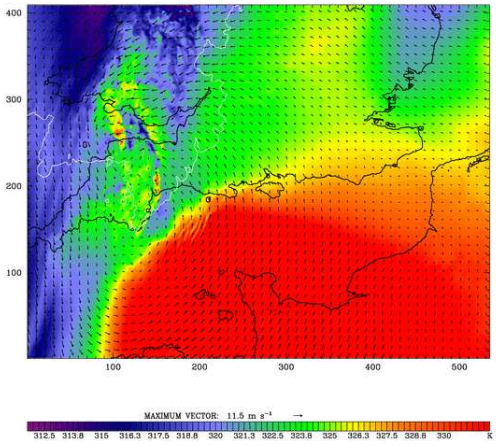

(B) NOEVP

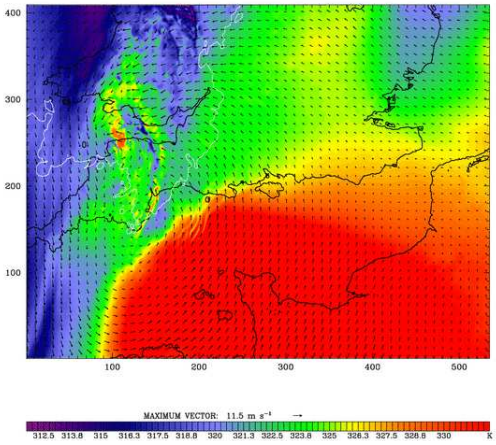

(C) NOSUB

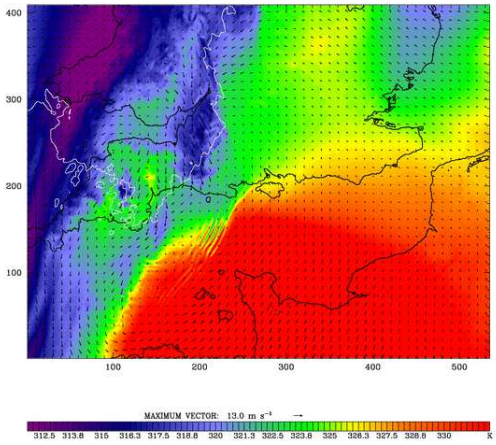

(D) NOMLT

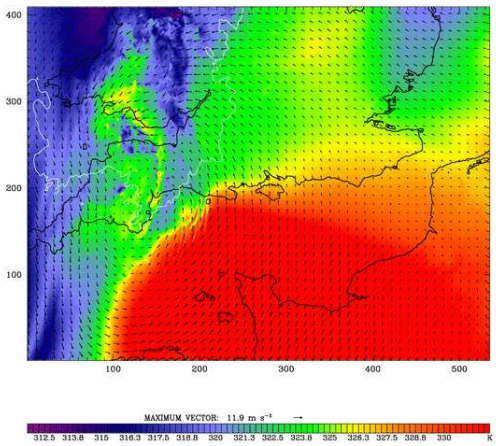

(E) NOCOOL

FIGURE 4.27: θ_e (K, colour contour), maximum reflectivity (dBZ, white line contour) and horizontal wind vectors at 950 hPa at 0700 UTC from the inner domain of the CTL, NOEVP, NOSUB, NOMLT and NOCOOL runs. Distances are in km.

precipitation in the NOEVP, NOSUB and NOCOOL runs was over a region of high-valued (330 K and greater) θ_e air at 950 hPa at 1200 UTC (Figures 4.28b, 4.28c and 4.28e), whereas in the CTL and NOMLT runs the intense precipitation at 950 hPa at this time was over air with lower values (322 K) of θ_e (Figures 4.28a and 4.28d).

The convection in the CTL and NOMLT runs was surface-based at 1400 UTC. In these runs the leading edge of the intense precipitation had only just reached the boundary between the low-valued θ_e air from the cold pool and the high-valued θ_e air ahead of the system (Figures 4.29a and 4.29d). Both the CTL and NOMLT runs had cold pool outflow and the transition to surface-based convection occurred later than in the other runs. The convection in the NOEVP, NOSUB and NOCOOL runs had been surface-based for some time at 1400 UTC and the intense precipitation at this time occurred far into the eastern region of high-valued θ_e air at 950 hPa (Figures 4.29b, 4.29c and 4.29e).

There were trailing cells of precipitation in the NOEVP, NOSUB and NOCOOL runs at 1400 UTC (Figures 4.29b, 4.29c and 4.29e). These may have formed because the values of θ_e at low-levels behind the MCS in these runs was greater than it was in the CTL and NOMLT runs (Figures 4.29a and 4.29d), so the low-level air behind the MCS was more unstable. Cooling by evaporation and sublimation in the CTL and NOMLT runs caused the the low-level air behind the MCS to have lower values of θ_e, making it more stable. The simulated MCS in the CTL and NOMLT runs remained elongated at 1400 UTC due to the initiation of cells to the south caused by the outflow of evaporatively- and sublimationally-cooled air (Figures 4.29a and 4.29d).

In summary, the diabatic cooling processes had several effects on the low-level flow and its interaction with the simulated convective systems. Cold pool outflow of low-valued θ_e air formed in the north of the convective system in the CTL and NOMLT runs during the early stages of the simulation (Figure 4.27). No cold pool formed in the NOEVP, NOSUB or NOCOOL runs so the outflow in the CTL and NOMLT runs was therefore air that had been cooled by evaporation and sublimation. The low-valued θ_e flowed to the south and turned back on itself, towards the convective system. It therefore strengthened the undercurrent in the CTL and NOMLT runs by contributing to the low-level flow in the opposite direction to the MCS and by contributing low-valued θ_e air at low-levels (Figure 4.27). This mechanism also suppressed the weakening of the undercurrent by the

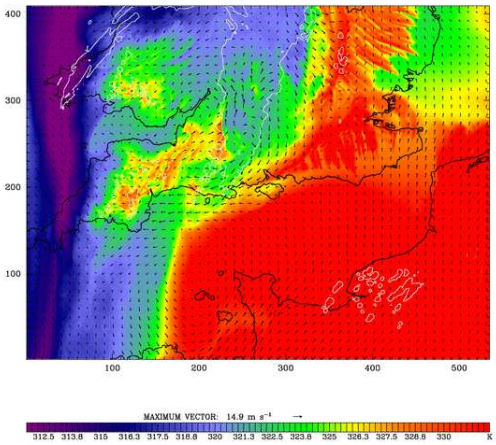

(A) CTL

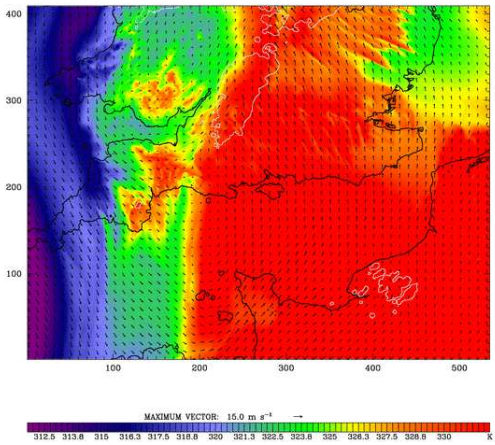

(B) NOEVP

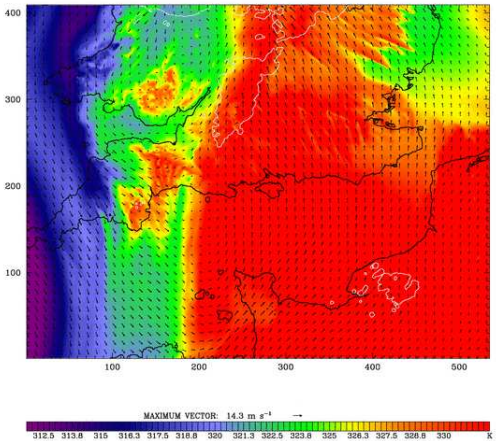

(C) NOSUB

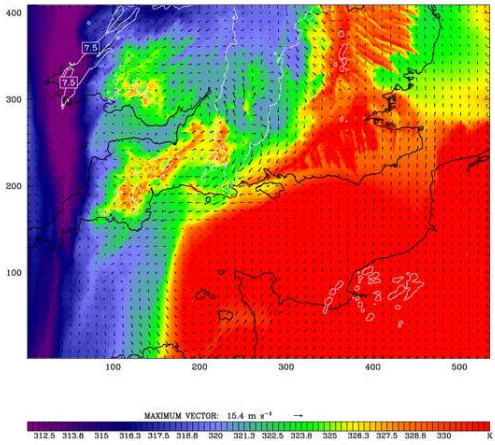

(D) NOMLT

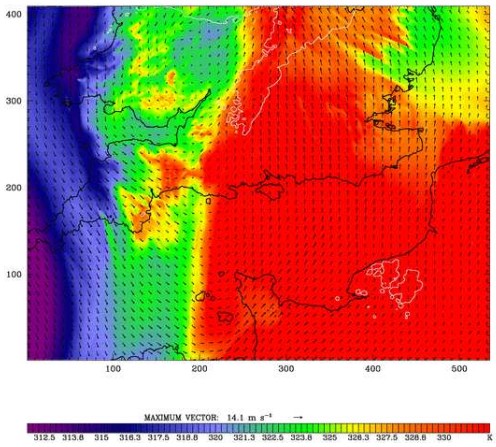

(E) NOCOOL

FIGURE 4.28: As Figure 4.27 but at 1200 UTC.

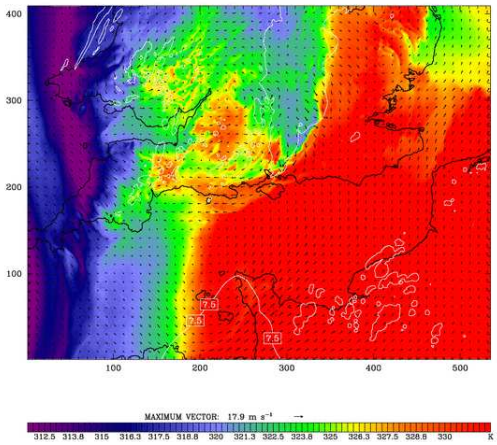

(A) CTL

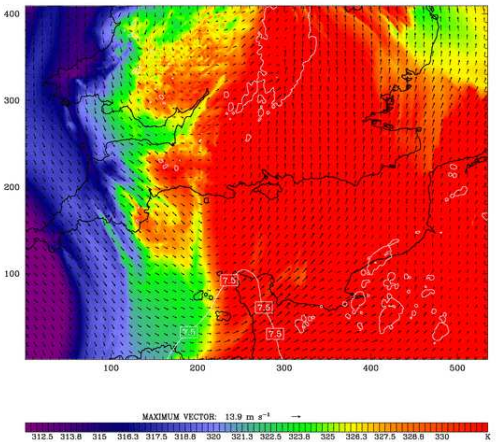

(B) NOEVP

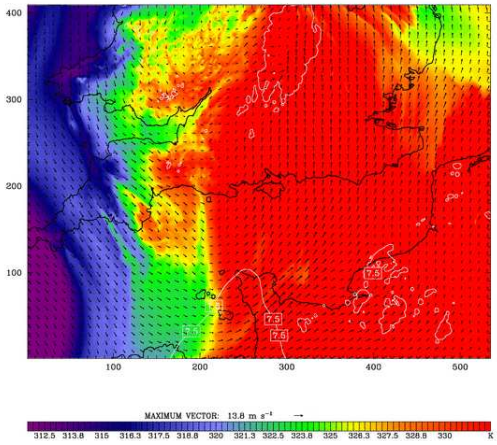

(C) NOSUB

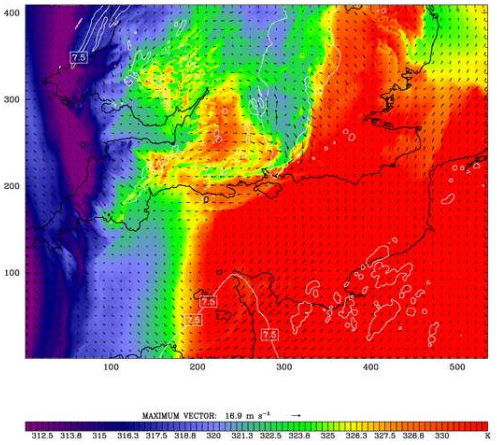

(D) NOMLT

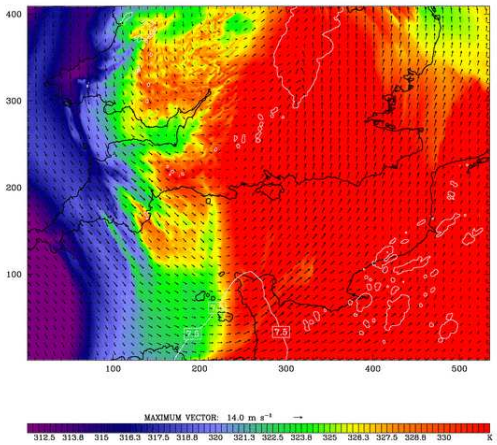

(E) NOCOOL

FIGURE 4.29: As Figure 4.27 but at 1400 UTC.

advection of high-valued θ_e air from the south of the model domain. New convective cells initiated at the southern end of the low-valued θ_e flow, causing the MCSs in the CTL and NOMLT runs to be elongated in comparison to the MCSs in the NOEVP, NOSUB and NOCOOL runs (Figure 4.28). The outflow of low-valued θ_e air from the MCS in the CTL and NOMLT runs also caused the transition from elevated to surface-based convection to be delayed in comparison to the NOEVP, NOSUB and NOCOOL runs (Figure 4.29).

4.2.5 The vertical structure of the convection and its near-environment

The effect of diabatic cooling processes on the 3D structure of the convection was investigated by analysing a series of vertical sections of θ_e and system-relative winds for each of the sensitivity runs. Sections were made along several lines through the simulated MCSs, oriented perpendicular to its direction of propagation, in a similar manner to the vertical sections taken through the CTL run discussed in Chapter 3. Due to the number of vertical sections that this analysis produced, the variability in the structure of the convection in each run is discussed, but only the pertinent vertical sections taken through the centre of the convective systems are shown for comparison. Because the MCS did not have exactly the same location in every run, the sections through the centre of the storm are not in identical geographical locations. Therefore there are small differences in the background environment between some of the vertical sections.

The NOEVP run

Evaporational cooling had a significant effect on the vertical structure of the convection. The inflow to the MCS that formed in the NOEVP run was initially from an elevated layer of high-valued θ_e (329 K) air centred at a height of about 2 km at 0815 UTC (Figure 4.30a). The elevated source layer in the CTL run had a slightly different structure to that of the CTL run at 0815 UTC (Figure 4.30b) because the sections through the centre of the storms were in different geographical locations. An undercurrent was present in the NOEVP run in the sense that the low-level flow opposed the direction of motion of the MCS (Figure 4.30a). However, in contrast to the CTL run, values of θ_e in the undercurrent were significantly greater ahead of the MCS, with values of 318 K or less occupying a layer that was 500 m deep at its maximum depth at 0815 UTC (Figure 4.30a). In contrast, the low-valued θ_e air in the undercurrent ahead of the MCS in the CTL run was about

1 km deep at this time (Figure 4.30b). Although the different locations of the sections may account for this to some extent, it has already been shown that the undercurrent in the CTL run was strengthened by evaporatively- and sublimationally-cooled outflow from the north of the storm (Section 4.2.4). This caused it to be deeper than the undercurrent in the NOEVP run.

There was a RIJ in the NOEVP run at 0815 UTC that flowed into the rear of the MCS and descended to z=1.5 km at 90 km (Figure 4.30a). The RIJ in the NOEVP run did not descend as much as the RIJ in the CTL run at 0815 UTC, which reached z=1 km (Figure 4.30b). This shows that evaporative cooling strengthened the descent of the RIJ. Despite not descending as much as the RIJ in the CTL run, and despite the undercurrent being shallower than that in the CTL run, the descent of the RIJ in the NOEVP run constricted the undercurrent and caused a wave to form in the elevated layer of high-valued θ_e air ahead of the main convective region at 105 km (Figure 4.30a). The RIJ did not reach the surface at any time in the NOEVP run.

The MCS in the NOEVP run passed out of the region of low-valued θ_e undercurrent at 1030 UTC and the descending RIJ no longer generated a wave in the elevated layer of high-valued θ_e (Figure 4.30c), presumably because the absence of a low-level stable layer (the undercurrent) meant that wave-trapping could not occur. In contrast, the undercurrent was still present in the CTL run, because it had been reinforced by the outflow of evaporatively- and sublimationally-cooled air from the north of the MCS. The inflow to the MCS in the CTL run remained wave-lifted at 1030 UTC (Figure 4.30d).

The values of θ_e in the lowest 500 m ahead of the MCS had increased to about 300 K at 1030 UTC (Figure 4.30c). In contrast, there was still an undercurrent of low-valued θ_e air ahead of the MCS in the CTL run at 1030 UTC (Figure 4.30d). Because the undercurrent was strengthened by evaporation and sublimational, the removal of evaporative cooling from the NOEVP run meant that surface heating and the advection of high-valued θ_e air in the east caused a significant increase in the values of θ_e at low-levels ahead of the MCS.

The RIJ in the NOSUB run descended to about z=1 km at 140 km in the NOEVP run at 1030 UTC (Figure 4.30c). In the CTL run the RIJ descended further to about z=750 m at 1030 UTC (Figure 4.30d).

The low-level values of θ_e in the east continued to increase in the NOEVP run. The lowest 1 km ahead of the MCS had values of θ_e of 330 K or more at 1200 UTC (Figure 4.30e). At this time the convection in the NOEVP run had become surface-based. In comparison, elevated convection above an undercurrent was still occurring at 1200 UTC in the CTL run (Figure 4.30f), although the propagation of the MCS towards the region of high-valued θ_e air in the east meant that the transition to surface based convection would soon occur.

A gravity current never formed anywhere in the MCS in the NOEVP run. This shows that the gravity current outflow that formed in the CTL run was partly driven by evaporative cooling. No significant change in system velocity occurred in the NOEVP run (discussed in Section 4.2.3). This suggests that the change in system velocity in the CTL run was due to the formation of the gravity current.

The NOSUB run

The effects of sublimational cooling on the vertical structure of the convection were very similar to those of evaporative cooling. This is perhaps not surprising, as the values of the latent heats of evaporation and sublimation are of the same order of magnitude (List, 1984). The inflow to the MCS that formed in the NOSUB simulation was initially from an elevated layer of high-valued θ_e (329 K) air centred at a height of about 2 km at 0815 UTC (Figure 4.31a). The central section of the NOSUB run was in the same location as that of the NOEVP run, and was different from the CTL run. The structure of the undercurrent between 0 and 200 km in the NOSUB run at 0815 UTC (Figure 4.31a) was the same as that in the NOEVP run at this time (Figure 4.30a) and was about half as deep as the undercurrent in the CTL run at 0815 UTC (Figure 4.31b).

The RIJ in the NOSUB run descended to z=1.5 km at 0815 UTC (Figure 4.31a), the same height as in the NOEVP run at this time and not as low as the RIJ in the CTL run at 0815 UTC (Figure 4.31b). This shows that the relative contributions to the descent of the RIJ from evaporative and sublimational cooling were similar. The descent of the RIJ in the NOSUB run constricted the undercurrent and at 0815 UTC there was a wave in the elevated high-valued θ_e source layer ahead of the MCS (Figure 4.31a).

Due to the weaker undercurrent in the NOSUB run, the RIJ no longer caused a wave in the elevated layer of high-valued θ_e air in the NOSUB run at 1030 UTC (Figure 4.31c).

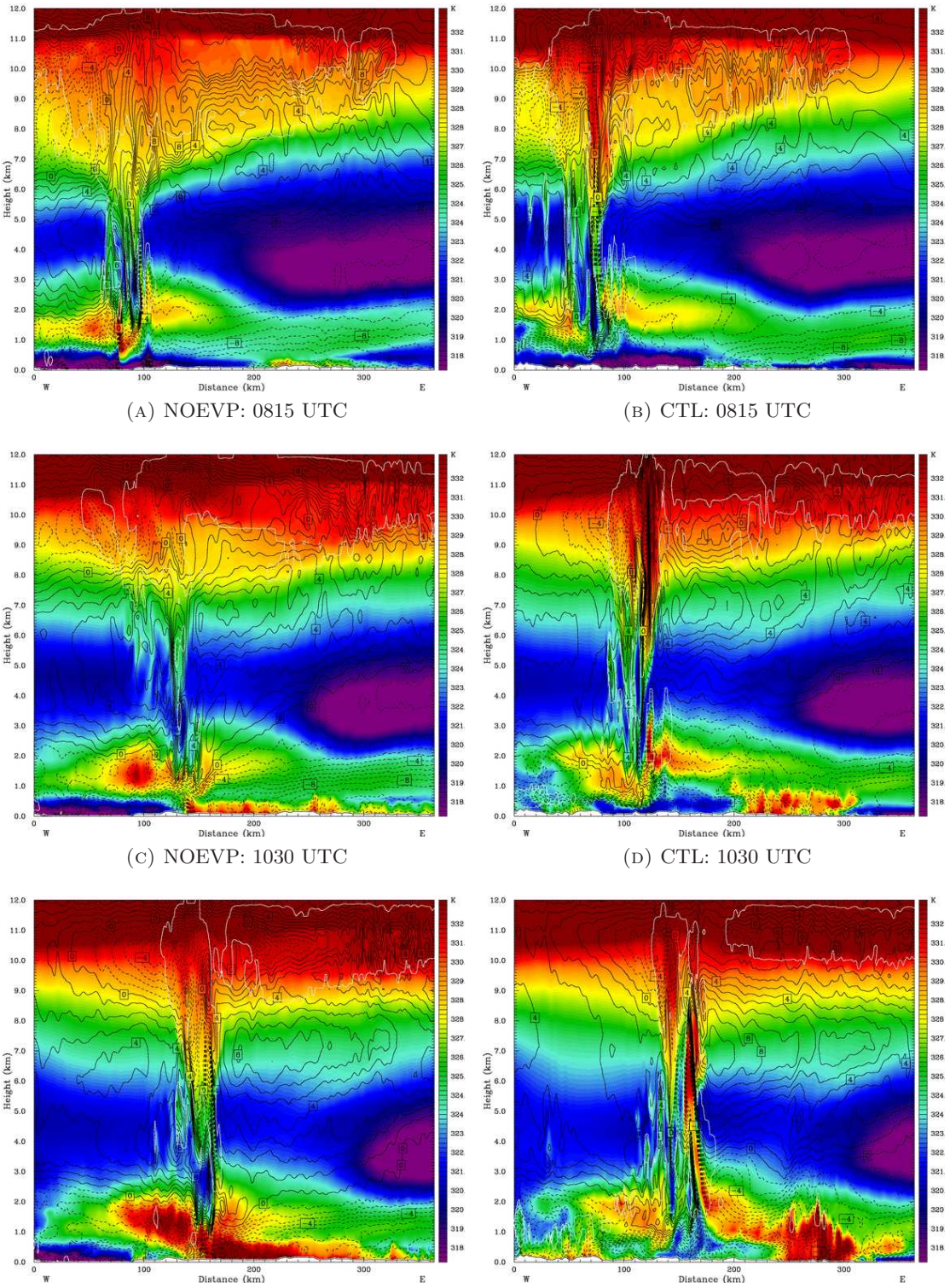

(A) NOEVP: 0815 UTC (B) CTL: 0815 UTC

(C) NOEVP: 1030 UTC (D) CTL: 1030 UTC

(E) NOEVP: 1200 UTC (F) CTL: 1200 UTC

FIGURE 4.30: Vertical section of θ_e (K, colour contour), system-relative horizontal winds (m s^{-1}, black line contour: solid positive and dashed negative) and total cloud mixing ratio (5x10^{-3} g kg^{-1}, white line contour) from the inner domain of the NOEVP and CTL runs.

The MCS in the CTL run remained elevated above an undercurrent at 1030 UTC (Figure 4.31d). The RIJ descended to about z=1 km in the NOSUB run at 1030 UTC (Figure 4.31c), the same height as in the NOEVP run at this time (Figure 4.30c).

Similarly to the NOEVP run, the combined effects of surface heating and advection of high-valued θ_e air in the east and the absence of an undercurrent strengthened by evaporatively- and sublimationally-cooled outflow caused the convection in the NOSUB run to be surface-based by 1200 UTC (Figure 4.31e), while the MCS in the CTL run was still elevated at this time (Figure 4.31f). The RIJ never penetrated to the surface in the NOSUB run and a gravity current never formed anywhere in the MCS. This shows that the gravity current outflow that formed in the CTL run was driven by sublimational as well as evaporative cooling. No significant change in system velocity occurred in the NOSUB run (discussed in Section 4.2.3), which also suggests that the change in system velocity in the CTL run was due to the formation of the gravity current.

The NOMLT run

Cooling by melting had a weak effect on the structure of the convection compared to the effects of evaporative and sublimational cooling. This is perhaps not surprising, since the latent heat of melting is an order of magnitude smaller than the latent heats of evaporation and sublimation (List, 1984). The vertical section through the centre of the MCS in the NOMLT run was in the same geographical location as that through the CTL run. The vertical structure of the MCS and its near-environment was very similar in both runs. The convection was elevated above a cool undercurrent at 0815 UTC (Figures 4.32a and 4.32b). The RIJ descended to z=1 km and caused a wave to form at the top of the undercurrent and in the elevated source layer ahead of the MCS at 0815 UTC. The undercurrent was strengthened by evaporatively- and sublimationally-cooled air from the north and the convection remained elevated above the undercurrent at 1030 UTC in both the NOMLT (Figure 4.32c) and CTL (Figure 4.32d) runs. The structure of the wave in the NOMLT run was slightly different from the wave in the CTL run at 1030 UTC. There was one cloud, with a cloud base at 2 km, above the wave in the NOMLT run at 130 km at 1030 UTC (Figure 4.32c). In the CTL run there were two clouds at this time, at 120 and 140 km (Figure 4.32d). This difference was probably due to differences between the RIJ in each

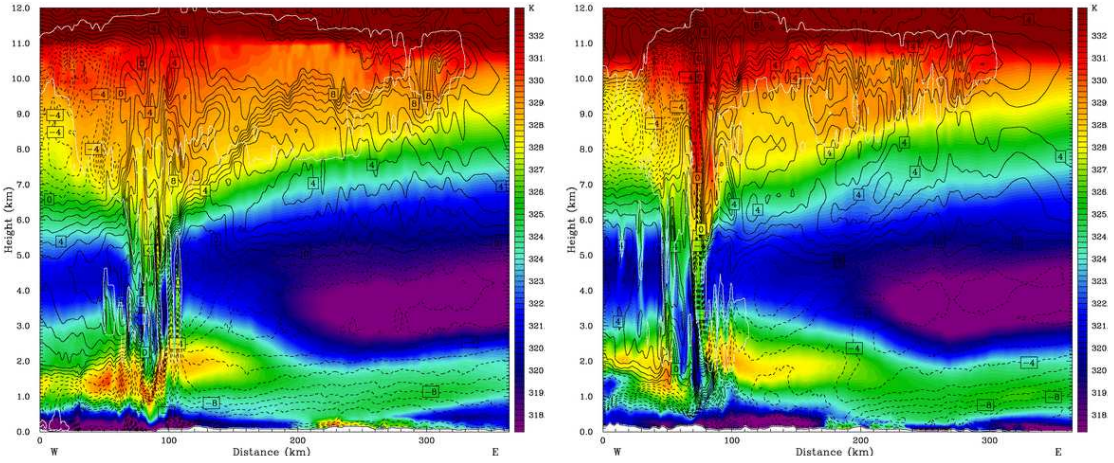

(A) NOSUB: 0815 UTC (B) CTL: 0815 UTC

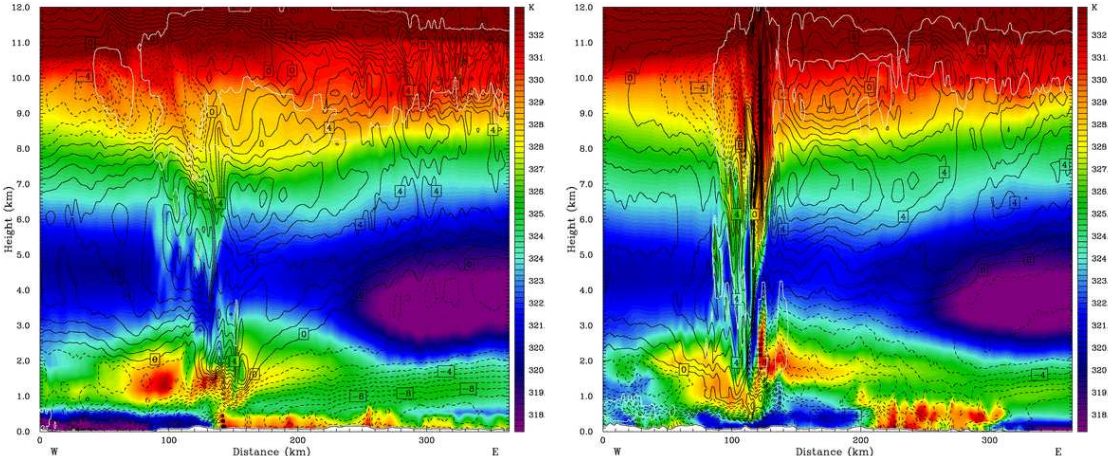

(C) NOSUB: 1030 UTC (D) CTL: 1030 UTC

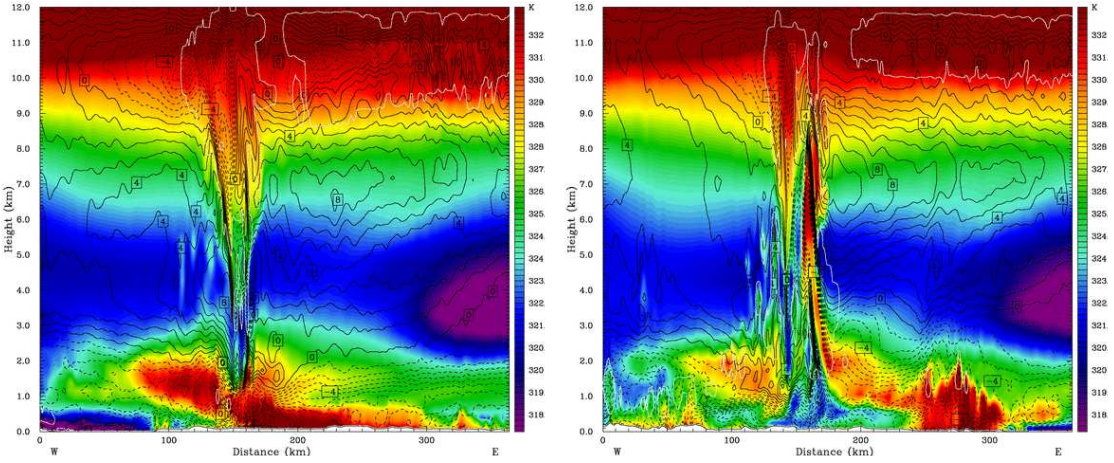

(E) NOSUB: 1200 UTC (F) CTL: 1200 UTC

FIGURE 4.31: As Figure 4.30 but for the NOSUB and CTL runs.

run, driven by cooling by melting. The values of θ_e at low-levels ahead of the MCS in both runs increased throughout the simulation.

The velocity of the MCS in the NOMLT run increased at 1500 UTC (Figure 4.24), the same time at which gravity current outflow formed from the MCS in the NOMLT (Figure 4.32e). In contrast, as previously discussed, the velocity of the MCS in the CTL run increased at 1330 UTC when it developed gravity current outflow. The gravity current in the CTL run propagated ahead of the MCS and there was a new cell of deep convection at the leading edge of the gravity current in the CTL run at 1500 UTC (Figure 4.32f). The delayed gravity current outflow in the NOMLT run shows that cooling by melting aided the development of a gravity current in the MCS. The effect was, however, smaller than the effects of evaporation or sublimation, as no gravity current ever occurred in the NOEVP or NOSUB runs.

The NOCOOL run

Removing all diabatic cooling processes from the model had a similar effect on the structure of the convection to the effect of removing just the evaporative or sublimational cooling. Given the orders of magnitude of the latent heats of evaporation, sublimation and melting, this is not surprising. The inflow to the MCS that formed in the NOCOOL simulation was from an elevated layer of high-valued θ_e (329 K) air centred at a height of about 2 km at 0815 UTC (Figure 4.33a). The vertical section through the centre of the storm in the NOCOOL run was in a different location from that of the CTL run, which explains the difference in the structure of the elevated source layer at 0815 UTC between the NOCOOL (Figure 4.33a) and CTL (Figure 4.33b) runs.

The values of θ_e at 50 to 90 km between z=1 and z=2 km beneath the RIJ and behind the convection were greater at 0815 UTC in the NOCOOL run (Figure 4.33a) than in the NOEVP (Figure 4.30a) and NOSUB (Figure 4.31a) runs. The location of the vertical section was the same in these three runs. The values of θ_e in this region in the NOCOOL run were greater because cooling by both evaporation and sublimation had been removed.

The RIJ in the NOCOOL run only descended to about z=2 km at 0815 UTC (Figure 4.33a). The RIJ in the NOCOOL run descended less than it did in the NOEVP and NOSUB runs, where it reached z=1.5 km at 0815 UTC (Figures 4.30a and 4.31a),

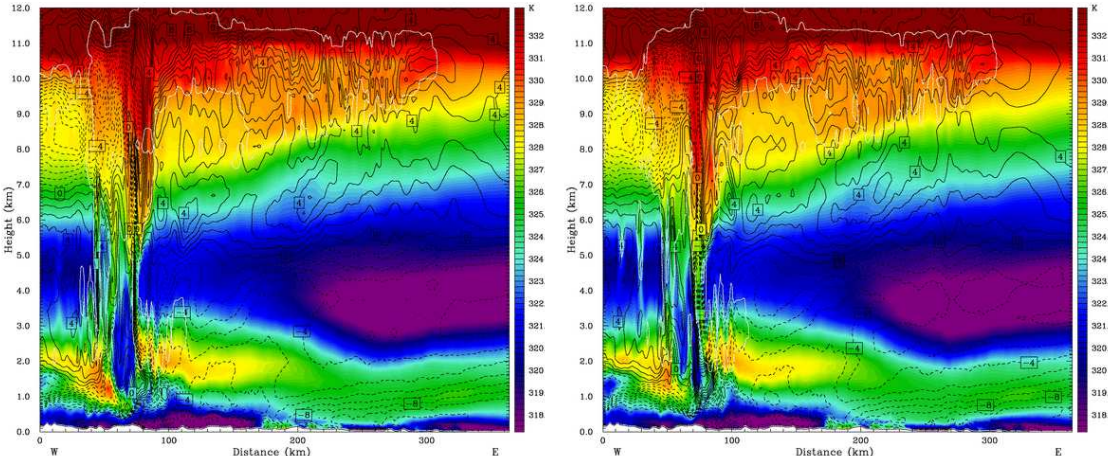

(A) NOMLT: 0815 UTC (B) CTL: 0815 UTC

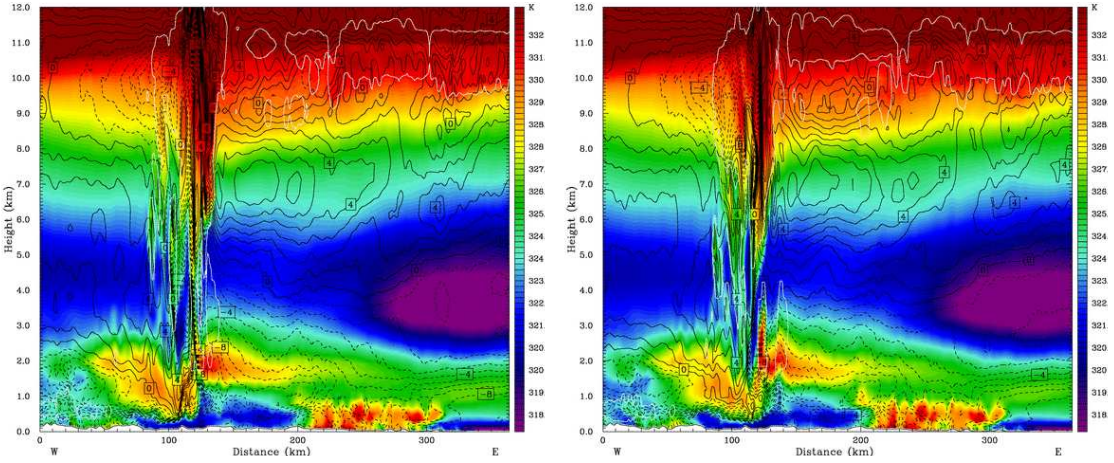

(C) NOMLT: 1030 UTC (D) CTL: 1030 UTC

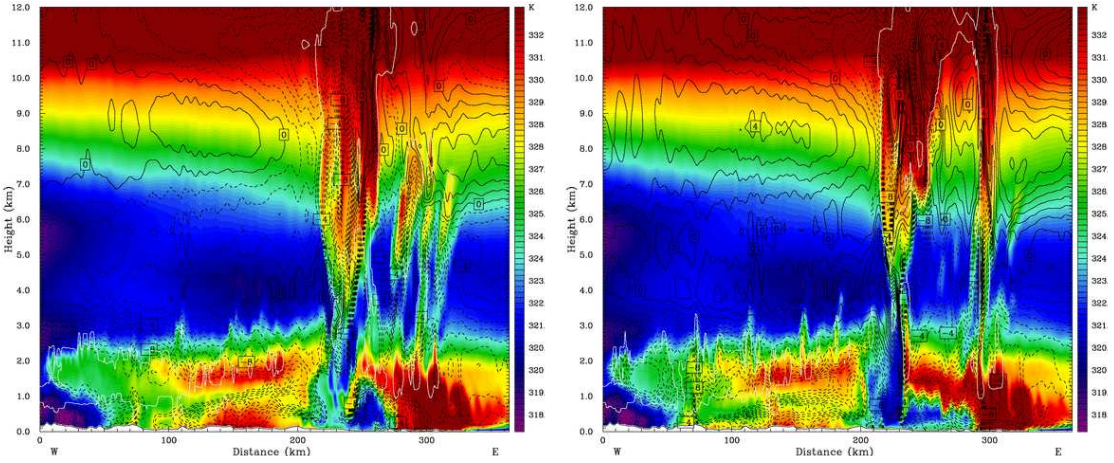

(E) NOMLT: 1500 UTC (F) CTL: 1500 UTC

FIGURE 4.32: As Figure 4.30 but for the NOMLT and CTL runs.

and the NOMLT and CTL runs, where it reached z=1 km at 0815 UTC (Figures 4.32a and 4.33b). This shows that cooling by evaporation and sublimation strengthened the descent of the RIJ and that the relative contributions of evaporation and sublimation to the descent of the RIJ were about the same. Even though the descent of the RIJ in the NOCOOL run was weak in comparison to the other runs, it nevertheless caused a wave to form ahead of the MCS in the undercurrent and elevated source layer at 0815 UTC (Figure 4.33a).

The descent of the RIJ in the NOCOOL run was always weaker than it was in the other runs. The RIJ descended to about z=1.5 km in the NOCOOl run at 1030 UTC (Figure 4.33c), whereas it reached z=1 km in the NOEVP and NOSUB runs (Figures 4.30c and 4.31c) and z=750 m in the NOMLT and CTL runs at this time (Figures 4.32c and 4.33d). The RIJ never penetrated to the surface in the NOCOOL run. The values of θ_e at 130 km in the RIJ at z=3 km were also greater in the NOCOOL run at 1030 UTC (Figure 4.33c) than they were in any of the other runs at this time (Figures 4.30c, 4.31c, 4.32c and 4.33d). This was because there were no diabatic coolings from microphysical processes occurring in the NOCOOL run. The fact that the RIJ descended in the NOCOOL run, even though its descent was weak, shows that the descent of the RIJ was caused by dynamic processes. The descent was, however, strengthened by diabatic cooling processes.

As in the NOEVP and NOSUB runs, the combined effects of surface heating and advection of high-valued θ_e air in the east and the absence of an undercurrent strengthened by evaporatively- and sublimationally-cooled outflow caused the convection in the NOCOOL run to be surface-based by 1200 UTC (Figure 4.33e). In the CTL run the convection was still elevated at this time (Figure 4.33f).

No gravity current outflow ever formed in the NOCOOL run and no significant change in system velocity occurred in the NOCOOL run (Section 4.2.3). This shows that the effects of cooling by evaporation and sublimation were important not only in the RIJ, but also in the convective region.

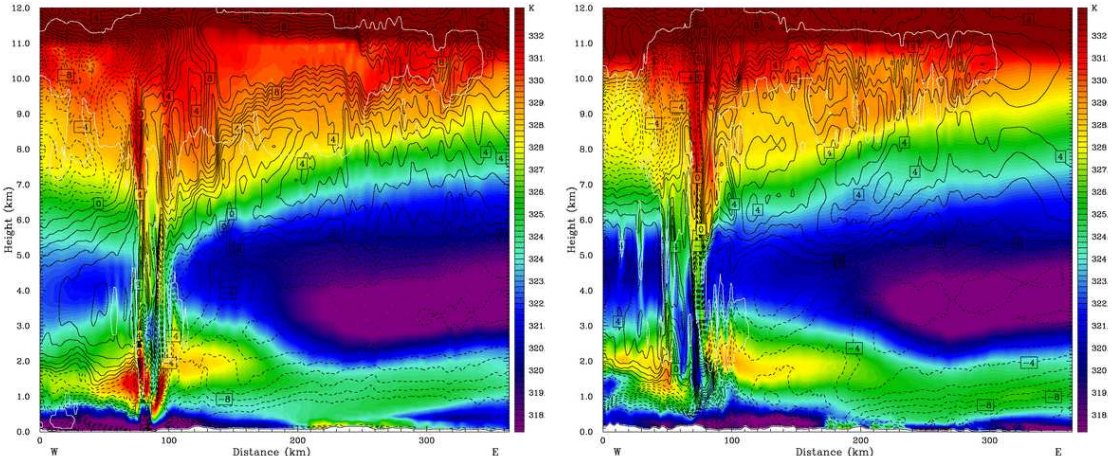

(A) NOCOOL: 0815 UTC (B) CTL: 0815 UTC

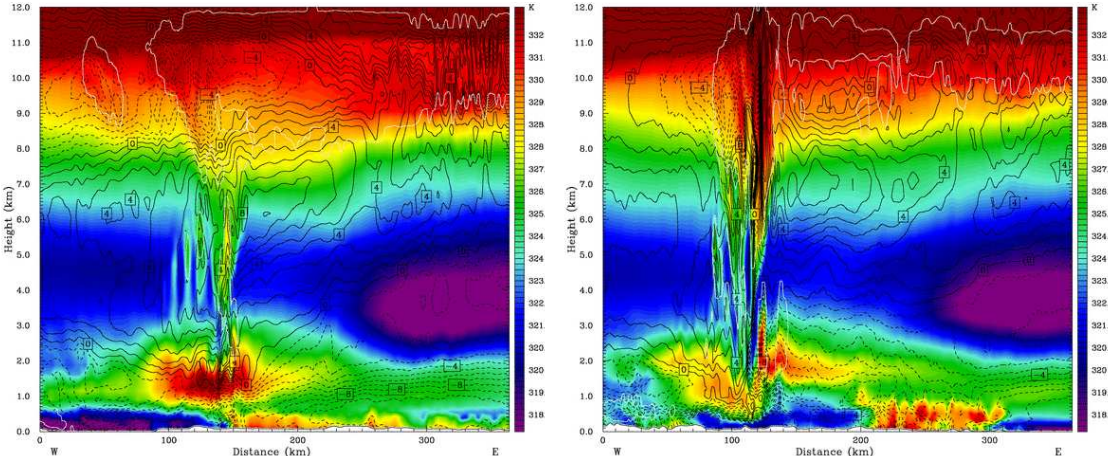

(C) NOCOOL: 1030 UTC (D) CTL: 1030 UTC

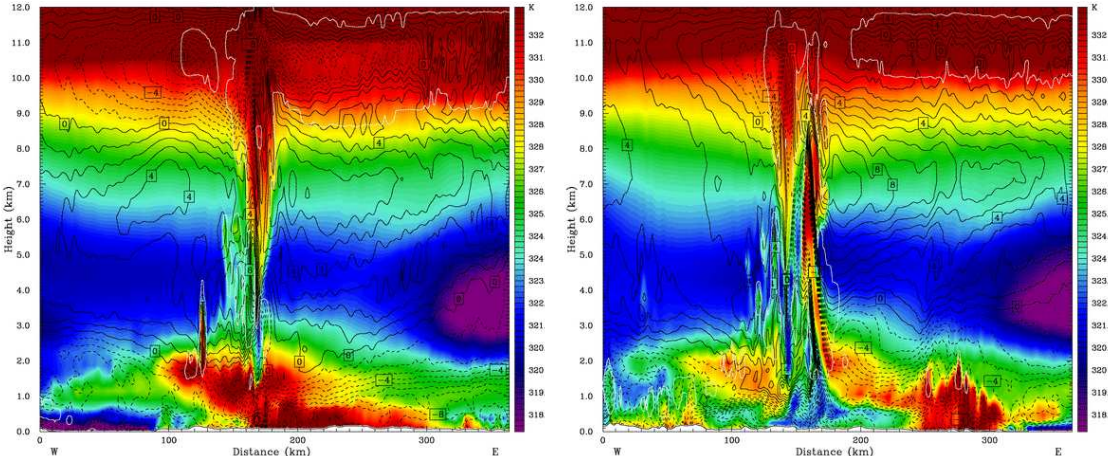

(E) NOCOOL: 1200 UTC (F) CTL: 1200 UTC

FIGURE 4.33: As Figure 4.30 but for the NOCOOL and CTL runs.

4.2.6 The effect of diabatic cooling processes on the cloud-scale structure of the MCS

The cloud-scale structure of the simulated MCSs was investigated in the same manner as the CTL run in Section 3.5.2 of Chapter 3. A comparison of vertical sections taken through the centre of the MCSs at 1015 UTC, during the elevated stage of convection, is given here. Variations in the background environment of the vertical sections are due to slight differences in the geographical location of the storm in each run.

There were two maxima in the horizontal wind speed in the RIJ in the CTL run at 1015 UTC. One was at 48 km and had a strength of 4 m s^{-1} and the other was at 57 km and had a strength of 7 m s^{-1} (Figure 4.34a). The first maximum was located at the back edge of the storm where the RIJ passed under the stratiform region, and the second was located in the convective region. There were also two maxima in the horizontal wind speed field in the NOEVP run at 1015 UTC. One was at 55 km in the stratiform region and had a strength of 8 m s^{-1} and the other was at 67 km in the convective region and had a strength of 5 m s^{-1} (Figure 4.34b). However, the horizontal wind speed maximum in the convective region had values of θ_e of about 326 K, while the equivalent maximum in the CTL run had θ_e values of about 321 K. The values of θ_e were higher in the NOEVP run due to the lack of evaporational cooling. There were horizontal wind speed maxima in the NOSUB run of 8 m s^{-1} at 52 km in the stratiform region and of 6 m s^{-1} at 67 km in the convective region (Figure 4.34c). However, as discussed below, the maximum in the stratiform region was actually ascending in the NOSUB run. The maximum in the convective region, like that of the NOEVP run, had values of θ_e of about 326 K and was therefore not associated with the descent of low-valued θ_e air. The two horizontal wind speed maxima in the NOMLT run occurred at 48 km under the stratiform region, which had a strength of 4 m s^{-1}, and at 56 km in the convective region, which had a strength of 7 m s^{-1} (Figure 4.34d). There was a maximum of 5 m s^{-1} in the horizontal wind speed at 72 km in the NOCOOL run (Figure 4.34e). However, the maximum was not associated with the descent of any low-valued θ_e air: the RIJ in the NOCOOL run remained horizontal and elevated.

Both of the horizontal wind speed maxima in the CTL run were associated with downdraughts. The maximum at 48 km in the stratiform region was descending at about

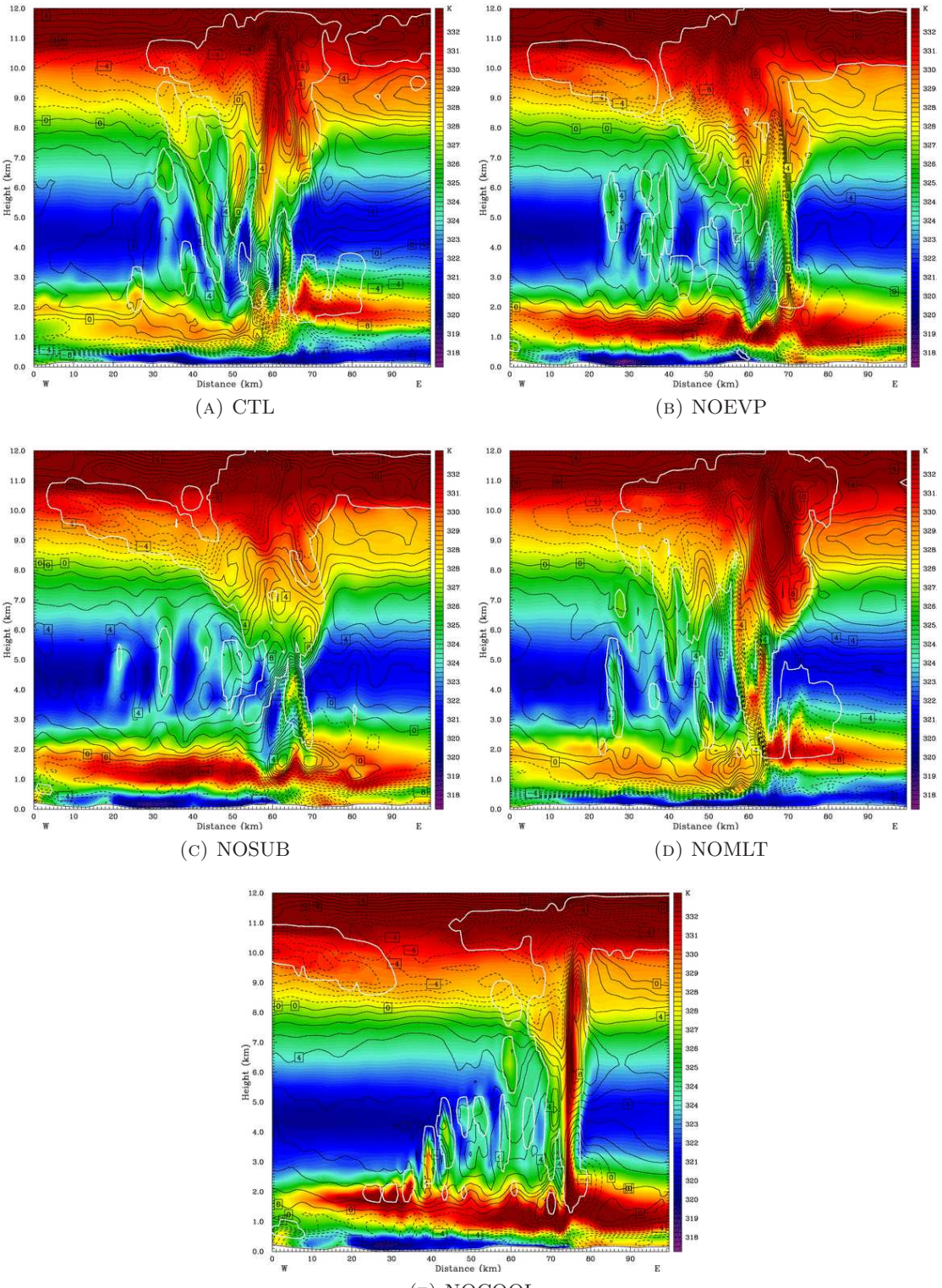

(A) CTL (B) NOEVP

(C) NOSUB (D) NOMLT

(E) NOCOOL

FIGURE 4.34: Vertical section of θ_e (K, colour contour), system-relative winds (m s^{-1}, solid black line contour showing positive system-relative winds and dashed black line contour showing negative system-relative winds) and a single contour of total cloud mixing ratio (5x10^{-3} g kg^{-1}, white line contour) for each of the microphysics sensitivity runs at 1015 UTC.

1 m s^{-1} and the maximum in the convective region at 57 km was descending at about 2 m s^{-1} (Figure 4.35a). The RIJ descended to 1 km in the CTL run (Figure 4.35a). The main convective updraught in the CTL run had a strength of about 12 m s^{-1}. The horizontal wind speed maxima in the NOEVP run were both associated with downdraughts, of 1 m s^{-1} and 2 m s^{-1} in the stratiform region (at 55 km) and in the convective region (at 67 km), respectively (Figure 4.35b). The RIJ descended to 1 km in the NOEVP run (Figure 4.35b). The strength of the convective updraught in the NOEVP run was about 14 m s^{-1}, stronger than that in the CTL run at this time, and was also much deeper, reaching 8 km. The horizontal wind speed maximum at 52 km in the stratiform region of the NOSUB run was, perhaps surprisingly, associated with a weak updraught of about 1 m s^{-1}, while the maximum at 67 km in the convective region was associated with a downdraught of about 2 m s^{-1} (Figure 4.35c). Like the NOEVP run, the RIJ in the NOSUB run also descended to 1.5 km (Figure 4.35c). The convective updraught in the NOSUB run had a strength of about 12 m s^{-1} and reached the same depth as that of the CTL run. The horizontal wind speed maximum in the stratiform region at 48 km in the NOMLT run was associated with a downdraught of about 2 m s^{-1}, and the maximum at 56 km in the convective region descended at about 1.5 m s^{-1} (Figure 4.35d). The RIJ descended to 1 km in the NOMLT run (Figure 4.35d). The maximum updraught speeds in the NOMLT run were about 14 m s^{-1}, similar to the NOEVP run. The updraughts were also about the same depth as those in the NOEVP run, and were about twice as deep as the updraughts in the CTL and NOSUB runs. The horizontal wind speed maximum at 72 km in the NOCOOL run occurred in a moderate updraught of about 4 m s^{-1} (Figure 4.35e). The RIJ in the NOCOOL run did not undergo any descent. Behind the cloud in the NOCOOL run were downdraughts which had a strength of about 2 m s^{-1} (Figure 4.34e). There was no horizontal component to the flow of the downdraughts and they were not part of the RIJ. The main updraught in the NOCOOL run was stronger and deeper than the updraught in any of the other runs, and had a strength of about 18 m s^{-1} (Figure 4.34e).

The maximum in the RIJ in the stratiform region at 48 km in the CTL run was associated with a local maximum in graupel and snow mixing ratios and occurred above a maximum in rain mixing ratio (Figure 4.36a). The maximum in the RIJ in the convective region at 57 km occurred beneath a maximum in graupel and snow mixing ratios and inside a

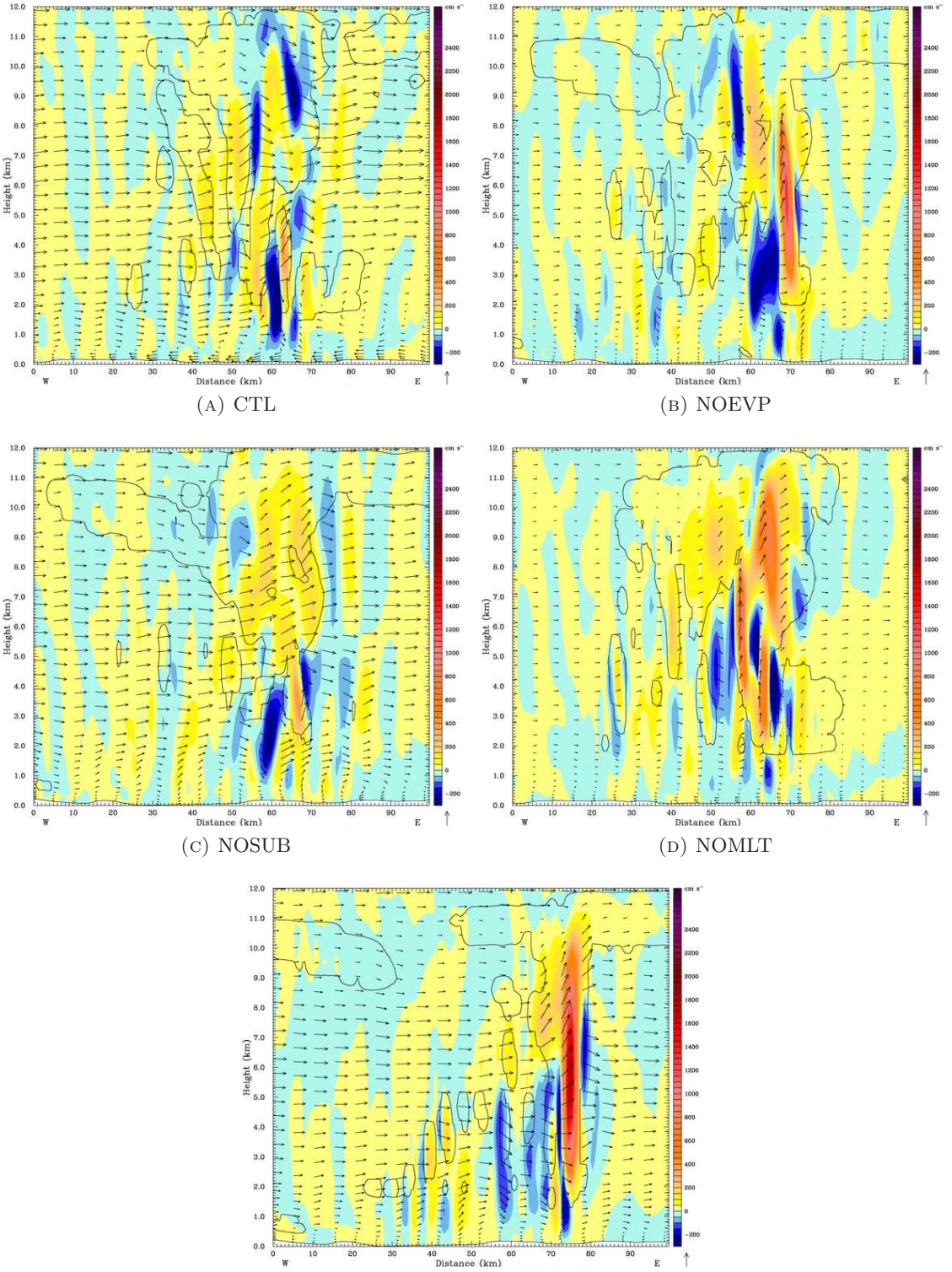

(A) CTL (B) NOEVP

(C) NOSUB (D) NOMLT

(E) NOCOOL

FIGURE 4.35: Vertical section of vertical velocity (m s^{-1}, colour contour), circulation vectors (not system-relative) and a single contour of total cloud mixing ratio (5x10^{-3} g kg^{-1}, black line contour) for each of the microphysics sensitivity runs at 1015 UTC.

maximum in the rain mixing ratio (Figure 4.36a). The same was true of the stratiform and convective RIJ maxima in the NOEVP run (at 55 km and 67 km, respectively, in Figure 4.36b). The RIJ maximum at 67 km in the convective region of the NOSUB run was also associated with a local maximum in graupel, rain and snow mixing ratios (Figure 4.36c). The ascending horizontal wind speed maximum at 52 km in the stratiform region of the NOSUB run also occurred beneath a local maximum in graupel and snow mixing ratios (Figure 4.36c). However, the storm in the NOSUB run had significantly less graupel than the CTL or NOEVP runs at 1015 UTC (Figures 4.36a and 4.36b). This is because, at the level where graupel was produced, the processes of evaporation and melting were weak compared to sublimation. The descent of the RIJ in the stratiform region was therefore sensitive to cooling by sublimation. The horizontal wind speed maximum at 48 km in the NOMLT run occurred below a maximum in graupel mixing ratio (Figure 4.36d). The maximum at 56 km in the convective region occurred just behind a maximum in rain mixing ratio (Figure 4.36d). As might be expected, significantly more rain formed when cooling due to melting was removed in the NOMLT run (Figure 4.36d), compared to the CTL, NOEVP and NOSUB runs (Figures 4.36a, 4.36b and 4.36c). The cloud in the NOCOOL run was significantly narrower than in any of the other runs. This is because removing the coolings allowed more evaporation and sublimation to occur, and increased the saturation point of air with respect to water and ice. The strong updraught at 72 km in the NOCOOL run (Figure 4.34e) was located in the centre of the narrow cloud, where the graupel, snow and rain mixing ratios were at a maximum (Figure 4.36e).

The sensitivity of the cloud-scale structure of the simulated MCS to diabatic cooling processes has shown the following:

- The cooling due to microphysical processes was responsible for the relative maxima in the RIJ. In every run the maxima in the RIJ, in both horizontal and vertical velocity, were associated with local maxima in the graupel, snow and rain mixing ratios. The RIJ formed in the NOCOOL run but neither descended significantly nor developed strong local maxima in its velocity field.

- The diabatic cooling processes did not significantly affect the strength of the horizontal wind speed maximum of the RIJ in the convective region, which had a strength of 6 to 7 m s^{-1} in the CTL, NOEVP, NOSUB and NOMLT runs. However, the

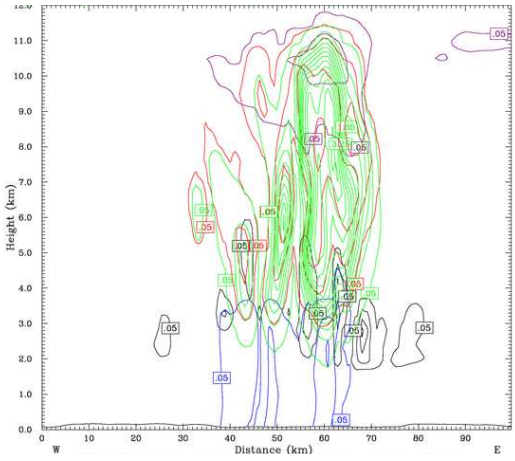

(A) CTL

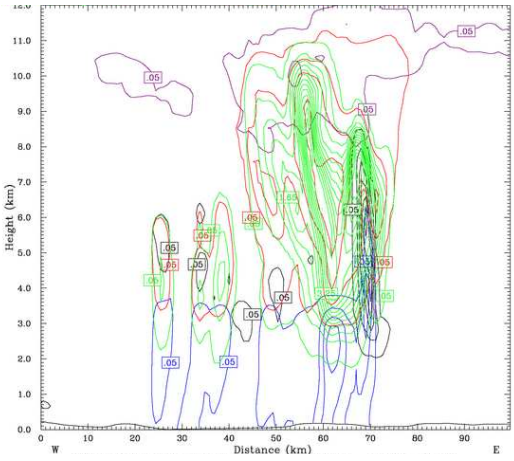

(B) NOEVP

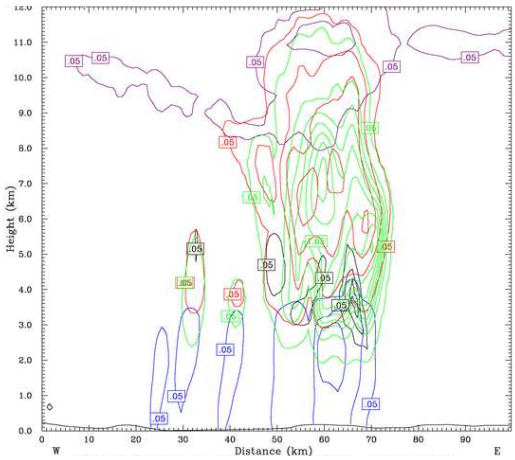

(C) NOSUB

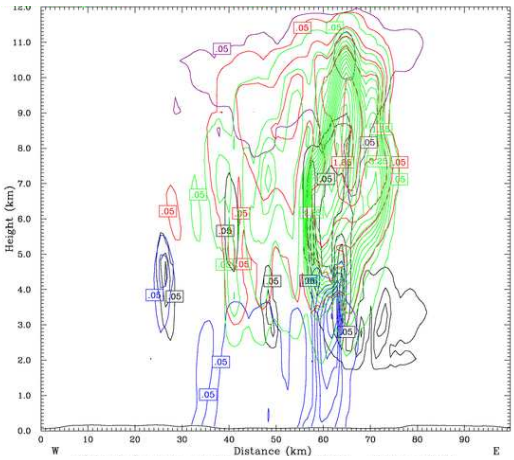

(D) NOMLT

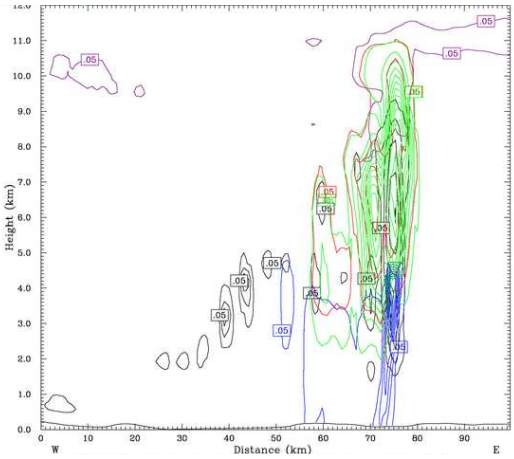

(E) NOCOOL

FIGURE 4.36: Vertical section of hydrometeor mixing ratios (g kg^{-1}, contour interval 0.4 g kg^{-1}): cloud water (black), cloud ice (purple), snow (red), graupel (green) and rain (blue) for each of the microphysics sensitivity runs at 1015 UTC.

diabatic cooling processes appeared to weaken the strength of the horizontal wind speed maximum of the RIJ in the stratiform region. In the CTL and NOMLT runs the maximum had a strength of 4 m s^{-1}, whereas it was 8 m s^{-1} in the NOEVP and NOSUB runs. This could have been due to increased subsidence in the CTL and NOMLT runs weakening the horizontal component of the velocity. The effect may not have been as significant in the convective region compared to the stratiform region due to the relative narrowness of the convective region and due to the dominance of convective updraughts and downdraughts.

- The convective updraught was weakened by cooling due to evaporation and melting. In the NOEVP and NOMLT runs the updraught was stronger (14 m s^{-1} compared to 12 m s^{-1}) and twice as deep as the updraught in the CTL run. The updraught in the NOCOOL run was even stronger, 18 m s^{-1}, and deeper. The updraught in the NOSUB run had a similar strength and depth to that in the CTL run.

- The downdraughts in the convective region were strengthened more by cooling by melting than they were by evaporative or sublimational cooling. The convective downdraughts in the NOMLT run were weaker and shallower than they were in the other runs.

- Cooling by evaporation and sublimation allowed the generation of the wave in the undercurrent. A wave formed in the CTL and NOMLT runs but did not in the NOEVP, NOSUB or NOCOOL runs. As discussed before, this was partly due to the strengthening of the undercurrent by outflow from the north that was generated by evaporative and sublimational cooling. However, cooling by sublimation also enhanced the descent of the RIJ in the stratiform region, which aided the generation of the wave. When sublimational cooling was removed, the horizontal wind speed maximum in the NOSUB run was associated with a region of weak ascent rather than descent. In the CTL, NOEVP and NOMLT runs the horizontal wind speed maximum of the RIJ in the stratiform region of the MCS descended.

- The diabatic cooling processes controlled the amount of descent in the RIJ. The RIJ descended to about 1 km in the CTL and NOMLT runs, but only reached 1.5 km in the NOEVP and NOSUB runs. The RIJ remained elevated and horizontal in the NOCOOL run and did not descend.

- The propagation and evolution of the storms in the NOEVP and NOSUB runs was very similar (Figures 4.17 to 4.21, discussed previously), even though a region of ascent developed in the RIJ in the NOSUB run that did not occur in the NOEVP run. The propagation of the storms was not affected by this region of ascent because there was no low-level stable layer in either the NOEVP or NOSUB runs, so no wave was generated by the RIJ and the convection was not wave-lifted. Therefore the descent of the RIJ, and the strength of its descent, was not as dynamically significant in the NOSUB and NOEVP runs as it was in the wave-lifted CTL and NOMLT runs.

4.2.7 The effect of diabatic cooling processes on the split of the MCS

As previously discussed, the convective system in the CTL run began to split into two at 1200 UTC (Figure 4.18a). The split was driven by diabatic cooling processes. No system split occurred in the NOEVP, NOSUB and NOCOOL runs (Figures 4.18b, 4.18c and 4.18e). The system in the NOMLT run showed some signs of splitting at 1200 UTC but the process never completed (Figure 4.18d). The diabatic cooling processes all acted to strengthen the RIJ and the convective downdraughts. It is hypothesised here that the system split in the CTL run was driven by the descending flow, which had a RTF velocity component from the RIJ, meeting the inflow from the elevated source layer at about z=2.5 km and increasing the horizontal convergence at this level.

The relationship between absolute vorticity and horizontal divergence is given by the vorticity equation

$$\left(\frac{D}{Dt}\right)_h \xi_{abs} = -\left(\xi_{abs}\right) \nabla_h . \underline{v}, \tag{4.1}$$

where ξ_{abs} is the absolute vorticity, $\underline{v}$ is the velocity field and the subscript h refers to the horizontal terms. Equation (4.1) shows that the magnitude of the absolute vorticity is decreased by horizontal divergence and increased by horizontal convergence. The increased convergence where the descending RIJ and downdraught flow met the elevated inflow would generate an increase in vorticity. The vorticity generated by this process may have been strong enough to split the storm in the CTL run. Removing the diabatic cooling processes

weakened the flow in the RIJ and the downdraughts, leading to weaker convergence where the descending flow met the inflow, and thereby weakening the vorticity.

There was a region of westerly flow at z=2.5 km through a region of low-valued θ_e from the centre of the storm to the leading edge of the precipitation in the CTL run at 1200 UTC (Figure 4.37a). Ahead of the storm there was an inflow of high-valued θ_e air (Figure 4.37a). The inflow met the westerly flow just behind the leading edge of the precipitation. There was a line of convergence about 50 km long at the boundary between the flows (Figure 4.37b). As expected from Equation (4.1), the line of convergence was associated with a large region of positive absolute vorticity (Figure 4.37b). There was no westerly component to the flow at z=2.5 km in the NOEVP, NOSUB or NOCOOL runs (Figures 4.37c, 4.37e and 4.37i, respectively). In these runs the inflow at z=2.5 km was also weaker. The convergence was weak at z=2.5 km in the NOEVP, NOSUB or NOCOOL runs, and the vorticity field did not develop a strong positive region (Figures 4.37d, 4.37f and 4.37j, respectively). The westerly component to the flow in the storm at z=2.5 km in the NOMLT run was weaker than that in the CTL run (Figure 4.37g). The line of convergence where the westerly flow in the NOMLT run met the inflow was about 30 km long, and the associated region of positive vorticity was not as large as that in the CTL run (Figure 4.37g).

These results support the hypothesis that the diabatic cooling processes favoured the split of the storm because vorticity was generated by the convective downdraughts and the RIJ meeting the elevated inflow. Cooling by melting had the weakest effect. The storm in the NOMLT run showed signs of splitting at 1200 UTC but the process never fully established. There was some convergence in the NOMLT run at the level where the RIJ and downdraughts met the inflow, but it was not as strong as the convergence in the CTL run. The region of positive vorticity at the leading edge of the NOMLT run was about half the size of that in the CTL run. Cooling by evaporation and sublimation were stronger than cooling by melting and had similar effects to each other. The storm in the NOEVP, NOSUB and NOCOOL runs never split. There was no strong convergence at the level where the RIJ and downdraughts met the elevated inflow in these runs, and there was no large area of positive vorticity.

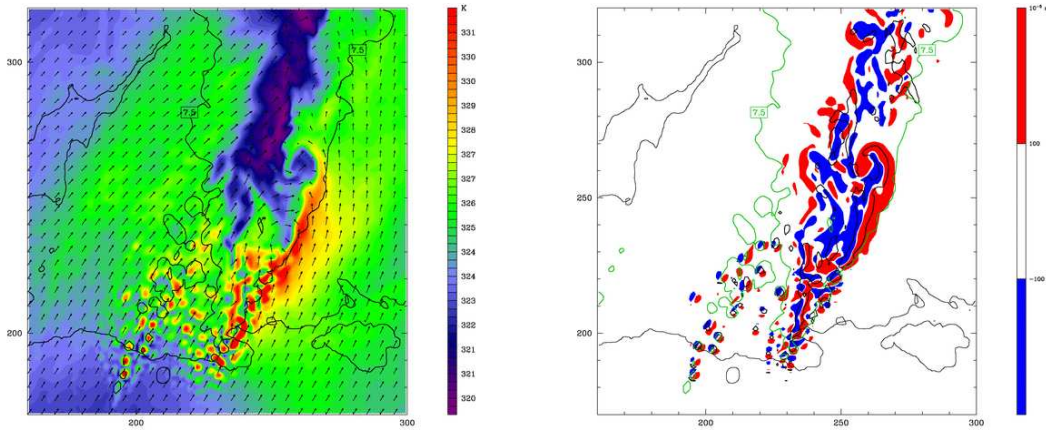

(A) CTL

(B) CTL

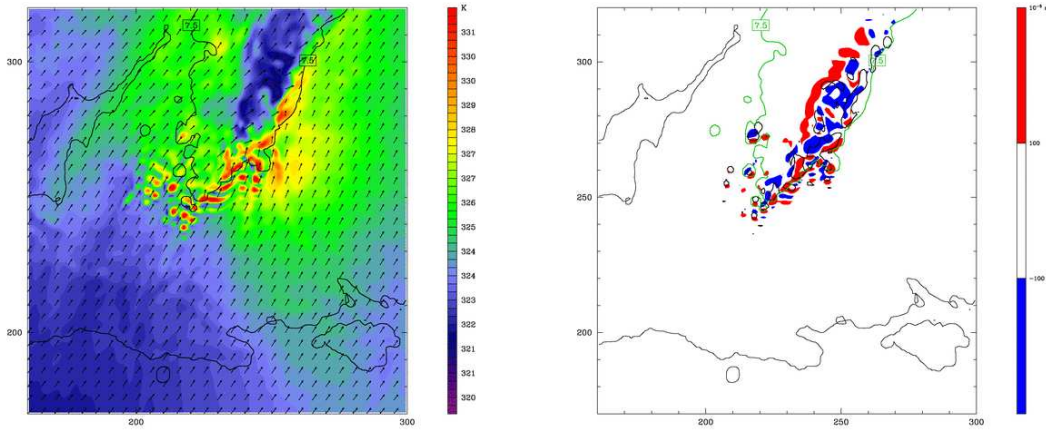

(C) NOEVP

(D) NOEVP

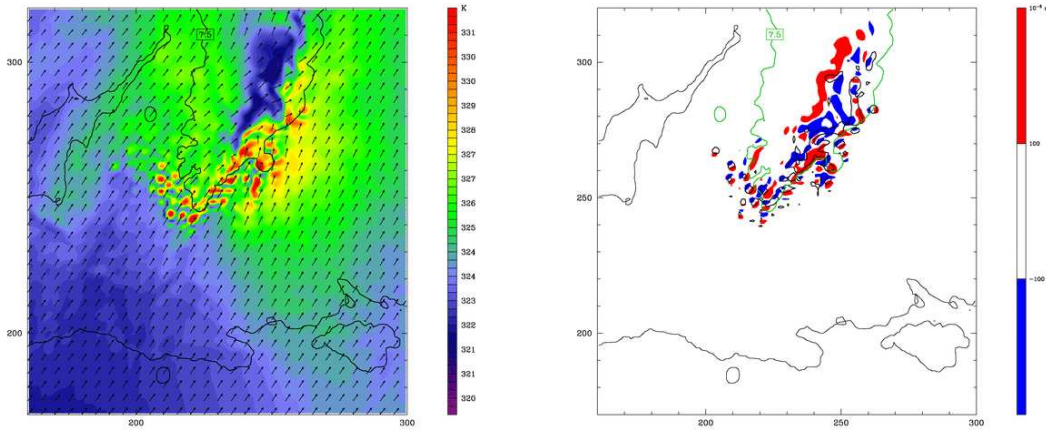

(E) NOSUB

(F) NOSUB

FIGURE 4.37: a-f: 1200 UTC data at z=2.5 km from the inner domain of the CTL, NOEVP and NOSUB runs. Figures 4.37a, 4.37c and 4.37e show θ_e (K, colour contour), maximum reflectivity (white line contour) and horizontal wind vectors (not system-relative). Figures 4.37b, 4.37d and 4.37f show absolute vorticity (10^{-5} s^{-1}, colour contour: red positive and blue negative), convergence (s^{-1}, black line contour) and maximum reflectivity (dBZ, green line contour).

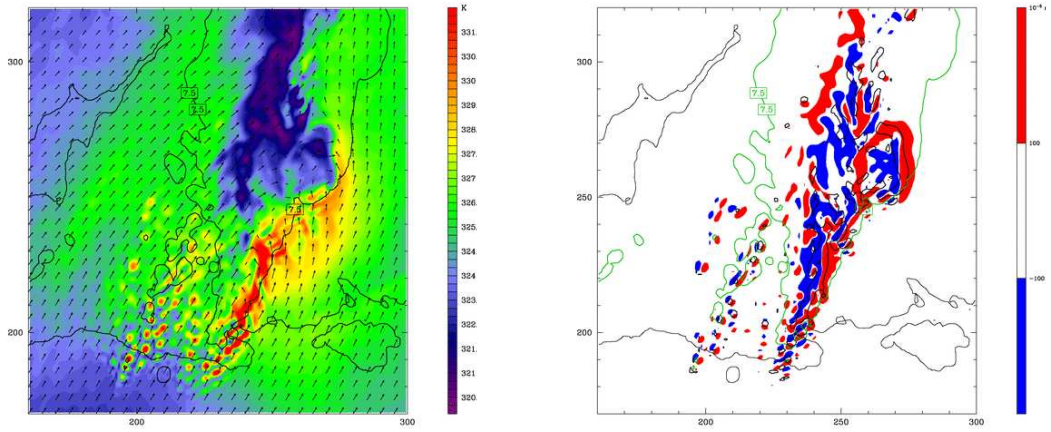

(g) NOMLT

(h) NOMLT

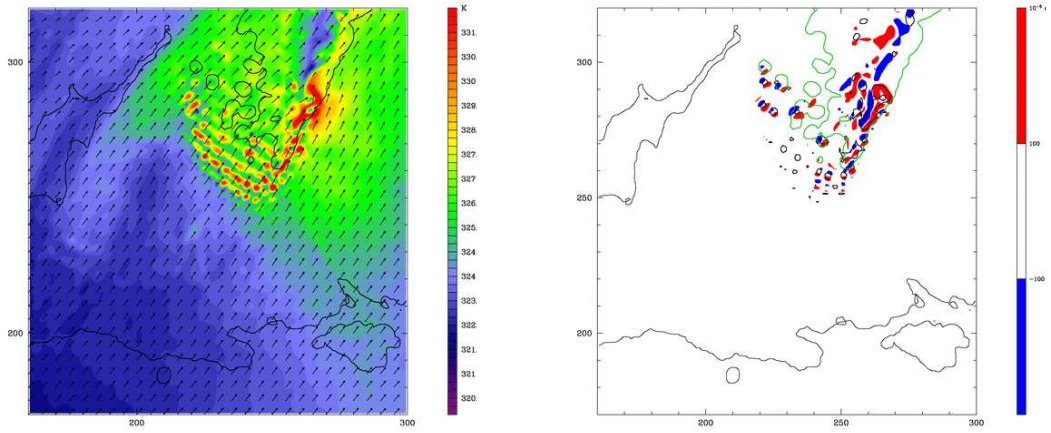

(i) NOCOOL

(j) NOCOOL

FIGURE 4.37: g-j: 1200 UTC data at z=2.5 km from the inner domain of the NOMLT and NOCOOL runs. Figures 4.37h and 4.37j show absolute vorticity (10^{-5} s^{-1}, colour contour: red positive and blue negative), convergence (s^{-1}, black line contour) and maximum reflectivity (dBZ, green line contour). Figures 4.37g and 4.37i show θ_e (K, colour contour), maximum reflectivity (white line contour) and horizontal wind vectors (not system-relative).

4.2.8 Summary of the effect of diabatic cooling processes on the simulated MCS

This is the first known study of the effect of diabatic cooling processes on the interaction between the RIJ and the undercurrent in an elevated MCS. The five diabatic cooling sensitivity runs show that the system persists, and the RIJ descends, without any diabatic coolings. This was similar to the results of Trier *et al.* (2011), who found that the reflectivity field in their simulations was similar when latent cooling was removed from the model. This suggests that large-scale effects may be important in maintaining convection in the absence of a cold pool. The observations of Browning *et al.* (2010) showed that during IOP 3 the CSIP region was in a baroclinic zone. The idealised modelling studies of Crook and Moncrieff (1988) and Schumacher (2009) both found that in conditionally unstable environments with large-scale convergence a significant surface cold pool was not necessary for the maintenance of deep convection.

The diabatic cooling processes all favoured the split of the MCS. This was probably because the cooling processes caused stronger descent in the RIJ and the convective downdraughts, which increased the horizontal convergence where the descending air met the elevated inflow. The increased horizontal convergence generated stronger vorticity, which was enough to split the storm in the CTL run.

Of all the diabatic cooling processes, cooling by melting had the least significant effect on the structure of the convection and its near-environment. This could have been because the value of the latent heat of melting is an order of magnitude weaker than that of evaporation or sublimation. This was consistent with the results of Chen and Cotton (1988), who found that turning off the melting of ice particles in their model did not significantly affect the structure of the simulated MCS or the strength of its RIJ.

In contrast, sublimation and evaporation had the greatest effect on the structure of the MCS: they strengthened the descent of the RIJ, strengthened the undercurrent, caused the extension of the MCS to the south and aided the development of the gravity current. Without evaporational or sublimational cooling the RIJ and the undercurrent were weaker and the convection did not remain wave-lifted for long. The effects of cooling by evaporation and sublimation were found to be similar to each other, perhaps because the values

of the latent heats are of the same order of magnitude. Cooling by evaporation and by sublimation had a significant effect on the structure of the MCS. This was consistent with the results of Braun (1995), who showed that, above the melting level, the RIJ in their model was more sensitive to latent cooling by sublimation. However, this result disagreed with the findings of Yang and Houze (1995), who showed that removing latent cooling by sublimation from their model did not alter the structure and evolution of their simulated storm. This was perhaps surprising, as Yang and Houze (1995) used a high-resolution cloud-resolving model. In a series of spiral aircraft descents in the stratiform region of convective lines, McFarquhar *et al.* (2007) found that sublimation was only significant in subsaturated air above the melting level. It is therefore possible that the results presented here, and those of Braun (1995), differ from the results of Yang and Houze (1995) due differences in the saturation of the air above the melting level in the simulations. For sublimation to have had a significant effect in the WRF simulation of IOP 3, the results of McFarquhar *et al.* (2007) suggest that the air above the melting level must have been subsaturated.

The relative maxima in the horizontal speed of the RIJ, occurring in the stratiform and convective regions, were similar to those observed by Smull and Houze (1987) and Klimowski (1994). Cooling due to microphysical processes was responsible for the relative maxima in the RIJ. In every run the maxima in the RIJ were associated with local maxima in the graupel, snow and rain mixing ratios. When all the diabatic cooling processes were removed from the model, a RIJ formed but neither descended strongly nor developed strong local maxima in its horizontal velocity field. Cooling by sublimation and evaporation appeared to weaken the wind speed maximum of the RIJ in the stratiform region. This disagreed with the findings of Braun and Houze (1997), who found that when sublimational cooling was removed from their model, no horizontal velocity maximum developed in their simulated RIJ. However, their simulations used a mesoscale model which did not resolve small-scale microphysical processes. Cooling by melting, however, appeared to strengthen the wind speed maximum of the RIJ in the stratiform region. This was consistent with the results of the high-resolution cloud model study of Yang and Houze (1995).

The convective updraughts were weakened by cooling due to evaporation and melting. This was consistent with the results of Trier *et al.* (2011), who found that removing latent

cooling processes from their simulation of a nocturnal elevated squall line led to weaker updraughts and downdraughts. This was also consistent with the results of Chen and Cotton (1988), who found that melting had the greatest impact on the strength of the convective-scale updraughts.

The combined effects of the diabatic cooling processes helped to generate the wave in the undercurrent. The undercurrent was strengthened by outflow from the north that was generated by evaporative and sublimational cooling. The diabatic cooling processes all enhanced the descent of the RIJ. The interaction of the RIJ with the stable undercurrent was responsible for the generation of the wave at the top of the undercurrent that lifted air from the elevated source layer to its level of free convection.

Cooling by evaporation and sublimation were responsible for the generation of gravity current outflow. This was consistent with the results of Trier *et al.* (2011), who found that gravity current outflow never formed when they removed latent cooling from their model, and that the horizontal speed of their simulated storm was much slower. Clark *et al.* (2012a) found that the the cold pool in their simulations was strengthened by the melting of snow and the evaporation of rain. Removing diabatic cooling from their model led to shallow surface cooling and a weak cold pool. Yang and Houze (1995) also found that removing latent cooling by evaporation from their model prevented a cold pool from forming. In contrast, Braun and Houze (1997) found that only minor changes occurred when they removed evaporational cooling from their model. However, their mesoscale model was not able to resolve small-scale microphysical processes.

Chapter 5

The interaction between Kelvin-Helmholtz billows and elevated convection

5.1 Kelvin-Helmholtz billows observed with an elevated mesoscale convective system during CSIP IOP 3

5.1.1 MCS B

Another MCS formed during CSIP IOP 3 that was associated with a large patch of billows, covering an area of about 2000 square kilometres. This was MCS B, labelled in Figures 3.2 a and c. MCS B was studied in detail by Browning *et al.* (2012). Details of the environment in which the billows formed and of the structure of the billows were determined from a radiosonde ascent close to the region of billows, the UK Met Office rain radar and the Chilbolton radars. The observations indicated that the billows may have had a forcing effect on the elevated convection occurring above. A summary of the analysis of the observations of MCS B made by Browning *et al.* (2012) is presented in this Section.

5.1.1.1 Billow development and structure

The large patch of billows formed in a region of moderate rainfall intensity behind MCS B. MCS B and MCS C formed in the same synoptic environment, described previously in Chapter 3, Section 3.1. The cool undercurrent flow was north to northeasterly, while the flow above it was south to southwesterly. The billows formed in the region of shear between these two flows.

Figures 5.1a and 5.1b are the network radar composite images showing the the rainfall pattern at 0945 and 1045 UTC. The range of the Chilbolton radar is marked by the white circle. There are several MCSs in Figure 5.1. The MCS in the bottom left of Figure 5.1 was MCS C that was studied in detail by Browning *et al.* (2010) and Marsham *et al.* (2010) and described in Chapter 3, Section 3.1.1. The MCS that was associated with the patch of billows occurred earlier than MCS C, was referred to as MCS B by Browning *et al.* (2010) and is labelled in Figures 3.2a and c. MCS B developed a line of heavy rain cells that were oriented in a north-south line. These rain cells reached Chilbolton at 0945 UTC (Figure 5.1a).

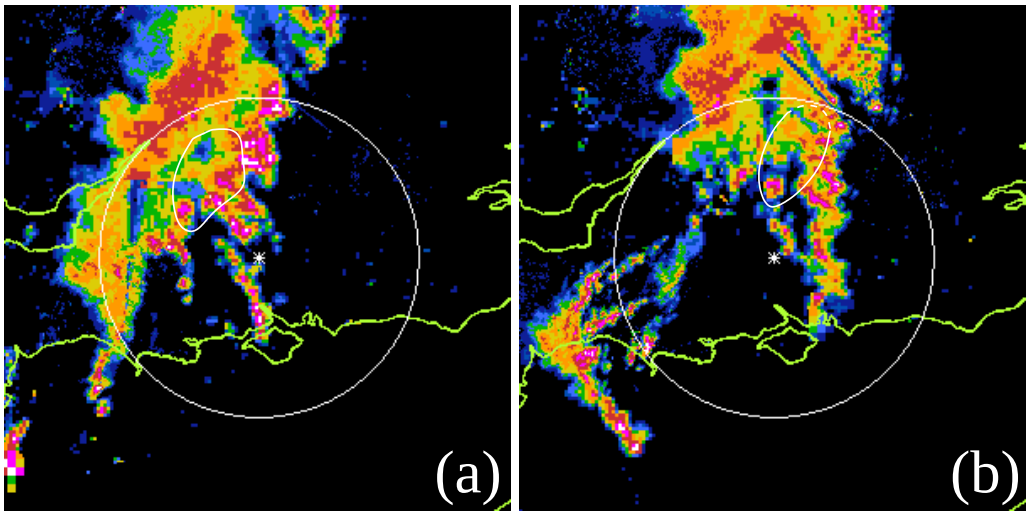

(A)
0945 UTC

(B)
1045 UTC

FIGURE 5.1: Rain echo pattern in southern England and Wales, obtained from the operational weather radar network at (a) 0945 and (b) 1045 UTC, 24 June 2005. The circle shows the 95 km radius coverage of the Chilbolton radar (not one of the network radars). The line of intense convective echoes extending north-south through Chilbolton at 0945 UTC corresponds to the leading edge of MCS B. The roughly elliptical contour behind the main rain area of MCS B shows the extent of the large-amplitude billows. A further area of precipitation associated with another, weakening, MCS is located to the north-west of the area of billows. From Browning *et al.* (2012).

RHI plots from a scan of the Chilbolton radar at 1023 UTC along 348° are shown in Figure 5.2. This scan was through the middle of the region of billows and was approximately parallel to, and to the west of, the north-south leading line of heavy precipitation associated with MCS B (Figure 5.1b). The scan passed through a region of weak rain at the rear of MCS B (Browning *et al.*, 2012). Weak convective cells could be seen in the reflectivity field (Figure 5.2a). The cells had a spacing of 2 to 4 km and reached a height of about 6 to 7 km (Browning *et al.*, 2012).

The billows formed in an inclined layer of strong shear (Doppler velocity, Figure 5.2b). The billows can be clearly seen in the orange and red braided patterns in Figure 5.2c. These structures were similar to the braided echo structure seen by Browning and Watkins (1970) and Chapman and Browning (1997) in their observations of large-amplitude billows. The billows were also clearly apparent in the spectral width (Figure 5.2d). At a range of 50 to 60 km the crest-to-trough amplitude of the billows was between 500 and 700 m. At closer ranges the amplitudes of the billows was about half this value. Beyond 70 km, quasi-horizontal filaments were seen (Browning *et al.*, 2012). These filaments were similar to those observed by Browning and Watkins (1970). The filaments may have corresponded to split shear layers left over after the billows had broken, or may have been due to pre-existing or previously split shear layers (Browning *et al.*, 2012).

Slanting oscillations occurred above the billows at a height of between 5 and 7 km and a range of 70 to 90 km (blue and green colours, Figure 5.2c). Browning *et al.* (2012) did not understand the cause of them but suggested that they may have been gravity waves that were forced either by the convection in the MCS or by the billows.

A radiosonde was launched from Larkhill at 1022 UTC. This was close in both time and space to the RHI scan (Figure 5.2). The RHI scan showed that the height of the shear layer in which the billows developed was between about 1 and 2 km (900 to 800 hPa) at the location of the Larkhill ascent. Figure 5.3 is a tephigram constructed from the Larkhill radiosonde data. The cool undercurrent can be seen in the lowest 1 km (1000 to 900 hPa). The height of the shear layer corresponded to a stable layer at the top of the undercurrent (Browning *et al.*, 2012). There was strong shear in the layer between 900 to 800 hPa (Figure 5.4).

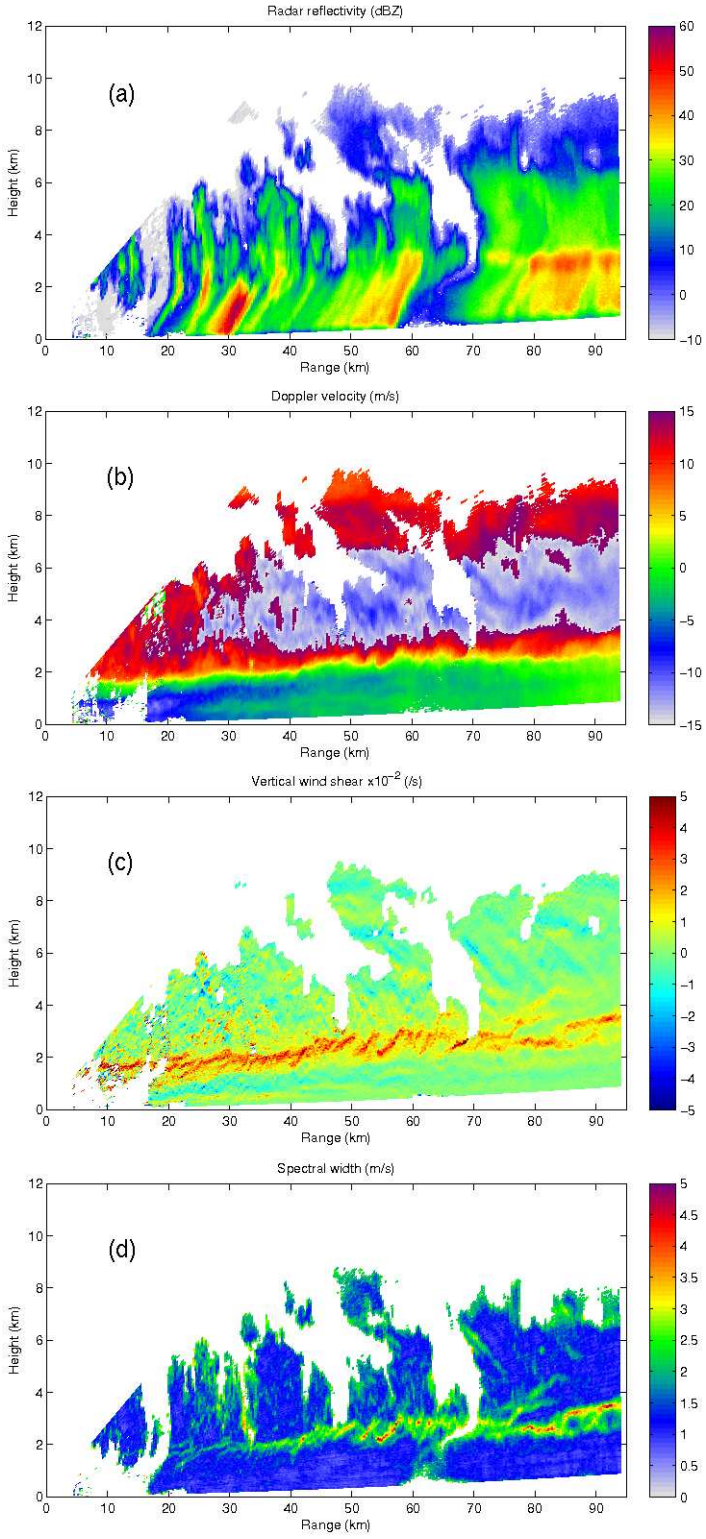

FIGURE 5.2: RHI scan from the Chilbolton Doppler radar along 348 ° at 1023 UTC, 24 June 2005, showing (a) reflectivity (dBZ), (b) Doppler velocity (m s^{-1}, velocities are 'folded' such that the upper-level grey and blue areas represent positive velocities greater than 15 m s^{-1}), (c) vertical shear of the Doppler velocity (s^{-1}) and (d) spectral width (m s^{-1}). Heights are shown above the radar dish (which is 100 m above mean sea level).

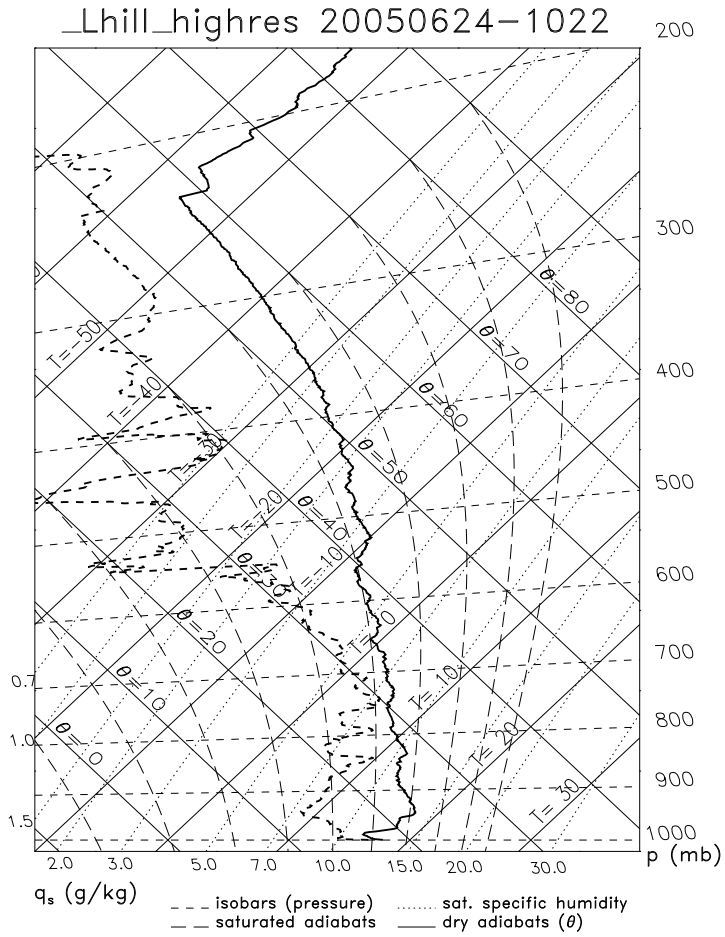

FIGURE 5.3: Tephigram constructed from data from a radiosonde ascent from Larkhill at 1022 UTC, 24 June 2005.

The largest billows were observed between 50 to 60 km range (Figure 5.2c). These had a wavelength of about 4 km and a crest-to-trough amplitude of about 700 m. Browning *et al.* (2012) used this wavelength and the theory of Miles and Howard (1964), Equation (1.6), to calculate that the shear layer in which the billows developed had a theoretical depth of roughly 500 to 900 m. This corresponded to the strong shear layer observed between 900 and 790 hPa in Figure 5.4. Smaller billow amplitudes observed elsewhere in Figure 5.2 tended to have shorter wavelengths. This was consistent with the shear instability occurring in a shallower layer (Browning *et al.*, 2012).

The edge of the region of billows passed over an AWS at North Farm between 0945 and 1100 UTC (Browning *et al.*, 2012). The pressure, temperature, relative humidity, wind speed and wind direction at North Farm between 1000 and 1200 UTC are shown in Figure 5.5. No fluctuations were observed in the surface temperature and relative

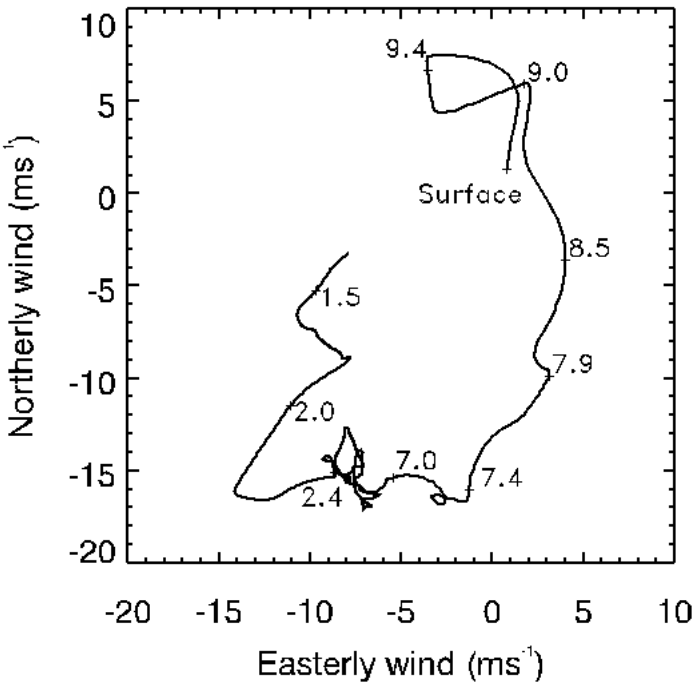

FIGURE 5.4: Hodograph constructed from data from a radiosonde ascent from Larkhill at 1022 UTC, 24 June 2005, pressure labelled in units of 100 hPa.

humidity. The wind speed was low (less than 1 m s^{-1}) during the observation period. Rapid fluctuations in surface pressure were observed between 1027 and 1100 UTC. The surface pressure perturbations had an amplitude of about ±0.3 hPa and a period of about 9 minutes (Browning *et al.*, 2012). The surface pressure perturbations occurred at about the same time as the billows passed over the AWS, suggesting that the billows may have caused the perturbations. This may have been due to the hydrostatic effect from overlying temperature anomalies caused by the billows lifting air parcels within the statically stable layer in which they were embedded (Browning *et al.*, 2012). Browning *et al.* (2012) assumed an advection velocity of the billows of 4 m s^{-1} from Figure 5.4, and using the 9 minute observed period of the billows calculated that the expected wavelength of the billows would have been about 2 km. This wavelength was shorter than that of the large-amplitude billows observed between ranges of 50 to 60 km in Figure 5.2, but was consistent with the wavelength of the smaller-amplitude billows seen elsewhere. The smaller-amplitude billows had crest-to-trough amplitudes of about 300 m. Browning *et al.* (2012) assumed that the observed surface pressure perturbations of ±0.3 hPa were hydrostatic effects of the overlying billows, and calculated that this would correspond to mean temperature anomalies of ±1°C over the 300 m depth of the billows. This was a reasonable estimate, as the potential temperature increased by 4°C km^{-1} over the 900-800 hPa layer (Figure 5.3)

(Browning *et al.*, 2012).

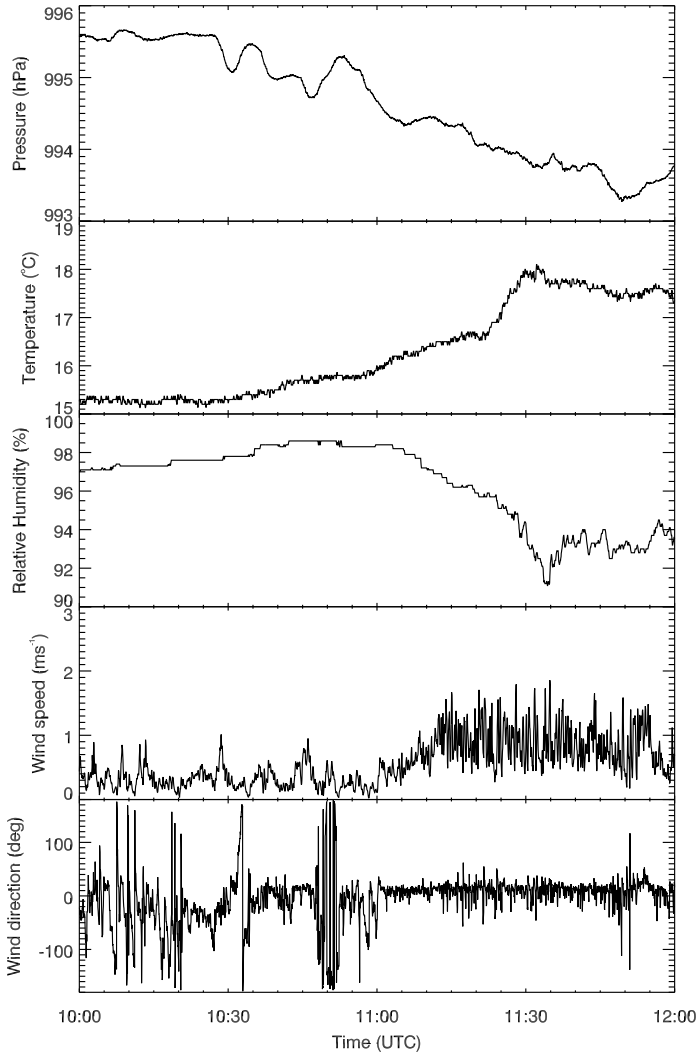

FIGURE 5.5: Data from the North Farm automatic weather station on 24 June 2005, showing pressure (hPa), temperature (°C), relative humidity (%), wind speed (m s^{-1}) and wind direction (degrees).

5.1.1.2 The relationship between the billows and the elevated convection

The shear layer in which the billows formed marked the transition between the cool north-easterly undercurrent flow and the warm, potentially unstable southerly flow above it. Air parcels with high values of wet-bulb potential temperature at 750 hPa required about 150 hPa of lifting to reach their level of free convection and would have been able to ascend to about 550 hPa (Figure 5.3) (Browning *et al.*, 2012). If some of the drier air above

750 hPa was lifted, convection to 550 hPa and above would have been possible with less lifting of the high wet-bulb potential temperature air (Browning *et al.*, 2012). Convection did occur up to and above 550 hPa (6 km) (Figure 5.2a).

Browning *et al.* (2012) showed that there was evidence of the large-scale ascent that was required to initiate convection. This lifting was associated with the deepening of the undercurrent to the north. This deepening can be seen in the slope of the strongly sheared layer at the top of the undercurrent in Figure 5.2b (Browning *et al.*, 2012). The air with high wet-bulb potential temperature at 750 hPa that fed the elevated convection had a greater southerly flow component than the air in the shear layer (Figure 5.4) (Browning *et al.*, 2012). The shear layer maintained its slope over time, so the high wet-bulb potential temperature air would have ascended above the inclined shear layer at the top of the undercurrent (Browning *et al.*, 2012). The source air for the elevated convection would have ascended by as much as 1 km as it travelled north and reached the centre of the region of billows. This process triggered the elevated convection and would have occurred whether the billows developed or not (Browning *et al.*, 2012). The cause of the slope in the undercurrent depth was not determined by Browning *et al.* (2012), but was suggested to be due to the large-scale dynamics associated with the baroclinic environment of IOP 3.

Elevated convection would probably have been initiated regardless of whether billows formed or not. However, data from a later RHI scan suggested that there was an interaction between the billows and the elevated convection. Browning *et al.* (2012) suggested that the precipitation cells in Figure 5.2 originated from elevated convection that had ceased at the time of the scan. A later scan showed ongoing convection above the patch of billows. This scan was along 025 ° at 1052 UTC and is shown in Figure 5.6.

Browning *et al.* (2010) showed that the boundaries of convective plumes rising in a region already filled with precipitation echo can sometimes be discerned by enhanced Doppler spectral width. Five such convective plumes are centred at 48, 63, 73, 84 and 91 km in the spectral width plot in Figure 5.6c. The plumes reached heights of 5 to 6 km. Each plume was 5 to 12 km wide. The plumes could also be seen in the Doppler velocity plot in Figure 5.6b as regions of lower-velocity air (red) from lower levels which ascended into a region of higher-velocity air (blue) (Browning *et al.*, 2012). Each of the plumes was associated with a region of precipitation (reflectivity plot in Figure 5.6a).

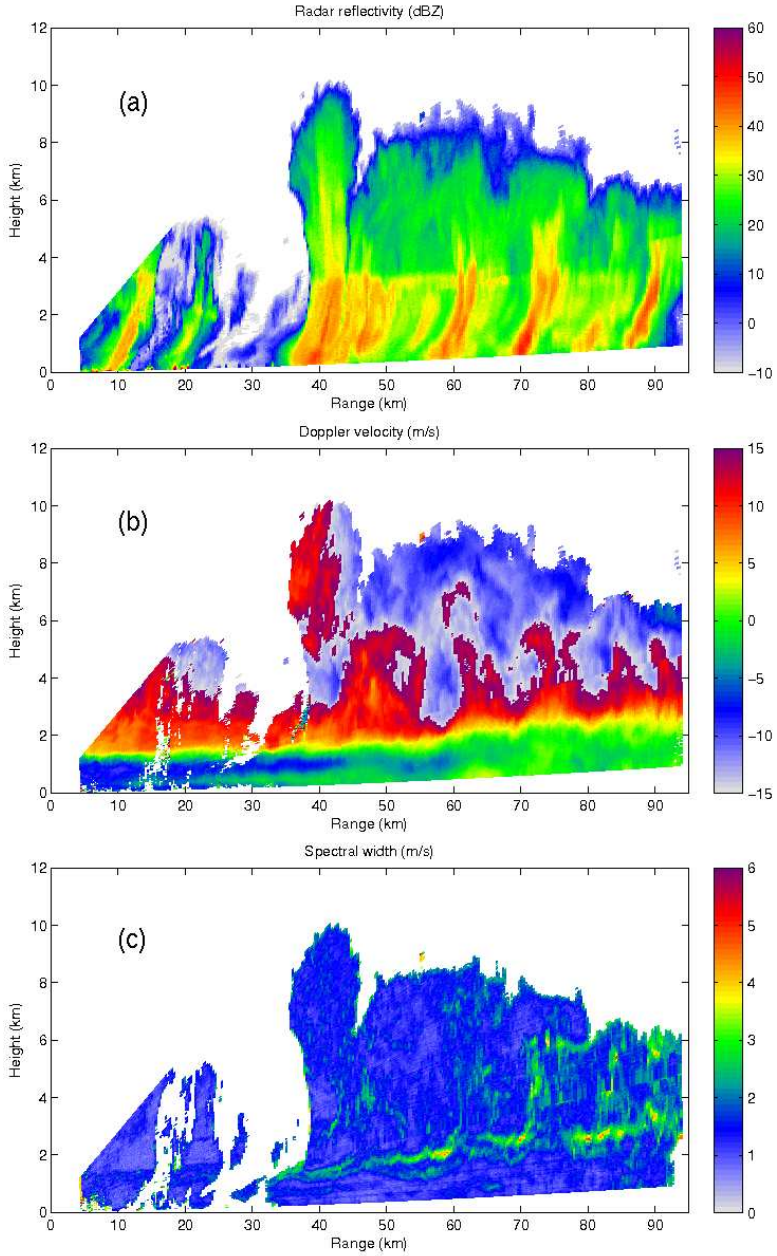

FIGURE 5.6: RHI scan from the Chilbolton radar along 25 ° at 1052 UTC, 24 June 2005, showing (a) reflectivity (dBZ), (b) Doppler velocity (m s^{-1}, velocities are 'folded' such that the upper-level grey and blue areas represent positive velocities greater than 15 m s^{-1}), and (c) spectral width (m s^{-1}). Heights are above the radar dish.

The convective plumes in Figure 5.6 originated just above the shear layer in which the billows developed. Browning *et al.* (2012) noted that the regions of high spectral width due to turbulence at the convective plume boundaries in Figure 5.6c originated from the layer of high spectral width due to the main sloping shear layer in which the billows developed. The billow at a range of 60 to 67 km was connected to the convective plume above it, leading Browning *et al.* (2012) to suggest that the billows helped trigger the convection, and/or the convection facilitated the development of shear instability.

Although the air with the greatest wet-bulb potential temperature was located at 750 hPa, above the strong shear layer, there were two other moist layers with a reasonably high wet-bulb potential temperature located at 790 hPa (at the top of the shear layer) and at 840 hPa (inside the shear layer) (Figure 5.3). Browning *et al.* (2012) suggested that when the billows broke, air from these other layers may have become entrained into the overlying convective updraughts. This would explain why the boundaries of the convective plumes in Figure 5.6c had their origin in the shear layer where the billows formed.

5.1.1.3 Summary of the MCS B and the patch of billows

MCS B was a case of elevated convection that was associated with a large patch of Kelvin-Helmholtz billows. The billows occurred at the sheared boundary between the cool north-easterly undercurrent and the overlying southwesterly potentially unstable flow. The elevated potentially unstable air was the source air for a series of elevated MCSs. The statically stable shear layer in which the billows formed was tilted and deepened to the north. Potentially unstable air ascended along the statically stable layer. Several convective plumes, or aggregates of plumes, were observed in MCS B. The large-scale ascent of the potentially unstable air along the statically stable layer would have provided sufficient lifting to trigger the elevated convection. However, Browning *et al.* (2012) found that the plumes originated from the shear layer in such a way that suggested an interaction between the billows and the elevated convection.

5.2 Studies of billows-convection interactions using the Met Office Large Eddy Model

5.2.1 Model set-up

The Met Office Large Eddy Model (LEM) (Derbyshire *et al.*, 1994; Gray *et al.*, 2001) was used to perform a series of 2D model runs to investigate the interaction between the billows and the convection. A description of the LEM is given in Section 2.2 of Chapter 2. The domain was 60 km wide and a horizontal grid spacing of 100 m was used. There were 162 vertical levels on a stretched vertical grid, with a spacing of about 25 m at the level of the billows. Each run was initialised using the Larkhill 1022 UTC profiles of temperature, moisture (Figure 5.3) and north-south wind component (Figure 5.4).

In order to simulate an environment similar to that observed, large-scale ascent was imposed in all model runs. Because periodic boundary conditions are used in the LEM, ascent could not be forced directly: mass cannot be moved in to or out of the model domain. Instead, the effects of large-scale ascent were simulated by forcing the temperature, water vapour and winds all over the domain. These temperature perturbation forcings corresponded to a zero rate of ascent at the surface and a rate of 20 cm s^{-1} above 2 km. The forcings were linearly interpolated between these heights. The forcings are referred to as "ascent" in this discussion. The forcings triggered convection in the model.

A set of runs was created to investigate whether there was an interaction between the billows and the elevated convection. In the control run, referred to as the "observed-shear" run, the horizontally-averaged winds were set to be those in the observed wind profile (after adjusting for imposed ascent). This controlled the mean wind profile while maintaining the perturbations from the mean. Ascent was imposed from the start of the run. Convective plumes developed in the control run, but after a time that corresponded to an imposed ascent of 1.5 km only very weak billows developed compared to those observed. A "low-shear" run was performed in order to produce a control run with no billows, in which the horizontally-averaged winds were set to zero. In order to study the effects of large billows, the winds in another two runs were set to $(1 + 0.1t)$ times the observed wind profile, where t is the simulation time in hours. In order to develop large billows,

ascent had to be imposed later than $t = 0$ in these runs (the shear in the model increased with time). These are referred to as "increasing-shear" runs. Shear was increased with time in these runs in order to explore a greater range of shears with the fewest possible simulations. It would also have been possible to simply set the shear to be larger than the observed shear (i.e. using greater but time-independent shear), but to explore the effect of this on billow development would have required many runs at different shear strengths. Ascent was imposed from 1.5 hrs in one run and from 2.0 hrs in another. The run with ascent imposed from 2.0 hrs developed unrealistically large billows which broke before convection developed. The run with ascent imposed from 1.5 hrs developed billows that compared favourably to those shown in Figure 5.2. This run was used to study the interaction between the billows and convection.

5.2.2 The development of billows in the LEM

Billows developed before convection in the two model runs with increasing shear. One of these runs had ascent imposed from 1.5 hrs and the other had ascent imposed from 2.0 hrs. The difference in time at which ascent was imposed significantly affected the development of billows in the model, due to the difference in shear at the time when ascent began. Billows developed at the beginning of ascent in the 2.0 hr run and after 315 m of ascent in the 1.5 hr run. The billows that developed in the 2.0 hr run grew rapidly and broke before convection developed.

In both cases, the billows initially formed at a height of about 1.5 km. In the 2.0 hr run the profile of the Richardson number was less than 0.25 between heights of 1.0 and 1.5 km at the onset of billow development (at the beginning of ascent, Figure 5.7a). In the 1.5 hr run the profile of the Richardson number was less than 0.25 between heights of 1.1 and 1.6 km at the onset of billow development (after 315 m of ascent, Figure 5.7b).

After 360 m of ascent in the 2.0 hr run the billows were centred at a height of about 1.5 km, corresponding to a height of approximately 1.9 km accounting for the imposed ascent (Figure 5.8a). The billows were deep, with a crest-to-trough amplitude of about 1400 m and a wavelength of about 4.6 km. There were two liquid water clouds above the crests of most of the billows, centred at heights of about 2.3 km and 3.0 km (which

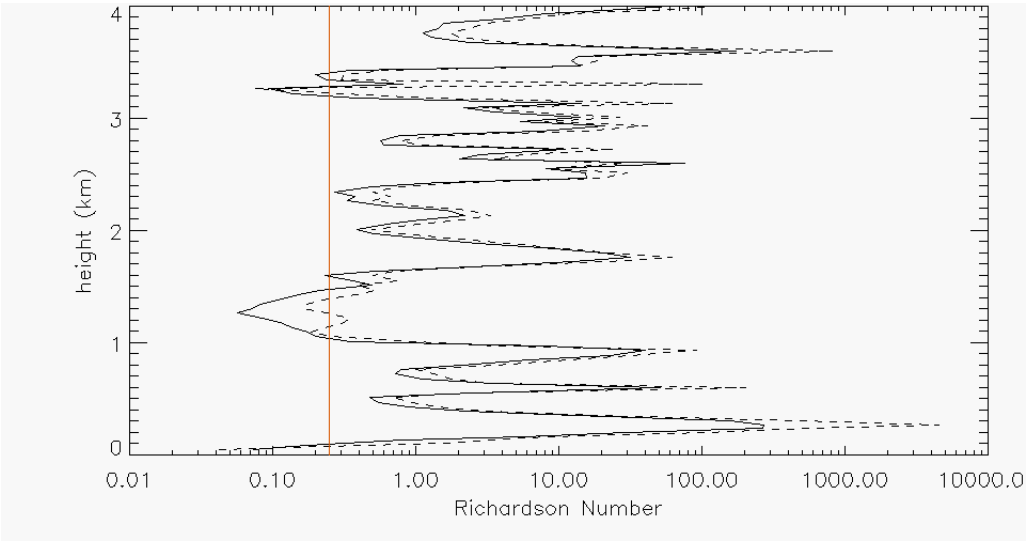

(A) Increasing-shear run with ascent imposed after 2.0 hrs.

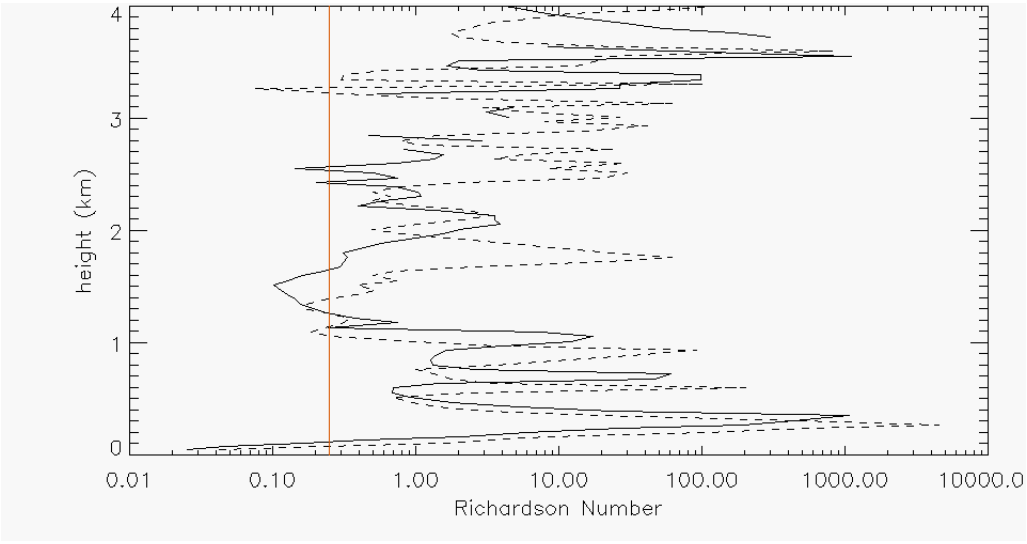

(B) Increasing-shear run with ascent imposed after 1.5 hrs.

FIGURE 5.7: Profile of the Richardson number for the two increasing-shear runs at the onset of billow development (solid line) and from the original sounding (dashed line). Vertical red line shows the critical value of Ri=0.25.

corresponded to "true" heights of 2.7 and 3.4 km, respectively, accounting for the imposed ascent). The deep billows showed evidence of rolling up and breaking even though deep convection had not yet developed in the 2 hr run.

After 855 m of imposed ascent in the 1.5 hr run the billows were centred at a height of about 1.75 km, equivalent to a height of approximately 2.6 km accounting for the imposed ascent (Figure 5.8b). This was similar to the observations. The billows had a crest-to-trough amplitude of about 800 m and a wavelength of about 5.0 km, broadly similar to the

observations shown in Section 5.1 which had a crest-to-trough amplitude of about 700 m and wavelength of about 4 km. Liquid water clouds formed above the billow crests, as in the 2 hr run. However, in the 1.5 hr run there was only one liquid cloud. In addition, convective clouds with cores of ice and graupel formed above the billow-crest clouds and rain fell from the clouds. Even though the billows were reasonably large and the convection was mature, the billows in the 1.5 hr run did not show any evidence of wave breaking after 855 m of ascent.

The billows in the 1.5 hr run formed at a similar height and had a wavelength and crest-to-trough amplitude that was broadly comparable to the observations. The billows did not break before convection developed in the 1.5 hr run. For these reasons the 1.5 hr run was used to investigate the nature of the interactions between the billows and convection. In the 1.5 hr run the model spin-up period completed before ascent was imposed. The observed-shear and low-shear runs, which originally had ascent imposed from the start, were therefore repeated with ascent imposed from 1.5 hrs. These runs are compared in the next Section.

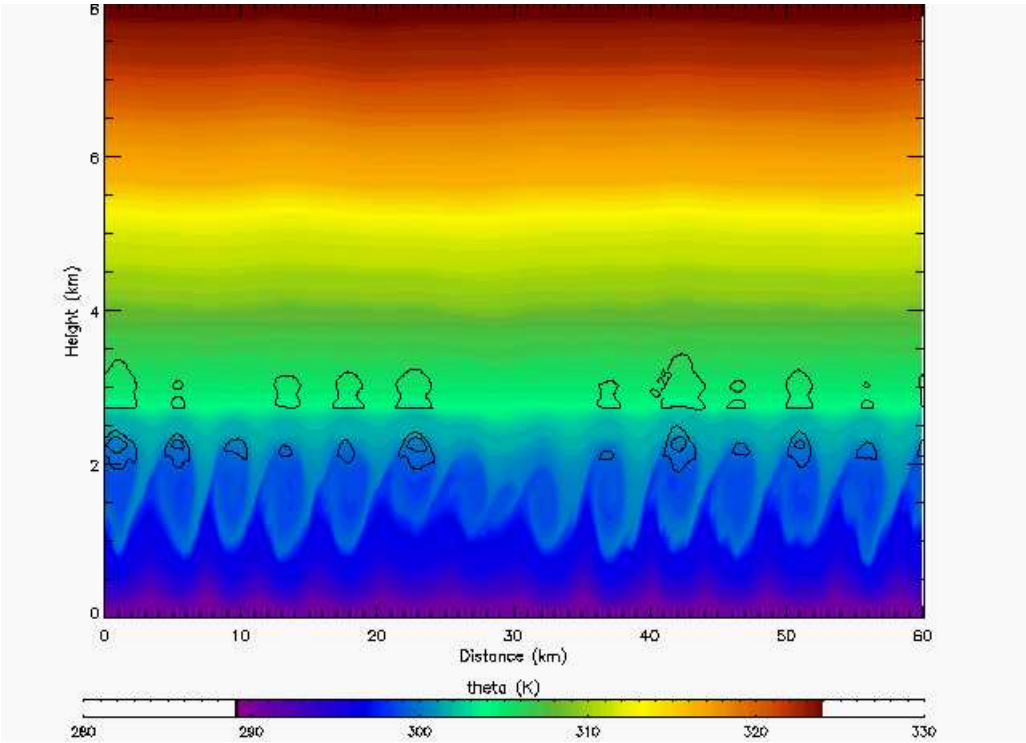

(A) Increasing-shear run with ascent imposed after 2.0 hrs: billow development after 360 m of ascent.

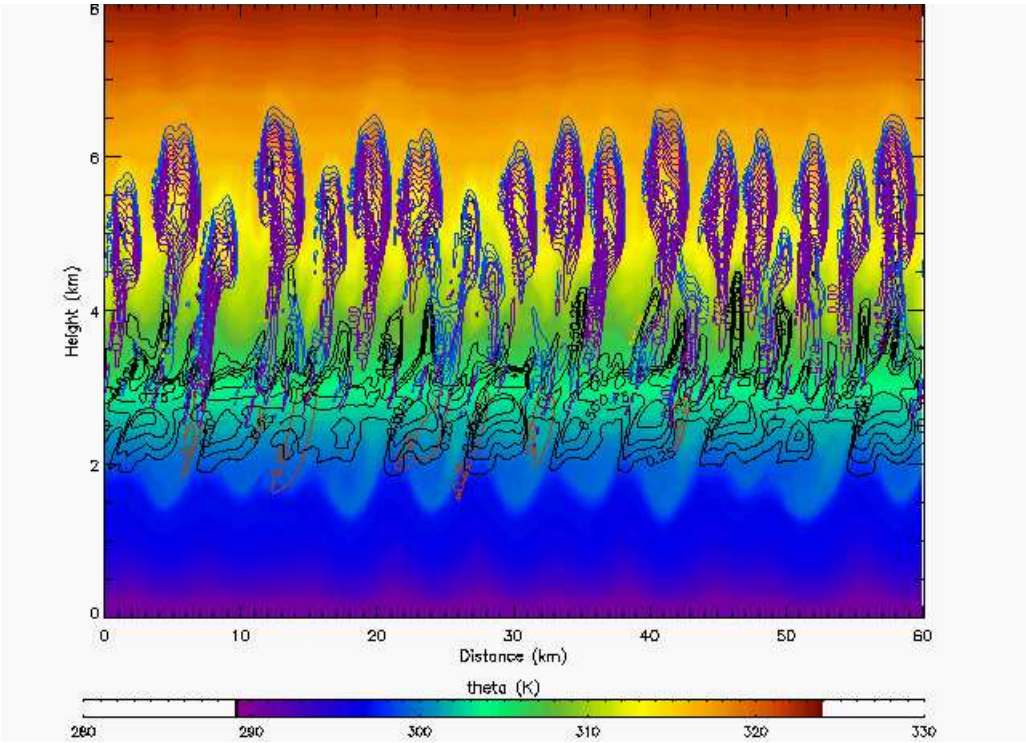

(B) Increasing-shear run with ascent imposed after 1.5 hrs: billow development after 855 m of ascent.

FIGURE 5.8: Potential temperature (K, colour contour) and hydrometeors (g kg^{-1}, line contours: black = cloud water, orange = snow, blue = ice, red = rain, purple = graupel).

5.2.3 The sensitivity to the time at which ascent was imposed

Imposing ascent later in the run led to the development of higher cloud tops for a given imposed ascent. The cloud top height (not adjusted for imposed ascent) as a function of total ascent for each of the six runs is shown in Figure 5.9. For ascent greater than about 720 m the low-shear run with ascent imposed from 1.5 hrs (dashed blue line) developed higher cloud tops than the low-shear run with ascent imposed from 0 hrs (solid blue line). For ascent greater than about 540 m the observed-shear run with ascent imposed from 1.5 hrs (dashed red line) had higher cloud tops than the observed-shear run with ascent imposed from 0 hrs (solid red line). For all values of imposed ascent, the increasing-shear run with ascent imposed from 2.0 hrs (dash-dot black line in Figure 5.9) developed higher cloud tops than the increasing-shear run with ascent imposed from 1.5 hrs (dashed black line in Figure 5.9).

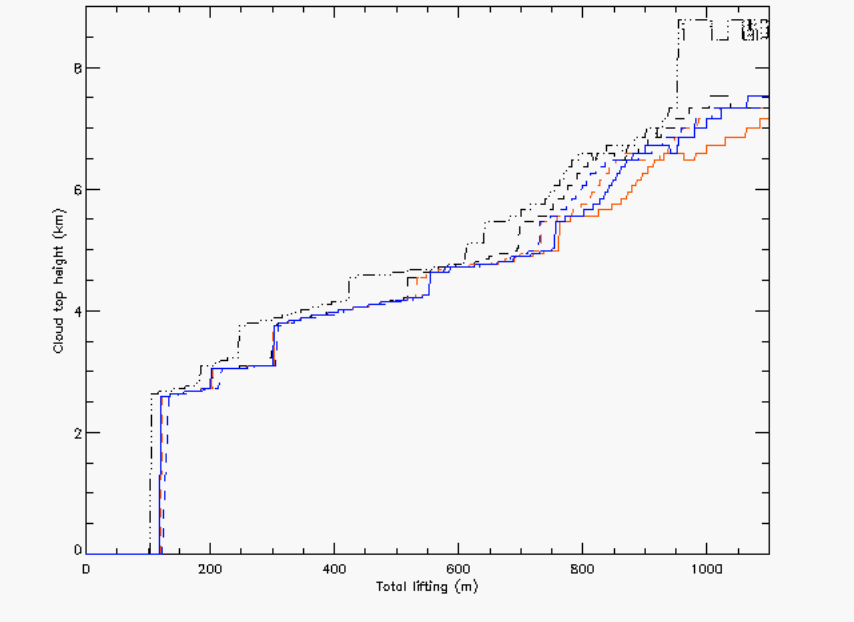

FIGURE 5.9: Cloud top height (km) as a function of total imposed ascent (m) for each of the six runs: black lines show increasing-shear runs, red lines show observed-shear runs, blue lines show low-shear runs; linestyles denote hours into the run from which ascent was imposed: solid: 0, dashed: 1.5, dash-dot: 2.0

Applying ascent later in the run led to the development of greater maximum vertical velocities for a given value of total ascent. The maximum vertical velocity as a function of total imposed ascent for each of the six runs is shown in Figure 5.10. For total ascent greater than about 500 m the low-shear run with ascent imposed from 1.5 hrs (dashed

blue line in Figure 5.10) developed greater maximum vertical velocities than the low-shear run with ascent imposed from 0 hrs (solid blue line in Figure 5.10). For all values of total ascent, the observed-shear run with ascent imposed from 1.5 hrs (dashed red line in Figure 5.10) had greater maximum vertical velocities than the observed-shear run with ascent imposed from 0 hrs (solid red line in Figure 5.10). This was also true for the increasing-shear run with ascent imposed from 2.0 hrs (dash-dot black line in Figure 5.10) compared to the increasing-shear run with ascent imposed from 1.5 hrs (dashed black line in Figure 5.10).

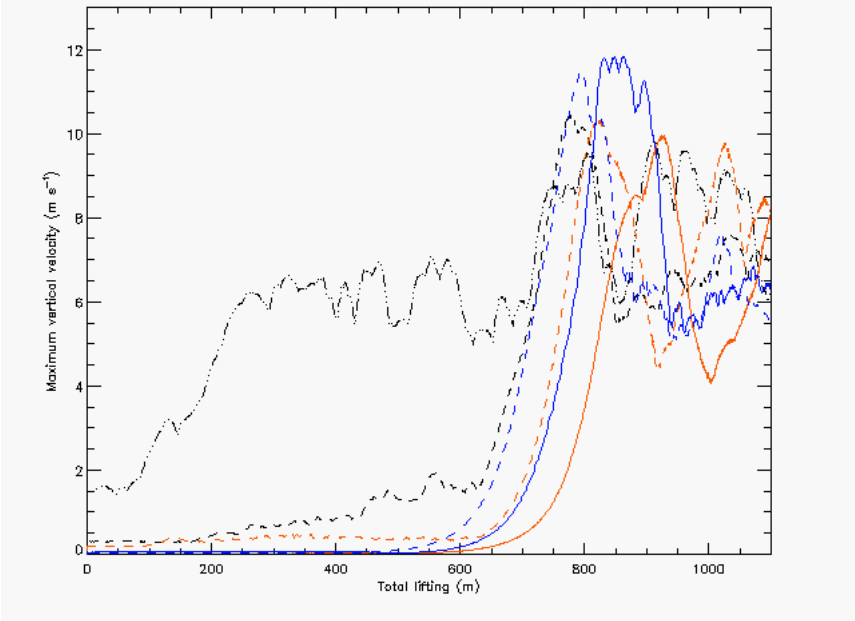

FIGURE 5.10: Maximum vertical velocity (m s^{-1}) as a function of total ascent (m). Line colours and styles as for Figure 5.9.

The results presented in Figure 5.9 and Figure 5.10 show that the time into the run at which ascent was imposed had a significant effect on the spin-up period of the model and therefore the subsequent behaviour of convection in the simulation. For this reason, detailed analysis was performed on the three runs which had ascent imposed from the same time into the run (1.5 hrs). These three runs are analysed in detail in Sections 5.2.4 to 5.3 and are referred to simply as the observed-shear, increasing-shear and low-shear runs.

5.2.4 The interaction between the billows and convection: onset and development of convection

Convective clouds formed in all three runs and the evolution of the clouds was similar in each run. The clouds initially consisted of liquid water only and then grew deep enough for ice, graupel and rain to develop. Secondary clouds formed in each of the runs. The amount of imposed ascent at which each of the steps of cloud evolution occurred depended on whether billows were present or not. These results are discussed in this Section.

Convection formed for less imposed ascent in the increasing-shear run than it did in either the observed-shear or the low-shear runs. In the latter two runs, convection formed at a similar amount of ascent. Convective clouds (referred to as 'primary clouds', due to the later development of secondary clouds) formed at 585 m of total imposed ascent in the increasing-shear run (Figure 5.11a), 630 m in the observed-shear run (Figure 5.11b) and 631 m in the low-shear run (Figure 5.11c). This is also shown in the wavelength analysis presented in Section 5.2.5. Convection formed for less imposed ascent in the increasing-shear run because the billows provided extra lifting.

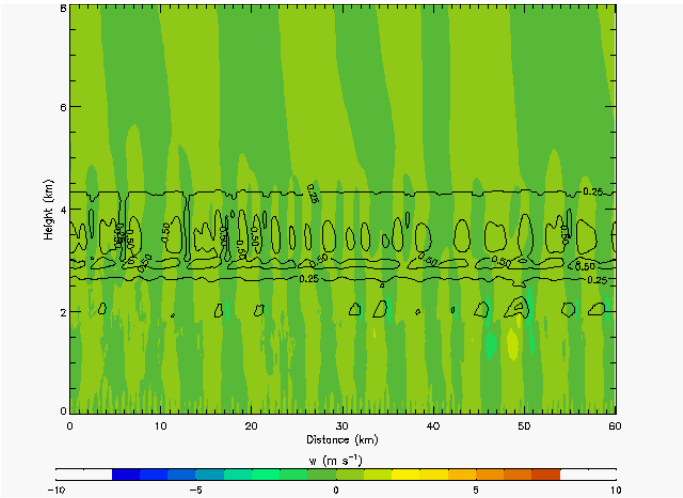

(A) Increasing-shear run: 585 m of imposed ascent.

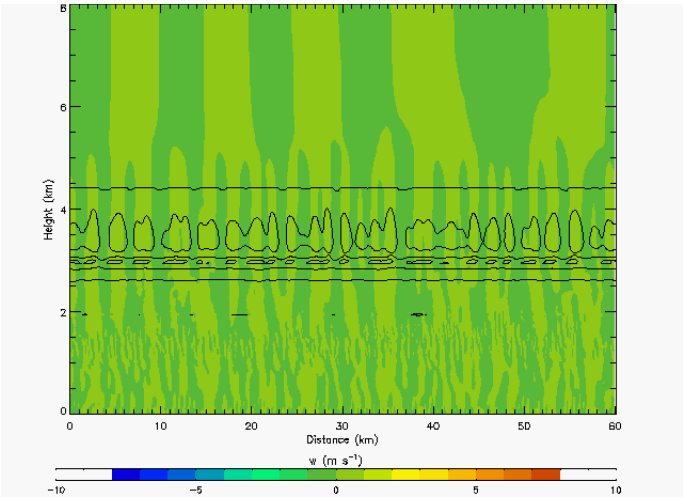

(B) Observed-shear run: 630 m of imposed ascent.

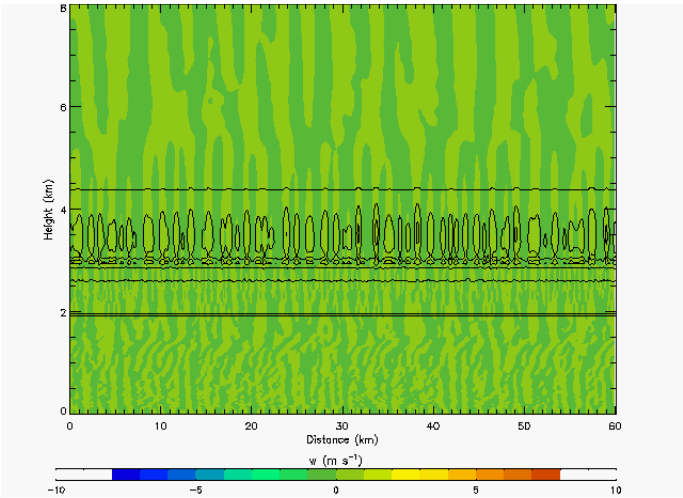

(C) Low-shear run: 631 m of imposed ascent.

FIGURE 5.11: Vertical velocity (m s^{-1}, colour contour) and hydrometeors (g kg^{-1}, black = cloud water, orange = snow, blue = ice, red = rain, purple = graupel) at the amount of imposed ascent at which convection first developed in each run.

There were fewer convective clouds in the presence of billows. The increasing-shear run had fewer clouds than either the observed-shear run or the low-shear run. The low-shear run (Figure 5.11c) had the most clouds, and the increasing-shear run (Figure 5.11a) had the fewest clouds. The number of clouds that developed in each run is discussed in detail in Section 5.2.5.

Initially there was no association between the number of clouds and the number of billows in the increasing-shear run. At the onset of convection in the increasing-shear run there were 19 clouds and 11 billows (Figure 5.8b).

Ice particles, graupel and rain all first occurred for less imposed ascent in the presence of billows. The extra lifting provided by the billows allowed the convective clouds to deepen more rapidly than in the runs without billows.

Secondary clouds formed for less imposed ascent in the presence of billows. The secondary clouds formed at the same imposed ascent at which rain first formed. The secondary clouds formed below the primary clouds at a height of about 4 km after 810 m of imposed ascent in the increasing-shear run (Figure 5.12a) and 900 m in the observed-shear (Figure 5.12b) and low-shear (Figure 5.12c) runs. Secondary clouds formed after the same amount of imposed ascent in the observed and low-shear runs.

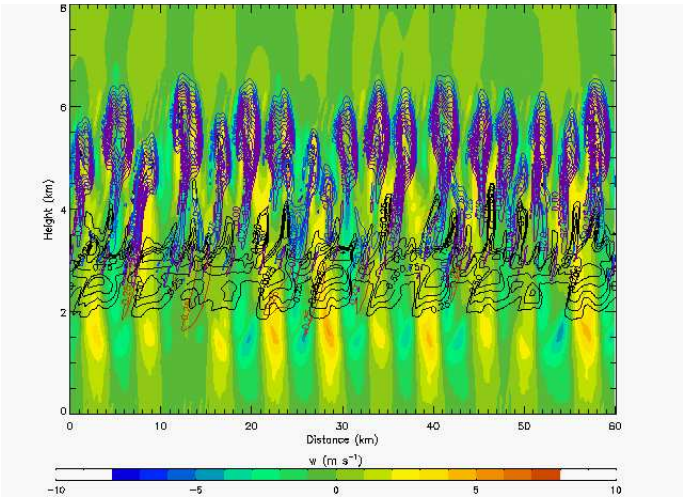

(A) Increasing-shear run: 855 m of imposed ascent.

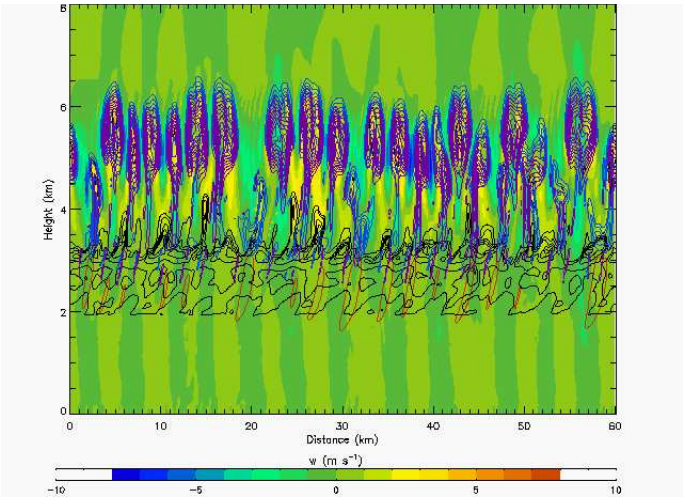

(B) Observed-shear run: 900 m of imposed ascent.

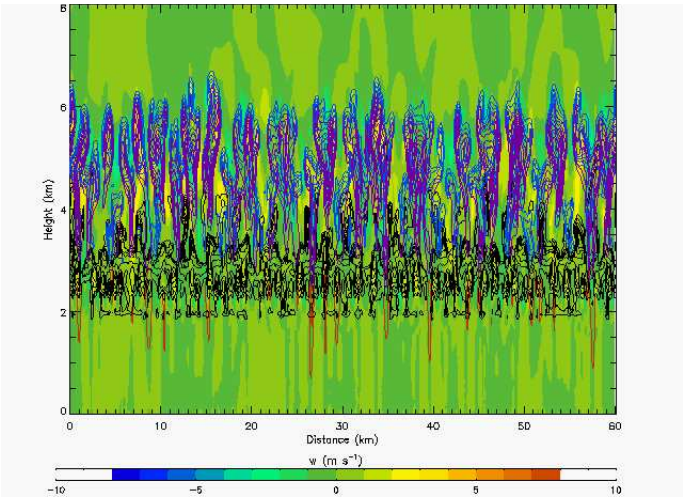

(C) Low-shear run: 900 m of imposed ascent.

FIGURE 5.12: Vertical velocity (m s^{-1}, colour contour) and hydrometeors (g kg^{-1}, black = cloud water, orange = snow, blue = ice, red = rain, purple = graupel) at the amount of imposed ascent at which rain was first seen in each run.

The cloud tops were higher in the presence of billows. Figure 5.9 in Section 5.2.3 showed the cloud-top height as a function of imposed ascent. For all values of imposed ascent the increasing-shear run had greater cloud-top heights than the observed-shear or the low-shear runs. The difference in cloud-top height tended to be only of the order of a few hundred metres.

The presence of billows led to the earlier development of large vertical velocities. Figure 5.10 in Section 5.2.3 showed the maximum vertical velocity as a function of imposed ascent. The evolution of maximum vertical velocity in the increasing-shear run was very similar to the low-shear run, but shifted such that the vertical velocities were attained for less imposed ascent.

5.2.5 The interaction between the billows and convection: wavelength analysis

The wavelength of the billows increased as the amount of imposed ascent increased (Figure 5.13a). Miles and Howard (1964) showed that the wavelength of the most unstable mode depended on the depth of the shear layer. This relationship was shown in Equation (1.6) in Section 1.9.1.2 of Chapter 1. The wavelength of the billows in the increasing-shear run increased because the depth of the shear layer increased. This was due to the wind forcing associated with the imposed ascent. At 765 m of ascent, the billow wavelength of (5.0±0.2) km should correspond to a shear layer depth of between 0.6 km and 1.2 km (Miles and Howard, 1964). The depth of the shear layer that developed billows was 0.75 km (between heights of 1.50 km and 2.25 km in Figure 5.14a), which is in agreement with the theory of Miles and Howard (1964). At an imposed ascent of 990 m, the wavelength of the billows was (6.7±0.4) km. Following Miles and Howard (1964), this should correspond to a shear layer depth of between 0.8 km and 1.6 km. The depth of the shear layer in which the billows were observed was 1.25 km (between heights of 1.25 km and 2.50 km in Figure 5.14b), which again agrees with the theory of Miles and Howard (1964).

The initial wavelength of the primary clouds was greater in the increasing-shear run than it was in the observed and low-shear runs. In the increasing-shear run (Figure 5.13a) the initial wavelength of the primary plumes was (2.9±0.1) km after 585 m ascent. In

the observed-shear run (Figure 5.13b) the initial wavelength of the primary plumes was (2.0±0.1) km after 630 m of ascent. In the low-shear run (Figure 5.13c) the initial wavelength of the primary plumes was (1.2±0.1) km after 630 m of ascent. Comparing the low-shear run with the observed-shear run indicated that shear increased the initial wavelength of the convection. However, the presence of billows further increased the initial wavelength of convection.

The wavelength of the primary clouds remained constant in the increasing-shear run for the first 5 steps of ascent, whereas in the other runs the wavelength of the primary clouds increased with every step of ascent. In the increasing-shear run, the wavelength of the primary clouds had a constant value of (2.9±0.1) km between 585 to 765 m of ascent (Figure 5.13a). For values of imposed ascent greater than 765 m the wavelength of the primary clouds in the increasing-shear run increased. In both the observed-shear run (Figure 5.13b) and the low-shear run (Figure 5.13c) the wavelengths of the primary clouds began to increase as soon as they developed. This indicates that an interaction was occurring between the billows and the convection. The extra lifting provided by the billows forced the clouds to form at the billow crests, whereas in the two runs that did not develop billows there was no such forcing mechanism for the initial cloud development.

In all three runs the wavelength of the primary clouds increased with the imposed ascent (Figure 5.13). In the increasing-shear run this happened after 765 m of imposed ascent, following a period in which the primary cloud wavelength remained constant. In the observed and low-shear runs the primary cloud wavelength increased as soon as the clouds formed. In the increasing-shear run the wavelength of the primary clouds was always greater than the wavelength of the primary clouds in the observed-shear and the low-shear runs (Figure 5.13). The initial wavelength of the secondary clouds was greater in the increasing-shear run than it was in the observed and low-shear runs (Figure 5.13). In all three runs the wavelength of the secondary clouds increased with the imposed ascent (triangle symbols in Figure 5.13). In the increasing-shear run the wavelength of the secondary clouds was always greater than the wavelength of the secondary clouds in the observed-shear and the low-shear runs.

The secondary clouds had the same wavelengths as the primary clouds. The wavelengths of the primary and secondary clouds were within the error limits of each other in the

increasing-shear and the low-shear runs (Figures 5.13a and 5.13c). In the observed-shear run (Figure 5.13b) the wavelengths of the secondary clouds were slightly longer than the wavelengths of the primary clouds. There was a 0.3 km difference between the upper limit of the primary cloud wavelength and the lower limit of the secondary cloud wavelength. However, the secondary clouds were harder to distinguish than the primary clouds. It is likely that this slight difference in wavelength was due to errors inherent to the visual analysis of the Figures and that the actual wavelengths of the primary and secondary clouds were the same in each of the runs.

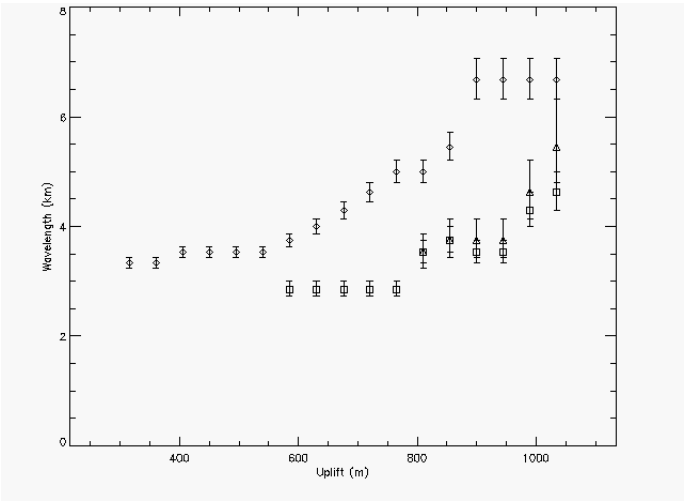

(A) Increasing-shear run.

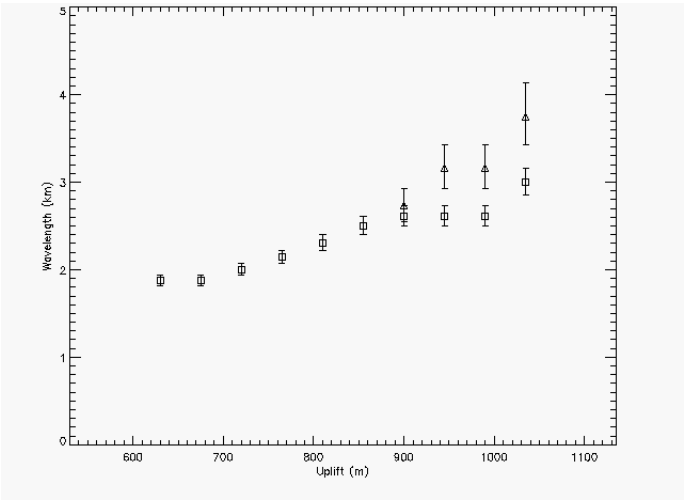

(B) Observed-shear run.

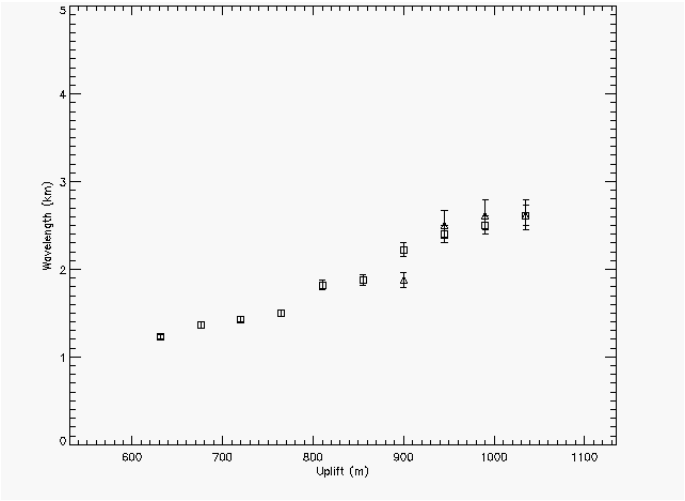

(C) Low-shear run.

FIGURE 5.13: Wavelength (km) of billows and clouds as a function of imposed ascent (m). Symbols show: diamonds = billows, squares = primary clouds, triangles = secondary clouds.

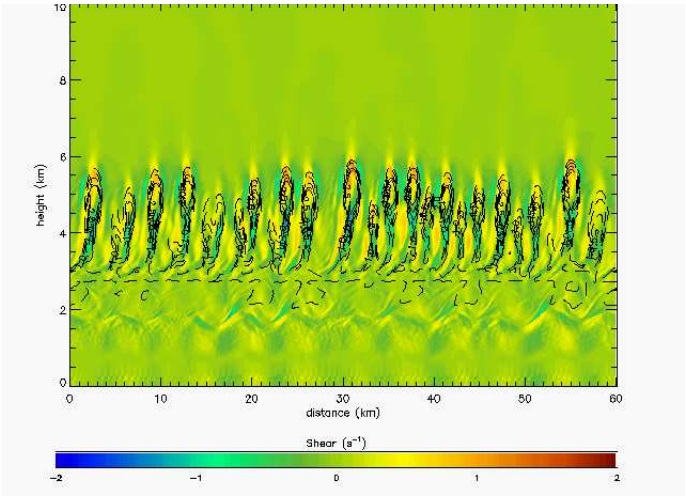

(A) 765 m of imposed ascent.

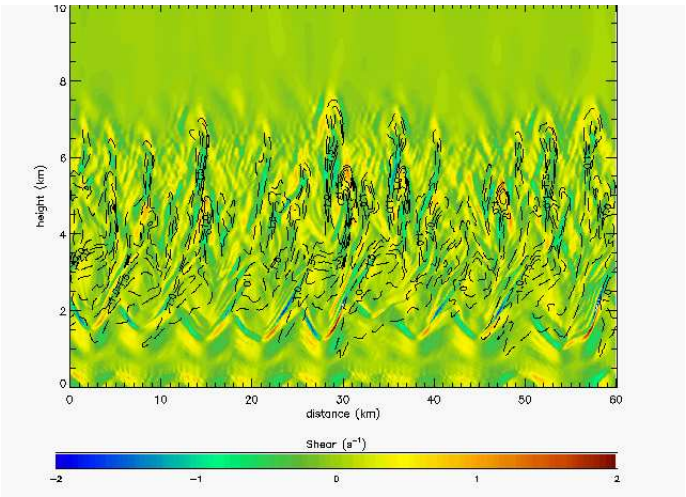

(B) 990 m of imposed ascent.

FIGURE 5.14: Increasing-shear run: vertical section of the shear field (s^{-1}).

The wavelength of both the primary and secondary clouds in the increasing-shear run tended towards a value that was half the wavelength of the billows. Two primary and two secondary clouds occurred per billow. The wavelengths of the primary and secondary clouds were the same (Figure 5.15). The ratio of the primary cloud wavelengths to the billow wavelengths tended towards a value of 0.5 as the amount of ascent increased (Figure 5.15). The same was true for the ratio of the secondary cloud wavelengths to the billow wavelengths.

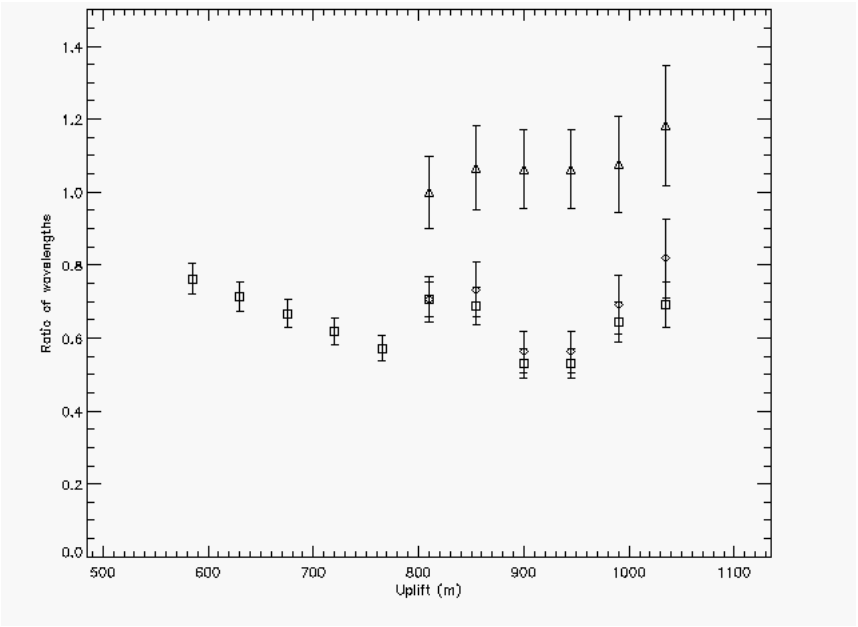

FIGURE 5.15: Ratio of wavelengths in the increasing-shear run. Symbols: squares = primary clouds : billows; diamonds = secondary clouds : billows; triangles = secondary clouds : primary clouds.

The wavelengths of the billows and clouds over values of imposed ascent for which primary clouds existed are summarised in Table 5.1. Data are shown between ascents of 585 m and 1035 m. Taking into consideration the error limits and the inherent limitations in performing this kind of analysis by eye, the cloud wavelengths were multiples of 0.5 or 0.6 of the billow wavelengths. The wavelengths of the primary and secondary clouds were the same in each of the runs that developed secondary clouds. These results show that two primary and two secondary clouds formed per billow. This is a new result that has not previously been noted in the literature on Kelvin-Helmholtz billows in the atmosphere.

The summary of the wavelengths of the billows and clouds shown in Table 5.1 also suggests an interaction between shear and the wavelength of the convective clouds in the absence

Wavelength Comparison				
Run	Imposed ascent (m)	λ (billows), km	λ (primary clouds), km	λ (secondary clouds), km
Increasing-shear	585	3.8±0.1	2.9±0.1	
	630	4.0±0.1	2.9±0.1	
	676	4.3±0.1	2.9±0.1	
	720	4.6±0.2	2.9±0.1	
	765	5.0±0.2	2.9±0.1	
	810	5.0±0.2	3.5±0.2	
	855	5.5±0.2	3.8±0.2	4.0±0.4
	900	6.7±0.4	3.5±0.2	3.8±0.3
	945	6.7±0.4	3.5±0.2	3.8±0.3
	990	6.7±0.4	4.3±0.3	4.6±0.5
	1035	6.7±0.4	4.6±0.3	5.5±0.7
Observed-shear	630		2.0±0.1	
	675		2.4±0.1	
	720		2.4±0.1	
	765		2.4±0.1	
	810		2.4±0.1	
	855		2.5±0.1	
	900		2.6±0.1	2.7±0.1
	945		2.6±0.1	3.2±0.2
	990		2.6±0.1	3.2±0.2
	1035		3.0±0.2	3.8±0.8
Low-shear	630		1.2±0.1	
	675		1.4±0.1	
	720		1.4±0.1	
	765		1.5±0.1	
	810		1.8±0.1	
	855		1.9±0.1	
	900		2.2±0.1	1.9±0.1
	945		2.4±0.1	2.5±0.1
	990		2.5±0.1	2.6±0.2
	1035		2.6±0.1	2.6±0.2

TABLE 5.1: Table showing billow and cloud wavelengths (km) for each of the runs shown in Figure 5.13.

of billows. The primary clouds in the low-shear run had the shortest wavelengths and the primary clouds in the increasing-shear run had the longest wavelengths. This interaction was not expected and has not been studied in this thesis.

To support the visual analysis of the billow and cloud wavelengths, Fourier analysis of the vertical velocity field was performed at 900 m of ascent. Power spectra of the vertical velocity field were calculated at heights of 1.5 km for the billows, 5.5 km for the primary clouds and 3.5 km for the secondary clouds. The following discussion shows that the results of the visual wavelength analysis and those of the Fourier analysis were consistent with each other.

There was a maximum in the billows power spectrum of the increasing-shear run at a wavenumber of 1.4 x 10 $^{-4}$ m^{-1}, corresponding to a wavelength of 7.1 km (Figure 5.16a). This value confirmed the billow wavelength determined by visual analysis at 900 m of ascent, which was (6.7±0.4) km (Table 5.1). There was a maximum in the primary cloud power spectrum of the increasing-shear run at a wavenumber of 2.8 x 10 $^{-4}$ m^{-1}, which corresponded to a wavelength of 3.6 km (Figure 5.16b). This confirmed the visual analysis wavelength, which was (3.5±0.2) km (Table 5.1). The circulations in the secondary clouds were much weaker than those in the primary clouds and the billows (Figure 5.12a). The maximum in the secondary cloud power spectrum of the increasing-shear run was less distinct than in the billows or primary cloud power spectra (Figure 5.16c). Maxima occurred at wavenumbers (wavelengths) of 1.1 x 10 $^{-4}$ m^{-1} (9.1 km), 1.4 x 10 $^{-4}$ m^{-1} (7.1 km) and 2.7 x 10 $^{-4}$ m^{-1} (3.7 km). The signal at 7.1 km was probably from the billows (Figure 5.16a). The maximum at 3.7 km was in agreement with the wavelength of the secondary clouds determined by visual analysis, which was (3.8±0.8) km (Table 5.1).

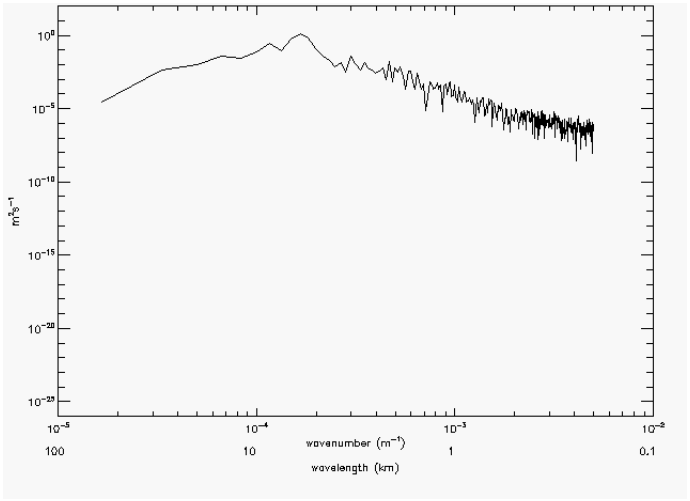

(A) Billows (spectral analysis at 1.5 km height).

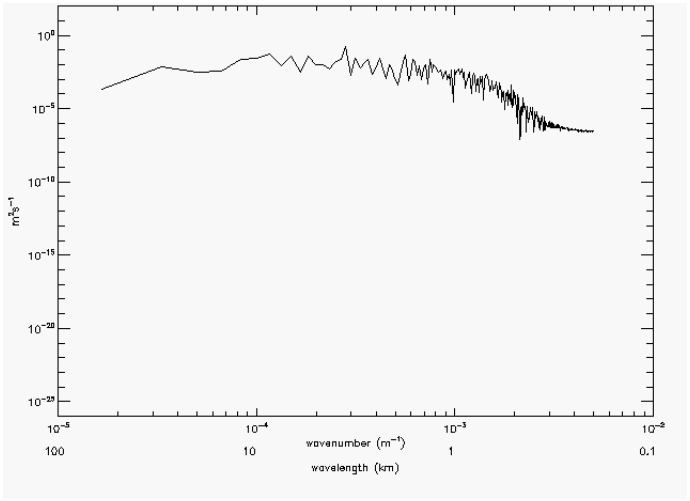

(B) Primary clouds (spectral analysis at 5.5 km height).

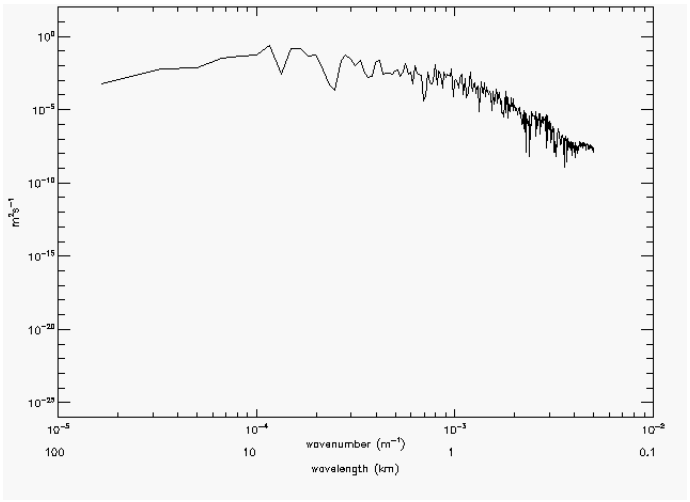

(C) Secondary clouds (spectral analysis at 3.5 km height).

FIGURE 5.16: Increasing shear run: power spectra of the vertical velocity field after ascent of 900 m. Note that because the wavelength is inversely proportional to the wavenumber, and that the power spectra are presented on a log-log scale, the wavelengths shown in the power spectra plots are only valid at the specific wavenumbers for which they are shown and do not share the same intermediate scale.

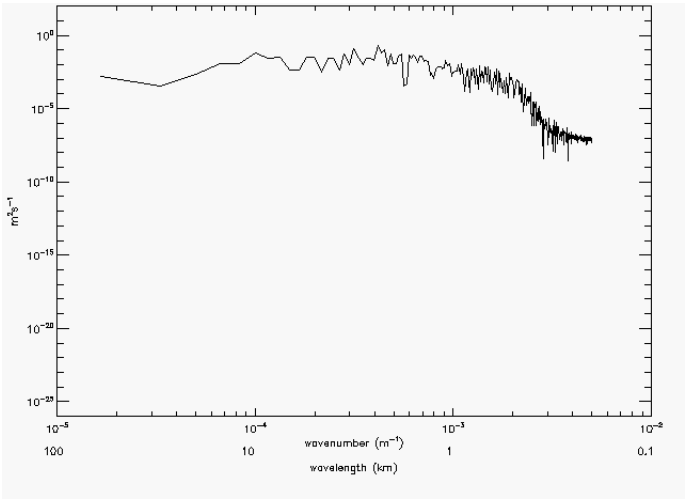

(A) Primary clouds (spectral analysis at 5.5 km height).

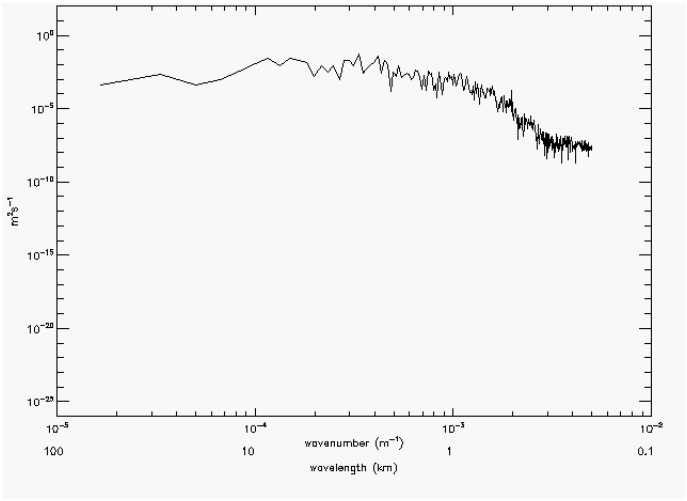

(B) Secondary clouds (spectral analysis at 3.5 km height).

FIGURE 5.17: As Figure 5.16 but for the observed-shear run.

A maximum in the primary cloud power spectrum of the observed-shear run occurred at a wavenumber of 4.0 x 10 $^{-4}$ m^{-1} (a wavelength of 2.5 km, Figure 5.17a), which agreed with the visual analysis wavelength of (2.6±0.1) km (Table 5.1). Like the increasing-shear run, the signal from the secondary clouds was weaker. There were two maxima in Figure 5.17b, at wavenumbers (wavelengths) of 3.1 x 10 $^{-4}$ m^{-1} (3.2 km) and 4.1 x 10 $^{-4}$ m^{-1} (2.4 km), respectively. The secondary cloud wavelength determined by visual analysis was (2.7±0.1) km. These results were in reasonable agreement.

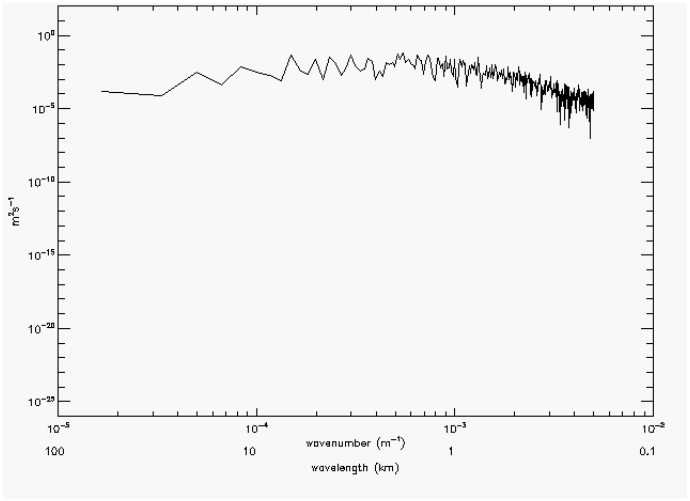

(A) Primary clouds (spectral analysis at 5.5 km height).

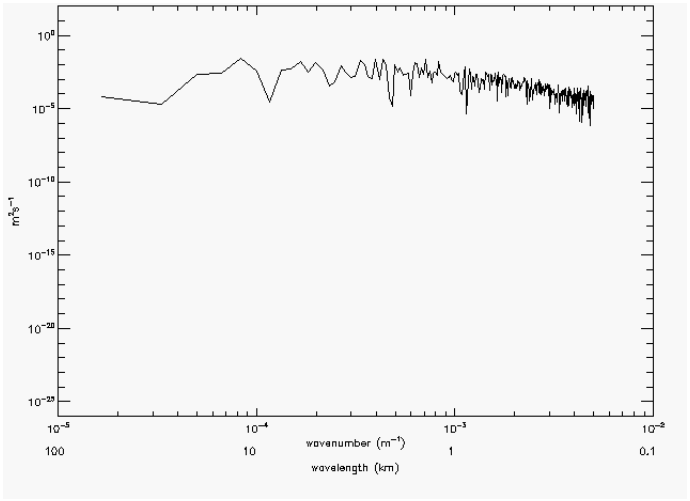

(B) Secondary clouds (spectral analysis at 3.5 km height).

FIGURE 5.18: As Figure 5.16 but for the low-shear run.

A maximum in the primary cloud power spectrum of the low-shear run occurred at a wavenumber of 5.4 x 10 $^{-4}$ m^{-1} (a wavelength of 1.9 km, Figure 5.18a). This confirmed the primary cloud wavelength determined by visual analysis, (2.2±0.1) km (Table 5.1). There was no clear maximum in the secondary cloud power spectrum in the low-shear run. Two peaks occurred at wavenumbers of 4.0 x 10 $^{-4}$ m^{-1} and 4.2 x 10 $^{-4}$ m^{-1}, corresponding to wavelengths of 2.5 km and 2.4 km, respectively. This was in reasonable agreement with the secondary cloud wavelength determined by visual analysis, (1.9±0.1) km (Table 5.1).

5.2.6 The interaction between the billows and convection: tracer analysis

To investigate whether air was exchanged between the updraughts of the billows and the convection, tracers were added to each of the three simulations. There were four layers of air with high values of θ_e in the increasing-shear run before any ascent was imposed, centred at heights of 1.5, 2.0, 2.5 and 3.0 km (Figure 5.19).

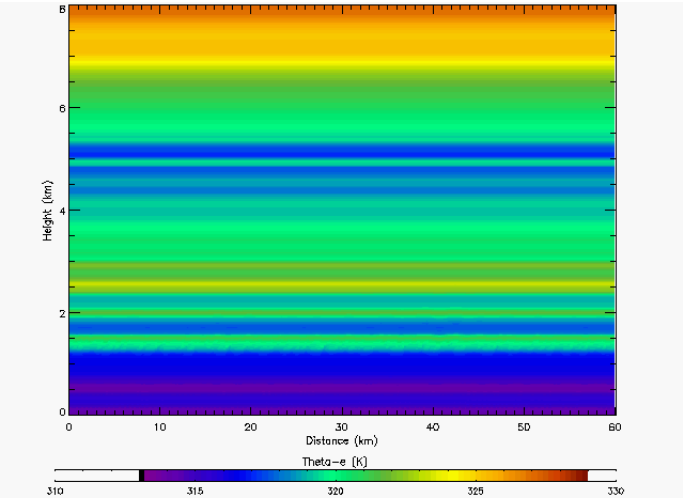

FIGURE 5.19: θ_e (K, colour contour) in the increasing-shear run at zero ascent.

The presence of billows did not affect which layers with high values of θ_e air fed the convection. After 900 m of ascent the billows were well-established in the increasing-shear run (Figure 5.12a). After 900 m of imposed ascent the tracer initialised at a height of 1.5 km had undergone more mixing in the increasing-shear run but had not been lifted significantly more than it had been in the the observed-shear or low-shear runs (Figure 5.20a). The tracer initialised at 2.0 km in the other layer of high-valued θ_e air near the billows (Figure 5.20b), was transported downward more than the tracer in the other two runs but did not undergo more lifting. These results show that the billows did not significantly alter the source of the air that fed the convection.

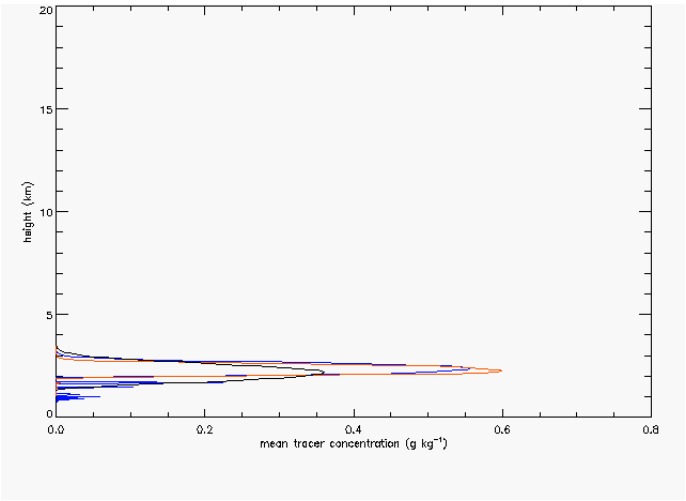

(A) Tracer initialised at a height of 1.5 km.

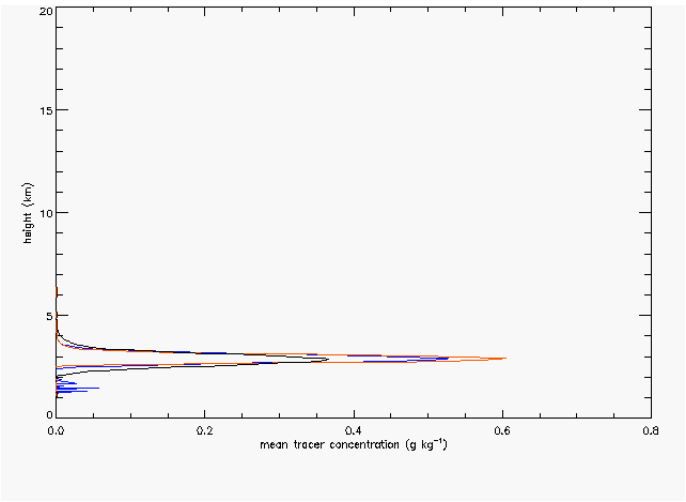

(B) Tracer initialised at a height of 2.0 km.

FIGURE 5.20: Profiles of mean tracer concentration (g kg^{-1}) after 900 m of imposed ascent. Runs are indicated by coloured lines: black = increasing-shear, red = observed-shear, blue = low-shear.

Although some of the air in the high-valued θ_e layer centred at an initial height of 2.0 km contributed to the convection, the billows did not significantly change this contribution. After 1035 m of ascent there was no significant difference between the amount of tracer that entered the cloud updraughts in each of the runs (Figure 5.21). The main effect of the billows in the increasing-shear run (Figure 5.21a) was to mix air from the high-valued θ_e layer down into the billows. This downward mixing did not occur in either the observed-shear (Figure 5.21b) or the low-shear (Figure 5.21c) runs.

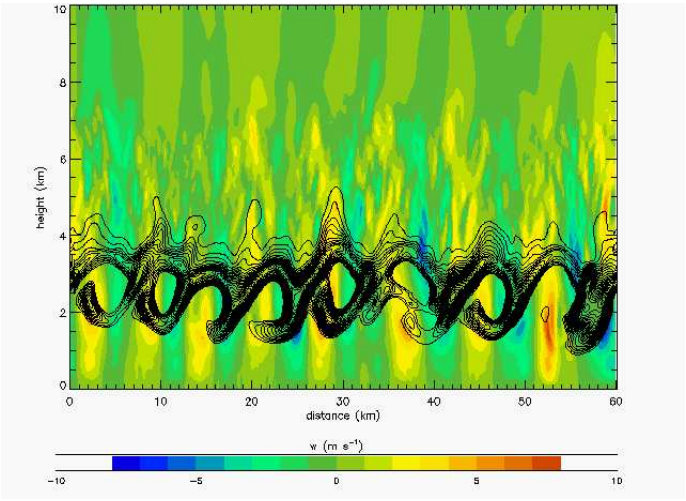

(A) Increasing-shear run.

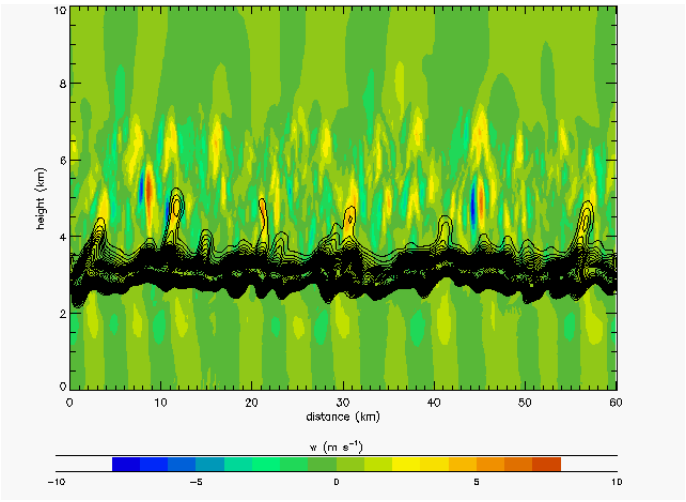

(B) Observed-shear run.

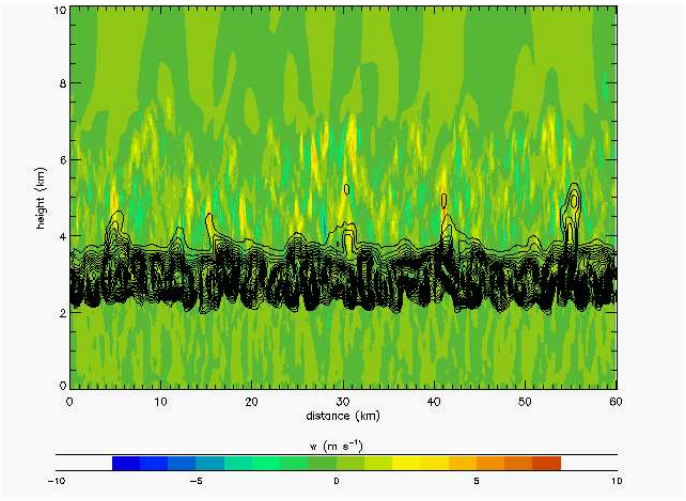

(C) Low-shear run.

FIGURE 5.21: Vertical sections of vertical velocity (ms^{-1}, colour contour) and concentration of a tracer initialised at a height of 2.0 km (g kg^{-1}, black line contours).

5.2.7 The interaction between the billows and convection: microphysical processes

5.2.7.1 Ice

The presence of billows did not significantly alter the production of ice particles in the clouds. The reason for this is that the billows provided lifting to aid the development of the convective clouds, but not enough lifting to alter the maximum vertical velocity, cloud top height or microphysical processes. The same total amount of ice developed in each of the runs, but the ice developed for less imposed ascent in the increasing-shear run than it did in the observed and low-shear runs (Figure 5.22). Although ascent was imposed in all three runs, the extra ascent provided by the billows aided the development of ice in the increasing-shear run.

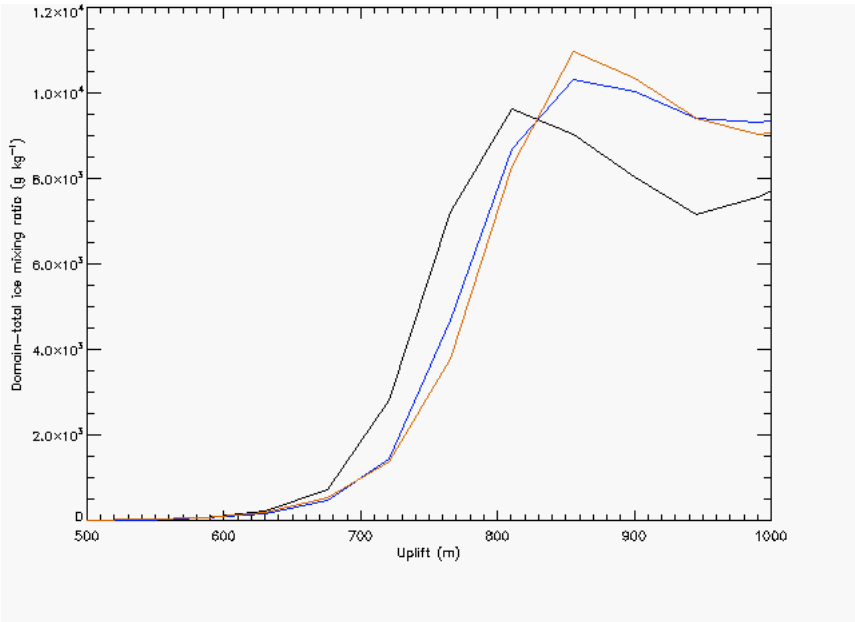

FIGURE 5.22: Domain-integrated ice mixing ratio (g kg^{-1}) as a function of imposed ascent for the increasing-shear run (black line), observed-shear run (red line) and low-shear run (blue line).

At equivalent stages in the development of ice (imposed ascent of 765 m in the increasing-shear run and 810 m in the observed and low-shear runs) the maximum height of the ice was about 6 km (Figure 5.23). The ice mixing ratio had a classic thermal plume structure in each of the runs. The similarity between the structure and extent of the ice in each of the runs suggested that the billows did not significantly alter the production of ice

particles. However, the structure of the ice mixing ratio after 765 m of ascent in the increasing-shear run (Figure 5.23a) was very similar to that of the ice mixing ratio after 810 m of ascent in the observed and low-shear runs (Figures 5.23b and 5.23c). This shows that ice development occurred for less imposed ascent in the increasing-shear run due to the extra lifting provided by the billows.

Maxima in ice mixing ratio occurred in the plume updraughts. At equivalent stages in the development of ice, peaks in the column-integrated ice mixing ratio corresponded to the location of the plume updraughts in each of the three runs (Figure 5.24).

5.2.7.2 Graupel

Similarly to the production of ice, the presence of billows did not significantly alter the production of graupel in the clouds. At equivalent stages in the development of graupel (imposed ascent of 810 m in the increasing-shear run and 855 m in the observed and low-shear runs) the structure and extent of the graupel in each of the runs suggested that the billows did not significantly alter the production of graupel and that the extra lifting provided by the billows allowed graupel to develop for less imposed ascent in the increasing-shear run (Figure 5.25).

5.2.8 The interaction between the billows and convection: surface precipitation

The presence of billows did not significantly alter the surface precipitation rate. The surface precipitation rate in the LEM is a domain-wide quantity and has been converted from a time series to a function of imposed ascent. Surface precipitation began at a similar value of ascent in all three runs (800 m, Figure 5.26). The profile of the surface precipitation rate in the increasing-shear run was very similar to that of the observed-shear run, but shifted towards smaller values of imposed ascent. Although ascent was imposed in all three runs, the extra ascent provided by the billows allowed more rain to form for less lifting in the increasing-shear run than it did in either the observed or low-shear runs.

The billows altered the location at which rain reached the surface. After 1035 m of imposed ascent the rain mixing ratio at the surface in the low-shear run (Figure 5.27) had a fairly

high frequency compared to the other two runs. This was because there were more clouds in the low-shear run (Figure 5.12). The peaks in the rain mixing ratio at the surface in the observed-shear run had a lower frequency than the low-shear run (Figure 5.27). The peaks in the rain mixing ratio at the surface in the increasing-shear run occurred at different locations from those in the other two runs (Figure 5.27). For 1035 m of imposed ascent, the increasing-shear run had 9 billow updraughts and 9 peaks in the rain mixing ratio at the surface. This is clear evidence that there was a coupling between the billows and the surface rain.

5.2.9 The interaction between the billows and convection: time evolution and coupling between the billows and convection

The vertical velocity field at a height of 1500 m (the billows region) was strongly coupled to the vertical velocity field at a height of 3500 m (the convective region) in the increasing-shear run. Hovmöller diagrams of the vertical velocity in each of the three runs are shown in Figure 5.28. When updraughts and downdraughts formed after about 700 m of imposed ascent at a height of 1500 m due to the billows, there was a response in the cloudy updraughts and downdraughts at 3500 m (Figure 5.28a). This happened after a greater amount of imposed ascent, about 1000 m, in the observed-shear run (Figure 5.28b). A coupling of the vertical velocity fields at 1500 and 3500 m was not seen in the low-shear run (Figure 5.28c).

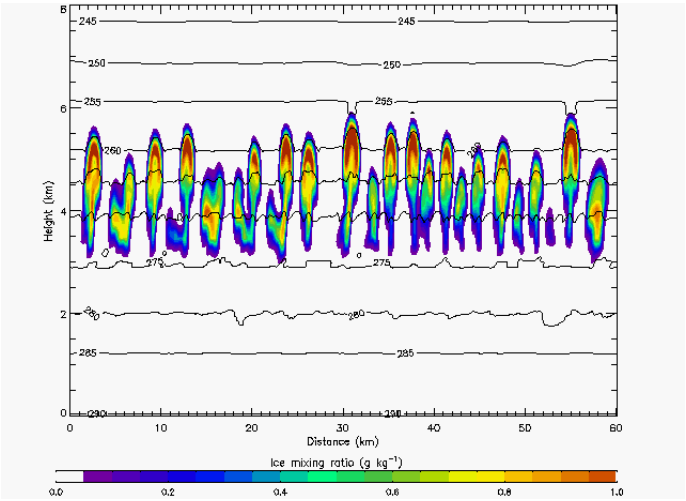

(A) Increasing-shear run, 765 m of imposed ascent.

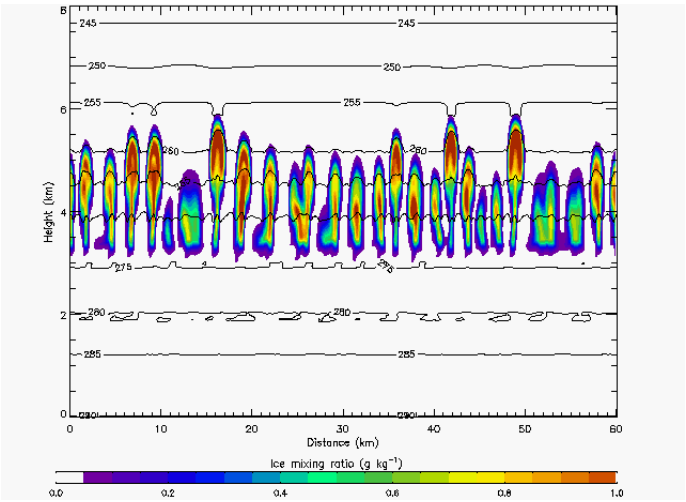

(B) Observed-shear run, 810 m of imposed ascent.

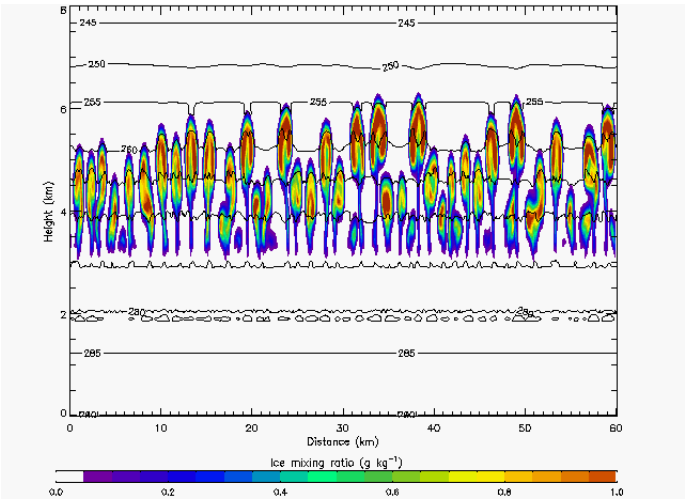

(C) Low-shear run, 810 m of imposed ascent.

FIGURE 5.23: Vertical sections of ice mixing ratio (g kg^{-1}, colour contour) and temperature (K, black line contour) at equivalent stages of ice development in the three runs.

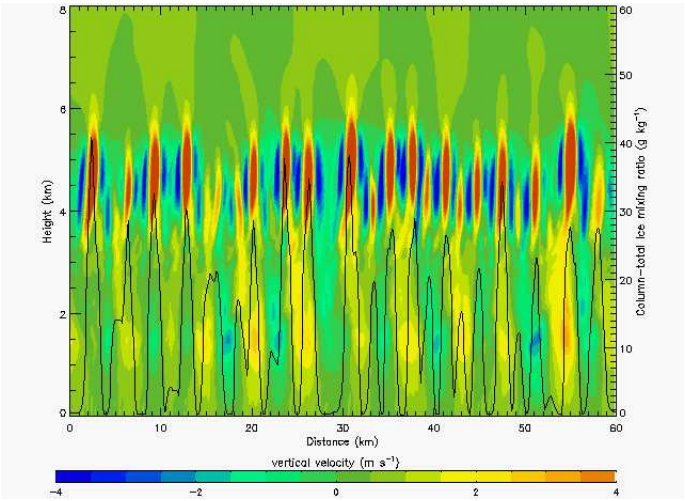

(A) Increasing-shear run, 765 m of imposed ascent.

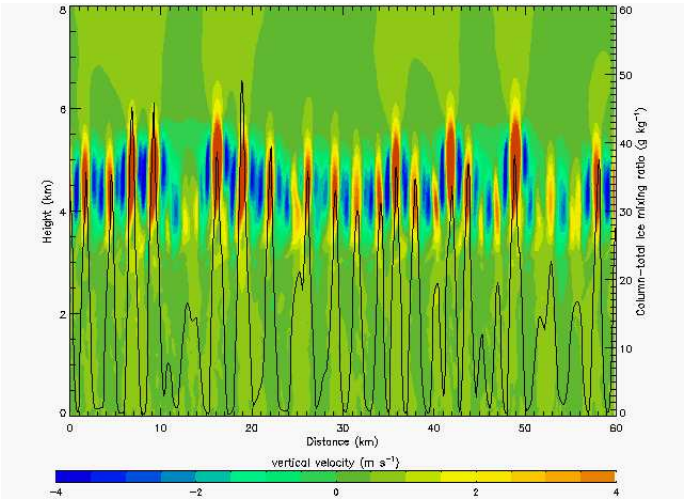

(B) Observed-shear run, 810 m of imposed ascent.

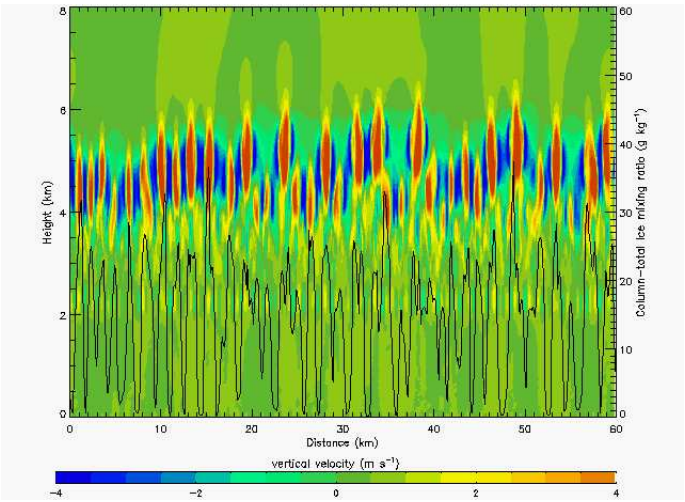

(C) Low-shear run, 810 m of imposed ascent.

FIGURE 5.24: Vertical sections of vertical velocity (m s^{-1}, colour contour) and column-integrated ice mixing ratio (g kg^{-1}, black line) at equivalent stages of ice development in the three runs.

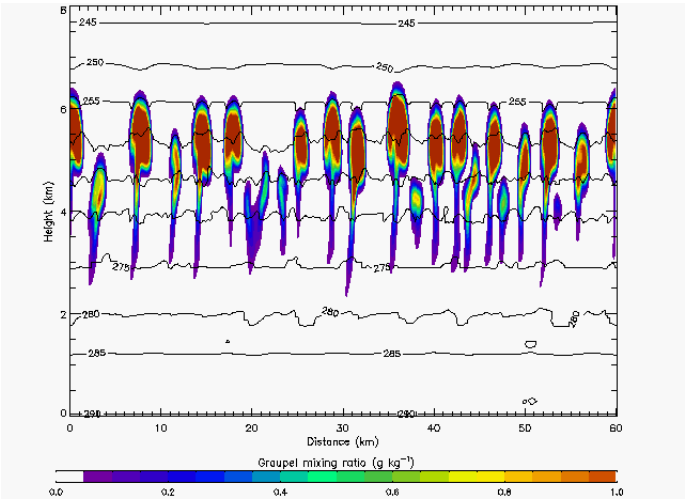

(A) Increasing-shear run, 810 m of imposed ascent.

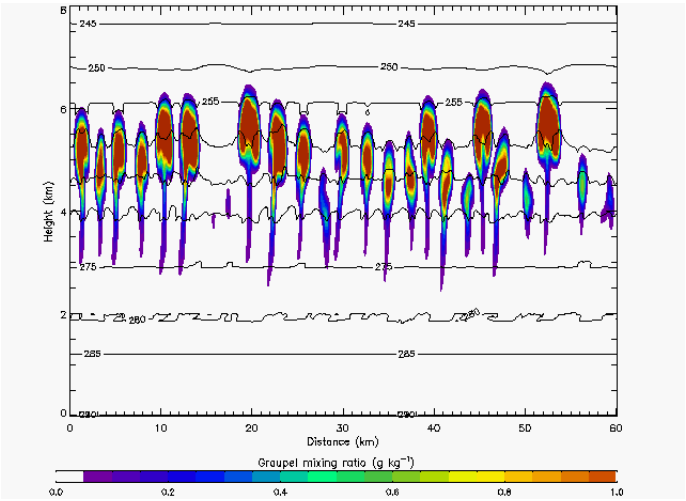

(B) Observed-shear run, 855 m of imposed ascent.

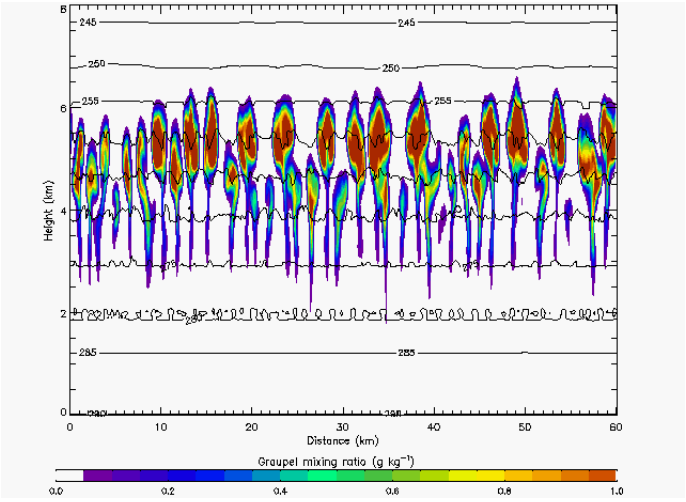

(C) Low-shear run, 855 m of imposed ascent.

FIGURE 5.25: Vertical sections of graupel mixing ratio (g kg^{-1}, colour contour) and temperature (K, black line contour) at equivalent stages of graupel development in the three runs.

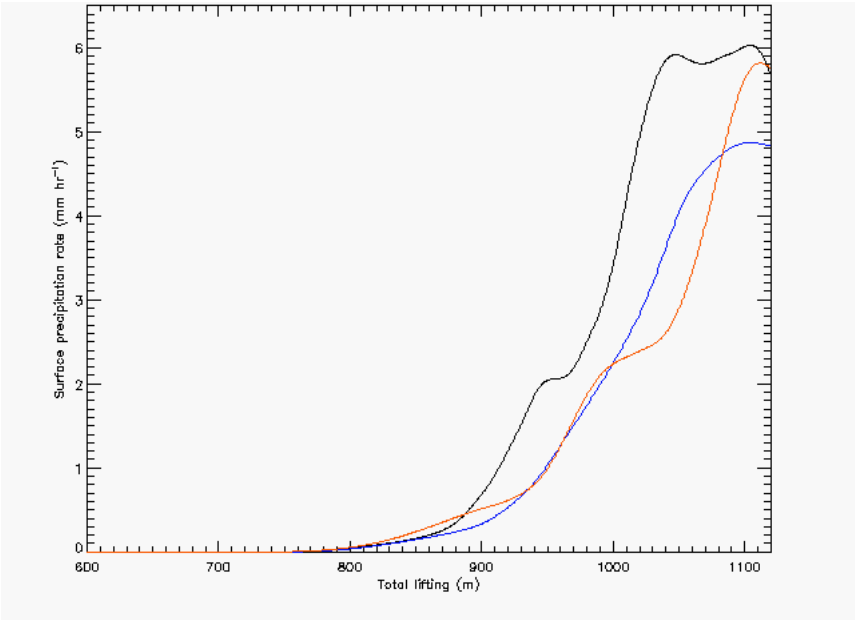

FIGURE 5.26: Surface precipitation rate (mm hr^{-1}) as a function of imposed ascent for the increasing-shear run (black line), observed-shear run (red line) and low-shear run (blue line).

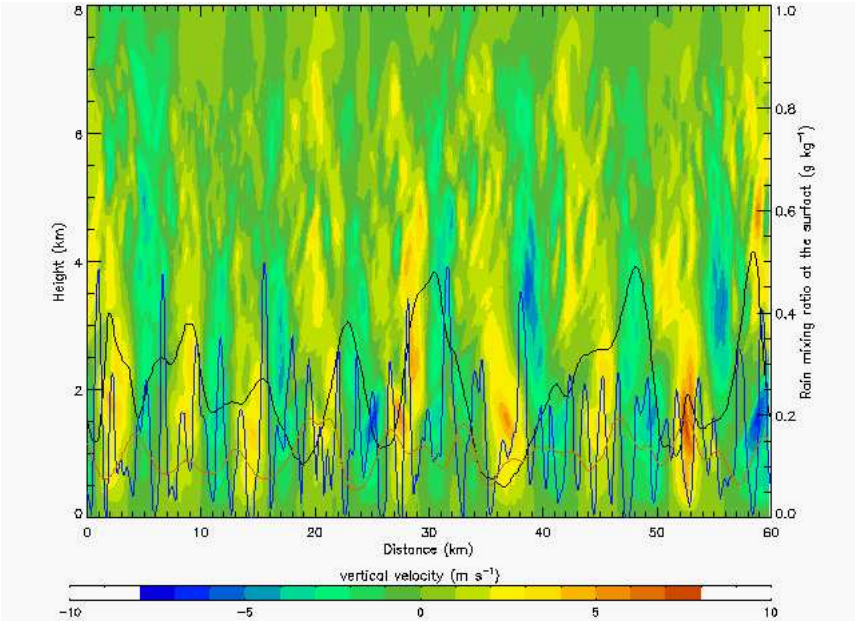

FIGURE 5.27: Rain mixing ratio (g kg^{-1}) at the surface after 1035 m of imposed ascent for the increasing-shear run (black line), observed-shear run (red line) and low-shear run (blue line), with vertical velocity (colour countour) of the increasing-shear run showing the location of the billows.

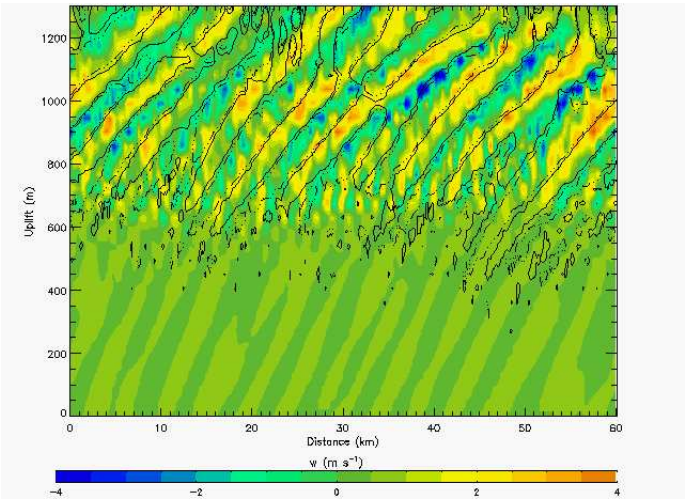

(A) Increasing-shear run.

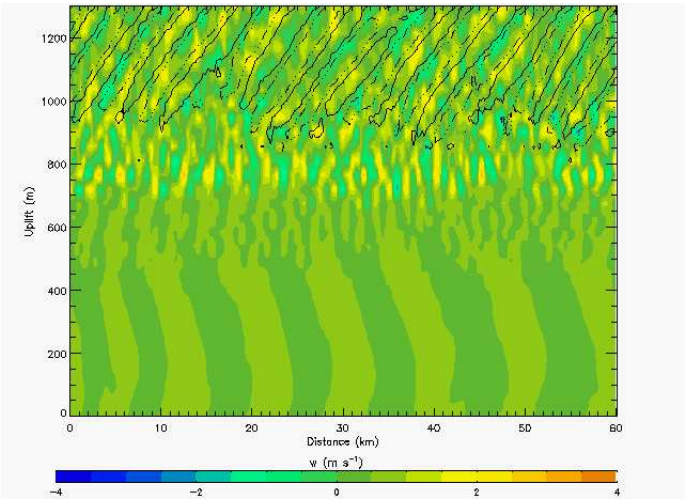

(B) Observed-shear run.

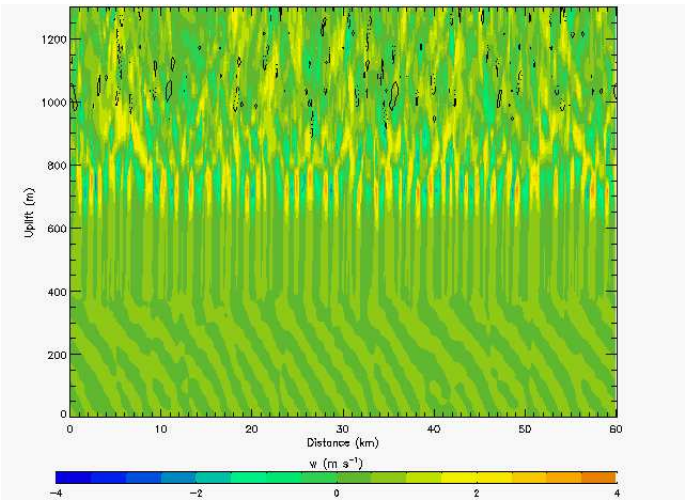

(C) Low-shear run.

FIGURE 5.28: Hovmöller diagrams for each of the three runs showing vertical velocity (m s^{-1}) at 3500 m (colour contour) and at 1500 m (black line contour, solid line representing updraughts and dashed line representing downdraughts) across the model domain as a function of imposed ascent.

The coupling between the vertical velocities of the billows and the convection was clearly evident at 810 m of imposed ascent. In the increasing-shear run the billow updraughts and downdraughts, centred at a height of 1500 m, extended up to a height of 4500 m where they coupled with the updraughts and downdraughts in the clouds (Figure 5.29a). No such coupling was seen in the observed-shear (Figure 5.29b) or low-shear (Figure 5.29c) runs.

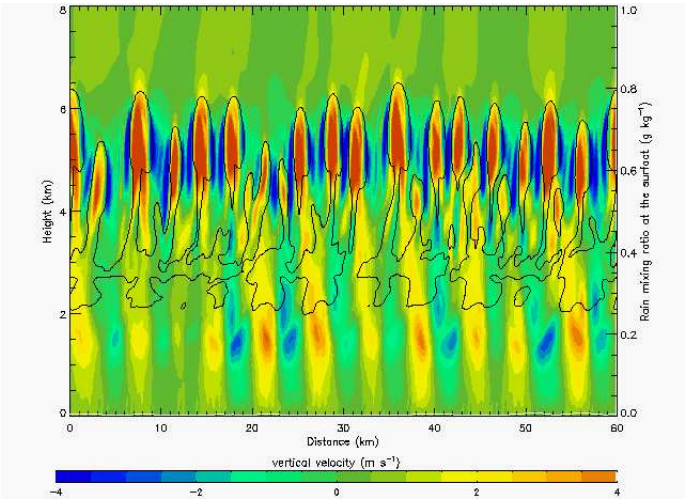

(A) Increasing-shear run.

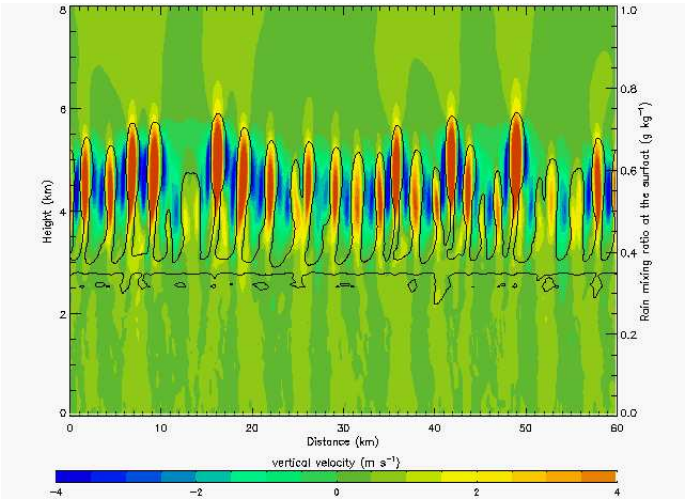

(B) Observed-shear run.

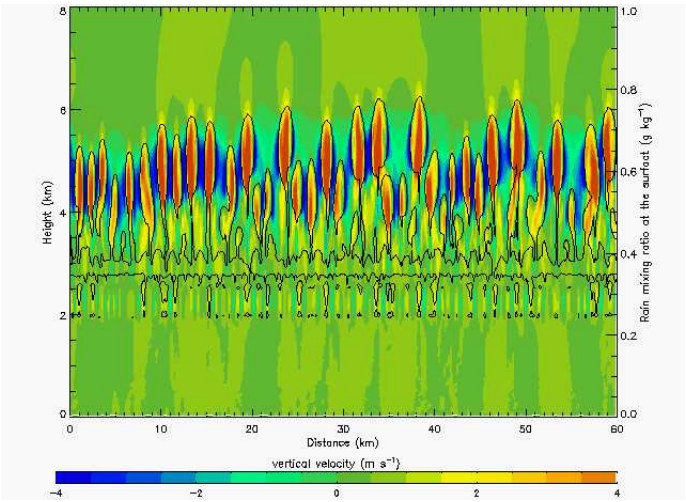

(C) Low-shear run.

FIGURE 5.29: Vertical velocity (m s^{-1}, colour contour), total hydrometeors (g kg^{-1}, black line contour) and rain mixing ratio at the surface (g kg^{-1}, white line) for each of the three runs after 810 m of imposed ascent.

5.3 Comparison of the billow development in the LEM with the observed billows

The wavelength of the billows that developed in the increasing-shear run was similar to that of the observed billows. The wavelength of the observed billows was about 4 km in the region where the crest-to-trough amplitude was 700 m (vertical wind shear panel in Figure 5.2 at a range of 50 to 60 km). The wavelength of the billows that developed in the increasing-shear run was (5.0±0.2) km in the initial stage of their development after 765 m of imposed ascent and increased to (6.7±0.4) km as the amount of total imposed ascent increased to 990 m (Table 5.1). This was discussed in Section 5.2.5. These wavelengths were reasonably similar to those of the observed billows (Figure 5.2).

The billows that developed in the increasing-shear run had a similar amplitude to the observed billows. The observed billows had a maximum crest-to-trough amplitude of between 500 and 700 m (Figure 5.2). The maximum crest-to-trough amplitude of the billows in the increasing-shear run was about 1 km (Figure 5.8b). The depth of the shear layer in the increasing-shear run was 1.25 km, which was similar to the depth of the observed shear layer (Figure 5.14b).

The strength of shear in the increasing-shear run was weaker than the observed shear. The maximum strength of shear that developed in the LEM was about 1.5 s^{-1} (Figure 5.14b) while that of the observed shear was about 5.0 s^{-1}.

As noted above, Browning *et al.* (2012) observed slanting oscillations in the upper-levels of the wind shear field (Figure 5.2). The wavelength of the oscillations was similar to that of the billows. Although not discussed in any depth, Browning *et al.* (2012) suggested that this structure may have been due to gravity waves excited either by convection in the MCS or by the billows. A similar structure occurred in the wind shear in the increasing-shear run between heights of about 4 and 7 km (Figure 5.14b). The strength of these upper-level oscillations in the wind shear of both the model and the observations was about 0.5 s^{-1}. There were similar oscillations above about 6 km in the wind shear fields in the absence of billows after 990 m of imposed ascent in the observed-shear (Figure 5.30a) and low-shear

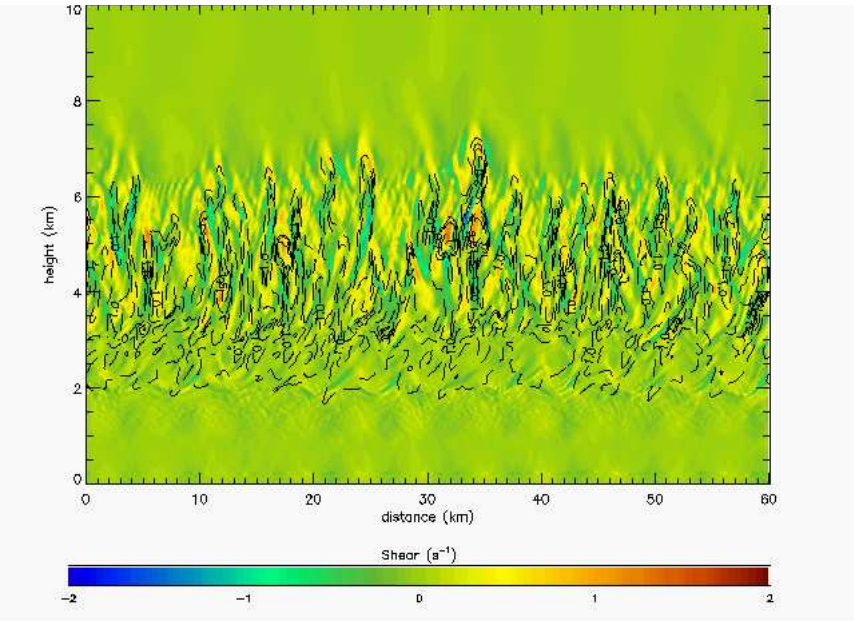

(A) Observed-shear run.

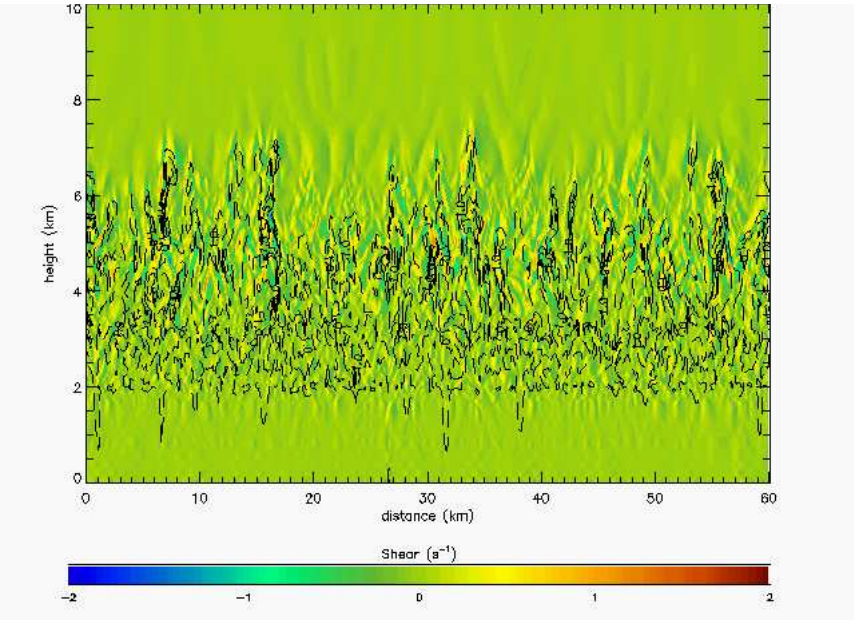

(B) Low-shear run.

FIGURE 5.30: Vertical section of the shear field (s^{-1}) after 990 m of imposed ascent for the observed and low-shear runs.

(Figure 5.30b) runs. This suggests that the upper-level oscillations that developed in the LEM were gravity waves excited by the convection and not by the billows.

The height of the cloud base in the increasing-shear run was similar to the height of the observed cloud base, which was in a sloping layer between 1.4 and 3.2 km height (Figure 5.2). The cloud base in the increasing-shear run was at a height of about 2.75 km (Figures 5.11a to 5.12a). The clouds formed above the shear layer in the increasing-shear run. In contrast, some of the observed clouds formed inside the shear layer (Figure 5.2).

The maximum cloud top height in the increasing-shear run was slightly greater than the observed cloud top height. The observed convective clouds (Figure 5.2) reached a height of 5 to 6 km. The maximum cloud top height in the increasing-shear run was about 7.5 km after 1035 m of imposed ascent (Figure 5.9). Taking the imposed ascent into account, this corresponded to a cloud top height of about 8.5 km.

The width of the clouds that developed in the increasing-shear run was similar to the width of the observed convective clouds, which were several kilometres wide. Browning *et al.* (2012) suggested that the observed plumes (Figure 5.6) were in fact clusters of separate clouds. The clouds that developed in the increasing-shear run were also several kilometres wide (Figure 5.12a).

The spacing of the clouds in the increasing-shear run was about half of the observed cloud spacing, which was about 10 km (Figure 5.6). The wavelength of the primary and secondary clouds in the increasing-shear run after 990 m of ascent were (4.3±0.3) km and (4.6±0.5) km, respectively (Table 5.1). The cloud spacings are in reasonable agreement considering the highly idealised nature of the LEM.

The magnitude of the surface pressure perturbations in the increasing-shear run was about ±0.3 hPa (Figure 5.31), the same as the surface pressure perturbations observed at the North Farm AWS (Figure 5.5). Time series from five points spaced evenly across the model domain were compared and found to be consistent with each other. Only the time series from the centre of the domain is shown in Figure 5.31. The period of the surface pressure perturbations in the increasing-shear run was about 15 minutes. This was longer than the period of the surface pressure perturbations observed at the North Farm AWS, which was 9 minutes (Figure 5.5). The difference was less than a factor of two.

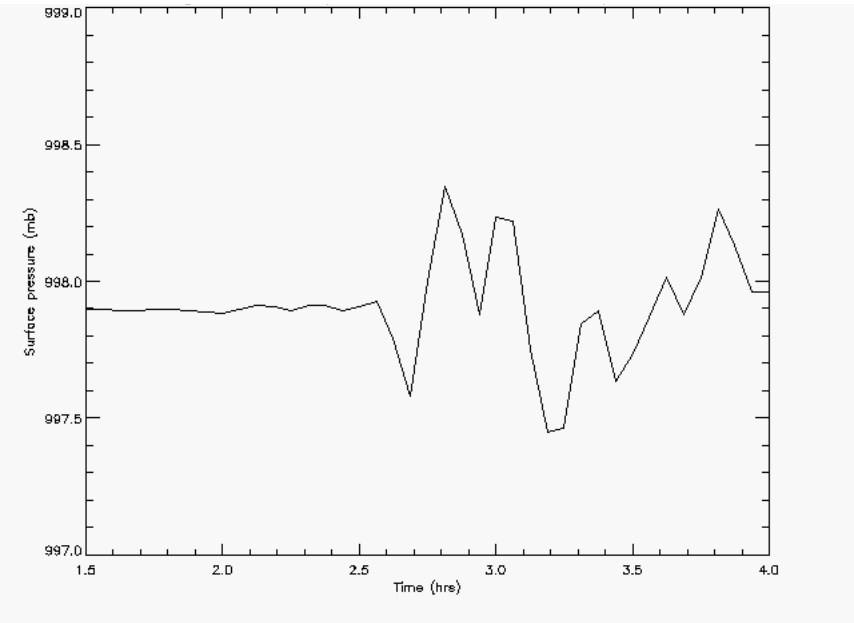

FIGURE 5.31: Time series of surface pressure (hPa) taken from a point in the centre of the domain of the increasing-shear run.

The surface pressure perturbations in the increasing-shear run were located with the billows (Figure 5.32). Pressure maxima occurred in the peaks of regions which had lower values of θ_e than their surroundings, and pressure minima occurred in the troughs of regions which had higher values of θ_e than their surroundings. The pressure maxima were probably attributable to the hydrostatic effect of lifting in the billows.

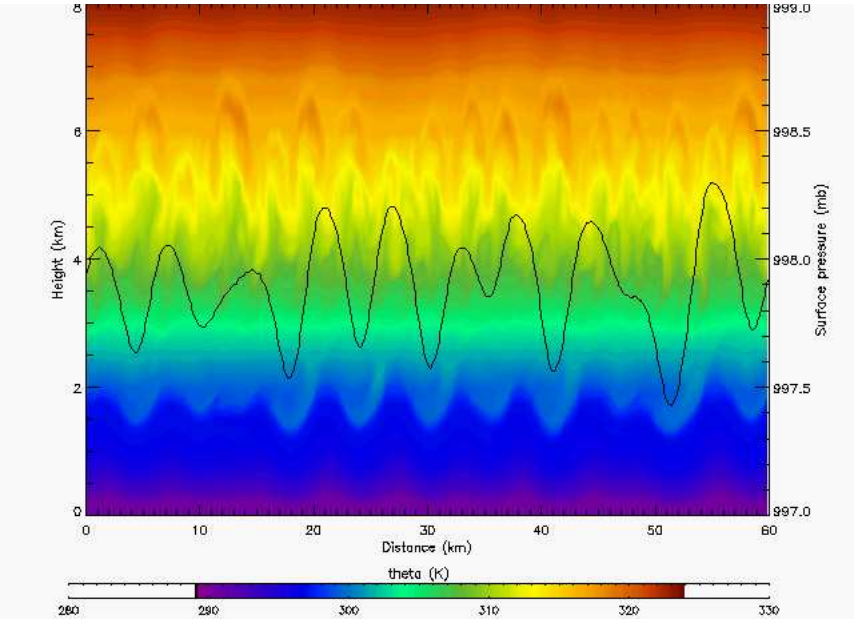

FIGURE 5.32: Potential temperature (K, colour contour) and surface pressure (hPa, black line) in the increasing-shear run after 855 m of total ascent.

5.4 Summary of the interaction between the billows and elevated convection

These results have added to the relatively small body of work that concerns the modelling of Kelvin-Helmholtz billows from atmospheric soundings, and provides the first known study of the interaction between billows and convection. The LEM was able to produce billows that had a similar wavelength and amplitude to the billows observed during MCS B. The presence of billows provided an extra lifting in addition to the imposed large-scale ascent. In comparison to the observed-shear and low-shear runs, the increasing-shear run developed convective plumes for less imposed ascent. Ice, graupel and rain were also first observed for less imposed ascent in the increasing-shear run than they were in the observed and low-shear runs (Section 5.2.4). The extra lifting provided by the billows allowed microphysical processes to develop for less imposed ascent, but did not appear to affect the total amount of ice, graupel or rain that developed (Section 5.2.7). Due to the limited nature of the observational data available, it was not possible to investigate more detailed effects of the billow dynamics on the microphysics.

The billows modulated the number of convective plumes that developed. Visual and Fourier analysis of the billow and cloud wavelengths showed that in the presence of billows, the wavelength of the convective plumes tended towards a value that was half that of the billows (Section 5.2.5), i.e. the number of clouds tended towards two per billow. There was a strong coupling between the vertical velocity fields of the billow up/down draughts and the convective up/down draughts (Section 5.2.9), showing that the billows directly affected the convection. Although the billows provided an extra lifting mechanism, they did not affect which layers of air became the source of inflow for the convection. The use of tracers in the model runs showed that there was no exchange of air between the billows and the convection (Section 5.2.6).

The billows did not affect the surface precipitation rate in any way other than to allow rain to form for less imposed ascent than it would have in the absence of billows. However, the modulation of the cloud spacing by the billows caused the location of the rainfall to be different from the location of rain in the absence of billows. This suggests that if numerical weather prediction models are unable to resolve billows, the accuracy of precipitation

forecasts may be adversely affected. The observed wavelength of the billows was 4 km. If this is a typical billow wavelength (the billow wavelength depends on the depth of the shear layer), then a horizontal resolution of at least 1 km would be required for numerical weather prediction models to resolve the billows.

The results from this modelling study have shown that the vertical velocity field of the billows had a forcing effect on the convection. Such an interaction may have occurred between the billows and the convection in the observations presented in Section 5.1.1. However, it is not possible to verify this from the current model results and observational data set. There are a number of limitations to the conclusions drawn here. This modelling study was performed under highly idealised conditions. The model runs were all initialised with one single profile of temperature, moisture and north-south wind component taken from the Larkhill 1022 UTC sounding. Although this sounding was close in time and space to the region in which the observed billows developed, it was not necessarily a true representation of the state of the atmosphere in which the billows developed. Due to the use of a 2D model, it has not been possible to capture any 3D interactions between neighbouring billows. Such interactions may have an effect on turbulent and mixing processes when the billows break (Fritts *et al.*, 1996). The analysis presented in Section 5.2 was confined mostly to the stages in billow development that occurred before wave breaking. However, the Chilbolton radar was only able to detect the billows once they had become turbulent, and so the billow observations presented in Section 5.1.1 are at a later stage in development than the billows that developed in the model runs. A logical extension to this work would be to use a 3D model and to investigate interactions between the billows and convection once the billows become turbulent.

The results from this study also suggested that the spacing of the convective clouds was, to some extent, modulated by the presence of shear as well as the billows. This effect has not been examined in this thesis but would be an interesting investigation.

Chapter 6

Conclusions

This thesis has presented detailed simulations of elevated MCSs, observed in southern England, which provide new information into the nature of elevated convective storms and the way in which they interact with the pre-convective environment. The thesis was presented in two parts: a simulation of MCS C and an investigation into the interaction between Kelvin-Helmholtz billows and elevated convection.

Modelling study of MCS C

The simulation of MCS C that occurred during IOP 3 of CSIP successfully reproduced many aspects of the structure and evolution of the observed storm. Elevated convection formed above a cold undercurrent. The simulated MCS developed a RIJ that descended to the top of the stable layer and, for the majority of the simulation, did not penetrate to the surface. The interaction of the descending RIJ with the stable undercurrent generated a wave at the top of the undercurrent ahead of the RIJ and ahead of the convection. The wave lifted air in the elevated source layer to its level of free convection. This was similar to the observed structure and evolution of MCS C (Browning *et al.*, 2010).

Although the simulation was broadly successful in reproducing MCS C, there were some significant differences between the modelled and observed storms. The simulated storm only had one elevated source layer, whereas Browning *et al.* (2010) observed two elevated source layers in MCS C. There was also only one RIJ in the simulated MCS, compared to the two RIJs observed by Browning *et al.* (2010). This difference suggests that the two RIJs in MCS C may have occurred due to the presence of two source layers. However,

the most significant difference between the model results and the observations was that the convection in the simulated storm became surface-based, whereas MCS C remained elevated throughout the observation period. The observed stable layer was about 2 km deep, while the stable layer in the simulation was about 1 km deep. The difference in the depth of the stable layer may have been partly responsible for the transition to surface-based convection that occurred in the model.

Several factors contributed to the transition from elevated to surface-based convection in the simulation. The buoyancy of the low-level air in the east of the domain ahead of the convection increased throughout the day. This was due to a combination of surface heating and the advection of high-valued θ_e air from the south of the domain. In addition, the buoyancy of the elevated source layer decreased to the north. As the storm propagated through the domain from the southwest to the northeast it encountered an ever-weakening elevated source layer and an increasingly unstable pre-convective boundary layer. The combined effects of the surface heat fluxes and the large-scale flow on the pre-convective environment contributed to the transition from elevated to surface-based convection.

When the simulated convection became surface-based it formed gravity current outflow. The speed of the storm in the model increased significantly when the gravity current formed. Deep convection was initiated at the leading edge of the gravity current. The ratio of the strength of the gravity current to the strength of the shear in the lowest 5 km was shown to be consistent with the "optimal state" criteria of Weisman and Rotunno (2004) for deep lifting at the leading edge of a gravity current. This indicated that the interaction between the gravity current outflow and the environmental shear may have been responsible for the maintenance of deep convection after the transition to surface-based convection. In contrast to the model, cold pool gravity current outflow was never observed from MCS C. This was consistent with the observed stable layer being deeper than the stable layer in the simulation. The deeper stable layer may have been too strong for convective downdraughts to reach the surface and form cold pool outflow. However, the speed of MCS C was observed by Browning *et al.* (2010) to increase late in its lifetime, even though no gravity current formed. This thesis has not been able to determine the mechanism responsible for the observed acceleration of MCS C.

It is well-known that the stable layer beneath elevated convection is not dynamically passive. In the presence of a low-level stable layer a storm can generate features such as waves and bores that lift air to its level of free convection, thereby maintaining convection (e.g. Marsham *et al.*, 2011). However, the study presented in this thesis provides a new insight into the nature of the stable layer that has not previously been noted in the literature. Convective outflow from the north of the storm in the simulation, cooled by evaporation and sublimation, acted to strengthen the undercurrent. This allowed wave-lifted elevated convection to be maintained for a longer period than it was in the absence of such an outflow. The low-level stable layer in elevated storms is therefore not necessarily independent of the convective processes. This suggests that the two-layer models that are sometimes used to describe elevated convection, although useful for giving an instantaneous view of the system, do not sufficiently account for the interaction of the storm with itself as well as with its environment.

There may be a positive feedback process that exists between the convection, the RIJ and the stable layer. Diabatic cooling processes in the storm can cause local velocity maxima in the RIJ and strengthen its descent. A stronger RIJ may generate a larger wave in the stable layer, which in turn may provide more lifting and lead to more intense convection. Stronger convective updraughts will lead to more vigorous microphysical processes, which in turn can further strengthen the RIJ. This suggests that there may be a critical strength of the RIJ, or the wave, for maintaining deep elevated convection. If the RIJ is too strong it will penetrate through the stable layer to the surface and either cause or strengthen gravity current outflow. Strong gravity current outflow can lift near-surface air parcels, leading to a transition to surface-based convection. However, this thesis has also shown that microphysical cooling processes can strengthen the low-level stable layer. The relative contributions of diabatic cooling to the maintenance of elevated convection via reinforcing the RIJ and via strengthening the undercurrent are at present unknown, and would make for a very interesting further study. It would also be of interest to determine whether there is a positive feedback process in the storm such as that described above, and whether there is a critical value of the strength of the RIJ for the maintenance of elevated deep convection.

The modelling study presented here has also shown that large-scale effects are important in maintaining convection in the absence of a cold pool. When all the diabatic coolings were

removed from the model the storm persisted and the RIJ descended. This was consistent with the studies of Crook and Moncrieff (1988), Schumacher (2009) and Trier *et al.* (2011), who found that in conditionally unstable environments with large-scale convergence a significant surface cold pool was not necessary for the maintenance of deep convection. Browning *et al.* (2010) showed that during IOP 3 the CSIP region was in a baroclinic zone. The persistence of the modelled MCS in the absence of diabatic coolings suggests that in this case the large-scale convergence in the baroclinic zone was able to maintain the system.

There are some limitations to the modelling study that has been presented in this thesis. Because the convection and the RIJ formed during the spin-up period of the model, this study has been unable to address any questions about the initiation of the convection and the processes responsible for the generation of the RIJ. The simulated convection was sourced from only one elevated layer, whereas the observations of Browning *et al.* (2010) described the presence of two elevated source layers. This may have been due to sensitivity in both the model and the observations to the location of the sounding. However, it is also possible that the vertical resolution of the simulation, which had 48 vertical levels, was insufficient to resolve both of the elevated source layers. This was a significant limitation of the modelling study and was due to the large computational power required to perform a simulation on a large domain at high horizontal resolution. Future studies would certainly benefit from an increased vertical resolution.

The interaction between Kelvin-Helmholtz billows and elevated convection

Another MCS formed during CSIP IOP 3 that was associated with a large patch of billows that formed in a region of shear between the cool undercurrent and the southwesterly flow above it. This thesis has presented the first known modelling study of the interaction between Kelvin-Helmholtz billows and elevated convection. Although not responsible for the initiation of elevated convection, the extra lifting provided by the updraughts in the billows enhanced the development and evolution of convection. It has been shown that the presence of billows affects the spacing of the convective clouds: in the presence of billows there are fewer clouds. The relationship between the billows and the clouds is such that two billows formed per cloud. One cloud tended to form above the billow peak, and one above the trough. The formation of a cloud above the billow peaks is perhaps not

a surprising result, as it is here that lifting occurs. The formation of a cloud above the billow troughs is more surprising, and the mechanism for this is not known. However, the results of this study clearly show that there is a strong coupling between the updraughts and downdraughts in the billows and the convection. The billows were shown to affect the location of the surface precipitation. This suggests that the accuracy of precipitation forecasts may be dependent on the ability of a numerical weather prediction model to resolve billows. A horizontal resolution of at least 1 km would be required for a model to resolve the billows studied in this thesis. Current operational models may therefore be unable to resolve billows.

The notable limitation to the study of Kelvin Helmholtz billows presented in this thesis is that the 2D model that was used was, by definition, unable to capture any 3D interactions between neighbouring billows. These interactions may have an effect on the turbulent and mixing processes that occur when the billows break (Fritts *et al.*, 1996). The Chilbolton radar could only detect the billows once they had become turbulent. The observations of the billows that occurred during IOP 3 were therefore at a later, turbulent, stage of development than the billows in the 2D modelling study presented here. Further investigation into the nature of the interaction between elevated convection and Kelvin-Helmholtz billows would benefit from the use of a 3D model that could simulate the interactions between the billows and convection once the billows become turbulent.

The results from the study of the interaction between Kelvin Helmholtz billows and elevated convection presented here also suggested that background shear can affect the spacing of convective clouds. This has not been studied in this thesis but would make an interesting future investigation.

Summary

In summary, the results presented in this thesis have shown that the evolution of an elevated MCS is dependent on processes that occur across a wide range of scales, from large-scale uplift and baroclinic processes to small-scale convective processes and even subgrid-scale turbulence. The accurate reproduction of individual elevated storms in numerical models appears to be crucially dependent on the representation of the depth and stability of the low-level stable layer that exists beneath the elevated convection.

References

Beljaars A. 1994. The parameterization of surface fluxes in large-scale models under free convection. *Quarterly Journal of the Royal Meteorological Society* **121**: 225–270.

Benjamin T. 1968. Gravity currents and related phenomena. *Journal of Fluid Mechanics* **31**: 209–248.

Bennett L, Browning K, Blyth A, Parker D, Clark P. 2006. A review of the initiation of precipitating convection in the United Kingdom. *Quarterly Journal of the Royal Meteorological Society* **132**(617): 1001–1020.

Bernardet L, Cotton W. 1998. Multiscale evolution of a derecho-producing mesoscale convective system. *Monthly Weather Review* **126**: 2991–3015.

Blanchard D. 1990. Mesoscale convective patterns of the southern high plains. *Bulletin American Meteorological Society* **71**: 994–1005.

Bosart L, Seimon A. 1988. A case study of an unusually intense atmospheric gravity wave. *Monthly Weather Review* **116**: 1857–1886.

Braun S. 1995. Multiscale process interactions associated with a midlatitude squall line. PhD thesis, University of Washington.

Braun S, Houze Jr R. 1997. The evolution of the 10-11 June 1985 PRE-STORM squall line: Initiation, development of rear inflow, and dissipation. *Monthly Weather Review* **125**: 478–504.

Brown A, Derbyshire S, Mason P. 1994. Large-eddy simulation of stable atmospheric boundary layers with a revised stochastic subgrid model. *Quarterly Journal of the Royal Meteorological Society* **120**: 1485–1512.

Brown J. 1979. Mesoscale unsaturated downdrafts driven by rainfall evaporation: A numerical study. *Journal of the Atmospheric Sciences* **36**: 313–338.

Browning K, Blyth A, Clark P, Corsmeier U, Morcrette C, Agnew J, Ballard S, Bamber D, Barthlott C, Bennett L, Beswick K, Bitter M, Bozier K, Brooks B, Collier C, Davies F, Deny B, Dixon M, Feuerle T, Forbes R, Gaffard C, Gray M, Hankers R, Hewison T, Kalthoff N, Khodayar S, Kohler M, Kottmeier C, Kraut S, Kunz M, Ladd D, Lean H, Lenfant J, Li Z, Marsham J, McGregor J, Mobbs S, Nicol J, Norton E, Parker D, Perry F, Ramatschi M, Ricketts H, Roberts N, Russell A, Schulz H, Slack E, Vaughan G, Waight J, Wareing D, Watson R, Webb A, Wieser A. 2007. The Convective Storm Initiation Project. *Bulletin American Meteorological Society* **88**: 1939–1955.

Browning K, Hill F. 1984. Structure and evolution of a mesoscale convective system near the British Isles. *Quarterly Journal of the Meteorological Society* **110**: 897–913.

Browning KA. 1971. Structure of the atmosphere in the vicinity of large-amplitude Kelvin-Helmholtz billows. *Quarterly Journal of the Royal Meteorological Society* **97**: 283–299.

Browning KA, Bryant GW, Starr JR, Axford DN. 1973. Air motion within Kelvin-Helmholtz billows determined from simultaneous Doppler radar and aircraft measurements. *Quarterly Journal of the Royal Meteorological Society* **99**: 608–618.

Browning KA, Marsham JH, Nicol JC, Perry FM, White BA, Blyth AM, Mobbs SD. 2010. Observations of dual slantwise circulations above a cool undercurrent in a mesoscale convective system. *Quarterly Journal of the Royal Meteorological Society* **136**(647): 354–373.

Browning KA, Marsham JH, White BA, Nicol JC. 2012. A case study of a large patch of billows surmounted by elevated convection. *Quarterly Journal of the Royal Meteorological Society* .

Browning KA, Watkins CD. 1970. Observations of clear air turbulence by high power radar. *Nature* **227**: 260–263.

Bryan G, Knievel J, Parker M. 2006. A multimodel assessment of RKW theory's relevance to squall-line characteristics. *Monthly Weather Review* **134**: 2772–2773.

Bryant GW, Browning KA. 1975. Multi-level measurements of turbulence over the sea during the passage of a frontal zone. *Quarterly Journal of the Royal Meteorological Society* **101**: 35–54.

Burt S. 2005. Cloudburst upon Hendraburnick Down: the Boscastle storm of 16 August 2004. *Weather* **60**: 219–227.

Busack B, Brümmer B. 1988. A case study of Kelvin-Helmholtz waves within an off-shore stable boundary layer: observations and linear model. *Boundary-Layer Meteorology* **44**: 105–135.

Buzzi A, Fantini M, Lippolis G. 1991. Quasi-stationary organized convection in the presence of an inversion near the surface: experiments with a 2-D numerical model. *Meteorology and Atmospheric Physics* **45**: 75–86.

Carbone R, Conway J, Crook N, Moncrieff M. 1990. The generation and propagation of a nocturnal squall line. Part I: Observations and implications for mesoscale predictability. *Monthly Weather Review* **118**: 26–49.

Chapman D, Browning KA. 1997. Radar observations of wind-shear splitting within evolving atmospheric Kelvin-Helmholtz billows. *Quarterly Journal of the Royal Meteorological Society* **123**: 1433–1439.

Chapman D, Browning KA. 1999. Release of potential shearing instability in warm frontal zones. *Quarterly Journal of the Royal Meteorological Society* **125**: 2265–2289.

Charba J. 1974. Application of gravity current model to analysis of squall-line gust front. *Monthly Weather Review* **102**: 140–156.

Chen S, Cotton W. 1988. The sensitivity of a simulated extratropical mesoscale convective system to longwave radiation and ice-phase microphysics. *Journal of the Atmospheric Sciences* **45**: 3897–3910.

Chilson PB, Muschinski A, Schmidt G. 1997. First observations of Kelvin-Helmholtz billows in an upper-level jet stream using VHF frequency domain interferometry. *Radio Science* **32**: 1149–1160.

Chong M, Amayenc P, Scialom G, Testud J. 1987. A tropical squall line observed during the COPT 81 experiment in West Africa. Part I: Kinematic structure inferred from dual-Doppler radar data. *Monthly Weather Review* **115**: 670–694.

Clark P, Browning K, Forbes R, Morcrette C, Blyth A, Lean H. 2012a. The evolution of an MCS over southern England. Part II: Model simulations and sensitivity to microphysics. *Quarterly Journal of the Royal Meteorological Society* Submitted.

Clark P, Browning K, Morcrette C, Blyth A, Forbes R, Brooks B, Perry F. 2012b. The evolution of an MCS over southern England. Part I: Observations. *Quarterly Journal of the Royal Meteorological Society* Submitted.

Colman B. 1990. Thunderstorms above frontal surfaces in environments without positive CAPE. Part I: A climatology. *Monthly Weather Review* **118**: 1103–1122.

Coniglio M, Brooks H, Corfidi S, Weiss S. 2007. Forecasting the maintenance of quasi-linear mesoscale convective systems. *Weather and Forecasting* **22**: 556–570.

Coniglio M, Stensrud D. 2001. Simulation of a progressive derecho using composite initial conditions. *Monthly Weather Review* **129**: 1593–1616.

Coniglio M, Stensrud D, Richman M. 2004. An observational study of derecho-producing convective systems. *Weather and Forecasting* **19**: 320–337.

Corfidi S, Corfidi S, Schultz D. 2008. Elevated convection and castellanus: Ambiguities, significance, and questions. *Weather and Forecasting* **23**: 1280–1302.

Cran J, Pielke R, Cotton W. 1992. Numerical simulation and analysis of a pre-frontal squall line. Part II: Propagation of the squall line as an internal gravity wave. *Journal of the Atmospheric Sciences* **49**: 209–225.

Crook N. 1986. The effect of ambient stratification and moisture on the motion of atmospheric undular bores. *Journal of the Atmospheric Sciences* **43**: 171–181.

Crook N. 1988. Trapping of low-level internal gravity waves. *Journal of the Atmospheric Sciences* **45**: 1533–1541.

Crook N, Moncrieff M. 1988. The effect of large-scale convergence on the generation and maintenance of deep moist convection. *Journal of the Atmospheric Sciences* **45**: 3606–3624.

Cullen MJP. 1993. The unified forecast/climate model. *Meteorological Magazine* **122**: 81–94.

Cunning J. 1986. The Oklahoma-Kansas preliminary regional experiment for STORM-Central. *Bulletin American Meteorological Society* **67**: 1478–1486.

Dabberdt W, Schlatter T, Carr F, Friday E, Jorgensen D, Koch S, Pirone M, Ralph F, Sun J, Welsh P, Wilson J, Zou X. 2004. Multifunctional mesoscale observing networks. *Bulletin American Meteorological Society* **86**: 961–982.

De Silva IPD, Fernando HJS, Eaton F, Hebert D. 1996. Evolution of Kelvin-Helmholtz billows in nature and laboratory. *Earth and Planetary Science Letters* **143**: 217–231.

Derbyshire S, Brown A, Lock A. 1994. The Meteorological Office Large-Eddy Simulation model. *Turbulence and Diffusion Note* (213). Met Office, Exeter,UK.

Doswell C. 2001. Severe convective storms - An overview. *Severe Convective Storms, Meteorological Monographs* (50): 1–26.

Doviak R, Ge R. 1984. An atmospheric solitary gust observed with a Doppler radar, a tall tower and a surface network. *Journal of the Atmospheric Sciences* **41**: 2559–2573.

Drazin PG. 1958. The stability of a shear layer in an unbounded heterogeneous inviscid fluid. *Journal of Fluid Mechanics* **4**: 214–224.

Dudhia J, Moncrieff M, So D. 1987. The two-dimensional dynamics of West African squall lines. *Quarterly Journal of the Royal Meteorological Society* **113**: 121–146.

Dyer A, Hicks B. 1970. Flux-gradient relationships in the constant flux layer. *Quarterly Journal of the Royal Meteorological Society* **96**: 715–721.

Edwards J, Slingo A. 1996. Studies with a flexible new radiation code. Part I. Choosing a configuration for a large-scale model. *Quarterly Journal of the Royal Meteorological Society* **122**: 689–719.

Engerer N, Stensrud D, Coniglio M. 2008. Surface characteristics of observed cold pools. *Monthly Weather Review* **136**: 4839–4849.

Evans J, Doswell C. 2001. Examination of derecho environments using proximity soundings. *Weather and Forecasting* **16**: 329–342.

Forbes R, Clark P. 2003. Sensitivity of extra-tropical cyclone mesoscale structure to the parameterization of ice microphysical processes. *Quarterly Journal of the Meteorological Society* **129**: 1123–1148.

Fovell R. 1991. Influence of the Coriolis force on two-dimensional model storms. *Monthly Weather Review* **119**: 606630.

Fovell R, Mullendore G, Kim S. 2006. Discrete propagtion in numerically simulated nocturnal squall lines. *Monthly Weather Review* **134**: 3735–3752.

Fovell R, Ogura Y. 1988. Numerical simulation of a midlatitude squall line in two dimensions. *Journal of the Atmospheric Sciences* **45**: 3846–3879.

Fovell R, Ogura Y. 1989. Effect of vertical wind shear on numerically simulated multicell storm structure. *Journal of the Atmospheric Sciences* **46**: 3144–3176.

Franklin C, Holland G, May P. 2006. Mechanisms for the generation of mesoscale vorticity features in tropical cyclone rainbands. *Monthly Weather Review* **134**: 2649–2669.

French A, Parker M. 2010. The response of simulated nocturnal convective systems to a developing low-level jet. *Journal of the Atmospheric Sciences* **67**: 3384–3408.

Fritsch J, Forbes G. 2001. Mesoscale convective systems. *Severe Convective Storms, Meteorological Monographs* (50): 323–358.

Fritsch J, Kane R, Chelius C. 1986. The contribution of mesoscale convective weather systems to the warm-season precipitation in the United States. *Journal of Climate and Applied Meteorology* **25**: 1333–1345.

Fritts DC, Palmer TL, Andreassen O, Lie I. 1996. Evolution and breakdown of Kelvin-Helmholtz billows in stratified compressible flows. Part I: Comparison of two-and three-dimensional flows. *Journal of the Atmospheric Sciences* **53**: 3173–3191.

Fritts DC, Rastogi PK. 1985. Convective and dynamical instabilities due to gravity wave motions in the lower and middle atmosphere: Theory and observations. *Radio Science* **20**: 1247–1277.

Fukao S, Luce H, Mega T, Yamamoto MK. 2011. Extensive studies of large-amplitude Kelvin-Helmholtz billows in the lower atmosphere with VHF middle and upper atmosphere radar. *Quarterly Journal of the Royal Meteorological Society* **137**: 1019–1041.

Fulton R ZD, Doviak R. 1990. Initiation of a solitary wave family in the demise of a nocturnal thunderstorm density current. *Journal of the Atmospheric Sciences* **47**: 319–337.

Garner S, Thorpe A. 1992. The development of organized convection in a simplified squall-line model. *Quarterly Journal of the Royal Meteorological Society* **118**: 101–124.

Glickman T. 2000. *Glossary of Meteorology*. American Meteorological Society, second edn.

Goddard J, Eastment J, Thurai M. 1994. The Chilbolton Advanced Meteorological Radar: A tool for multidisciplinary atmospheric research. *Electronics and Communications Engineering Journal* **6**: 77–86.

Goff R. 1976. Vertical structure of thunderstorm outflows. *Monthly Weather Review* **104**: 1429–1440.

Golding B. 1998. Nimrod: A system for generating automated very short range forecasts. *Meteorological Applications* **5**: 1–16.

Golding B, Clark P, May B. 2005. Boscastle flood: Meteorological analysis of the conditions leading to flooding on 16 August 2004. *Weather* **60**: 230–235.

Goldstein S. 1931. On the stability of superposed streams of fluids of different densities. *Proceedings of the Royal Society A* **132**: 524–548.

Goss S, Thompson R, Bookbinder E. 2006. An elevated supercell with damaging wind from the morning of 12 March 2006. In: *23rd Conference on Severe Local Storms*.

Gray MEB, Petch J, Derbyshire SH, Brown AR, Lock AP, Swan HA. 2001. Version 2.3 of the Met Office Large-Eddy Simulation model. *Turbulence and Diffusion Note* : 275–277Met Office, Exeter,UK.

Haertel P, Johnson R. 2000. The linear dynamics of squall line mesohighs and wake lows. *Journal of the Atmospheric Sciences* **57**: 93–107.

Haertel P, Johnson R, Tulich S. 2001. Some simple simulations of thunderstorm outflows. *Journal of the Atmospheric Sciences* **58**: 504–516.

Hallett J, Mossop SC. 1974. Production of secondary ice particles during the riming process. *Nature* **249**: 26–28.

Hardy KR, Glover KM, Mather GK. 1973. Observation of Kelvin-Helmholtz billows and their mesoscale environment by radar, instrumented aircraft, and a dense radiosonde network. *Quarterly Journal of the Royal Meteorological Society* **99**: 279–293.

Horgan K, Schultz D, Hales Jr J, Corfidi S, Johns R. 2007. A five-year climatology of elevated severe convective storms in the United States east of the Rocky Mountains. *Weather and Forecasting* **22**: 1031–1044.

Houser JL, Bluestein HB. 2011. Polarimetric Doppler radar observations of Kelvin-Helmholtz waves in a winter storm. *Journal of the Atmospheric Sciences* **68**: 1676–1702.

Houze Jr R. 2004. Mesoscale Convective Systems. *Reviews of Geophysics* **42**.

Houze Jr RA, Rutledge S, Biggerstaff M, Smull B. 1989. Interpretation of Doppler Weather Radar Displays of Midlatitude Mesoscale Convective Systems. *Bulletin American Meteorological Society* **70**(6): 608–619.

James PK, Browning KA. 1981. An observational study of primary and secondary billows in the free atmosphere. *Quarterly Journal of the Royal Meteorological Society* **107**: 351–365.

Janish P, Johns R, Crawford K. 1996. An evaluation of the 17 August 1994 Lahoma, Oklahoma supercell/MCS event using conventional and non-conventional analysis and forecasting techniques. In: *18th Conference on Severe Local Storms.*

Janjic Z. 1994. The step-mountain eta coordinate model: Further developments of the convection, viscous sublayer and turbulence closure schemes. *Monthly Weather Review* **122**: 927–945.

Janjic Z. 2000. Comments on 'development and evaluation of a convection scheme for use in climate models'. *Journal of the Atmospheric Sciences* **57**: 3686.

Johnson R. 2001. Surface mesohighs and meslows. *Bulletin of the American Meteorological Society* **82**: 13–31.

Jorgensen DP, Murphey H, Wakimoto R. 2004. Rear-inflow evolution in a non-severe bow-echo observed by airborne Doppler radar during BAMEX. In: *22nd Conference on Severe Local Storms.*

Karyampudi V, Koch S, Chen C, Rottman J, Kaplan M. 1995. The influence of the Rocky Mountains on the 13-14 April 1986 severe weather outbreak. Part II: Evolution of a prefrontal bore and its role in triggering a squall line. *Monthly Weather Review* **123**: 1423–1446.

Kessler E. 1974. Model precipitation and vertical air currents. *Tellus* **26**: 519–542.

Klimowski B. 1994. Initiation and development of rear inflow within the 28-29 June 1989 North Dakota mesoconvective system. *Monthly Weather Review* **122**: 765–779.

Klostermeyer J, Rüster R. 1980. Radar observation and model computation of a jet stream-generated Kelvin-Helmholtz instability. *Journal of Geophysical Research* **85**: 2841–2846.

Knupp K. 2006. Observational analysis of a gust front to bore to solitary wave transition within an evolving nocturnal boundary layer. *Journal of the Atmospheric Sciences* **63**: 2016–2035.

Koch S, Clark W. 1999. A nonclassical cold front observed during COPS-91: Frontal structure and the process of severe storm initiation. *Journal of the Atmospheric Sciences* **56**: 2862–2890.

Koch S, Dorian P, Ferrare R, Melfi S, Skillman W, Whiteman D. 1991. Structure of an internal bore and dissipating gravity current as revealed by Raman lidar. *Monthly Weather Review* **119**: 857–887.

Lafore J, Moncrieff M. 1989. A numerical investigation of the organization and interaction of the convective and stratiform regions of tropical squall lines. *Journal of the Atmospheric Sciences* **46**: 521–544.

Laing A, Fritsch J. 1997. The global population of mesoscale convective complexes. *Quarterly Journal of the Royal Meteorological Society* **123**: 389–405.

Laprise R. 1992. The Euler equations of motion with hydrostatic pressure as an independent variable. *Monthly Weather Review* **120**: 197–207.

Lean H, Clark P, Dixon M, Roberts N, Fitch A, Forbes R, Halliwell C. 2008. Characteristics of high-resolution versions of the Met Office Unified Model for forecasting convection over the United Kingdom. *Monthly Weather Review* **136**: 3408–3424.

Leary C, Houze Jr RA. 1979. Melting and evaporation of hydrometeors in precipitation from the anvil clouds of deep tropical convection. *Journal of the Atmospheric Sciences* **36**: 669–679.

Lee I. 1989. Evaluation of cloud microphysics parametrizations for mesoscale simulations. *Atmospheric Research* **24**: 209–220.

LeMone M BG, Zipser E. 1984. Momentum flux by lines of cumulonimbus over the tropical oceans. *Journal of the Atmospheric Sciences* **41**: 1914–1932.

LeMone M. 1983. Momentum transport by a line of cumulonimbus. *Journal of the Atmospheric Sciences* **40**: 1815–1834.

Lin Y, Deal R, Kulie M. 1998. Mechanisms of cell regeneration, development, and propagation within a two-dimensional multicell storm. *Journal of the Atmospheric Sciences* **55**: 18671886.

Lindzen R, Tung K. 1976. Banded convective activity and ducted gravity waves. *Monthly Weather Review* **104**: 1602–1617.

List R (ed). 1984. *Smithsonian meteorological tables*. Smithsonian Institution Press, sixth edn.

Locatelli J, Stoelinga M, Hobbs P. 2002. A new look at the super outbreak of tornadoes on 3 April 1974. *Monthly Weather Review* **130**: 1633–1651.

Locatelli J, Stoelinga M, Hobbs P, Johnson J. 1998. Structure and evolution of an undular bore on the high plains and its effects on migrating birds. *Bulletin of the American Meteorological Society* **79**(6): 1043–1060.

Luce H, Hassenpflug G, Yamamoto M, Fukao S, Sato K. 2008. High-resolution observations with MU radar of a K-H instability triggered by an inertia-gravity wave in the upper part of a jet stream. *Journal of the Atmospheric Sciences* **65**: 1711–1718.

Luce H, Mega T, Yamamoto MK, Yamamoto M, Hashiguchi H, Fukao S, Nishi N, Tajiri T, Nakazato M. 2010. Observations of a Kelvin-Helmholtz instability at a cloud base with the middle and upper atmosphere (MU) and weather radars. *Journal of Geophysical Research* **115**.

Ludlam FH. 1967. Characteristics of billow clouds and their relation to clear-air turbulence. *Quarterly Journal of the Royal Meteorological Society* **93**: 419–435.

Maddox R. 1980. Mesoscale convective complexes. *Bulletin American Meteorological Society* **61**: 1374–1387.

Maddox R, Perkey D, Fritsch J. 1981. Evolution of upper tropospheric features during the development of a mesoscale convective complex. *Journal of the Atmospheric Sciences* **38**: 1664–1674.

Marsham J, Morcrette C, Browning K, Blyth A, Parker D, Corsmeier U, Kalthoff N, Kholer M. 2007. Variable cirrus shading during CSIP IOP 5. I: Effects on the initiation of convection. *Quarterly Journal of the Meteorological Society* **133**: 1643–1660.

Marsham J, Parker D. 2006. Secondary initiation of multiple bands of cumulonimbus over southern Britain. Part II: Dynamics of secondary initiation. *Quarterly Journal of the Meteorological Society* **132**: 1053–1072.

Marsham J, Trier S, Weckwerth T, Wilson J. 2011. Observations of elevated convection initiation leading to a surface-based squall line during 13 June IHOP_2002. *Monthly Weather Review* **139**: 247–271.

Marsham JH, Browning KA, Nicol JC, Parker DJ, Norton EG, Blyth AM, Corsmeier U, Perry FM. 2010. Multi-sensor observations of a wave beneath an impacting rear-inflow jet in an elevated mesoscale convective system. *Quarterly Journal of the Meteorological Society* **136**: 17881812.

McFarquhar G, Timlin M, Rauber R, Jewett B, Grim J, Jorgensen D. 2007. Vertical variability of cloud hydrometeors in the stratiform region of mesoscale convective systems and bow echoes. *Monthly Weather Review* **135**: 3405–3428.

Miles JW. 1961. On the stability of heterogeneous shear flows. *Journal of Fluid Mechanics* **10**: 496–508.

Miles JW, Howard LN. 1964. Note on a heterogeneous shear flow. *Journal of Fluid Mechanics* **20**: 331–336.

Moore J, Czarnetzki A, Market P. 1998. Heavy precipitation associated with elevated thunderstorms in a convectively unstable layer aloft. *Meteorological Applications* **5**: 373–384.

Moore J, Glass F, Graves C, Rochette S, Singer M. 2003. The environment of warm-season elevated thunderstorms associated with heavy rainfall over the central United States. *Weather and Forecasting* **18**: 861–878.

Morrison H CJ, Khvorostyanov V. 2005. A new double-moment microphysics parameterization for application in cloud and climate models. Part I : Description. *Journal of the Atmospheric Sciences* **62**: 1665–1677.

Morrison H, Pinto J. 2006. Intercomparison of bulk microphysics schemes in mesoscale simulations of springtime Arctic mixed-phase stratiform clouds. *Monthly Weather Review* **134**: 1880–1900.

Morrison H TG, Tatarskii V. 2009. Impact of cloud microphysics on the development of trailing stratiform precipitation in a simulated squall line: Comparison of one- and two-moment schemes. *Monthly Weather Review* **137**: 991–1007.

Mueller C, Carbone R. 1987. Dynamics of a thunderstorm outflow. *Journal of the Atmospheric Sciences* **44**: 1879–1898.

Nappo CJ. 1991. Sporadic breakdowns of stability in the PBL over simple and complex terrain. *Boundary-Layer Meteorology* **54**: 68–97.

Ogura Y, Liou M. 1980. The structure of a midlatitude squall line: A case study. *Journal of the Atmospheric Sciences* **37**: 553–567.

Pandya R, Durran D. 1996. The influence of convectively generated thermal forcing on the mesoscale circulation around squall lines. *Journal of the Atmospheric Sciences* **53**(20): 2924–2951.

Parker M. 2008. Response of simulated squall lines to low-level cooling. *Journal of the Atmospheric Sciences* **65**: 1323–1341.

Parker M, Johnson R. 2000. Organizational modes of midlatitude mesoscale convective systems. *Monthly Weather Review* **128**: 3413–3436.

Parker M, Johnson R. 2004. Structure and dynamics of quasi-2D mesoscale convective systems. *Journal of the Atmospheric Sciences* **61**: 545–567.

Patnaik PC, Sherman FS, Corcos GM. 1976. A numerical simulation of Kelvin-Helmholtz waves of finite amplitude. *Journal of Fluid Mechanics* **73**: 215–240.

Paulson C. 1970. The mathematical representation of wind speed and temperature profiles in the unstable atmospheric surface layer. *Journal of Applied Meteorology* **9**: 857–861.

Peltier WR, Hallé J, Clark TL. 1978. The evolution of finite-amplitude Kelvin-Helmholtz billows. *Geophysical and Astrophysical Fluid Dynamics* **10**: 53–87.

Perry F. 2008. Quantification of coherent structures in the atmospheric boundary layer. PhD thesis, University of Leeds.

Raymond D, Rotunno R. 1989. Response of a stably stratified flow to cooling. *Journal of the Atmospheric Sciences* **46**: 2830–2837.

Rochette S, Moore J. 1996. Initiation of an elevated mesoscale convective system associated with heavy rainfall. *Weather and Forecasting* **11**: 443–457.

Rockwood A, Maddox R. 1988. Mesoscale and synoptic scale interactions leading to intense convection: The case of 7 June 1982. *Weather and Forecasting* **3**: 51–68.

Rottman J, Simpson J. 1989. The formation of internal bores in the atmosphere: A laboratory model. *Quarterly Journal of the Meteorological Society* **115**: 941–963.

Rotunno R, Klemp J, Weisman M. 1988. A theory for strong, long-lived squall lines. *Journal of the Atmospheric Sciences* **45**: 463–485.

Rutledge S, Houze Jr R, Biggerstaff M, Matejka T. 1988. The Oklahoma-Kansas mesoscale convective system of 10-11 June 1985: Precipitation structure and single-Doppler radar analysis. *Monthly Weather Review* **116**: 1409–1430.

Schmidt J, Cotton W. 1989. A high plains squall line associated with severe surface winds. *Journal of the Atmospheric Sciences* **46**(3): 281–302.

Schmidt J, Cotton W. 1990. Interactions between upper and lower tropospheric gravity waves on squall line structure and maintenance. *Journal of the Atmospheric Sciences* **47**(10): 1205–1222.

Schumacher R. 2009. Mechanisms for quasi-stationary behaviour in simulated heavy-rain-producing convective systems. *Journal of the Atmospheric Sciences* **66**: 1543–1568.

Schumacher R, Johnson R. 2006. Characteristics of U.S. extreme rain events during 1999-2003. *Weather and Forecasting* **21**: 69–85.

Schumacher R, Johnson R. 2008. Mesoscale processes contributing to extreme rainfall in a midlatitude warm-season flash flood. *Monthly Weather Review* **136**: 3964–3986.

Scorer R. 1949. Theory of waves in the lee of mountains. *Quarterly Journal of the Meteorological Society* **75**: 41–56.

Scorer RS. 1969. Billow mechanics. *Radio Science* **4**: 1299–1308.

Scotti RS, Corcos GM. 1972. An experiment on the stability of small disturbances in a stratified free shear layer. *Journal of Fluid Mechanics* **52**: 499–528.

Simpson J. 1969. A comparison between laboratory and atmospheric density currents. *Quarterly Journal of the Royal Meteorological Society* **95**: 758–765.

Simpson J. 1997. *Gravity Currents in the Environment and Laboratory*. Cambridge University Press, second edn.

Singh S, Mahajan KK, Choudhary RK. 1999. Detection of Kelvin-Helmholtz instability with the Indian mesosphere-stratosphere-troposphere radar: A case study. *Journal of Geophysical Research* **104**: 3937–3945.

Skamarock W, Klemp J, Dudhia J, Gill D, Barker D, Duda M, Huang X, Wang W, Powers J. 2008. A description of the advanced research WRF version 3 NCAR technical note June 2008. Technical Report TN-475+STR, NCAR.

Slingo A, Schrecker H. 1982. On the shortwave radiative properties of stratiform water clouds. *Quarterly Journal of the Royal Meteorological Society* **108**: 407–426.

Smull B. 1995. Convectively induced mesoscale weather systems in the tropical and warm-season midlatitude atmosphere. *Reviews of Geophysics* **33**.

Smull B, Houze Jr R. 1987. Rear inflow in squall lines with trailing stratiform precipitation. *Monthly Weather Review* **115**: 2869–2889.

Stensrud D, Coniglio M, Davies-Jones R, Evans J. 2005. Comments on " 'A theory for strong long-lived squall lines' revisited". *Journal of the Atmospheric Sciences* **62**: 2989–2996.

Sutherland B. 2002. Interfacial gravity currents. I. Mixing and entrainment. *Physics of Fluids* **14**: 2244–2254.

Swann H. 1996. The development and validation of a microphysics scheme for cloud resolving simulations of deep convection. PhD thesis, University of Reading.

Sykes RI, Lewellen WS. 1983. A numerical study of breaking Kelvin-Helmholtz billows using a Reynolds-stress turbulence closure model. *Journal of the Atmospheric Sciences* **39**: 1506–1520.

Taylor GI. 1931. Effect of variation in density on the stability of superposed streams of fluid. *Proceedings of the Royal Society A* **132**: 499–523.

Thorpe SA. 1968. A method of producing shear in a stratified fluid. *Journal of Fluid Mechanics* **32**: 693–704.

Thorpe SA. 1969. Experiments on the stability of stratified shear flows. *Radio Science* **4**: 1327–1331.

Thorpe SA. 1971. Experiments on the instability of stratified shear flows: Miscible fluids. *Journal of Fluid Mechanics* **46**: 299–319.

Thorpe SA. 1973a. Experiments on instability and turbulence in a stratified shear flow. *Journal of Fluid Mechanics* **61**: 731–751.

Thorpe SA. 1973b. Turbulence in stably stratified fluids: A review of laboratory experiments. *Boundary-Layer Meteorology* **5**: 95–119.

Thorpe SA. 2002. The axial coherence of Kelvin-Helmholtz billows. *Quarterly Journal of the Royal Meteorological Society* **128**: 1529–1542.

Trapp R, Schultz D, Ryzhkov V, Holle R. 2001. Multiscale structure and evolution of an Oklahoma winter precipitation event. *Monthly Weather Review* **129**: 486–501.

Trier S, Davis C, Ahijevych D, Weisman M, Bryan G. 2006. Mechanisms supporting long-lived episodes of propagating nocturnal convection within a 7-day WRF model simulation. *Journal of the Atmospheric Sciences* **63**: 2437–2461.

Trier S, Marsham J, Davis C, Ahijevych D. 2011. Numerical simulations of the post-sunrise reorganization of a nocturnal mesoscale convective system during 13 June IHOP_2002. *Journal of the Atmospheric Sciences* **68**: 2988–3011.

Tritton DJ. 1985. *Physical fluid dynamics*. Van Nostrand Reinhold (UK).

Wakimoto RM. 1982. The life cycle of thunderstorm gust fronts as viewed with Doppler radar and rawinsonde data. *Monthly Weather Review* **110**: 1060–1082.

Wang PY, Parsons DB, Hobbs PV. 1983. The mesoscale and microscale structure and organization of clouds and precipitation in midlatitude cyclones. VI: Wavelike rainbands associated with a cold-frontal zone. *Journal of the Atmospheric Sciences* **40**: 543–558.

Webb E. 1970. Profile relationships: The log-linear range, and extension to strong stability. *Quarterly Journal of the Royal Meteorological Society* **96**: 67–90.

Weckwerth T, Parsons D, Koch S, Moore J, LeMone M, Demoz B, Flamant C, Geerts B, Wang J, Feltz W. 2004. An overview of the International H2O Project IHOP_2002 and some preliminary highlights. *Bulletin American Meteorological Society* **85**: 253–277.

Weckwerth TM, Wilson JW, Wakimoto R. 1996. Thermodynamic variability within the boundary layer due to horizontal convective rolls. *Monthly Weather Review* **124**: 769–784.

Weisman M. 1992. The role of convectively generated rear-inflow jets in the evolution of long-lived mesoscale systems. *Journal of the Atmospheric Sciences* **49**: 1826–1847.

Weisman M, Klemp J, Rotunno R. 1988. Structure and evolution of numerically simulated squall lines. *Journal of the Atmospheric Sciences* **45**: 1990–2013.

Weisman M, Rotunno R. 2004. "A theory for strong long-lived squall lines" revisited. *Journal of the Atmospheric Sciences* **61**: 361–382.

Weisman M, Rotunno R. 2005. Reply. *Journal of the Atmospheric Sciences* **62**: 2997–3002.

Wicker L, Skamarock W. 2002. Time splitting methods for elastic models using forward time schemes. *Monthly Weather Review* **130**: 2088–2097.

Wilson J, Roberts R. 2006. Summary of convective storm initiation and evolution during IHOP: Observational and modelling perspective. *Monthly Weather Review* **134**: 23–47.

Wood I, Simpson J. 1984. Jumps in layered miscible fluids. *Journal of Fluid Mechanics* **140**: 329–342.

Wulfmeyer V, Behrendt A, Bauer HS, Kottmeier C, Corsmeier U, Blyth A, Craig G, Schumann U, Hagen M, Crewell S, Di Girolamo P, Flamant C, Miller M, Montani A, Mobbs S, Richard E, Rotach M, Arpagaus M, Russchenberg H, Schlüssel P, König M, Gärtner V, Steinacker R, Dorninger M, Turner D, Weckwerth T, Hense A, Simmer C. 2008. The Convective and Orographically-induced Precipitation Study: A research and development project of the World Weather Research Program for improving quantitative precipitation forecasting in low-mountain regions. *Bulletin of the American Meteorological Society* **89**: 1477–1486.

Yang M, Houze Jr R. 1995. Sensitivity of squall-line rear inflow to ice microphysics and environmental humidity. *Monthly Weather Review* **123**: 3175–3193.

Yuter S, Houze R. 1995. Three-dimensional kinematic and microphysical evolution of Florida cumulonimbus. Part I: Spatial distribution of updrafts, downdrafts and precipitation. *Monthly Weather Review* **123**: 1921–1940.

Zhang D, Gao K. 1989. Numerical simulation of an intense squall line during 10-11 June 1985 PRE-STORM. Part II: Rear inflow, surface pressure perturbations and stratiform precipitation. *Monthly Weather Review* **117**: 2067–2094.

Zipser E. 1982. *Use of a conceptual model of the life cycle of mesoscale convective systems to improve very-short-range forecasts.* Academic Press, pp. 191–204.